

## University of Southampton Research Repository

Copyright © and Moral Rights for this thesis and, where applicable, any accompanying data are retained by the author and/or other copyright owners. A copy can be downloaded for personal non-commercial research or study, without prior permission or charge. This thesis and the accompanying data cannot be reproduced or quoted extensively from without first obtaining permission in writing from the copyright holder/s. The content of the thesis and accompanying research data (where applicable) must not be changed in any way or sold commercially in any format or medium without the formal permission of the copyright holder/s.

When referring to this thesis and any accompanying data, full bibliographic details must be given, e.g.

Thesis: Author (Year of Submission) "Full thesis title", University of Southampton, name of the University Faculty or School or Department, PhD Thesis, pagination.

Data: Author (Year) Title. URI [dataset]



**University of Southampton**

Faculty of Natural and Environmental Sciences

Chemistry

**Efficient Investigation of Continuous Reaction Processes Using Gradients**

by

**Stephen Thomas Alston**

ORCID ID: 0000-0003-3829-0077

Thesis for the degree of Doctor of Philosophy

May 2019





# University of Southampton

## Abstract

Faculty of Natural and Environmental Sciences

Chemistry

Thesis for the degree of Doctor of Philosophy

Efficient Investigation of Continuous Reaction Processes Using Gradients

by

Stephen Thomas Alston

Continuous chemistry has become a commonplace tool in laboratories in both academic and industry settings. The ease of automation and an accurate control over parameters have allowed continuous chemistry to excel in reaction optimisation and investigation as well as extraction of kinetic data. Additionally, several methods have been reported in the literature which utilise unique aspects of performing a reaction continuously such as varying the reaction time or temperature during an experiment.

Presented herein are two flow methodologies which utilise the generation of gradients to extract large amounts of data from a single experiment. The first is the switch-off method for the optimisation of irradiance time in a single flow photoreaction and is tested using a [2+2] photocyclisation reaction with both in-line and off-line data acquisition.

The second methodology is the concentration gradient methodology for extraction of reagent concentration data in a single experiment. The gradients are used in reagent concentration optimisation, ligand concentration optimisation, functional group compatibility scoping, and reaction troubleshooting.

A third methodology is presented which utilises multi-port valves to redirect the flow of a reagent plug repeatedly through an in-line detector to generate multiple time points in a single reaction. Several different setups are reported, and the methodology is combined with the concentration gradient method to generate both concentration and time data in a single experiment.



# Table of Contents

<b>Table of Contents .....</b>	<b>i</b>
<b>Research Thesis: Declaration of Authorship.....</b>	<b>iii</b>
<b>Acknowledgements.....</b>	<b>v</b>
<b>Abbreviations .....</b>	<b>vii</b>
<b>Chapter 1 Introduction .....</b>	<b>1</b>
1.1 Flow chemistry: A tool for production and process intensification.....	1
1.2 Going beyond synthesis: Rapid optimisation and reaction kinetics .....	2
1.3 Summary .....	26
<b>Chapter 2 Characterisation of Reactor Properties and Flow Regimes .....</b>	<b>28</b>
2.1 Introduction .....	28
2.2 Fluid mechanical properties and their characterisation .....	28
2.3 Reagent mixing.....	51
2.4 Summary .....	54
<b>Chapter 3 Optimisation of Irradiance Times – The Switch-Off Method.....</b>	<b>55</b>
3.1 Photochemistry .....	55
3.2 The switch-off method .....	59
3.3 Summary .....	71
<b>Chapter 4 The concentration gradient method .....</b>	<b>72</b>
4.1 Introduction .....	72
4.2 Concentration gradient method .....	73
4.3 Testing the methodology: The Heck cross-coupling reaction .....	81
4.4 Copper-free Sonogashira .....	104
4.5 Summary .....	122
<b>Chapter 5 Multi time point generation .....</b>	<b>124</b>
5.1 Introduction .....	124
5.2 Reciprocating flow .....	124
5.3 Non-reciprocating flow .....	131

5.4	Case study: Triazole formation .....	155
5.5	Summary.....	171
<b>Chapter 6</b>	<b>Conclusion .....</b>	<b>173</b>
<b>Chapter 7</b>	<b>Experimental .....</b>	<b>175</b>
7.1	Instrumentation and techniques .....	175
7.2	Procedures.....	177
7.3	Python .....	235
<b>Chapter 8</b>	<b>References.....</b>	<b>246</b>

## Research Thesis: Declaration of Authorship

Print name:	Stephen Thomas Alston
-------------	-----------------------

Title of thesis:	Efficient Investigation of Continuous Reaction Processes Using Gradients
------------------	--

I declare that this thesis and the work presented in it are my own and has been generated by me as the result of my own original research.

I confirm that:

1. This work was done wholly or mainly while in candidature for a research degree at this University;
2. Where any part of this thesis has previously been submitted for a degree or any other qualification at this University or any other institution, this has been clearly stated;
3. Where I have consulted the published work of others, this is always clearly attributed;
4. Where I have quoted from the work of others, the source is always given. With the exception of such quotations, this thesis is entirely my own work;
5. I have acknowledged all main sources of help;
6. Where the thesis is based on work done by myself jointly with others, I have made clear exactly what was done by others and what I have contributed myself;
7. None of this work has been published before submission

Signature:		Date:	28-May-2019
------------	--	-------	-------------



## Acknowledgements

I would like to thank my supervisor Prof. Richard Whitby for his knowledge, enthusiasm, and encouragement throughout my time at Southampton. Particularly his support in generating and discussing new and interesting ideas to test in flow was invaluable for this project. I would also like to thank the members of the Whitby group and my industry supervisor Matt Hughes for providing support throughout this project.

I would also like to thank Dr John Langley, Ms Julie Herniman in Mass Spectrometry, Dr Neil Wells in NMR and the glassblowing staff at Southampton. Additionally, Mark and Keith in stores were always helpful not only in providing the stores service but for entertainment and many conversations over the years.

I would like to particularly thank the people who through various means, helped ensure I kept my sanity over the years:

- My friends within chemistry who provided a never-ending source of gossip and entertainment
- My friends outside of chemistry for providing an escape from chemistry
- My family for putting up with me throughout my education

Without all of these people, I would not be where I am today.

Finally, I would like to express my gratitude to the EPSRC and Syngenta for the funding this project.





## Abbreviations

Abbreviation/Acronym	Definition
°C	Degrees Celsius
μL	Microlitre
BORIS	Bristol online reaction investigation software
Bipy	2,2'-Bipyridine - Wikipedia
[BMIm ]	1-Butyl-3-methylimidazolium
C22	Cryptand 22
CSTR	Continuous stirred tank reactor
cm	Centimetre
CuAAC	Copper catalysed alkyne azide cycloaddition
DABCO	1,4-Diazabicyclo[2.2.2]octane
DBU	1,8-Diazabicyclo(5.4.0)undec-7-ene
DEPT	Distortionless enhancement by polarization transfer
DFT	Density Functional Theory
DIPEA	<i>N,N</i> -Diisopropylethylamine
Dm	Decimetre
DMC	Dimethyl carbonate
DMF	<i>N,N</i> -Dimethylformamide
DMSO	Dimethylsulfoxide
DoE	Design of experiment
DPPB	Bis(diphenylphosphino)butane
DPPE	Bis(diphenylphosphino)ethane
DPPF	1,1'-Bis(diphenylphosphino)ferrocene
DPPM	Bis(diphenylphosphino)methane
DPPP	Bis(diphenylphosphino)propane
DTBPF	1,1'-Bis(di- <i>tert</i> -butylphosphino)ferrocene
ETFE	Ethylene tetrafluoroethylene
FEP	Polyfluoroethylenepropylene
FT-IR	Fourier-transform infrared spectroscopy
FWHM	Full width at half maximum
g	Gram
GC	Gas chromatography
GLC	Gas-liquid chromatography
h	Hour
HPLC	High performance liquid chromatography
HRMS	High resolution mass spectrometry

Abbreviation/Acronym	Definition
Hz	Hertz
ID	Internal diameter
IR	Infrared
JohnPhos	(2-Biphenyl)di- <i>tert</i> -butylphosphine
kJ	Kilojoules
LED	Light emitting diode
LRMS	Low resolution mass spectrometry
M	Molarity
m	Metre
min	Minute
mL	Millilitre
mm	Millimetre
mol	Mole
MOXA	3-Methyl-2-oxazolidinone
MS	Mass spectrometry
NHC	<i>N</i> -Heterocyclic carbene
nm	Nanometre
NMR	Nuclear magnetic resonance
PFA	Perfluoroalkoxy alkane
Phen	1,10-Phenanthroline
PMA	Phosphomolybdic acid
ppm	Parts per million
rbf	Round bottom flask
r.t	Room temperature
s	Second
SMS	Super modified simplex
SNOBFIT	Stable noisy optimisation by branch and fit
TBAB	Tetra- <i>n</i> -butylammonium bromide
Terpy	2,2';6',2''-terpyridine
<i>tert</i> -butyl-MePhos	2-Di- <i>tert</i> -butylphosphino-2'-methylbiphenyl
THF	Tetrahydrofuran
TTBP	Tri- <i>tert</i> -butylphosphonium tetrafluoroborate
TUV	Tunable ultra violet
UV	Ultraviolet
W	Watt
wrt	With respect to
XantPhos	4,5-Bis(diphenylphosphino)-9,9-dimethylxanthene

# Chapter 1 Introduction

## 1.1 Flow chemistry: A tool for production and process intensification

### 1.1.1 Why continuous chemistry?

Continuous chemistry has several well-described benefits over traditional batch chemistry<sup>1</sup> which have increased its occurrence in the fields of production and process intensification. These include excellent control over reaction conditions and temperature due to an increase in surface area<sup>2</sup>, this combined with the comparatively small reactor volumes allows for highly energetic or dangerous reagents to be used<sup>3–9</sup> enabling previously “forgotten and forbidden” chemistries<sup>10,11</sup> to be attempted both in research and at an industrially useful scale. An increase in mass transfer<sup>12</sup> is also seen due to a decrease in mixing distance over batch and additional mixing effects due to the nature of pumping through tubes (Section 2.2). These advantages combined with an overall minimisation of waste make flow chemistry an excellent tool for green chemistry<sup>13–15</sup>.

Multi-step reactions can be simpler to accomplish in flow with a smaller footprint and setup compared to batch methods<sup>16–18</sup> resulting in multi-step synthesis of key pharmaceutical compounds in an apparatus approximately the size of a refrigerator<sup>19</sup>. Employing flow chemistry has been simplified by several commercial examples of reactor technologies from the mg to the tonne scale<sup>20–22</sup>. As such continuous processes have been applied across all stages of chemical manufacture<sup>17,23–25</sup> including within production<sup>26</sup>, discovery<sup>27</sup> and process intensification<sup>28–31</sup>.

### 1.1.2 Why not continuous chemistry?

Whilst there are numerous advantages to continuous chemistry, there are several disadvantages which have been limiting the applicability of flow chemistry<sup>32–34</sup>.

#### 1. Cost

Whilst several different commercial options exist for flow systems, the cost of pumps, reactors, in-line monitoring equipment and control software is still high and this creates a large barrier for a lot of groups especially those who only have a single use case for continuous chemistry.

The cost is not a one-time issue either as maintaining the systems also costs money with necessary replacement parts such as ferrules, tubing, check valves and back pressure regulators regularly needing to be purchased for a high price.

Several groups<sup>35–37</sup> have designed their own flow systems to minimise this cost however this is not suitable or possible for every academic or industrial group.

### 2. Solids

The use of solids as starting materials, intermediates, or products in the reaction can cause a restriction in the reactor<sup>38</sup> leading to a potentially dangerous increase in pressure or even a complete blockage of the flow path ending the reaction.

Whilst several technologies do exist for handling of solids<sup>39</sup> such as sonication<sup>40</sup> or the use of peristaltic pumps<sup>41</sup> or CSTRs<sup>42,43</sup>, they suffer from high cost from new equipment which generally increases the barrier to entry for research chemists and does not guarantee a solution to the problem.

### 3. Specialist knowledge

The successful application of continuous chemistry requires a skill set not frequently taught to chemistry undergraduates, fluid mechanics and engineering/maintenance of the pump systems. Without this knowledge, the chemist may encounter problems such as blockages or mixing and be unaware of potential solutions or simple engineering fixes to pump issues.

## 1.2 Going beyond synthesis: Rapid optimisation and reaction kinetics

### 1.2.1 The status quo

Traditionally the optimisation of reactions and the extraction of reaction kinetics using batch chemistry has been easier than utilising flow chemistry because of the ability to sample multiple time points easily, throughout the course of the reaction. Whereas with flow you are limited to either a single in-line measurement or a single measurement from a sample collected at the outflow of the system. Therefore, to generate reaction time data, you have to run several reactions in flow to match the output of kinetic information from a single batch. Additionally, when obtaining a measurement, it is conventionally desired to monitor the steady state of the reaction mixture, which requires pumping at least 1.5 reactor volumes under the required conditions meaning that it can take 5 times as long when using flow compared to batch to generate a kinetic profile of a reaction.<sup>32</sup> However, an advantage in using flow chemistry to obtain kinetic data is a tighter control over reaction conditions as well as mass and heat transfer leading to a greater robustness in the acquired data. A general feature of reaction profiling is that if mixing is poor, transport phenomena may hinder accurate collection of intrinsic reaction kinetics<sup>44</sup>.

Presented herein are recent reported examples of rapid reaction optimisation and kinetic analysis utilising flow chemistry.

### 1.2.2 Automation of reactions – optimisation of reaction conditions

Most equipment used in flow chemistry is controllable *via* a computer interface, either through proprietary software<sup>45,46</sup> or directly through RS232 commands<sup>47</sup>. As such flow chemistry has been a key technology for the automation of organic synthesis<sup>48,49</sup>, allowing complex multi-step syntheses to be automatically performed including downstream processing steps. Detailed here is a representative selection from the recent literature.

Ley *et al*<sup>50</sup> have reported an example where the Flow Commander software was used to automatically probe a variety of conditions for the formation of a imidazopyridine compound in the preparation of casein kinase I inhibitors (Figure 1.1).

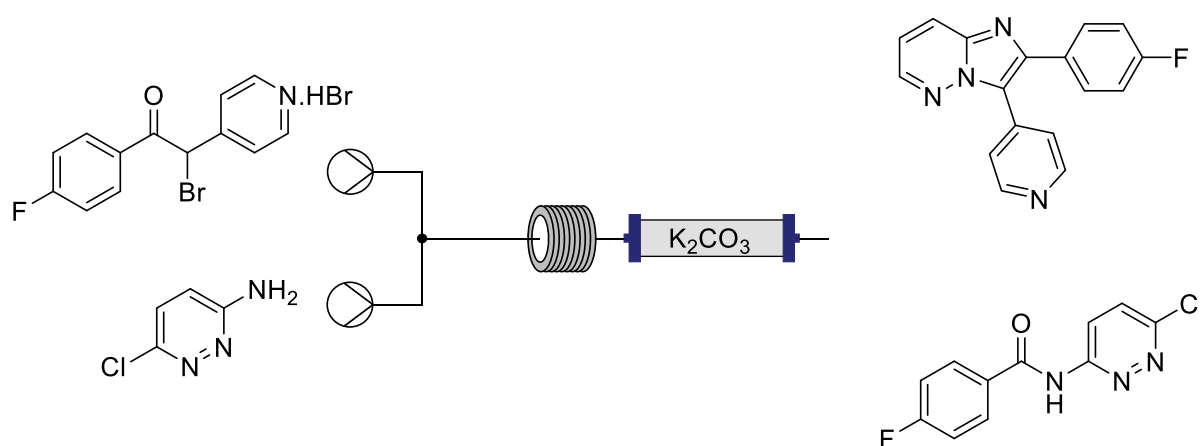
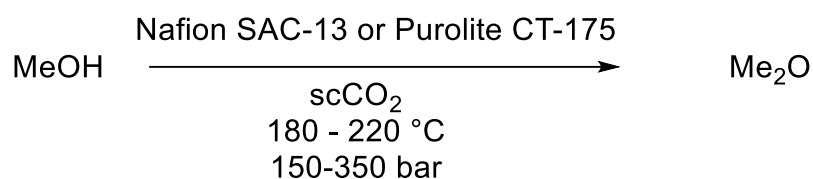


Figure 1.1: Flow setup for formation of imidazopyridine compounds. Residence time, temperature, stoichiometry all varied in a series of DoE experiments to optimise product formation.

They set up a series of DoE<sup>51</sup> type reactions to run automatically from feeds of reagents and found that when varying reaction time, temperature, ratio of starting materials and the inclusion of an additive, around 20 experiments were required to optimise a reaction. In total this optimisation took 14.7 hours of reaction time however only 30 minutes of this involved user intervention, allowing the chemist to focus on other activities. A downside to this is it requires a large amount of starting material, 1.5 g reported in this case, resulting in expense and waste. However switching to a microfluidic reactor<sup>52,53</sup> would lower the total amount needed although this could introduce problems such as clogging of the pathways<sup>54</sup> or issues stemming from the high pressure drop of the system<sup>55</sup>

Poliakoff *et al* have also reported an automated reactor which utilises supercritical  $CO_2$ <sup>56</sup>. They obtain rapid data acquisition and reaction screening by having a small volume reactor bed combined with in-line GC monitoring running an isothermal method to remove wait times for

cooling the oven. Automation of reaction conditions was achieved by pre-programming the pumps to change flow rates after the system had reached steady state and a sample had been taken. A controllable heated reactor was timed to synchronise with this so both residence time and reactor temperature could be probed. Using this reactor, they tested the acid catalysed reaction of MeOH to form Me<sub>2</sub>O (Scheme 1.1) probing 85 different reaction conditions, and found that as residence time and temperature increases, so too does yield of Me<sub>2</sub>O. The use of the methodology demonstrated a large saving in time over manual reactions as they calculated it would take approximately 30 working days with the manual reactor compared to 14 hours with the automated.



Scheme 1.1: Reaction scheme for the formation of Me<sub>2</sub>O from MeOH in a scCO<sub>2</sub> solvent.

Ley *et al*<sup>57</sup> took the automation a step further by introducing a Raspberry Pi<sup>58</sup> computer and a custom written python<sup>59</sup> control system for the control and monitoring of a flow setup. Initially the system was used as a monitoring device for continuous heterogeneous hydration of pyrazine-2-carbonitrile (Figure 1.2), with the control software taking input from in-line IR and the temperature and pressure readouts of the reactor. Collection of the product was only taken when these monitored values were constant and upon deviation, the reaction stream was sent to waste for a set length of time to allow the steady state to be reached.

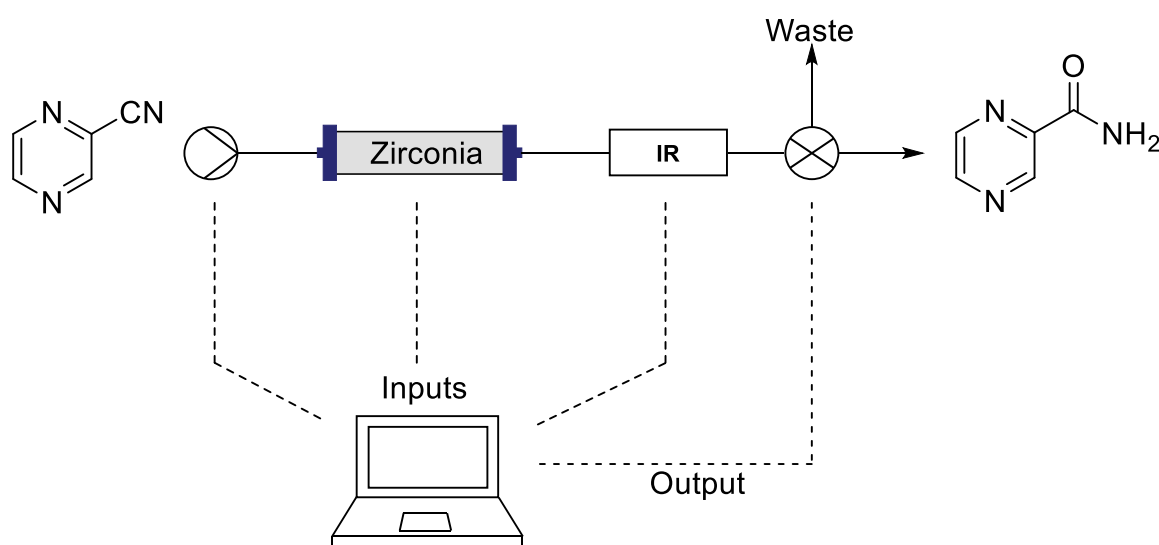


Figure 1.2: Flow setup for heterogeneous hydration of pyrazine-2-carbonitrile. Computer takes inputs from IR, pump and reactor to determine whether to send the output to waste or collection.

They then applied the system to the reduction of the aromatic carboxamide utilising their control system to perform a series of DoE experiments to optimise the reaction. 12 experiments were automatically performed using the software and it was found that increasing the pressure of hydrogen caused an increase in conversion to the product with a similar positive dependence on temperature and flow rate.

They then combined the two steps with the first transformation being fed into a reservoir, which the second step drew from. In order to ensure that there was sufficient reagent for the second step a coloured float was placed into the reservoir, which a webcam was constantly measuring the location of and feeding this into the control software. The second reaction would only start when the reservoir was sufficiently full and would automatically switch to pumping solvent when the feedstock was low (Figure 1.3).

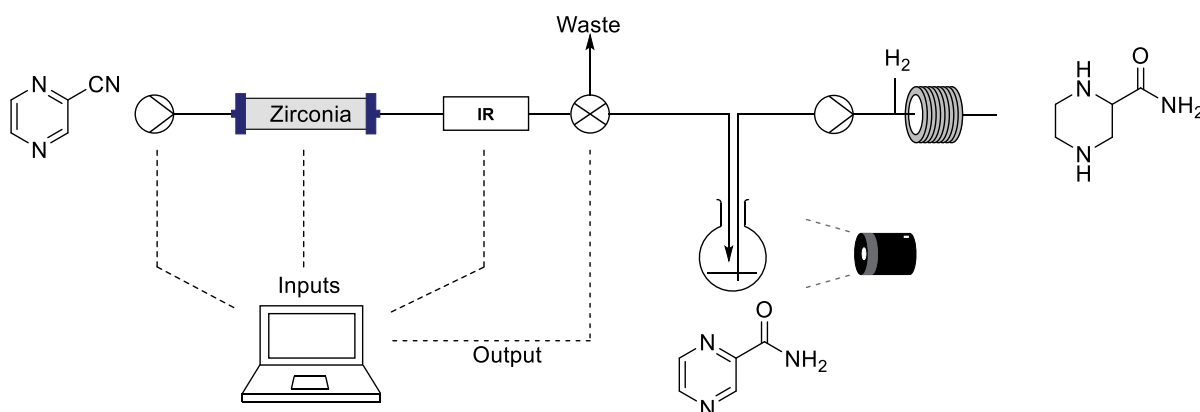


Figure 1.3: Combined flow setup for two step synthesis. Camera detects level of reservoir to start/stop the second stage depending on the level of the output from the first step.

### 1.2.3 Closed loop optimisation

Whilst the pre-planning of reactions and use of DoE does save the chemist time when optimising that reaction, there is the possibility that the optimal conditions will be reached after the first couple of experiments. Therefore, unless the chemist routinely checks the results after each experiment, which somewhat takes away the advantage of automated reactions, experimental time and reagents will be wasted on sub-optimal conditions.

Closed loop optimisation can overcome this by using the result from the in-line analysis of one reaction, to determine the best conditions for the subsequent reactions using various optimisation algorithms (Figure 1.4).

## Chapter 1

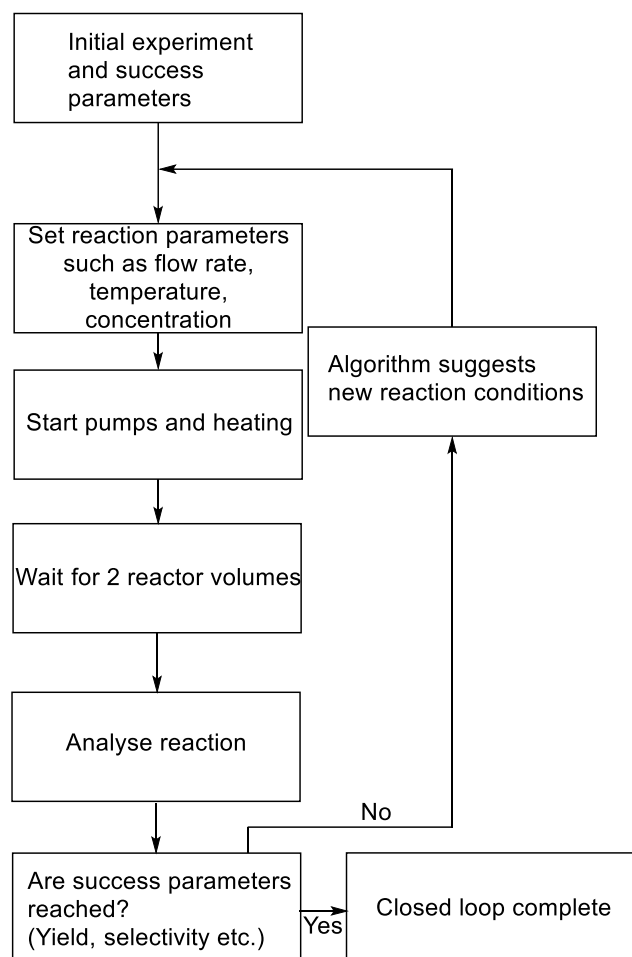


Figure 1.4: Flow chart for basic closed loop reaction automation. After an initial experiment or set of experiments are performed, an algorithm determines the next reaction conditions. This cycle continues until pre-set end conditions are reached such as yield or number of experiments.

Examples of common optimisation algorithms are:

1. Nelder-Mead simplex method<sup>60</sup> which works by performing an initial set of experiments across the reaction space which are then ordered by decreasing reaction success ( $x_1, \dots, x_{n+1}$  where  $n$  = number of dimensions).

The centroid ( $x_o$ ) of all of the points except  $x_{n+1}$  is then calculated and a reflected point is calculated and tested using  $x_r = x_o + \alpha(x_o - x_{n+1})$  where  $\alpha > 0$ .

If  $x_r$  is not the highest result but is better than the second worst, then the worst result is replaced by  $x_r$  and the process is repeated.

If  $x_r$  is the highest result, then an expanded point ( $x_e$ ) is tested where  $x_e = x_o + \gamma(x_r - x_o)$  and  $\gamma > 1$ .



If  $x_e > x_o$  then replace the worst point with the expanded point and repeat the process, else replace the worst point with the reflected result and repeat.

If it is certain that  $x_r$  gives a better result than the second-best point, then it is highly likely that better conditions will be inside the simplex. As such, a contraction of the simplex can be calculated using  $x_c = x_o + \rho(x_{n+1} - x_o)$  where  $0 < \rho \leq 0.5$ . If  $x_c$  is better than the worst point, replace that point with  $x_c$  and repeat the process. These steps are repeated until predefined stop conditions are reached.

The method has been adapted in the Super Modified Simplex (SMS)<sup>61</sup> method which varies the location of the new vertices of the simplex. After the worst result is determined and the reflected and centroid locations are calculated, a second-order polynomial curve is fitted to  $x_n$ ,  $x_o$ , and  $x_r$ . Extrapolation of the curve beyond the vertices and taking the maximum point gives the new reaction conditions allowing the method to more easily cope with noise in the results and give the optimum in fewer reactions (Figure 1.5).

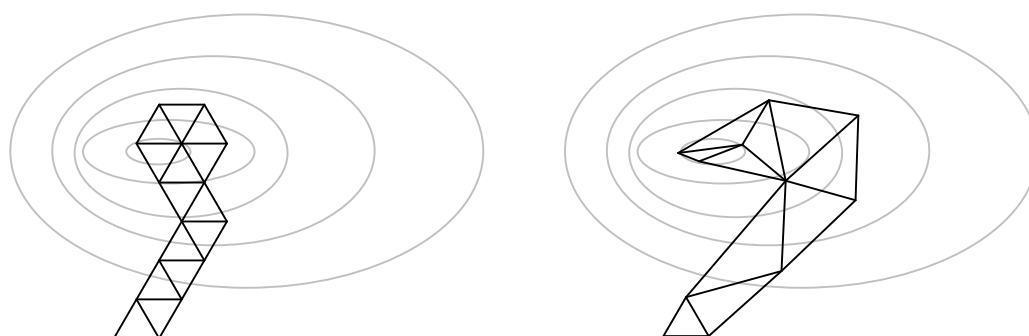


Figure 1.5: Graphical representation of experiment optimisation by basic Simplex (Left) and SMS (Right). Of note is the smaller number of reactions for SMS and the slightly increased coverage of the reaction space.

3. Gradient descent method<sup>62</sup>, which works by performing an initial set of reactions, usually chosen by DoE, and fitting the results to a plane. After calculation of the gradients for the data, the next conditions to be tested can be calculated using Equation 1.1, with the start point being the centre of the DoE experiments. The process is then repeated until the optimal conditions are found.

$$b = a - \gamma \Delta f(a)$$

*b = New condtions*

*a = Current conditions*

*$\gamma$  = Step size*

*$f(a)$  = Direction of gradient*

Equation 1.1: General equation for calculation of new reaction conditions using gradient descent method

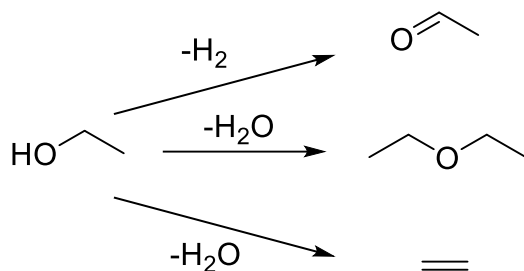
These methods listed, only find local maxima and if the reaction has several peak areas under the varying conditions, then the algorithms may finish in a non-optimal local maxima rather than the global maxima.

Global algorithms do exist such as the Stable Noisy Optimisation by Branch and Fit (SNOBFIT)<sup>63</sup> which works by performing an initial set of experiments covering a wide range of the set reaction boundaries. It then uses any maxima it finds as new evaluation areas to find the local maxima and also performs experiments in regions of unexplored conditions to test for the global maxima. The method also benefits from needing only boundaries on the variables set whereas the other methods require initial experiments to be planned or performed, however due to the global nature of the method, it will usually entail more experiments than its local equivalents.

However most reaction conditions that chemists will test tend to only have a single maximum<sup>64,65</sup> making the simpler and quicker to perform local algorithms, usually the better choice.

Poliakoff *et al*<sup>66</sup> reported using the SMS method initially for the automated optimisation of ethanol dehydration over  $\gamma$ -alumina (Scheme 1.2). The monitored yield increased from 2 to 75% with a selectivity of 87% for diethyl ether over ethene and acetaldehyde. The method stopped at only 87% conversion as any further change in parameters caused a drop in selectivity. They then tested a multiple component reaction, the carboxymethylation reaction of dimethyl carbonate (DMC) with 1-pentanol. Initial conditions were chosen from previous work they had reported<sup>67</sup> however, when the optimisation method was applied with the goal to maximise methyl pentyl carbonate, only a small 2% increase in yield was observed. The carbonate species is an intermediate in an overall substitution process and when the goal was changed to target the 1-methoxypentane product, the maximum yield was increased to 70% and it searched a significantly different area of the reaction space compared to the previous attempt. Performing both of these

optimisations took 35 hours, much less time than would be taken using their previously reported automated reactor to cover the same reaction space.<sup>56</sup>



Scheme 1.2: Reaction scheme for the dehydration of ethanol over  $\gamma$ -alumina. The formation of diethyl ether was set as the goal for the optimisation algorithm.

They expanded the optimisation to different methylating agents and to four parameters: temperature, pressure, flow rate, and molar ratio of pentanol:methylating agent<sup>68</sup>. Using the SMS method, they were able to find optimal conditions for DMC as a methylating agent giving 98% yield after 47 measurements, with 90% reached after 10. The results for methanol required 125 reactions and only reached 68% yield showing that DMC is a better methylating agent than methanol however, these optimisations took 25 and 74.3 hours to complete due to the length of time taken to obtain a measurement with their chosen in-line analysis, GLC.

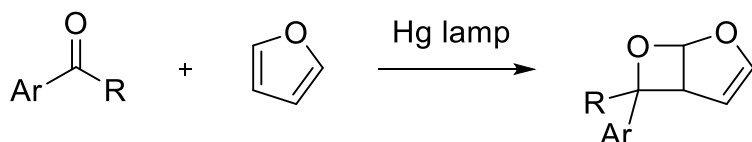
To overcome this they utilised the in-line IR-spectrometer, React IR<sup>69,70</sup>, to allow rapid acquisition of reaction data<sup>71</sup> compared to their previous method (3.2 minutes compared to 35 minutes). They again utilised the SMS method to optimise the methylation of pentanol and found that the optimisation was complete after 150 minutes giving a 99% yield, with the drop in time due to both the shortened measurement time but also due to being able to monitor exactly when the system reaches steady state. They then applied the SNOBFIT optimisation method to the system to ensure a global maximum was found. The method took slightly longer per experiment, 8 minutes compared to 3.2 minutes, due to the reaction conditions being further apart between runs compared to SMS, however this distance is necessary in order to ensure the global maximum is found. The results from the SNOBFIT are slightly different from that of SMS (Table 1.1) as the optimal conditions for this reaction covers a region of the reaction space rather than a defined peak. They showed this as they assessed 252 different reaction conditions covering the entire reaction space which validated both of the methods.

Parameter	SMS	SNOBFIT
Temperature / °C	200	246
1-pentanol / mLmin <sup>-1</sup>	0.24	0.20

DMC / mLmin <sup>-1</sup>	1.28	1.44
Yield / %	>99%	>99%

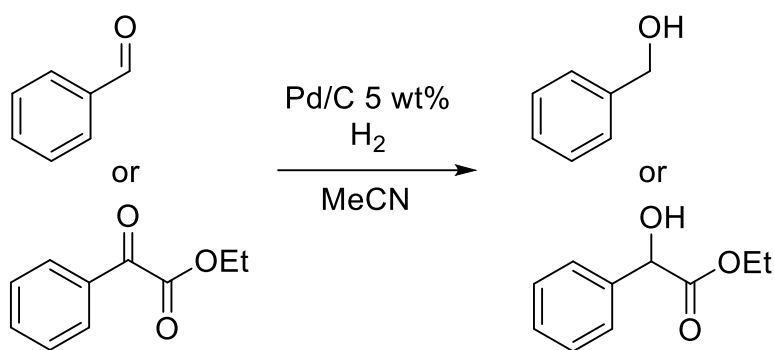
Table 1.1: Optimised conditions from SNOBFIT and SMS optimisation methods. Results between the two methods are similar but not identical due to SNOBFIT only testing the general region of the reaction space.

Reuping *et al*<sup>48</sup> used the modified simplex method<sup>72</sup> combined with in-line IR monitoring to optimise the [2+2] photochemical reaction between benzophenone and furan (Scheme 1.3) with respect to overall concentration of benzophenone and the residence time in the reactor. An initial set of 10 reaction conditions were chosen after which the algorithm decided the subsequent conditions. 25 reaction conditions were tested with the optimal configuration giving 95% conversion. During one of the experiments, the IR gave a blank spectrum due to solvent evaporation during the reaction. Despite this negative result the system was able to optimise into a local maximum in a total of 48 hours.



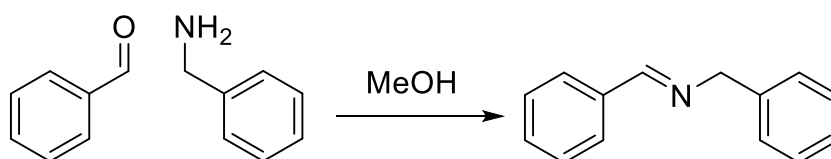
Scheme 1.3: Reaction scheme for the [2+2] photocyclisation between benzophenone and furan. Residence time and concentration of benzophenone were varied for the optimisation.

The research group has also used the algorithm for the optimisation of the hydrogenation of benzaldehyde and  $\alpha$  or  $\beta$ -ketoesters<sup>73</sup> using an H-Cube<sup>74</sup> system which generates H<sub>2</sub> *via* electrolysis of H<sub>2</sub>O (Scheme 1.4). In this system they were able to automatically optimise for three parameters: H<sub>2</sub> pressure, flow rate and reactor temperature and they monitored the output with in-line IR spectroscopy. 99% conversion was reached in 17 reactions taking 24 hours for each substrate.



Scheme 1.4: Reaction scheme for the hydrogenation of benzaldehyde and  $\alpha$  or  $\beta$ -ketoesters with heterogeneous Pd/C.  $\text{H}_2$  is supplied from an H-Cube. Pressure of  $\text{H}_2$ , flow rate and temperature were varied in the optimisation.

Cronin *et al*<sup>75</sup> have reported the use of the simplex method combined with in-line flow NMR<sup>76</sup> spectroscopy to optimise the formation of an imine from benzaldehyde and aniline (Scheme 1.5) with the  $^1\text{H}$  NMR peaks for the imine and starting aldehyde used to assess the yield of the reaction. The reaction was optimised using equation 1.2 which aims to maximise yield of product and minimise the reaction time.



Scheme 1.5: Reaction scheme for the reaction of benzaldehyde and aniline. Residence time and volumetric fraction of benzaldehyde were varied for the optimisation.

$$J = \frac{A_{im}}{A_{im} + A_{ald}} x_1 t_R^{-1}$$

$J = \text{Fitness function}$

$A_{im} = \text{Area of imine NMR signal}$

$A_{ald} = \text{Area of aldehyde NMR signal}$

$x_1 = \text{Volumetric fraction of aldehyde}$

$t_R = \text{Residence time}$

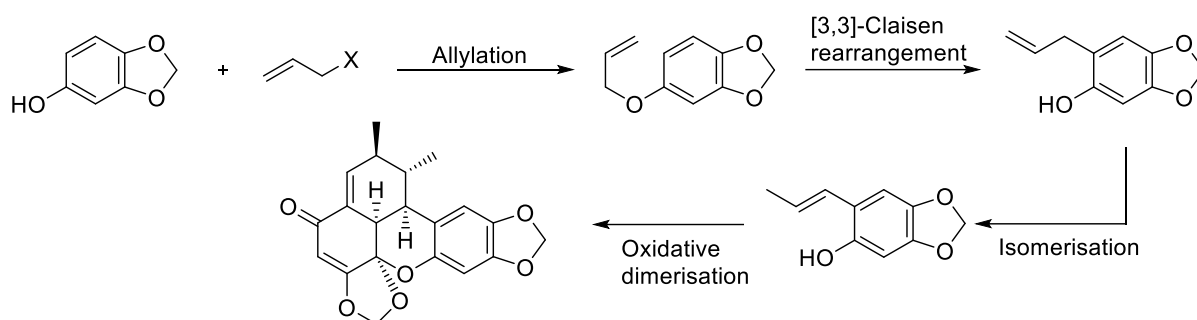
Equation 1.2: Calculation of fitness function for optimisation of product formation

Iteration	$x_1$	$t_R$ /min	Yield / %	$J$
1	0.03	9.1	76.5	0.003
5	0.49	2	11.5	0.028
10	0.45	4.4	89	0.092
15	0.66	2	5.6	0.019
20	0.48	2	80.7	0.192
25	0.63	2	50.4	0.158
29	0.71	2	73.9	0.264

Table 1.2: Selection of experimental results and conditions from the optimisation *via* simplex algorithm. The system was stopped after 29 experiments.

The reaction conditions were chosen using the simplex algorithm varying the residence time and the volumetric fraction of aldehyde. The system was allowed to run for 29 iterations which resulted in (Table 1.2) optimised conditions which gave 73.9% yield in 2 minutes. Although this was not the highest yielding conditions the system found, it was the most productive giving 11.82 kg h<sup>-1</sup>. However, in-line NMR can only be operated in concentrated systems or long acquisition times must be used and the optimisation algorithm requires distinct peaks to be able to calculate the area accurately.

Felpin *et al*<sup>77</sup> overcame this issue by utilising either in-line NMR or in-line HPLC depending on the reaction conditions being tested. They aimed to optimise the synthesis of carpanone from commercially available sesamol (Scheme 1.6). The initial optimisation involved the combination of allyl iodide with sesamol and KOH in a MeOH/H<sub>2</sub>O mixture using a simplex method modified with a golden section search<sup>78</sup> with the aim to optimise yield by varying the reaction time, temperature and reaction stoichiometry. In-line HPLC was used as the monitoring device as the <sup>1</sup>H peaks for sesamol overlapped with the reaction product. 13 experiments were performed which resulted in a maximum yield of 80%.



Scheme 1.6: Formation of carpanone from sesamol. Each step was optimised separately over a total of 66 experiments.

Acetone was chosen as the solvent for the second step, a Claisen rearrangement, taking advantage of the pressure control and lack of headspace associated with flow reactors, the system could easily be heated to above the boiling point of acetone. As the reaction was at high concentration (2 M), in-line NMR was used as the monitoring device with a gradient-based solvent suppression<sup>79</sup> used to minimise the acetone peak. The optimisation was performed varying the residence time and temperature of the reaction and 100% yield was achieved after 7 experiments with the final conditions being 222 °C and 27.6 minute reaction time. However, the longer reaction time provides quite a low reaction throughput of 854 mg h<sup>-1</sup>. To increase this the optimisation was repeated with the initial simplex conditions at a higher starting point than the previous attempt with the allowed distance between experiments lowered. Under these conditions the simplex reached the temperature boundary after 2 experiments which required switching to the golden section method as a simplex cannot have more vertices than the degrees of freedom on the boundary. The golden section method reduces the number of dimensions in the search, in this case converting it into a linear search of residence times at the maximum temperature. The second optimisation sequence performed 19 experiments with the optimum conditions being 250 °C and 2.5 minute residence time, increasing the output to 7.5 g h<sup>-1</sup> in a single working day.

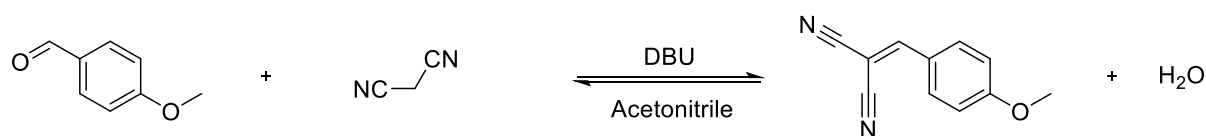
The third step was the isomerisation of allyl sesamol to desmethoxycarpacine using *t*-BuOK in DMSO. The reaction can form both the *E*- and *Z*- isomer of the product, both of which are highly sensitive to oxygen. The reaction was optimised by varying the temperature, residence time, and base loading with in-line HPLC as the monitoring device. The search area was restricted by planes which automatically disallowed experiments which were predetermined to fail, i.e. reactions with low reaction times and low temperatures. The initial optimisation attempt reached the lower boundary for base loading after 4 experiments with a yield of 15%, the dimensions were reduced as before however the search was unable to increase the yield which triggered the system to perform a random restart where it picks a new simplex in an unexplored region of the reaction

## Chapter 1

space. The new start reached the predefined maximum number of experiments, 23, without reaching a maximum, however it did provide a yield of 91% E-isomer and a trace amount of Z with a residence time of only 3 minutes, which was deemed satisfactory, so optimisation was not continued.

For the final oxidative dimerisation step, a  $\text{Co}^{\text{II}}(\text{salen})$  complex was chosen as the catalyst due to solubility issues with the more traditional  $\text{PdCl}_2$  or  $\text{CuCl}_2$  systems. The reaction was optimised again by varying the temperature, reaction time and catalyst loading. After 13 experiments the system had reached the boundary of catalyst loading (10 mol%) and as such the catalyst loading dimension was subsequently removed from the search by keeping it constant at 10 mol%. The 2D search gave similar values to the 3D search and as such the optimisation was terminated with optimal conditions of 40 °C, 40 minute residence time, and 10 mol% catalyst giving 92% yield. Use of the method overall resulted in the 4-step synthesis of carpanone being optimised in 66 experiments giving an overall yield of 67% with minimal chemist intervention.

Jensen *et al*<sup>80</sup> reported the optimisation of a Heck cross coupling reaction using a 140  $\mu\text{L}$  microreactor with in-HPLC to monitor the reaction. The simplex method was used as the optimisation algorithm with residence time and equivalents of alkene being the variables leading to an optimised yield of 83%, which took 19 experiments, and 6.3 hours of experimental time. They then attempted to scale up the reaction from the microreactor to a 7 mL reactor, a 50-fold increase, to see if the same results could be obtained at the larger scale. A series of 9 different reaction conditions were chosen which surrounded the optimal region found in the microreactor and yield monitored by HPLC. The results from the 7 mL reactor were all in close agreement with the microreactor; thus implying that optimisation can be performed on a microscale, saving resources compared to optimisation on a larger scale.



Scheme 1.7: Knoevenagel condensation between p-anisaldehyde and malonitrile. 3 different algorithms were used to optimise the temperature and residence time for this reaction.

Jensen *et al*<sup>81</sup> also reported an automated microfluidic system with in-line HPLC in which they optimised the Knoevenagel condensation reaction between p-anisaldehyde, malononitrile and DBU (Scheme 1.7). The variables being optimised were temperature and residence time, and three optimisation algorithms were tested, Simplex, SNOBFIT, and Gradient Decent, to demonstrate the ease of applying different optimisation methods to the microreactor system. All



three of the methods reached the same optimal conditions (Table 1.3) with SNOBFIT performing the most experiments and thus taking the longest experimental time. Plotting the data from the reactions (Figure 1.6) demonstrates the difference between the local and the global search methods with SNOBFIT covering a large percentage of the reaction space whereas Simplex and Gradient Descent very quickly narrow down into a single area. In this case that area happens to be the global maximum, but this will not always be true.

Algorithm	No of experiments	Temperature / °C	Reaction time / s	Yield / %	Total time / h
Gradient descent	13	100	30	77	4.5
Simplex	30	99	30	76	8
SNOBFIT	36	99	30	74	11

Table 1.3: Final optimisation results from three optimisation algorithms. All three algorithms reached the same optimal reaction conditions suggesting that the global maximum was reached.

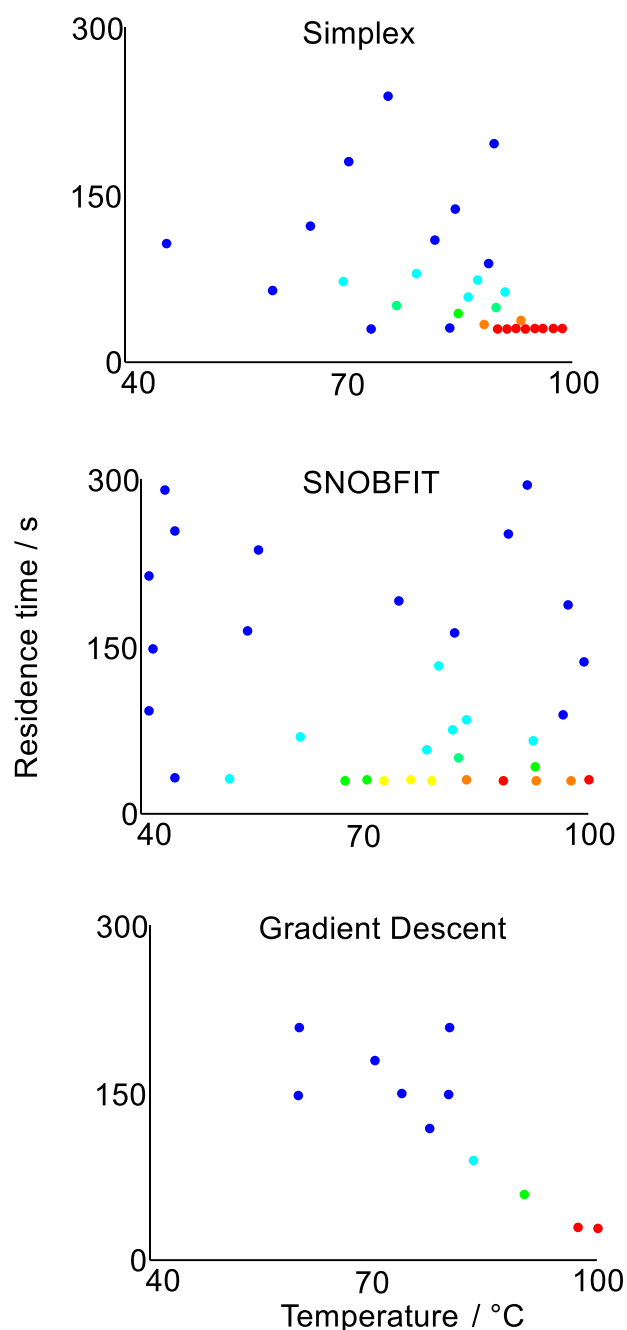
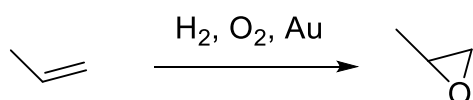


Figure 1.6: Graphical depiction of experiments covered by each algorithm demonstrating the varying spread. SNOBFIT covers the largest portion of the reaction space, simplex has a medium spread, and gradient descent covers a very narrow portion.

#### 1.2.4 Extracting kinetic data

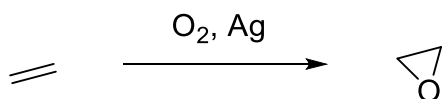
Schouten *et al*<sup>82</sup> studied the kinetics of the industrial relevant propene oxide formation from propene in the presence of hydrogen, oxygen and a gold catalyst (Scheme 1.8). A microreactor was utilised to allow use of the gas mixture safely inside of the explosive regime by minimising the total volume of mixed reagents.

Several reactions were performed varying temperature and reagent concentration with repeat reactions yielding identical results even when using a different reactor demonstrating the excellent control given by continuous chemistry. Catalyst deactivation and reactivation rate constants were generated from the experiments and rate of reaction was found to be dependent upon the concentration of hydrogen and oxygen which led to the conclusion that the formation of peroxide on the gold catalyst is the rate limiting step rather than the epoxidation to form the product. A test reaction with increased oxygen and hydrogen levels compared to the typical reaction conditions led to a rate increase by a factor of 4 and a yield increase from 1.3 to 2.4%.



Scheme 1.8: Reaction scheme for the epoxidation of propene. The use of microreactors allowed the safe use of gas mixtures in an explosive regime. Catalyst deactivation and reactivation rates were generated using this system.

Salmi *et al*<sup>83</sup> reported a kinetic study on the formation of ethylene oxide on a silver catalyst from ethylene gas and oxygen (Scheme 1.9). Three parameters were varied: system pressure, oxygen concentration and ethylene concentration keeping residence time and temperature constant. It was found that conversion and selectivity increased as oxygen concentration increased with reaction order of 0.89, whereas increasing ethylene concentration decreased overall conversion. With a constant 1:1 ratio of ethylene to oxygen, increasing the concentration was found to give an increase to the overall rate of formation. The role of oxygen in the system was also probed by plotting the square root of oxygen concentration against the rate of reaction. As this plot did not intercept the axis at 0, it was determined that atomic oxygen was not an active surface species in the reaction.

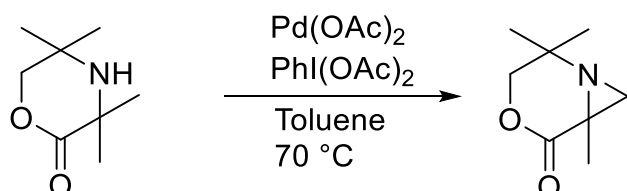


Scheme 1.9: Reaction scheme for the epoxidation of ethylene. The rate of formation and role of O<sub>2</sub> in the system were probed using traditional flow steady state reactions.

Lapkin *et al*<sup>84</sup> reported a variation to the DoE approach which incorporated a model of the reaction into the DoE parameters<sup>85</sup>. Using this method requires prior knowledge of the reaction mechanism which in this case, the Pd-catalysed aziridination of aliphatic amines by C-H activation (Scheme 1.10), is obtained from previous literature<sup>86</sup> and DFT calculations of the Gibbs free energies<sup>87</sup>.

Using the model-based DoE approach they were able to calculate the rate constants and

activation energies for the different steps in the mechanism with only 8 experiments and 71 samples. A vast improvement in time over the batch method which took 38 experiments and 10 samples for each experiment. The results for the rate constant and activation energies for the first step were significant with sufficiently low uncertainty and the second only slightly differed from the initial guess provided by the model. However, the results for the other steps had a large amount of uncertainty as t-values failed to exceed the reference t-values from the model and the confidence intervals were larger than the calculated results.



Scheme 1.10: Reaction scheme for the aziridation of aliphatic amine. A model for this reaction was created using available data and a DoE performed to calculate rate constants and activation energies.

Jensen *et al*<sup>88</sup> reported an automated reactor setup capable of determining rate constants and determining a model for the reaction. 4 potential reaction models are chosen and an initial series of reactions are performed. The results of these reactions are combined with the reaction models to choose the conditions for the following reactions and this process continues until a model is chosen as the most likely and kinetic data can be extracted from that model. The methodology was tested on the Diels-Alder reaction of isoprene and maleic anhydride (Scheme 1.11) and after 6 reactions a model was chosen which gave an activation energy of 56.3 kJmol<sup>-1</sup> which is in good agreement with previous literature data of 58.5 kJmol<sup>-1</sup>.



Scheme 1.11: Reaction scheme for the Diels-Alder reaction of isoprene and maleic anhydride.

Results from automated reactions determine the most likely correct reaction model from a series and extract kinetic data from this.

Further development on this methodology has been reported<sup>89</sup> with the estimation of multi-step reactions. After the initial experiments are performed, a second series of experiments aim to access each step of the reaction pathway separately. A final series of experiments then is then performed to generate the kinetic parameters simultaneously based upon the previous reaction

results. The reaction of 2,4-dichloropyrimidine and morpholine was chosen as a model reaction with the aim to form the 2-substituted aminopyrimidine selectively. A total of 24 experiments were performed which resulted in a model which overlapped well with the experimental data. Further improvement on the kinetic model was achieved by separating each step of the reaction and repeating the methodology. In total this took 78 automated experiments to fully extract the kinetics of the system and 7 days of cumulative time.

### 1.2.5 Obtaining the minimal number of experiments

The above methods are effective in minimising the amount of experimental time taken when optimising a reaction however they still require several experiments to be performed which can amount to a large total reaction time waiting for each reaction condition to reach the steady state in the detector or output.

Two groups of methodologies have been developed which can overcome this flaw, obtaining reaction data equivalent to having performed multiple experiments, in only one or two and thus drastically increasing the efficiency of the flow experiment.

#### 1.2.5.1 Movable probe

The use of multi position in-line probes allows a single steady state to be used for several reaction time points, as reaction time is related to distance along the reactor. In 2010 Mozharov *et al* published a method for the monitoring of reaction progress by utilising such a movable Raman probe<sup>90</sup>. They monitored the esterification of butanol with acetic anhydride to give butyl acetate and acetic acid at room temperature in a 13  $\mu\text{L}$  serpentine microfluidic chip. Initially the probe was used to test the mixing ability of the microreactor by pumping the reagents into the setup at either 5 or 20  $\mu\text{L}/\text{min}$  and monitoring the Raman spectra at different locations after the streams were combined and they found that for this setup the mixing was sufficient to not require an additional micromixer. Monitoring of the reaction progress was achieved by pumping the reagents into the system at 10  $\mu\text{L}/\text{min}$  with the probe starting at line 8 in the serpentine structure and then monitoring every other line. Using this method, the reaction was completed after 62 lines with a calibrated conversion of  $97.0 \pm 3.2$  and  $107.7 \pm 11.1\%$  for the concentrations of acetic anhydride and butyl acetate respectively obtained from a single experiment at a single flow rate resulting in a faster and more efficient method than the traditional route. Unfortunately this method requires accurate positioning of the probe to obtain the spectra as well as a reactor design which allows the probe access to the flow path which is not always the case for example the Vapourtec heated reactors and most photochemical reactor designs<sup>91–93</sup> as such, a more generally applicable solution was required.

### 1.2.5.2 Transient Flow

The use of transient flow, where the system is not at steady state, has been applied to overcome these issues. Mozharov *et al*<sup>94</sup> published a method which utilises a step change in flow rate to generate time-series data. The method comprises of a microfluidic reactor, which contains a mixing zone with a volume negligibly small compared to the rest of the system to minimise any effect the mixing time has on the output, and an in-line detector capable of a high frequency of measurements. Reaction mixture is pumped through the reactor at a low flow rate until a steady state has been reached. At this point, there is a reaction time gradient as you travel through the reactor and increasing the flow rate by an order of magnitude causes this time gradient to pass through the detector and reaction data can be extracted. Calculation of the exact reaction time from this method is difficult due to two factors. Firstly, the reaction mixture continues to react after the increase in flow rate, so all the reaction mixture will have additional reaction time however, the solution at the start of the reactor will have extra reaction time compared to that near the detector. Secondly, when increasing the pump flow rate, the pump does not immediately reach the desired flow rate and the exact reaction time during this change could not be determined. The additional reaction time can be solved by using equation 1.3 however this does not work for the regions of uncertainty caused by the non-instantaneous flow change.

$$t_r = -\frac{F_2 - F_1}{F_1} \tau + \frac{V + sN}{F_1}$$

$t_r$  = Reaction time

$F_1$  = Initial flow rate

$F_2$  = Final flow rate

$\tau$  = Experimental time

$V$  = Volume

$s$  = Cross sectional area

$N$  = Distance fluid travels during uncertain flow rate

Equation 1.3: Calculation of reaction time from Mozharov transient flow method

These regions can only be calculated by using graphically estimated values for the location of the uncertain regions (Figure 1.7) and then utilising equation 1.4 to calculate the reaction time, which leads to uncertainty in the true reaction time. The uncertainty can be minimised by reducing  $\Delta\tau(F_2/F_1)$  where  $\Delta\tau$  is the time between measurements.

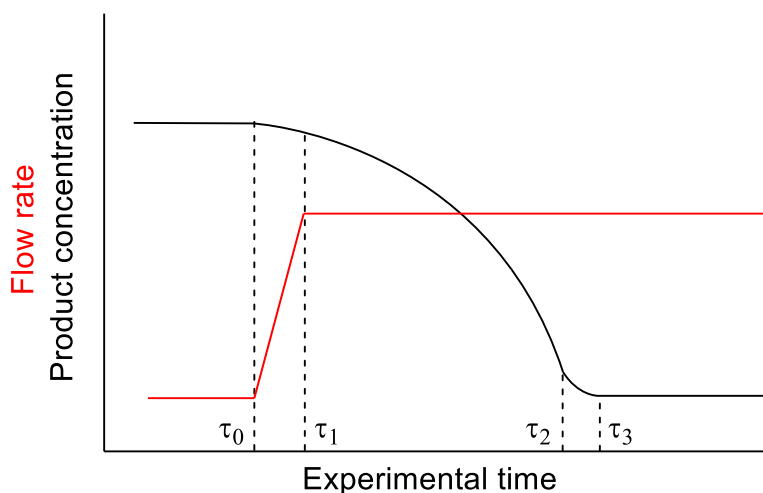


Figure 1.7: Graphical representation of the output when utilising the step change in flow rate.

Areas depicted by dashed lines indicate regions of uncertainty caused by the non-instantaneous increase in flow rate.  $\tau_0$ - $\tau_1$  is the output of the reactor during the flow rate change, and  $\tau_2$ - $\tau_3$  is the material which was entering the reactor as the flow rate change occurred.

$$t_r = -\frac{F_2 - F_1}{F_1} \tau + \frac{F_2}{F_1} \tau_2$$

Equation 1.4: Estimation of reaction time in uncertain regions

Rate constants ( $k$ ) and reaction order ( $n$ ) for the Knoevenagel condensation between ethyl cyanoacetate and benzaldehyde were obtained using both the described method and traditional steady state experiments over two temperatures and the results (Table 1.4) show good agreement between the methods. However, the traditional steady state method took roughly five times the experimental time as well as requiring more material than the transient flow method.

Methodology	10 °C	40 °C
Transient	$k: 0.0356 \pm 0.0008 \text{ mol}^{-0.3} \text{ dm}^{0.9} \text{ s}^{-1}$ $n: 1.3$	$k: 0.24 \pm 0.018 \text{ mol}^{-0.1} \text{ dm}^{0.3} \text{ s}^{-1}$ $n: 1.1$
Steady state	$k: 0.0335 \pm 0.0032 \text{ mol}^{-0.4} \text{ dm}^{1.2} \text{ s}^{-1}$ $n: 1.4$	$k: 0.244 \pm 0.032 \text{ mol}^{-0.3} \text{ dm}^{0.9} \text{ s}^{-1}$ $n: 1.3$

Table 1.4: Calculated rate constants and reaction order from both methodologies. Steady state methodologies took 5 times as long to reach the end result.

The application of this method to commercially available mesoscale reactors was reported by Whitby *et al*<sup>95</sup> who utilise in-line IR and UV monitoring to calculate rate constants and activation energies for the thermolysis of 1,3-dioxin-4-ones across 100 to 140 °C (Figure 1.8) . Initial

## Chapter 1

attempts at performing the method were hindered at high flow rates by the poor thermal transfer when using the air-heated Vapourtec reactors and results were inconsistent with that from steady state calculations. Additionally, it was clear from the results that the heating was uneven throughout the reactor, specifically between the inner and outer coils, as two different slopes were present on the kinetic plot (Figure 1.9). Switching to heating the reactor with an oil bath solved these issues and allowed the method to be performed accurately and the results (Table 1.5) show good overlap between the steady state, the push-out method and literature results<sup>96</sup> regardless of which in-line analysis or data processing was used.

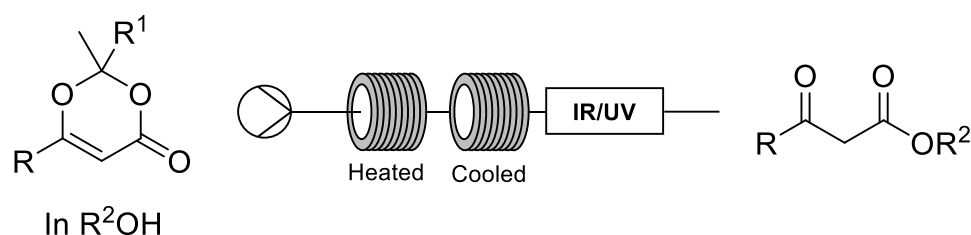


Figure 1.8: Flow setup for thermolysis of 1,3-dioxin-4-ones with in-line IR/UV monitoring with an alcohol quench.

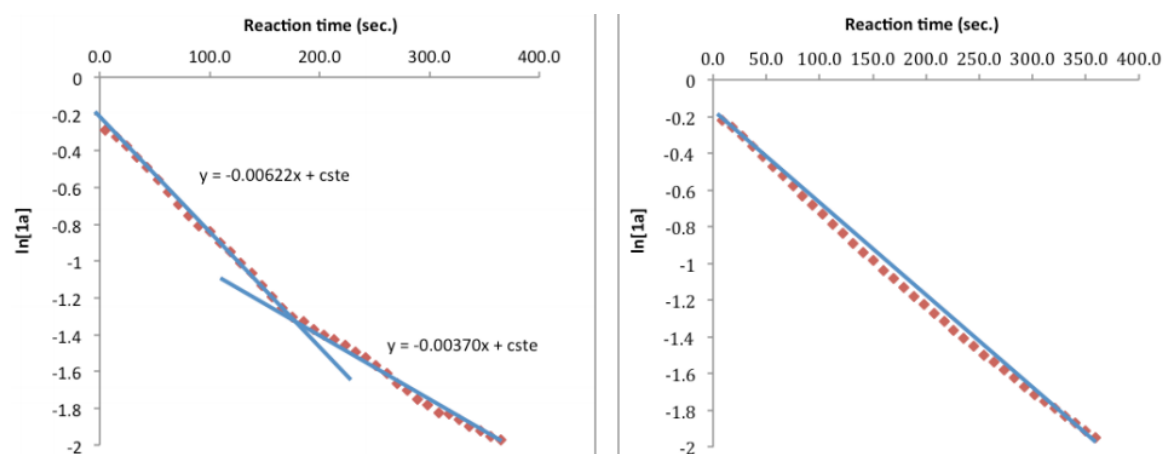


Figure 1.9: Kinetic slopes generated under two different temperature sources. Left = Air heater. Right = Oil heated reactor. Two distinct slopes are present under air heating representing the different layers of the reactor.

Methodology	$E_a$ / kJmol <sup>-1</sup>
Steady state	126.7
Push-out	124.7
Batch <sup>96</sup>	130.1

Table 1.5: Calculated activation energies generated using different methodologies. A good agreement between steady state, push-out and batch is shown.



Additionally, they report a simple method for minimising the error caused by the non-immediate change in flow rate, the 'reverse push-out' method. In which rather than increasing from low to high flow rate the reverse is done which has the effect of elongating the transitional period and minimising  $\Delta\tau(F_2/F_1)$ . The downside is that this requires additional solvent compared to the traditional push-out method.

Jensen and Moore<sup>97</sup> reported a different solution to this issue where, instead of a step change in flow rate, a controlled ramp in flow rate is used instead. Analogous to the reverse push-out method, the system is allowed to reach steady state after which the flow rate is reduced in a controlled manner, increasing the residence time. Throughout the ramp, monitoring of the outflow *via* in-line analysis gives the reaction profile and the corresponding residence time can be calculated using equation 1.5.

$$\tau = \frac{S}{\alpha} \tau_0 + S t_f$$

$\tau$  = Residence time

$\alpha$  = Rate of residence time increase

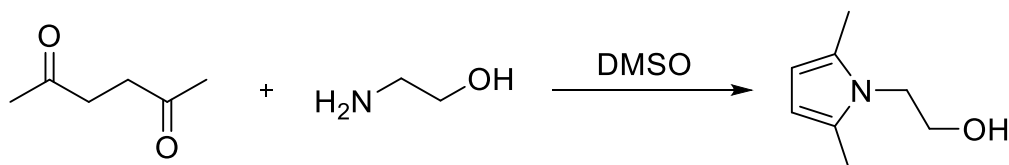
$\tau_0$  = Initial residence time

$S = (1 - e^{-\alpha})$

$t_f$  = Final time monitored fluid exits reactor

Equation 1.5: Residence time calculation throughout the controlled flow rate ramp change

Validation of the method using the Paal-Knorr reaction (Scheme 1.12) initially revealed a deviation from the steady state results as  $S$  approached 1. The deviation was due to the presence of a thermal quenching zone and the tubing that joins the microreactor to the in-line monitoring, adding additional volume for the fluid to pass through which was not accounted for in the initial calculation. Adapting equation 1.5 to include this volume gave equation 1.6 and replotting of the data resulted in consistent results between steady state and all different  $S$  values tested.



Scheme 1.12: Scheme for Paal-Knorr reaction. Activation energies were calculated utilising a controlled flow rate ramp to overcome the uncertain regions previously described.

$$\tau = Se^{\frac{V_d}{V_r}\alpha} \left( t_m + \frac{\tau_0}{\alpha} \right)$$

$V_d$  = Delay volume

$V_r$  = Reactor volume

$t_m$  = Measurement time

Equation 1.6: Adjusted equation 1.5 to include the volume between the reactor and detector

The method was repeated three times at several temperatures and the data fitted to a kinetic model, based on the assumed mechanism, allowing calculation of the activation energies for the two kinetic parameters,  $k_1 = 12.2 \pm 0.4 \text{ kJmol}^{-1}$  and  $k_2 = 20.0 \pm 0.9 \text{ kJmol}^{-1}$ , in eight hours and using only 5 mL of each reagent mixture. Comparatively, traditional steady state reactions would have taken two days and 13.5 mL of reagent. Whilst this method removes the uncertainty caused by the step change in flow rate, it does require a setup capable of delivering a constant flow rate change, which is not possible natively on all flow platforms.

Bourne *et al*<sup>98</sup> reported the use of a controlled flow rate ramp using mesoscale reactors rather than the microscale used previously. The setup included 3 HPLC pumps (Figure 1.10) to apply the ramp, with one containing only solvent to allow different concentrations of starting material to be assessed from a single stock solution by varying the ratio of the flow rates, and in-line HPLC monitoring.

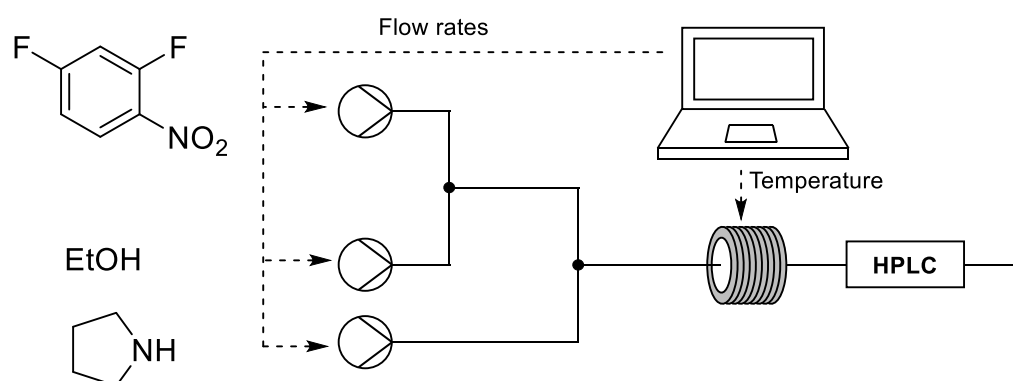


Figure 1.10: Flow setup for  $S_NAr$  reaction. Concentration of starting materials is varied utilising a flow rate ramp over a range of temperatures for rapid extraction of kinetic data.

The  $S_NAr$  reaction of pyrrolidine with 2,4-difluoronitrobenzene was used to illustrate the method with starting molar pyrrolidine concentrations of 1.5, 4 and 7 and temperatures from 30 to 120 °C with each experiment and flow rate ramp controlled automatically using MATLAB software. Calculation of the residence time for each HPLC was different to previous methods, due to

considering the varying thermal expansion of EtOH at the different temperatures giving rise to equation 1.7.

$$\tau = \frac{-(F_1 - \alpha t) + \sqrt{(F_1 + \alpha t)^2 + \frac{2\alpha V}{\beta}}}{\alpha}$$

$$\beta = 1 + \alpha_v(T_1 - T_0)$$

$$\alpha_v = \text{Change in volume}$$

$$T_0 = \text{Start temperature}$$

$$T_1 = \text{End temperature}$$

Equation 1.7: Calculation of residence time adjusting for the thermal expansion of the solvent.

Using this method they generated 12 concentration-time profiles in less than 3 hours experimental time each of which gave a good fit with that of a kinetic model with  $R^2 = 0.9995$ .

Aroh and Jensen reported a method which utilised both a flow rate ramp and a temperature ramp<sup>99</sup> in the same experiment to minimise the number of experiments required. Validation of the method using the Paal-Knorr reaction of ethanolamine and 2,5-hexanedione was performed with a temperature ramp of 1 °C/min, with boundaries of 40 to 100 °C, and a flow rate ramp with  $\alpha = 0.4$ . The method was performed with both a positive and negative temperature ramp. Comparison of the results with that of a kinetic model and that of steady state experiments showed that when the two ramps were analysed separately, there was a poor fit at the higher residence times. However, when the ramps were combined they gave a good overlap with the model and steady state experiments with a high coefficient of determination,  $R^2 = 0.99$ . They ascribed this to a single ramp being inefficient to decouple the effect of temperature and time. Combining both the positive and negative ramps gave orthogonal conditions which allowed the parameters to be decoupled.

A temperature ramp was also reported by Gomez *et al*<sup>100</sup> utilising a microfluidic reactor combined with nanolitre in-line NMR. The methodology utilises the non-instantaneous heating of the reactor to access the various temperatures, which was turned on after the reactor had reached steady state. The reactor volume, and the reactor volume that follows, are split into 4 distinct areas (Figure 1.11). 'A+B' is the first fluid to leave the reactor and it has experienced both a residence time gradient and a temperature gradient. 'B' is the first portion of the initial reactor volume to reach the steady state however it has also experienced the temperature ramp which means in analysis it will have a lower starting concentration than that of A or B, and will also

continue the residence time gradient. 'C' is the reaction mixture that enters as A is leaving and as such, experiences a temperature gradient. However, each portion of C experiences the same residence time unlike A. 'D' is the steady state of the reaction experiencing both a constant temperature and residence time. The various conditions experienced by the reaction mixture means that from one experiment, it is possible to obtain a large amount of reaction information and this was demonstrated by utilising the method to obtain rate constants, pre-exponential factors and activation energies for a series of pyrazole derivatives from one experiment per derivative.

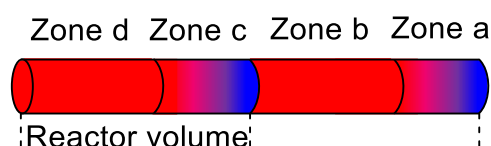


Figure 1.11: Graphical representation of the zones obtained from the temperature ramp. Zones A and B are equal to the first reactor volume when the temperature gradient begins. Zones C and D are the reaction mixture which follows. Zone A experiences a residence time gradient and a temperature gradient. Zone B has a lower initial concentration due to the temperature ramp but the segment as a whole has a constant temperature but has experienced a residence time gradient. Zone C undergoes a temperature gradient but a constant residence time. Zone D has a constant temperature and residence time.

### 1.3 Summary

Recent years have seen creative and varied application of flow chemistry towards highly efficient optimisation and kinetics investigations.

The high level of control that the majority of flow systems gives the user has allowed for multiple experiments to be queued and executed automatically. The conditions of these experiments has been decided both by manual choice and dynamically generated computer algorithms which has allowed reaction conditions to be optimised automatically with minimal chemist interaction. However, these methods still rely on running several experiments which can lead to an increase in waste production.

Transient flow methods were reported which overcome this disadvantage, utilising continually changing variables, such as reaction time, concentration or temperature, rather than a single reaction to rapidly extract a series of reaction data from a single experiment. This equates to a

large increase in productivity, and potential waste reduction as fewer experiments need to be performed to extract the same information as traditional methods. However, these methods tend to rely on specific reactor technologies, such as being able to vary the flow rate dynamically, which is not possible on every flow system.

Overall, both of these classes of methods combine modern pump and reactor technology with fundamental concepts at the interface of chemistry and chemical engineering to rapidly optimise reactions and extract kinetic data far more efficiently than is possible with traditional methods.

Presented within this thesis are methods for the extraction of concentration data, irradiance time and multiple reaction times, which attempt to access the efficiency of the transient flow methods but with minimal additional requirements, allowing for the methods to be utilised with any flow system.

## Chapter 2 Characterisation of Reactor Properties and Flow Regimes

### 2.1 Introduction

Whilst the benefits of flow chemistry (safety, reproducibility of results, excellent control of reaction parameters) are well documented<sup>14,101,102</sup>, a basic understanding of chemical engineering and fluid mechanics (mixing, heat and mass transfer, dispersion) is important to ensure that these benefits are properly utilised otherwise inaccurate yields or kinetic data could result.

As such a brief description of the most important aspects of fluid mechanics will be presented in this chapter and calculations and measurements of these parameters will be performed. From these calculations, reaction parameters such as flow rate range, reactor design, heating regime, tubing length, mixer, and diameter will be defined for the reactions performed in this thesis.

### 2.2 Fluid mechanical properties and their characterisation

#### 2.2.1 Flow regime and the Reynolds number

There are two regimes to consider when using continuous flow chemistry, laminar<sup>103</sup> and turbulent flow<sup>104</sup> (Figure 2.1). Turbulent flows are characterised by irregular fluid motion and vortices causing excellent mixing across the axial dimension of the tube. Whereas laminar flow consists of regular layers of varying fluid velocity with lower velocities closer to the walls of the tube and mixing only due to molecular diffusion between the layers. The relationship that characterises these two regimes is the Reynolds number (Equation 2.1) with the higher the Reynolds number, the more turbulent the flow is with full turbulence at  $Re > 4000$ <sup>105</sup>.

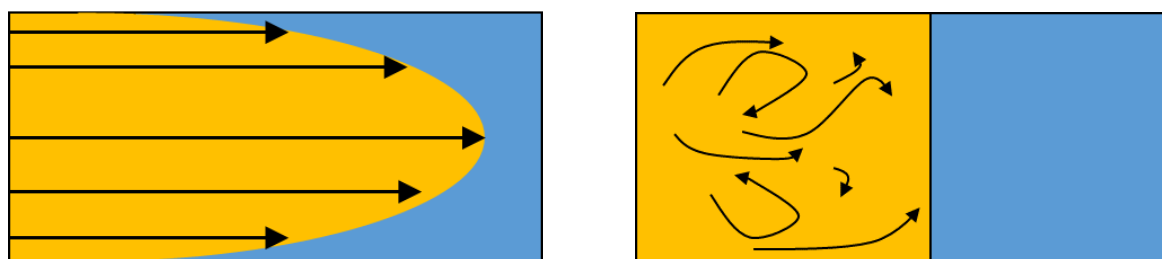


Figure 2.1: Exaggerated graphical depictions of the laminar (Left) and turbulent (Right) flow regimes

$$Re = \frac{\rho u D_H}{\mu}$$

$\rho$  = Fluid density

$u$  = Mean fluid velocity

$D_H$  = Hydraulic diameter

$\mu$  = Dynamic viscosity

Equation 2.1: Reynolds number equation

Calculations of the Reynolds number for the range of systems used in this thesis (Table 2.1), show that the system is always going to be under laminar flow and the requirements for reaching the full turbulence limit are far outside of the ranges possible with the flow equipment used. To reach the boundary for full turbulent flow at 0.5 mL/min, you would require a tube diameter of 0.0025 mm. Similarly, for the standard 1.0 mm ID tubing used, you would need a flow rate of near 180 mL/min.

Flow rate / mL·min <sup>-1</sup>	$D_H$ / mm	$Re$
0.1	1.0	2.3
0.5	1.0	11.3
0.1	0.5	4.5
0.5	0.5	22.6
0.1	0.25	9.1
0.5	0.25	45.3
10	1.0	230

Table 2.1: Calculations of the Reynolds number across various systems which will be used in this thesis. 10 mL/min is the maximum flow rate for the Vapourtec pump and 1.0 mm ID is the standard tubing diameter

Laminar flow presents problems for performing flow reactions, reagent mixing when combining multiple streams and Taylor dispersion<sup>106</sup>.

### 2.2.2 Taylor Dispersion

Dispersion is the spreading out of a plug, a unit volume of fluid moving within a tubular flow system, as it travels through a tube, this is caused by the varying velocity in the radial axis across

the tube, which occurs under the laminar flow regime (Figure 2.2). The amount of dispersion which occurs in a system is described by the Taylor dispersion coefficient<sup>107</sup> (Equation 2.2).

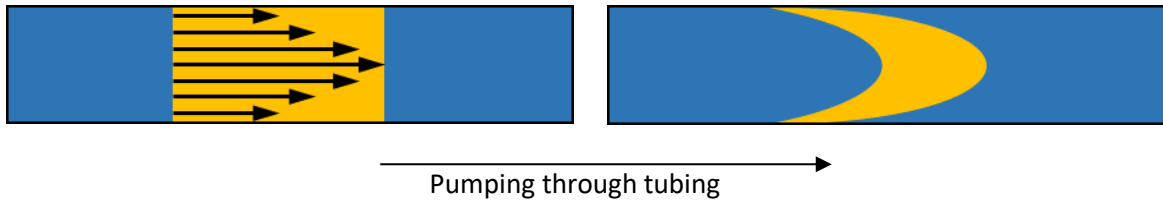


Figure 2.2: Graphical representation of the effect of laminar flow on a plug as it travels through a tube.

$$D = D_{diff} + \frac{u^2 d_t^2}{4\beta D_{diff}}$$

$D_{diff}$  = Diffusion coefficient

$d_t$  = Tube diameter

$\beta$  = Channel geometry parameter

Equation 2.2: Calculation of the dispersion by the diffusion coefficient and flow setup parameters

Jensen *et al*<sup>108</sup> reported a guide for when dispersion will become an issue in a flow system.

Combination of the Bodenstein number, the ratio of convection to dispersion (Equation 2.3), with the equation for dispersion provides an estimate of the magnitude of the effect of dispersion on the system<sup>107</sup>.

$$Bo = \frac{uL}{D} = \frac{4\beta D\tau}{d_t^2}$$

$L$  = Reactor length

$\tau$  = Mean residence time

Equation 2.3: Calculation of the Bodenstein number

If  $Bo < 100$  then you can expect the system to experience a large amount of dispersion. If  $100 < Bo < 1000$  then you would expect a small amount of dispersion in the system. If  $Bo > 1000$  then you would expect the system to behave in a 'plug flow' manner where the velocity profile of the plug is constant across the tube. Estimates of  $Bo$  for a representative system, 1.5 mL reactor and 0.1 mL/min flow rate, show that dispersive effects will be seen in all situations which agrees with the previous calculations for the Reynolds number (Table 2.2).

$d_t$ / mm	$Bo$
1.0	171.9
0.5	690.4



Table 2.2: Calculations of the Bodenstein number over two diameters with a 1.5 mL reactor volume and 0.1 mL/min flow rate.

As dispersion will be a factor in the flow systems used it is necessary to experimentally measure the effect of dispersion on the system.

### **2.2.3 Measuring the effects of dispersion**

To monitor the effect on dispersion that changes to the various flow parameters has, we require a method to measure the amount of dispersion seen in a system, which in this thesis is called the dispersion profile.

To measure the dispersion profile the flow system is setup in the desired configuration (flow rate, reactor volume, temperature) and either in-line monitoring or a sample collector located at the outlet of the reactor.

A short pulse of a solution of compound visible by the detection method used is pumped through the flow setup using predefined reaction conditions (flow rate, reactor volume, reactor ID), generating the dispersion profile for the system (Figure 2.3). As close to a Dirac pulse as possible should be used for determining differences in dispersion.

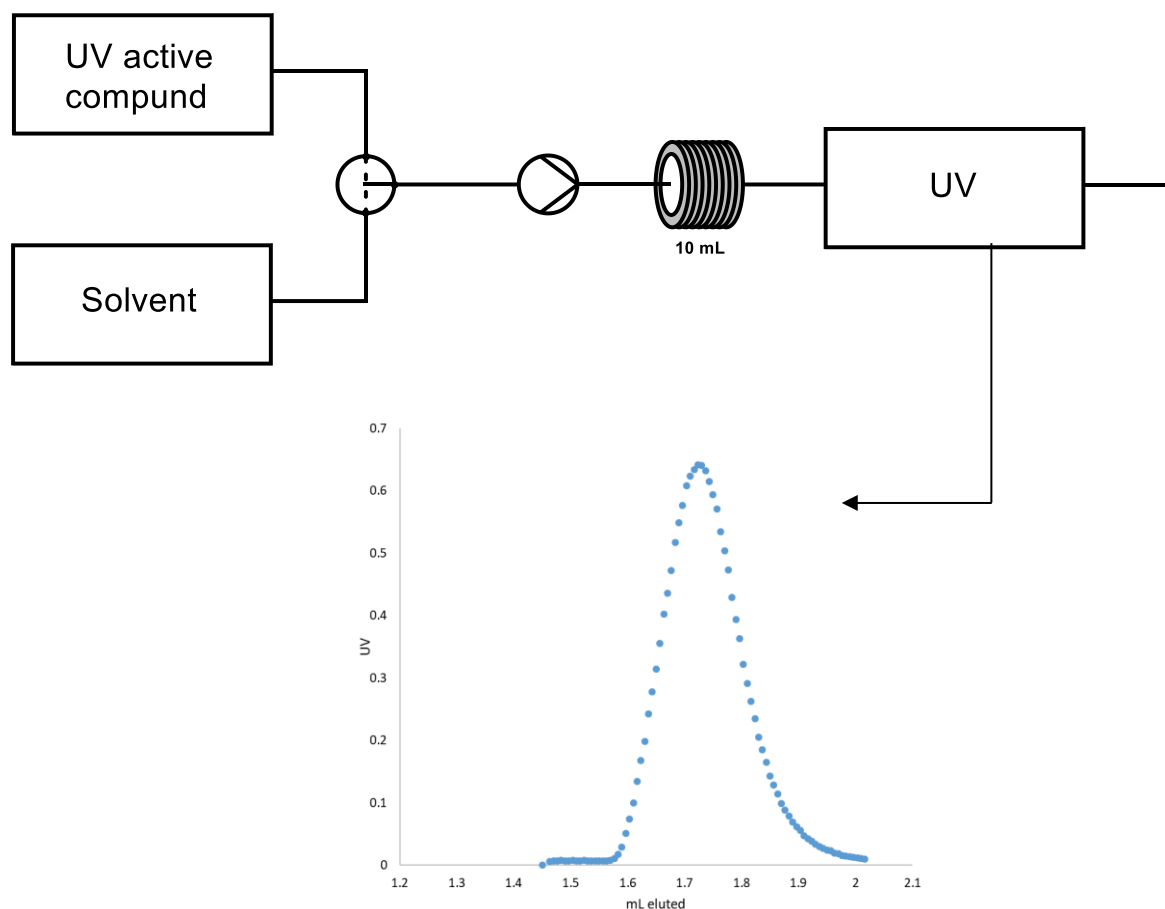


Figure 2.3: Flow setup for measuring the dispersion profile of the system. Initial square plug disperses through the 10 mL dispersion coil and is measured by the in-line UV spectrometer. Plug is generated by the switching of the T-valve prior to the pump to create a plug of reaction mixture surrounded by solvent.

It is possible to evaluate the amount of dispersion from this graph in several ways.

1. Comparison to a standard.

If changing a single variable and comparing between the results, then a 'minimal dispersion' standard can be made by sending a plug of the same visible compound directly to the detector. Comparison of the peak height, the FWHM, or the front gradient can then all be used as estimates for the amount of dispersion which occurs within the reactor (Figure 2.4).

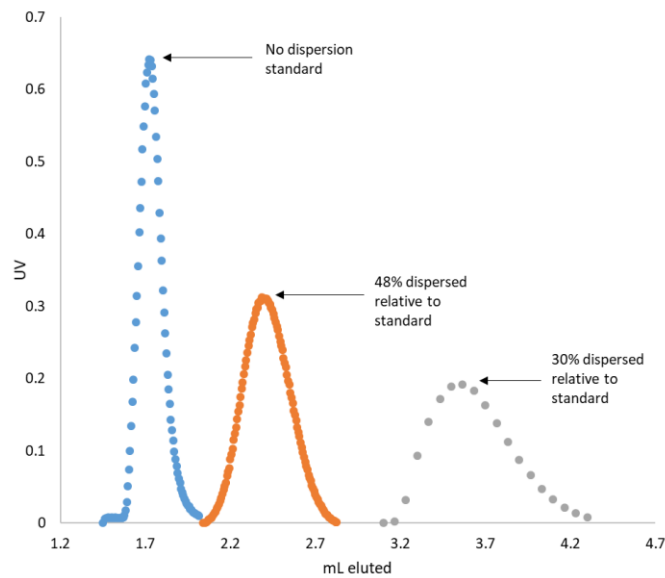


Figure 2.4 : Graph depicting the comparison technique with two dispersed plugs and the 'no dispersion' standard with no dispersion coil. 'No dispersion' is equivalent to the inherent dispersion generated by the flow setup.

## 2. Calculating $\frac{D}{uL}$ .

Various measurements on the curve (Figure 2.5) can be used to calculate  $\frac{D}{uL}$  which is the vessel dispersion number. The larger the value of  $\frac{D}{uL}$ , the larger the amount of dispersion.

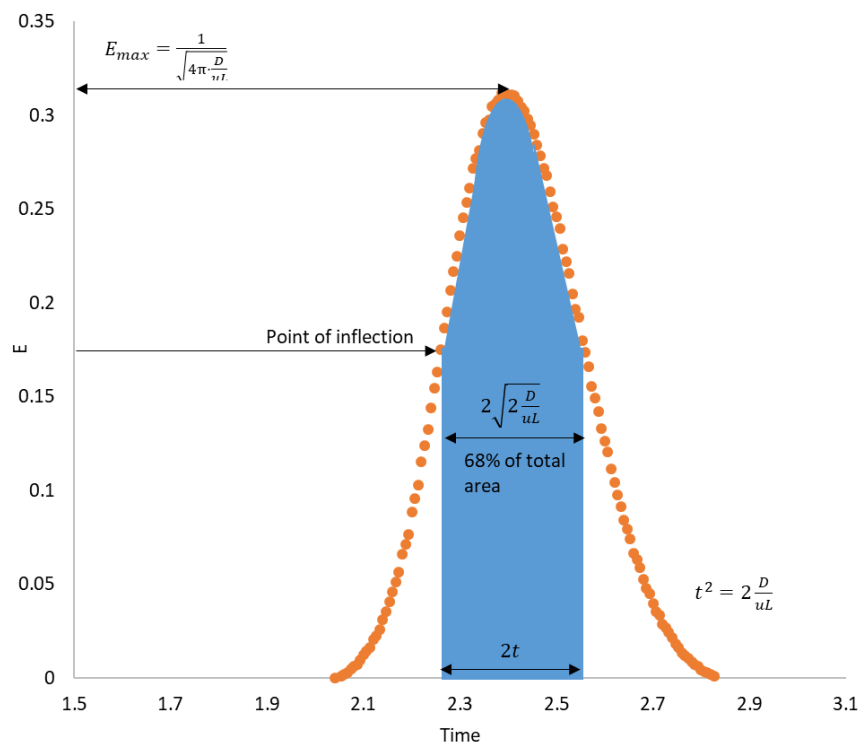


Figure 2.5: Various methods for calculating  $D$  using the dispersion profile

Use of either of these methods will give data which can be used to evaluate the effect of changing the flow setup variables.

### 2.2.4 The Dean number

The Dean number ( $De$ , Equation 2.4) describes vortices which are created due to centripetal forces changing the direction of the fluid motion. Fluid at the outer side of the curve will be moving faster relative to the inner side of the pipe and thus a pressure gradient will exist between the two areas due to the Bernoulli effect<sup>109,110</sup>. The gradient causes a secondary motion radially across the tube in the form of Dean vortices (Figure 2.6).

$$De = \frac{\rho u D_H}{\mu} \cdot \left(\frac{d}{R}\right)^{0.5}$$

$D_H$  = Hydraulic diameter of tube

$d$  = Diameter

$R$  = Radius of curvature of tube

Equation 2.4: Calculation of the Dean number

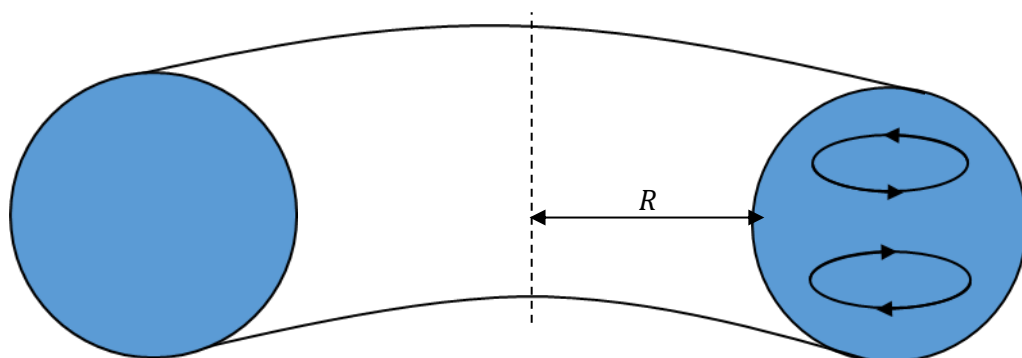


Figure 2.6: Dean vortices (right side) present in flow along curved reactors. Size and nature of vortices depends upon the flow rate, viscosity, internal diameter and radius of tube coils. Vortices induce mixing across the tube.

Values of  $De$  below 40 are insufficient to create secondary motion and the flow is considered fully laminar. Values between 40 and 75 begin to introduce small amplitude secondary flows and values above 75 create the twin vortices seen above<sup>111</sup>. To test the effect of the Dean number, three reactors were created with equal volume (1.5 mL) and internal diameter (1.0 mm) which varied only in the radius of the curvature of the tube. 70 mm (the smallest reactor size easily synthesised), 8 cm (equivalent to the Vapourtec standard reactors) coil diameters, and a 'linear' tube (due to size limitations in the fumehood, the linear reactor consists of linear sections of tubing across a fumehood with 30 cm turns at the fumehood walls to obtain as close to zero Dean

circulation as possible) were chosen to give a range of values of  $De$  and they were all tested across a range of flow rates using the dispersion profile method previously mentioned (Table 2.3).

Radius of curvature of tube / cm	Flow rate / mL·min <sup>-1</sup>	Calculated $De$	Secondary motion expected
0.35	0.1	1.2	✗
0.35	2	45.3	✓
0.35	10	121.0	✓
4	0.1	0.4	✗
4	2	7.2	✗
4	10	35.8	✗
Linear	0.1	0.1	✗
Linear	2	2.6	✗
Linear	10	13	✗

Table 2.3: Range of Calculation of the Dean number for three 1.5 mL reactors of varying curvature radii. Linear corresponds to a reactor stretching between either side of a fumehood with 30 cm turns where necessary which is accounted for in the calculated  $De$ .

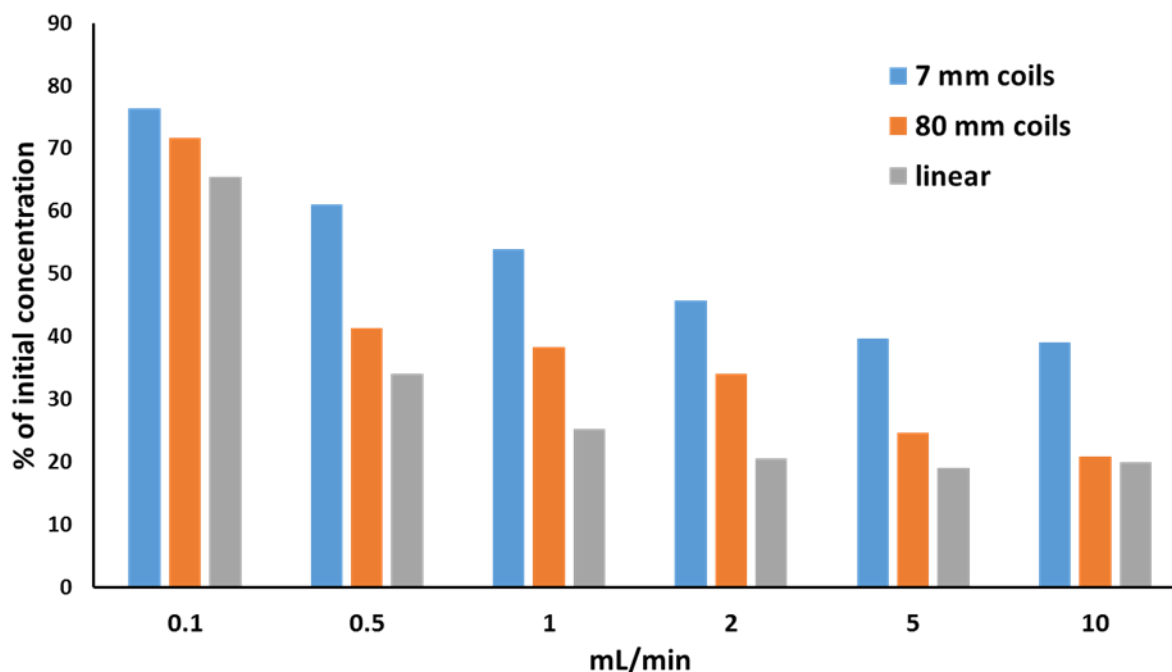


Figure 2.7: Amount of dispersion by comparison of peak height with ‘no dispersion’ plug, across varying reactor curvatures at different flow rates. Dispersion increases as flow rates and radius of reactor coils increases. Lower value = more dispersion.

As shown by Figure 2.7, across all flow rates the linear reactor produced the most dispersion and decreasing the size of the radius gives a corresponding decrease in the amount of dispersion. The effect is more noticeable at the higher flow rates with the 7 mm coil giving nearly half the amount of dispersion at 10 mL/min than both other reactors although this increase in mixing is not enough to fully negate the dispersion. However, to minimise dispersion most reactions will be run at low a flow rate as possible, usually 0.1 - 0.3 mL/min, and at this flow rate the difference between 80 and 7 mm is much smaller and as the 7 mm reactors are significantly more difficult to create especially at large volumes, 80 mm reactors are the best choice. These results show that an effect is present in all systems however, the calculations predicted only two systems to have any Dean-related secondary motion suggesting an additional effect may be present.

### 2.2.5 Internal diameter and flow rate

Flow rate and internal diameter are both factors in the equation for dispersion and are the most common parts of a flow setup to change as they directly affect the residence time of a reaction, as such their effect on dispersion needs to be understood. To this end, the dispersion profile was measured for 0.1 mL plugs of a Rose Bengal in acetonitrile solution, after being pumped through three 1.5 mL reactors of varying internal diameters: 0.25, 0.5 and 1.0 mm. The dispersion profiles were collected at multiple flow rates (Figure 2.8) and the experimental results agree with the

equation for dispersion in that increasing flow rate and internal diameter of the system increases the amount of dispersion occurring. When using the 0.25 mm ID reactor, dispersion was reduced greatly compared to the standard 1.0 mm ID used, unfortunately this tubing is not suitable for all reactions as the increased back pressure generated when using either a large volume reactor or high flow rate could exceed the recommended limits of the Vapourtec system. Additionally, with small internal diameters comes increased risk of blockage from insoluble materials in the reaction mixture. 0.5 mm ID provides a good decrease in the amount of dispersion but only a minor increase in the pressure making it an excellent choice for flow setups.

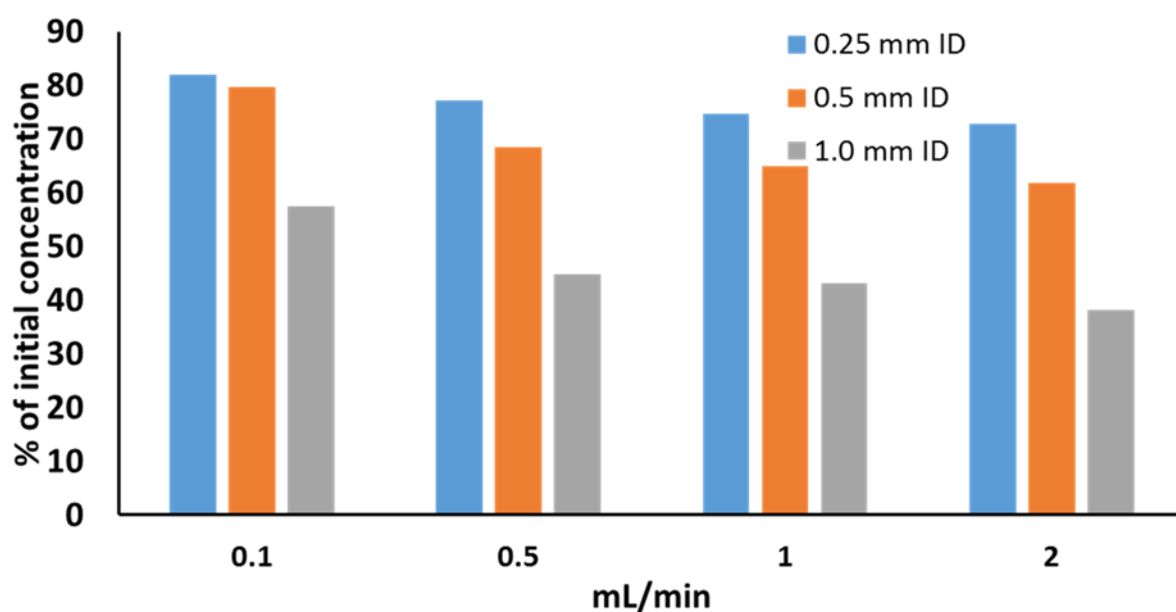


Figure 2.8: Amount of dispersion by comparison of peak height with a 'no dispersion' standard, in a 1.5 mL reactor with varying internal diameters, measured at different flow rates. Dispersion increases as flow rate and internal diameter increases. Lower value= more dispersion

As the flow rate increased, so too did the amount of dispersion. Unfortunately, this setup was limited to 2 mL/min maximum flow rate due to the pressure generated by the 0.25 mm ID loop. To explore the higher flow rates a 0.9 mL, 4 mm radius, 1.0 mm ID loop was used, and the dispersion profiles measured again across a range of flow rates. The results (Table 2.4) show a similar increase in dispersion as flow rate increases, however above 1 mL/min the amount of dispersion stays constant, this could be due to an increase in the turbulent nature of the flow regime causing additional mixing or Dean vortices being formed and causing mixing that counter balances the increase in dispersion caused by the increased flow rate. Calculations of the expected values for the Reynolds and Dean numbers for this system show that the Reynolds number is the most likely cause however the values are still far from full turbulence suggesting another factor is also present in the system.

Flow rate / mL·min <sup>-1</sup>	% of initial concentration from peak height	<i>Re</i>	<i>De</i>
0.1	48.7	2.23	0.35
1	29.9	22.4	3.53
5	32.4	111.9	17.7
10	31.4	223.9	35.4

Table 2.4: Calculated values for the Reynolds number and Dean number with the extracted amount of dispersion from dispersion profiles. A general increase in Reynolds number and Dean number shows an expected decrease in dispersion.

### 2.2.6 Molecular diffusion

The diffusion coefficient (Equation 2.5) is present in the calculation for dispersion. Therefore, there could be a difference in the magnitude of dispersion for molecules of varying size and of varying temperature. An important parameter in molecular diffusion is the Schmidt number (Equation 2.6) which is the ratio of momentum diffusivity and mass diffusivity which can all vary depending on the choice of solvent.

$$D_{diff} = \frac{k_B T}{6\pi\mu r}$$

$k_B$  = Boltzmann constant

$T$  = Temperature

$r$  = Radius of molecule

Equation 2.5 Calculation of the diffusion coefficient

$$Sc = \frac{\mu}{\rho D}$$

Equation 2.6: Calculation of the Schmidt number

#### 2.2.6.1 Molecular radius

To test the variance of molecular radius it was assumed that molar mass was directly related to the radius. A range of molecules from 58 to 1018 g·mol<sup>-1</sup> were dispersed through a 2.5 mL loop with various flow rates and internal diameters and the amount of dispersion was compared to a non-dispersed plug as before. The results (Table 2.5) showed no effect of molecular mass on the



amount of dispersion seen. The data matches that of Kamm *et al*<sup>112</sup> who reported that molecular diffusion only becomes a factor when the value of  $De^2Sc < 100$  apart from results 4 and 5 which still does not show any mass dependence despite having a  $De^2Sc$  value of below 5.

Number	Flow rate / mL·min <sup>-1</sup>	Internal diameter / mm	$De^2Sc$	Molecular mass dependence
1	0.1	1.0	107.5	X
2	0.5	1.0	2686.9	X
3	0.1	0.25	429.9	X
4	0.01	0.25	4.3	X
5	0.01	1.0	1.1	X

Table 2.5: Calculation of the  $De^2Sc$  for various tested flow setups combined with the results from the molecular dependence tests.

Thus, in the tested systems the effect of molecular diffusion is minimal compared to the effects of dispersion and Dean circulation.

## 2.2.7 Temperature

### 2.2.7.1 Effect on dispersion

The effect of temperature was explored by a previous PhD student in the group, Cyril Henry<sup>113</sup>. He measured the dispersion profile in a 10 mL stainless steel reactor across a range of flow rates and two temperatures, 100 °C and room temperature. He found that at the higher temperature dispersion was lower across all flow rates (Figure 2.9) with a larger difference at higher temperatures.

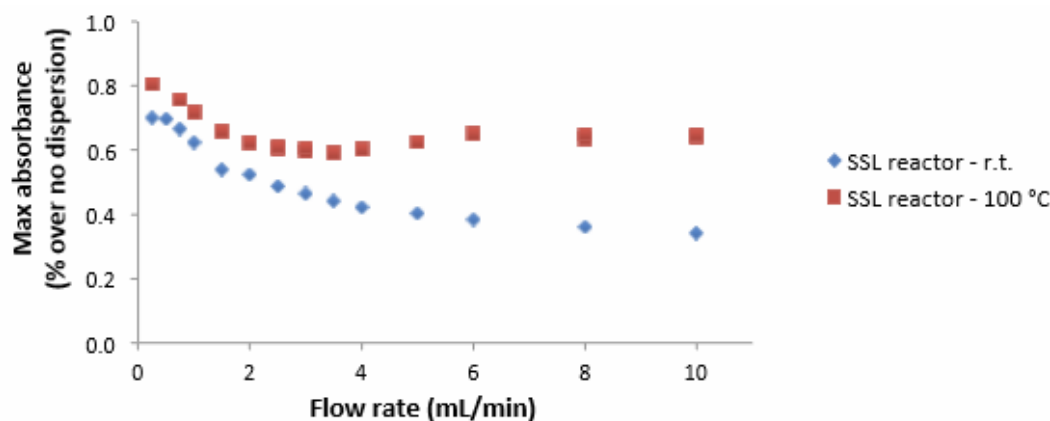


Figure 2.9: Effect of temperature on dispersion. 1 mL plug of a  $5 \times 10^{-4}$  M stock solution of 4,4'-dimethoxybenzophenone in MeCN pumped at various flow rates through a 10 mL stainless steel Vapourtec reactor.

The decrease in dispersion is caused by three factors:

1. The increase in molecular diffusion causing mixing between the laminar flow layers.
2. The raised temperature causing a decrease in the dynamic viscosity which in turn gives an increased Reynolds number which will cause the flow regime to have more turbulent nature minimising dispersion.
3. An increase in the Dean number due to the same reasons as above causing an increase in the mixing by Dean vortices.

Molecular diffusion is only likely to play a large factor at the lower flow rates and temperatures as calculations of  $De^2Sc$  (Table 2.6) show only the room temperature at 0.1 mL/min get close to the boundary for molecular diffusion.

The effect of the Reynolds number increase is only likely to have a small effect as even at the most extreme conditions, it is still far from the complete turbulence boundary. However, it may contribute to the larger difference between the two temperatures at higher flow rates as the differences in  $Re$  become much larger as flow rate increases.

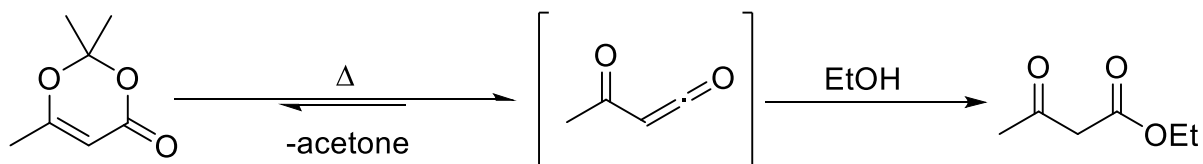
The effect of increasing  $De$  is most likely the largest effect as at room temperature the value of  $De$  only increases above 40 at above 5 mL/min meaning no secondary flow will be present at lower flow rates. Whereas at 100 °C, the boundary for secondary flow is reached at 3 mL/min with full vortices being reached above 5 mL/min. The earlier introduction of secondary flow at 3 mL/min is seen in the graph as the point where the difference between the two temperatures starts increasing.

	Room temperature				
Flow rate / mL·min <sup>-1</sup>	0.1	2	3	5	10
<i>Re</i>	3.63	72.7	109.1	181.7	363.4
<i>De</i>	0.6	11.5	17.2	28.7	57.5
<i>De</i> <sup>2</sup> <i>Sc</i>	193.74	7.8×10 <sup>4</sup>	1.7×10 <sup>5</sup>	4.8×10 <sup>5</sup>	1.9×10 <sup>6</sup>
	100 °C				
Flow rate / mL·min <sup>-1</sup>	0.1	2	3	5	10
<i>Re</i>	7.77	155.4	234.5	388.5	777.0
<i>De</i>	1.2	24.7	37.1	61.8	123.6
<i>De</i> <sup>2</sup> <i>Sc</i>	416.55	1.7×10 <sup>5</sup>	3.8×10 <sup>5</sup>	1.0×10 <sup>6</sup>	4.2×10 <sup>6</sup>

Table 2.6: Calculations of *Re*, *De*, *De*<sup>2</sup>*Sc* under different flow rates and temperatures. Calculations suggest dispersion should decrease as temperature increases which is seen in previous experimental results.

#### 2.2.7.2 Heat transfer

Henry<sup>113</sup> also tested the efficiency of the heat transfer of the built-in air heated system of the Vapourtec compared to a heated oil bath. The thermal fragmentation of a dioxinone derivative to form an acyl ketene (Scheme 2.1) was used as a model reaction to probe the heat transfer. By looking at the conversion of this reaction, it showed that the system required an additional period of heating after the Vapourtec had reported reaching the set temperature to truly reach steady state conditions. Similar issues with heat transfer have also been reported within the group as discussed earlier in section 1.2.4.2.



Scheme 2.1: Thermal fragmentation of 2,2,6-trimethyl-4H-1,3-dioxin-4-one and trapping with ethanol

### 2.2.8 Methods for minimising dispersion

As dispersion is an issue when working under flow, several mesoscale reactor designs have been reported which aim to minimise the amount of dispersion which occurs. Reducing dispersion allows for smaller plugs to be used, saving money on potentially expensive reagents and ensuring confidence in the results obtained due to minimal averaging effects.

#### 2.2.8.1 Oscillatory baffled reactors

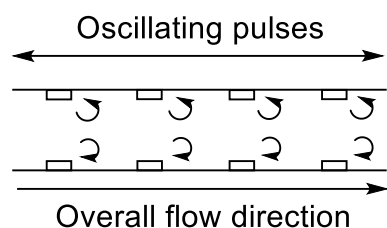


Figure 2.10: Simplified reactor scheme for oscillatory baffled reactors. Flow is provided by two pumps, one provides the flow direction, the second oscillates the flow back and forth to create mixing after the baffles.

Oscillatory baffled reactors<sup>114,115</sup> consist of tubing which contain baffles throughout the volume of the reactor (Figure 2.10). Two pumps are used in the setup, the first acts as a standard pump pushing the plug through the reactor, and the second pump oscillates the flow continuously. The design works in two ways, the baffles aid in disrupting the laminar flow layers and the oscillatory motion creates axial and radial eddies<sup>116</sup> between the baffles which result in excellent mixing and provides near plug flow conditions<sup>117</sup>. Typically these reactors have been used on large scale chemistry which presents large costs however meso-scale options have been presented recently<sup>118,119</sup> however these reactors only work within a band of pump conditions. The value of the oscillatory Reynolds number (Equation 2.7) must be greater than 100 for eddies to form and greater than 300 for chaotic flow<sup>120</sup> otherwise no benefit over traditional reactors would be seen.

$$Re_o = \frac{2\pi f x_o \rho d}{\mu}$$

$f$  = Frequency of oscillation

$x_o$  = Amplitude of oscillation

Equation 2.7: Calculation of the oscillatory Reynolds number

### 2.2.8.2 Coiled flow inverter reactors

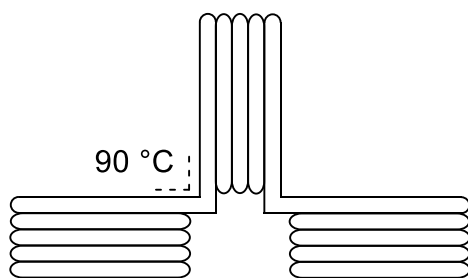


Figure 2.11: Reactor design for coiled flow inverter reactor. Dean vortices are created in the coils, after the 90 °C turn, the flow is inverted and new Dean vortices are created increasing the amount of mixing.

Coiled flow inverter reactors<sup>121</sup> (Figure 2.11) work *via* maximising the amount of Dean vortices by having tight coils and introducing 90° bends in the coil. These bends invert the flow and change the direction of the centripetal forces which will create new Dean vortices and as the number of these bends increases so too does the amount of mixing. A benefit of this design is that it is simple and cheap requiring only tubing to create and it does work over a larger range of conditions than the oscillatory baffled reactors. However, the residence time distribution is further from plug flow than oscillatory baffled reactors and controlling the temperature of the reaction would be difficult due to the size and geometry of the reactor.

### 2.2.8.3 Continuous stirred tank reactors

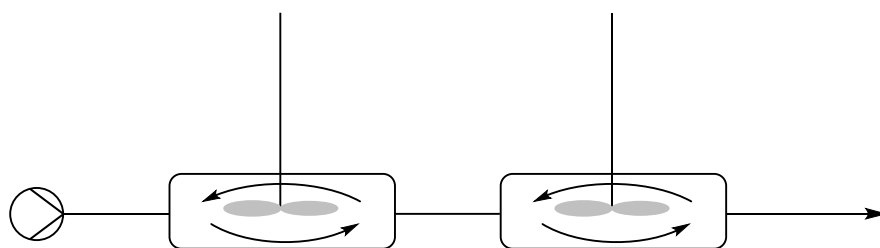


Figure 2.12: Reactor diagram for continuous stirred tank reactors. Reaction mixture is pumped through reactors with active mixing from a stirrer bar/agitator depending on scale.

Continuous stirred tank reactors (Figure 2.12) are one of the main classes of reactor used for large scale chemical synthesis as they provide excellent mixing throughout the process<sup>122</sup>. Miniaturised versions of these reactors have been reported<sup>42,43</sup> consisting of a plastic enclosure containing a stirrer bar. Multiple CSTRs can be combined in a chain to generate the required volume and additional ports added for combination with further reagents or quench lines as well as varying conditions such as temperature throughout the system. The excellent mixing generated by these reactors provides a narrow residence time distribution and can easily handle the generation of

solids and the use of slurries which other reactor designs struggle with. These reported miniaturised designs are limited by their maximum pressure rating (10 bar) which will affect the range of chemistry able to be performed in them.

### 2.2.8.4 Knitted reactor

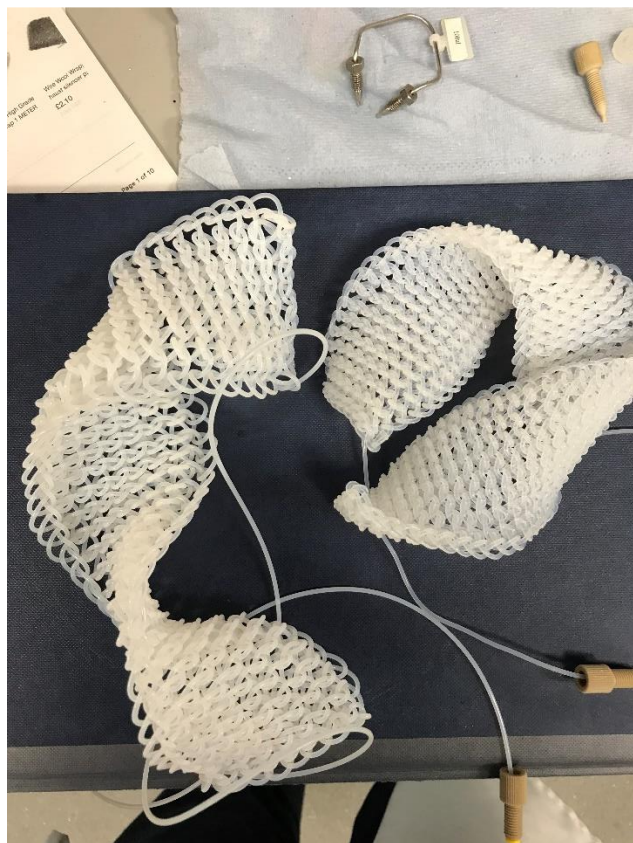


Figure 2.13: Photo of knitted reactor. Mixing is generated by vortices caused by the sharp turns in the reactor design.

Knitted reactors<sup>123</sup> are standard tubular reactors which have been woven into a pattern (Figure 2.13) containing a large amount of sharp turns initially designed to input a delay into a HPLC method to allow for MS detection of the elute to be achieved or post column modification to be performed. These reactors minimise dispersion by forcing the layers to mix as they travel round the corners of the reactor in a similar method to the coiled flow inverter reactors<sup>124</sup>.

Measurements of the amount of dispersion were tested as described above and it was found that, against standard 0.5 mm ID tubing of the same volume, the knitted reactors performed better across all flow rates (Figure 2.14) however above 1 mL/min, the amount of dispersion seen in the knitted reactor decreases. An increase in the amount of mixing *via* Dean vortices or turbulence forming at the tight bends is the most likely reason for this decrease in dispersion. These reactors have the benefit of being purchasable and relatively inexpensive (£400 for 4 mL), however the decreased internal diameter and sharp turns do create a large pressure increase which limits the

maximum flow rate and temperature achievable, above 5 mL/min was not achievable with the flow setup used.

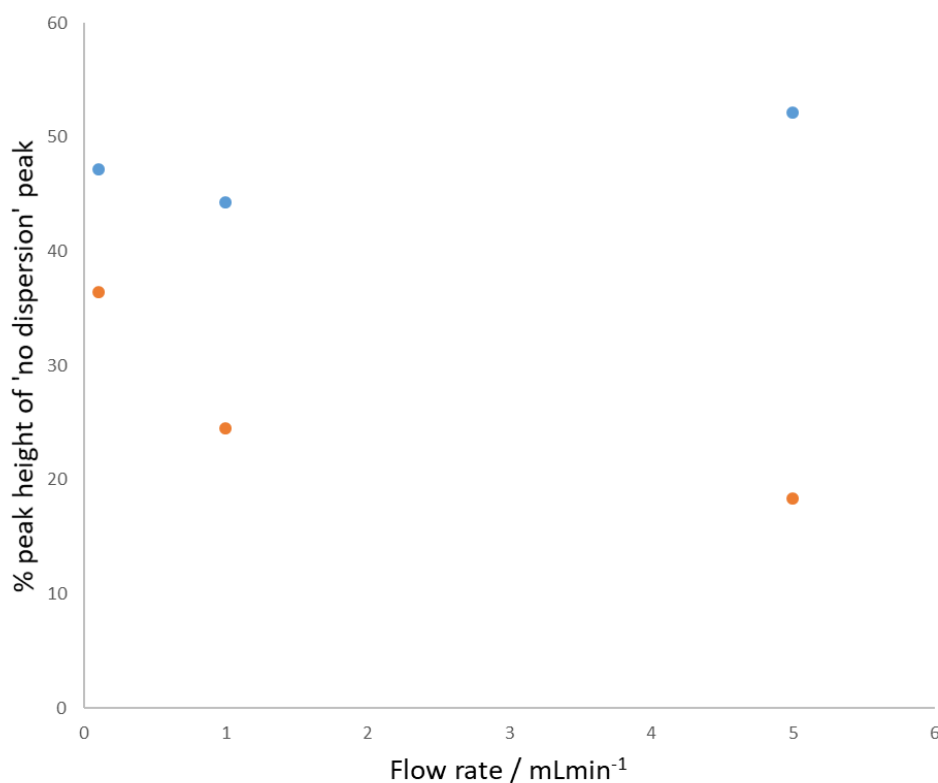


Figure 2.14: Amount of dispersion relative to 'no dispersion' peak, in a 4 mL reactor at various flow rates. A 0.1 mL plug of (0.02070 g, 0.08 mmol) diphenylfulvene in 15 mL DMF was pumped at various flowrates. Orange = standard 0.5 mm ID. Blue = knitted 0.5 mL ID.

#### 2.2.8.5 Glass bead filled reactor

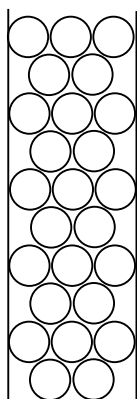


Figure 2.15: Reactor setup for a glass bead filled reactor. Density of packing will affect the pressure drop of the system.

## Chapter 2

Packed bed reactors are tubular reactors filled with a solid bed of various shapes<sup>125</sup> (Figure 2.15). Its typical use is for reactions with solid catalyst<sup>126</sup> where the catalyst would either be attached to the solid of the packed bed or the catalyst itself would make up the bed. The packed bed provides excellent mixing<sup>127,128</sup> which helps to minimise the velocity difference between the laminar flow layers. However, at high flow rates or when utilising high viscosity solvents, the pressure drop generated can be very large limiting the range of usable conditions.

To test how capable these reactors were at minimising dispersion, a method for creating a similar reactor design was devised. The examples found in the literature used recycled HPLC columns and 1.6 mm ID tubing however I opted to use the standard 1 mm ID due to its availability in the lab, the minimisation of dispersion due to lower ID, and the ease of creating more reactors without having to rely on a supply of used HPLC columns.

The packing material needed to be inert, have smaller than 1 mm ID, be a regular size to allow efficient packing, and be cost effective compared to other reactors. For these reasons 0.5 mm glass beads<sup>129</sup> were chosen. The use of large diameter beads resulted in far fewer particles per layer than a traditional packed bed however, this lowered the pressure drop across the reactor and minimised the formation of bridges which could block the flow path.

Initially packing was attempted by applying a vacuum to one end of the tube and attempting to suck up the glass beads. Unfortunately, the beads rapidly blocked the tube preventing further addition. A gravity-fed method was more successful with the beads in a syringe attached to the tubing *via* a Luer adapter. Manual agitation of the syringe by vigorous up and down arm movements allowed the beads to fall into the tubing unfortunately regular blockages still occurred. To overcome this, the entire system was filled with water, which minimised blockages and simplified the clearing process to physical interference at the blockage site. The manual method allowed for a reactor of 0.9 mL to be formed in a day. Testing the dispersion of this reactor against an open tubular reactor of the same volume (Figure 2.16) shows an improvement across all flow rates however, as with the knitted reactor, at high flow rates ( $> 2$  mL/min), a dramatic decrease in the amount of dispersion is seen as well as a corresponding increase in system pressure. The decrease in dispersion at higher flow rates can be attributed to switching from laminar flow to transitional flow<sup>130</sup> as the calculated packed bed Reynolds number<sup>131</sup> (Equation 2.8) increases above 10 at 1 mL/min (Table 2.7).



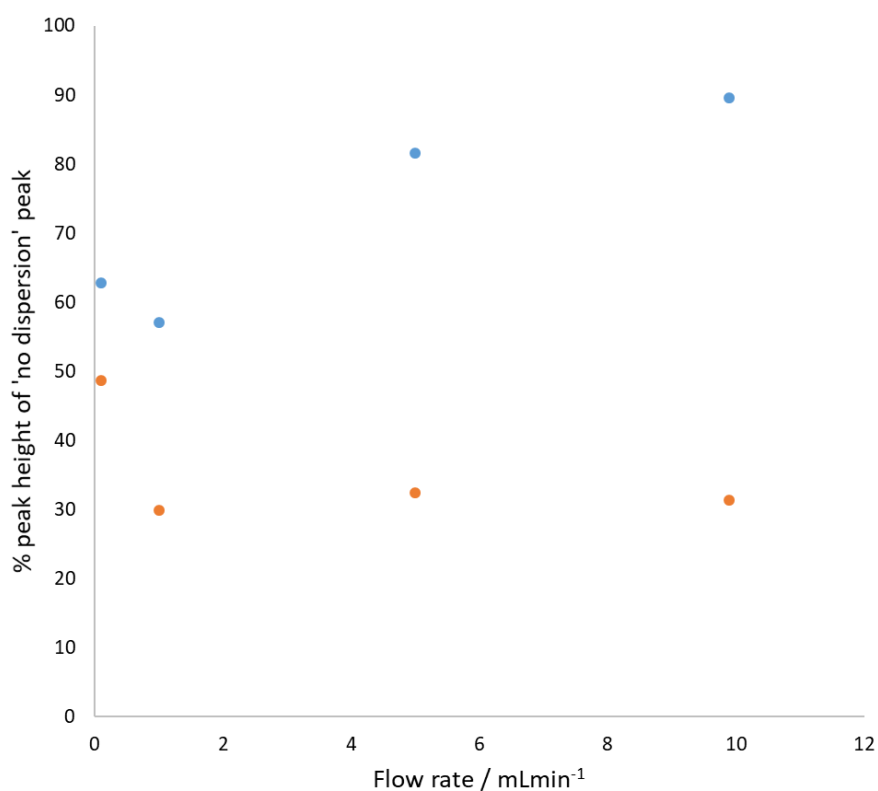


Figure 2.16: Amount of dispersion relative to a 'no dispersion' peak in a 0.9 mL reactor. A 0.1 mL plug of a stock solution of (0.02140 g, 0.08 mmol) diphenylfulvene in 15 mL DMF was pumped at various flowrates. Orange = standard 1.0 mm ID. Blue = glass bead filled reactor.

$$Re_p = \frac{\rho v_s d_b}{\mu \varepsilon}$$

$v_s$  = Superficial velocity

$d_b$  = Diameter of beads

$\varepsilon$  = Voidage

Equation 2.8: Calculation of the packed bed Reynolds number

Flow rate / mL·min <sup>-1</sup>	0.1	1	2	5	9.99
$Re_p$	1	11	22	53	112

Table 2.7: The calculated packed bed Reynolds number for the flow setup at various flow rates.

As the reactors are very efficient at minimising dispersion, larger volumes were desired unfortunately this method is limited by the height of the room and the height and fitness of the person creating the reactor. An automated larger scale version was designed which attached the

syringe of beads to a vortex mixer and suspended the tubing down a 6-floor staircase. The mixer provided the necessary agitation of the beads to send them into the tube and manual intervention was only needed to refill the syringe and to clear any blockages which occurred. A 7 mL reactor could be created in a day using this method, however with multiple/larger mixers, this output could be increased.

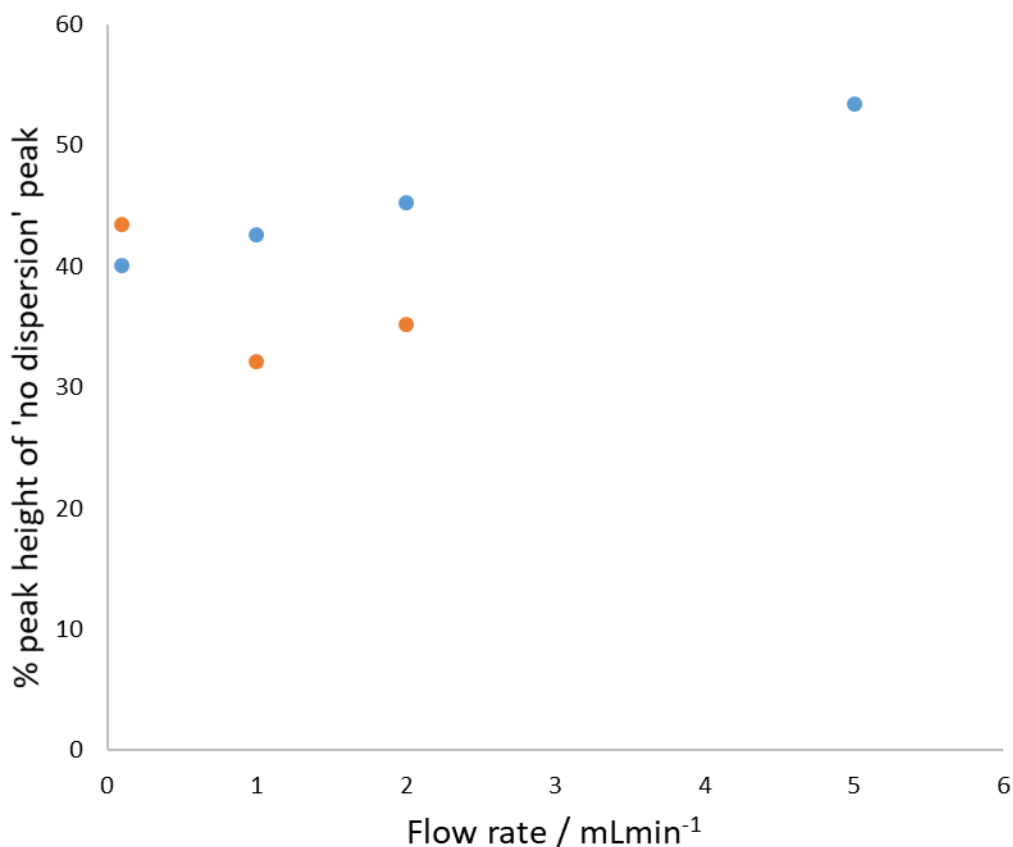


Figure 2.17: Amount of dispersion in a 4.4 mL reactor. A 0.1 mL plug of a stock solution of (0.02112 g, 0.1 mmol) diphenylfulvene in 15 mL DMF, at various flow rates. Orange = Knitted 4 mL reactor. Blue = glass bead filled reactor.

With the larger reactors being created, a more accurate comparison between the glass bead filled and knitted reactors can be made. Dispersion profiles were generated for a range of flow rates using a 4.4 mL packed reactor the results of which (Figure 2.17) show an almost identical result to that of the knitted reactor at high flow rates however at low flow rates the knitted reactor performs much better. The glass bead filled reactor has the advantage of being able to easily fit in an oil bath or air heated reactor however it does take time and a large vertical space to create.

#### 2.2.8.6 Segmented flow

Another method for the minimisation of dispersion is the use of segmented or compartmentalised flow. In this approach, the reaction plug is sandwiched with either immiscible solvent or an inert

gas segment to attempt to minimise the spreading caused by dispersion (Figure 2.18). Sample dispersion is not removed entirely however as a film of the reaction mixture is left on the reactor walls which can then mix with plugs which follow<sup>132,133</sup>, with the amount of mixing dependant on factors such as reactor material, flow rate, solvent viscosity and size of plugs and spacers<sup>134</sup>.

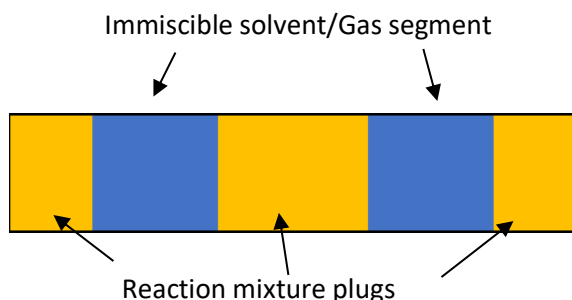


Figure 2.18: Graphical representation of segmented flow. Plugs of reaction mixture are separated by either immiscible solvent or gas segments, preventing inter-plug mixing.

The segmented flow was tested by addition of  $N_2$  plugs to a flow stream ethyl-2-cyanoacetate in DMSO. The addition was accomplished using a VICI 2-position 6-port valve (Figure 2.19) and the size of the  $N_2$  loop was chosen to be 1 mL as when smaller loops were used, the  $N_2$  segments would disappear upon addition into the reaction stream, most likely due to the increased pressure in the reactor allowing the  $N_2$  to dissolve into the solvent.  $N_2$  segments were introduced into the 15 mL ethyl-2-cyanoacetate plug every 2 minutes and the resulting segmented flow was pumped through a 32 mL reactor at 1 mL/min.

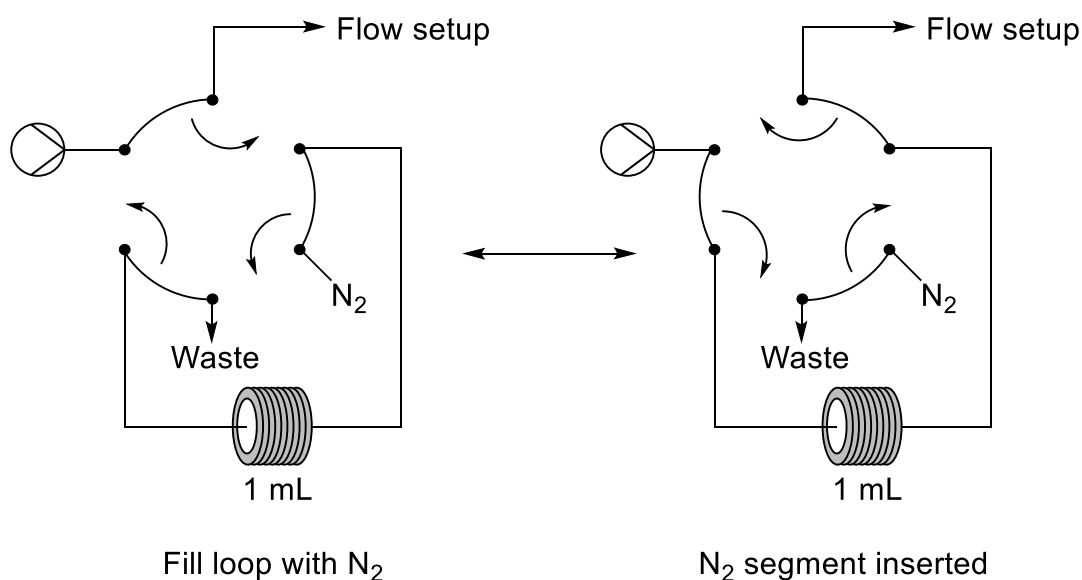


Figure 2.19: 6-port valve setup for inserting a  $N_2$  segment into a flow stream. The  $N_2$  segment is pushed out by the reaction mixture which is sent to waste when the valve is switched to replenish the  $N_2$  segment.

## Chapter 2

The resulting dispersion profile (Figure 2.20) shows a much steeper gradient at either end of the steady state, however there is not a large increase in the amount of steady state present, this is due to the large amount of reaction mixture which is removed when inserting the N<sub>2</sub> segments as the reaction mixture pushes the segment out of the loop and when the valve is switched back, that 1 mL of reaction mixture is sent to waste. On the leading edge of the plug, it is possible to see the distinct segments separated by the N<sub>2</sub> segments represented as areas where the IR response rapidly increases. Whilst the segmentation does decrease the sharpness of the gradient, the large decrease of initial reaction mixture does increase waste. Additionally, as the segments only cause a marginal difference, the increase in cost and effort for including N<sub>2</sub> segments is not worth the benefit gained.

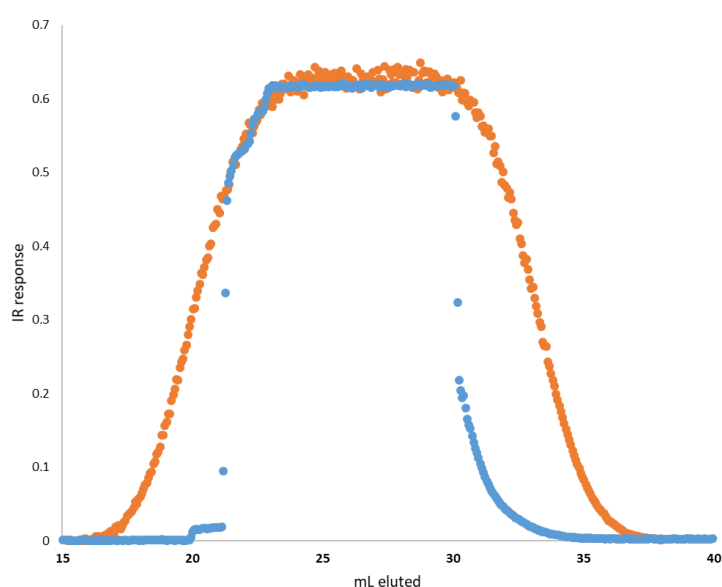


Figure 2.20: Dispersion profile for a 15 mL plug pumped through a 32 mL reactor. The overall segmented flow size is less than 15 mL due to the removal of segments when pushing N<sub>2</sub> bubbles out. Orange = standard. Blue = Segmented flow

The utilisation of T-switching valves in combination with a 6-port valve could circumvent this issue by adapting the design of the gas segment insertion (Figure 2.21). These valves are located between holding loops which will be the reaction mixture segments. When the loops are full, the valves are switched and N<sub>2</sub> or immiscible solvent segments are introduced in between the reaction mixture plugs. The amount of mixture lost would be minimised consisting only of the volume of tubing connecting the T-switching valves, but this could easily be minimised to compared to the mL lost using the previous method. Additionally, this would also allow easy adjustment of the size of the gas and reaction mixture segments by adjusting the loop sizes. However, this design is expensive as it requires 2 T-switching valves and 1 6-port valve for every

N<sub>2</sub> segment and would require a larger amount of starting material to ensure all the loops are full of steady state.

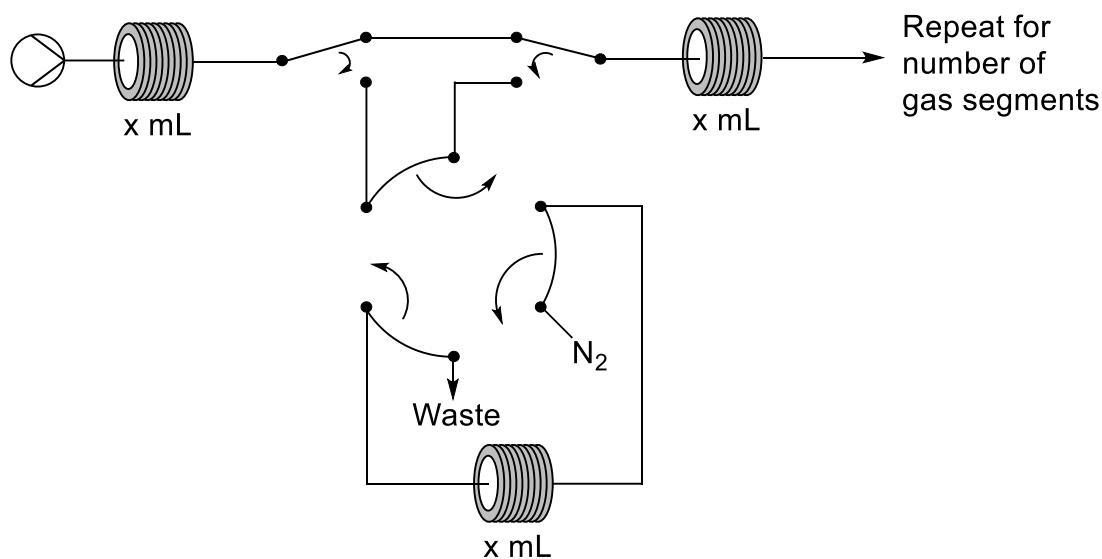


Figure 2.21: Flow setup for creation of segmented flow minimising reaction mixture loss. Setup consists of two T-valves and one six port valve.

### 2.3 Reagent mixing

Reagent mixing is a key factor in flow chemistry as inefficient mixing can result in increased reaction times and potentially decreased yields from side reactions in the starting materials under the reaction conditions. As such it is important to understand the amount of mixing occurring in the system. Jensen *et al* have reported<sup>108</sup> a method for determining whether use of a mixer is required based on the Damköhler number (Equation 2.9) and a coefficient ( $\chi$ ) which depends on the reaction kinetics. If your reaction conditions fall above the  $Da = 1$  curve for the specific  $\chi$  value, then mixing is required. Several designs and commercial products are available<sup>135,136</sup> and a selection of easily implantable mixers are presented here.

$$Da = \frac{\chi d_t^2}{4\tau D_{diff}}$$

$\chi$  = Coefficient for system kinetics and feed ratios

Equation 2.9: Calculation of the Damköhler number

### 2.3.1 Types of mixers

#### 2.3.1.1 T and Y-mixers

The standard mixer utilised in this project is the T and Y-mixer<sup>137</sup>. These mixers have been shown to give inefficient mixing at below 1 mL/min<sup>138,139</sup> which means that issues may occur when reactive starting materials are being used at these low flow rates. It is less of an issue for longer reactions due to mixing *via* diffusion, which is relatively fast (125 s assuming  $D_{diff} = 10^{-9} \text{ m}^2 \text{ s}^{-1}$ ) at 1.0 mm ID and mixing *via* Dean circulation providing the correct reactor conditions are met.

#### 2.3.1.2 Magnetic field induced flow mixer

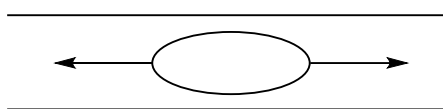


Figure 2.22: Reactor diagram for magnetic field induced flow mixer. Inner ellipse is a magnetic stirrer which is moved up and down the tube by a magnetic field causing mixing in the tube.

In 2011 Ley *et al* published<sup>140</sup> an in-line flow mixer utilising a magnetic stirrer placed inside of a length of tube (Figure 2.22). Two solenoids are located at either end of the mixing tube which alternate between on and off causing the stirrer to be repelled back and forth between the solenoids, which generates the mixing. The magnetic field induced mixer also has the benefit of preventing blockages by agitation of formed solids to form a suspension however it does require some knowledge of electronics to create.

#### 2.3.1.3 Screw-tube mixer

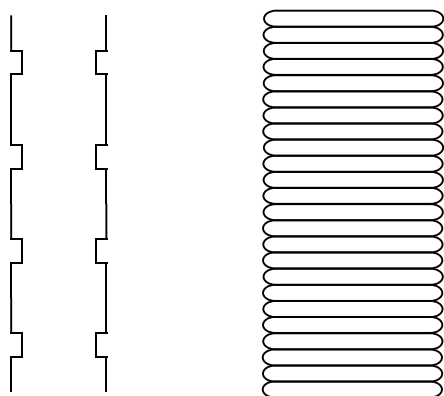


Figure 2.23: Reactor diagram for screw-tube mixer. Left: Zoomed in diagram of tube showing reactor structure. Right: Overall mixer design.

Jensen *et al* also reported a mixer created from reactor tubing by thermoforming the tubing into a screw-shaped tube<sup>141</sup> (Figure 2.23). PFA, ETFE and FEP tubes were placed into metal moulds with engraved screw patterns and then the setup was heated to close to the melting point of the plastics for several hours. The resulting screw-mixers were characterised by pumping two dye streams through the mixers and visually observing the amount of mixing. Full mixing was observed after only 1-2 cm at flow rates from 0.3 to 6 mL/min whereas the straight tube was entirely dependent on molecular diffusion and failed to fully mix in the length tested. At lower flow rates the mixer began to perform less efficiently however was still an improvement over open tubes. Additionally, only a small pressure drop is seen using these mixers which allows for the formation of an entire reactor of this design.

#### 2.3.1.4 Staggered herringbone mixer

A micromixer with herringbone type structures (Figure 2.24) has been reported<sup>142,143</sup> which creates transverse mixing flows at Reynolds numbers between 0 and 100. The switching of the orientation of the herringbones changes the centre of the rotation and ensures efficient mixing and a 3 cm section of staggered herringbone will fully mix all flows with Péclet number, the ratio of advective to diffusive transport (Equation 2.10), less than  $10^6$  which encompasses all flows likely to be experienced which require a mixer.

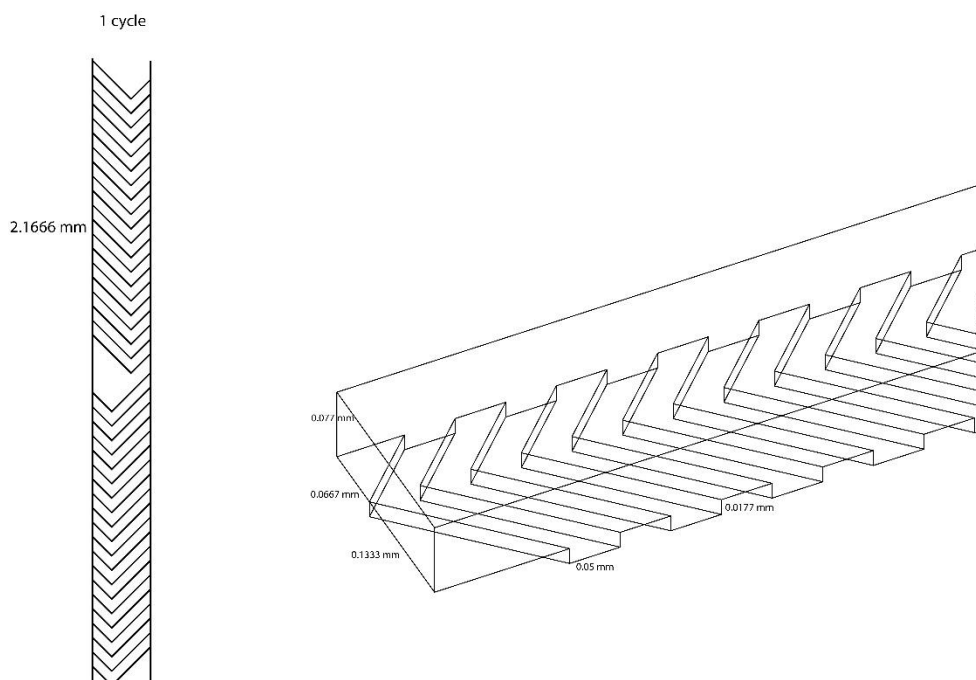


Figure 2.24: Schematic for staggered herringbone mixer. Structures in the mixer create rapid mixing across the mixer.

$$Pe = Re \cdot Sc$$

### Equation 2.10: Calculation of the Péclet number

Unfortunately, the dimensions of the design require a system like lithography to create the device and due to the small path size, pressure drop may become an issue at higher flow rates as well as potential fouling and blocking of the mixer.

#### 2.3.1.5 Dean vortices

In 2004 a mixer which utilised Dean vortices was reported<sup>144</sup> which used milling to create chips with varying curvature ratios. Unlike the open tubes which required relatively high Reynolds number to induce vortexes, the milled design used in this mixer begins to generate at Reynolds numbers between 1 and 10 which should allow mixing at the slowest conditions likely to be used in mesoscale flow chemistry. As with the screw-tube reactor this theory can be scaled up as described above with the coiled flow inverter reactors.

## 2.4 Summary

Several key factors which effect the performance of a flow chemistry system have been described or characterised here. The effect of flow rate, internal diameter, molecular diffusion, Dean vortices, and temperature on the amount of Taylor dispersion has been investigated. Additionally, several designs of reactor have been presented with the focus on their ability to minimise dispersion. The limit on when an additional mixer is required has also been presented with a comparison on various types of mixers which can be easily accessed in the laboratory.

These investigations have led to flow parameters and guidelines for the upcoming reactions presented in this thesis.

In order to minimise the effect of dispersion, flow rate and internal diameter will be minimised wherever possible.

Low dispersion reactors such as glass bead filled, knitted, or tightly coiled reactors will be used wherever possible.

The effect of molecular diffusion can safely be ignored in the flow systems presented.

Heat transfer when using air heaters may be ineffective and oil bath heated reactors should be used wherever possible.

Additionally, several designs of reactor have been presented with the focus on their ability to minimise dispersion. The limit on when an additional mixer is required has also been presented with a comparison on various types of mixers which can be easily accessed in the laboratory.



## Chapter 3 Optimisation of Irradiance Times – The Switch-Off Method

### 3.1 Photochemistry

Photochemistry is an area increasing in popularity over recent years<sup>145–152</sup>, this is due to providing simple access to complex structures and reactivity which often only requires the starting material and light making it an excellent choice for both green chemistry and general synthesis. In addition, photochemistry has been utilised in an increased scale or an industrial setting<sup>153–158</sup> to provide cheap clean routes to products such as caprolactam, which is produced on a >100,000 ton per annum scale for the production of Rose Oxide<sup>159</sup>.

#### 3.1.1 The fundamentals of photochemistry

##### 3.1.1.1 Mechanism

The basis of photochemistry is the absorbing of a photon of light by a molecule causing an excitation of the molecule from the ground state ( $S_0$ ) to an excited state ( $S_1$ ). From here several pathways are available for the excited molecule to decay back to the ground state by fluorescence or phosphorescence resulting in no change to the molecule (Figure 3.1).

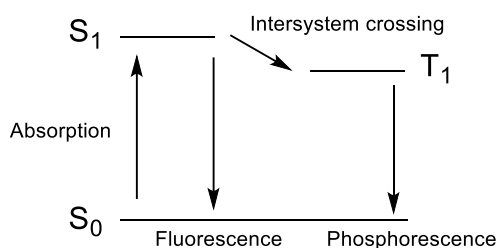


Figure 3.1: Simplified Jablonski diagram showing the basic excitation and relaxation pathways

However the molecule can undergo reaction whilst in the excited state, both intra and inter-molecularly, in reactions that are thermally disallowed by the Woodward-Hoffmann rules<sup>160</sup> such as [2+2] cycloadditions, allowing access to complex molecules and cyclic structures difficult or impossible to access *via* thermal reactivity.

For photochemistry to occur, the starting material must absorb the photon of light and become excited, for this to occur there must be an overlap in the absorption spectra of the molecule and the wavelength of the photon. Therefore, the choice of light is very important when planning a

photochemical reaction. However if there is no significant overlap in the region of light you wish to use, then the use of photosensitisers may provide an alternative route<sup>161</sup>.

Photosensitisers work by transferring the excitation energy obtained from absorbing a photon to another molecule, in this case the reaction starting material. They achieve this by having a large absorption in an accessible region of the light spectrum which ensures the molecule will absorb the light effectively. However, to transfer the energy to the starting material, the excited molecule and the starting material must interact before the photosensitiser decays to the ground state. For a standard molecule this transfer is unlikely to occur due to the rapid speed at which decay by fluorescence happens (Table 3.1). However, photosensitisers have a high rate of inter-system crossing which converts the molecule from the  $S_1$  state to the  $T_1$  state which can only decay *via* phosphorescence which is a much slower process. The longer time spent in the excited state increases the likelihood of the excitation energy being passed to the target molecule and allowing the photochemical reaction to occur.

Process	Average time / s
Fluorescence	$10^{-9} - 10^{-6}$
Intersystem crossing	$10^{-11} - 10^{-6}$
Phosphorescence	$10^{-3} - 100$

Table 3.1: Average range of time for excitation and relaxation pathways

### 3.1.1.2 Performing photochemistry: Batch vs flow

#### 3.1.1.2.1 Batch

Photochemical reactions in batch typically use an immersion well reactor (Figure 3.2) which consists of a high-power mercury lamp placed inside of a double-jacketed well. One jacket is for cooling of the setup and the other contains the reaction mixture.

Rayonet<sup>162</sup> has commercialised another photoreactor design which consists of a ring of six light sources inside of which the sample gets placed. The area of reaction material that is exposed to the light source is increased compared to the immersion well reactor however, this comes at an increased cost.

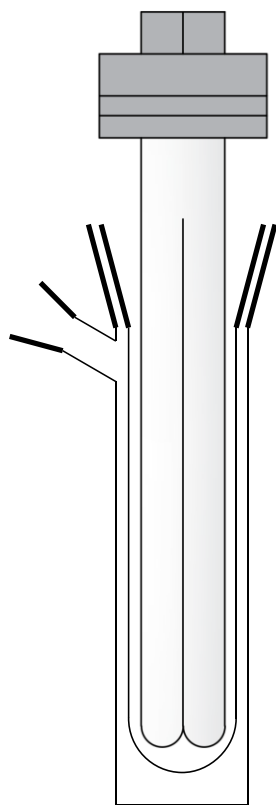


Figure 3.2: Diagram of an immersion well reactor. Reagent mixture is located between the walls and mixed *via* a stirrer located at the bottom.

Typically batch photochemical reactions require low reagent concentrations for two main reasons:

1. Side reactions.  
At higher concentrations dimerisation or polymerisation of the starting material can occur. Additionally, potential reactions between the product and starting material become more likely at higher concentrations. Whilst this issue is not limited to batch only, it is a worse issue due to poor mixing causing the reaction mixture closer to the light source to over react. The consequence of this inhomogeneity forces low concentrations to be used to minimise the side reaction however this creates the second major issue with batch photochemistry.
2. Long reaction times.  
The penetration of light into reaction mixture is limited by the concentration of the starting material. The Beer-Lambert law (Equation 3.1) combined with the equation for transmittance (Equation 3.2) show that for a 0.05 M solution with an extinction coefficient of  $20,000 \text{ M}^{-1}\cdot\text{cm}^{-1}$ , 90% of the light will be absorbed after 0.01 mm of reaction

mixture. The lack of light penetration results in increased reaction times in order to allow all starting material to transfer to the surface and absorb the light, and this situation only worsens as concentration increases<sup>163</sup> (Figure 3.3).

$$A = \varepsilon \cdot c \cdot l$$

$$A = \text{Absorbance}$$

$$\varepsilon = \text{Extinction coefficient}$$

$$l = \text{Path length}$$

Equation 3.1: Beer-Lambert law

$$A = -\log\left(\frac{I}{I_0}\right)$$

$$\frac{I}{I_0} = \text{Transmittance}$$

Equation 3.2: Equation relating the absorbance and transmittance

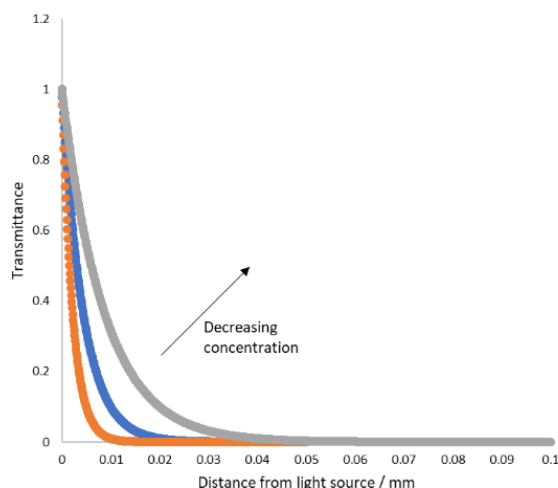


Figure 3.3: Graph detailing distance taken to reach zero transmittance with an extinction coefficient of  $20000 \text{ M}^{-1}\cdot\text{cm}^{-1}$ . Orange =  $0.025 \text{ M}$ , Blue =  $0.05 \text{ M}$ , Grey =  $0.1 \text{ M}$ .

### 3.1.1.2.2 Continuous

Flow photochemistry overcomes these issues by only having a small path length (around 1 mm for mesoscale, smaller for microscale) for the light to penetrate. A smaller path length means that shorter reaction times or higher concentrations can be used to increase the productivity of the reaction as a larger percentage of the reaction mixture is irradiated.

An additional benefit is the ease of setting up a photochemical reaction in flow. As described above batch technology tends to utilise expensive equipment or glassware combined with high-power lamps to minimise the issues described above. Comparatively, several reduced cost homemade flow reactors have been reported<sup>93,164–167</sup> many using low power light sources saving

on money and increasing safety, as well as commercial options<sup>168,169</sup> allowing a very simple, cost-effective route to photochemistry compared to batch configurations.

The reproducibility of flow chemistry also provides a benefit with uniformity in the irradiance profile of the product as each portion of reagent mixture has experienced the same intensity of light and irradiance time due to the control given by the flow rate, reactor volume, and small ID.

### 3.1.1.3 The limitation of flow

For the monitoring of reaction progress and optimisation of irradiance time, batch photochemistry, with its amenability to sampling analysis, has the advantage over flow chemistry which must rely on multiple runs at different flow rates (as varying reactor volume is not always feasible) to optimise with respect to irradiance times. Several methods involving transient flow have been described earlier (Section 1.2.4.2) however these are not suitable for all configurations of flow equipment and cannot be used automatically with some control software. As such the aim of the work presented in this chapter was to create a simple methodology which would allow for the extraction of irradiance time data from a single flow experiment.

## 3.2 The switch-off method

### 3.2.1 The methodology

In a continuous flow reaction, the residence time of the reaction mixture is a function of its distance travelled through the reactor (Equation 3.3).

$$Rt_x = \frac{V_x}{u}$$

$$V_x = \text{Volume travelled at point } x \text{ along reactor}$$

Equation 3.3: The relation of residence time to the reactor volume and flow rate

Both thermal and photochemical reactions have this property, and this means that throughout the reactor there is a reaction time gradient covering a range from 0 to the maximum set by the reactor volume and flow rate (Figure 3.4). Accessing this gradient would allow for the optimisation of irradiance times in a single experiment between the ranges set by the reaction parameters.

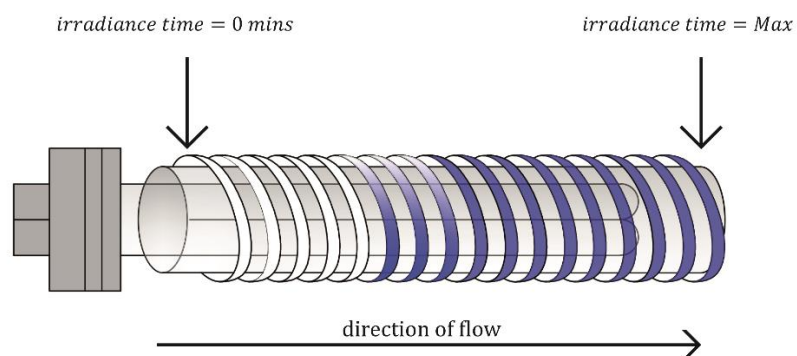


Figure 3.4: Graphical depiction of the flow reactor with the residence time gradient presented by the degree of colour shown. Blue = Product. White = Starting material

As mentioned before, transient flow methods could access this, however they are not easy to implement on every flow setup. A movable probe would allow several time points to be monitored along this gradient however, this may still miss the true optimum and some reactor designs, like the ones used for this thesis, are not suitable for a moving probe design.

A new methodology was designed called the “Switch-off” method, which locks the time gradient present in the reactor by switching off the light source. The gradient can then be pumped out of the reactor and monitored either by in-line or offline analysis extracting the irradiance time data.

### 3.2.2 The equipment

#### 3.2.2.1 Reactors

##### 3.2.2.1.1 Cylinder design

The reactor design used for flow photochemical reactions is described in the literature<sup>165</sup>. The basis of the reactor is a 3.8 x 30 cm hollow cylinder. The choice of cylinder material depends on the light source used. If UV irradiation is needed, then quartz should be used as this minimises the absorption of UV irradiation compared to pyrex (Figure 3.5). However, if visible light is the only source used then pyrex should be used as it is a much cheaper alternative which will give identical results under visible light irradiation.

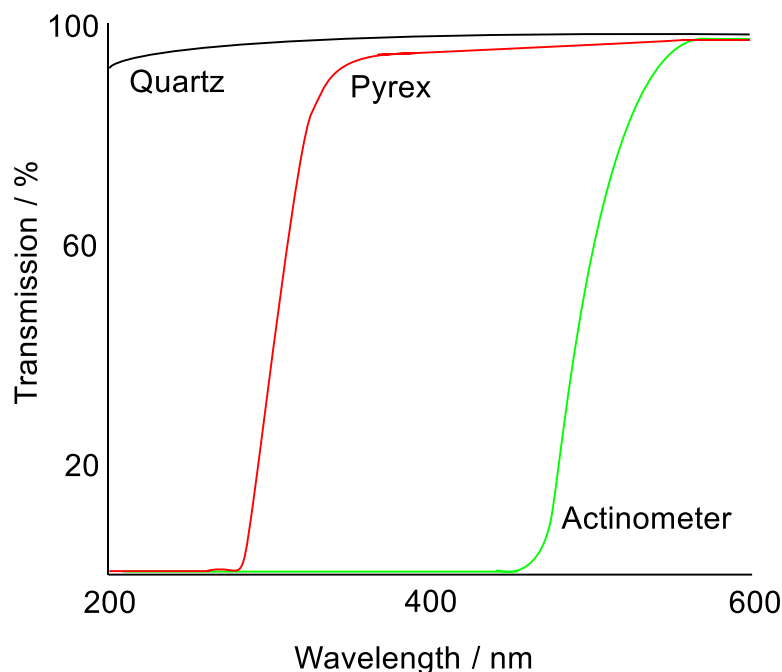


Figure 3.5: % Transmission for three materials across a range of wavelengths. Quartz will be the main material present in this thesis due to its excellent transmission across the UV spectrum.

Around the cylinder is wrapped a coil of tubing. Again, for the material of the tubing, considerations must be made for the type of irradiation likely to be used, although PFA tubing has excellent transmission across a large range of wavelengths<sup>170</sup>, as well as the thickness of the tubing walls. A thicker wall diameter will absorb more of the irradiation lowering the output of the reactor. A second layer can be added to the cylinder to increase the volume and output however this would complicate the analysis of this method, so only single coil reactors were used.

A layer of aluminium foil is then wrapped around the tubing to prevent release of UV radiation. Around this foil layer is coiled condenser tubing to allow for water cooling of the reaction mixture.

The light source is inserted into the hollow cylinder and this design gives the shortest distance between the light source and the reaction mixture (around 1 cm) and minimises the overall size of the reactor.

Two reactors were built to this design a 32 mL, 1.0 mm ID reactor and an 8 mL, 0.5 mm ID reactor (Figure 3.6).

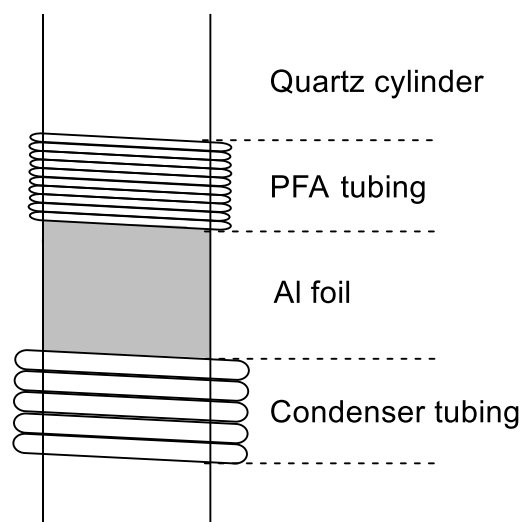


Figure 3.6: Schematic for the flow photoreactors showing the several layer design. PFA tubing is wrapped around the quartz cylinder. A layer of aluminium foil is then wrapped to aid in preventing the release of the UV light. Condenser tubing is then wrapped around to apply cooling to the reactor. Design can be either single or dual layered with respect to the PFA tubing.

#### 3.2.2.1.2 Box design

The design is similar to micro-photoreactors previously reported<sup>171</sup> in which tubing is placed inside of a container and a light source is placed above allowing for even irradiation across the reactor. Reactors can easily be switched out in this design allowing for greater adaptability. Additionally, any reactor design can be utilised such as the minimal dispersion reactor designs described in section 2.2.8, some of which would struggle to be incorporated into the cylinder design.

In this case the container was a cardboard box lined with aluminium foil, inside of which was four 4 mL knitted reactors. On the top side of the box were two cut-outs for the placement of floodlights, and two small holes were cut on the side to allow for flow input and outputs (Figure 3.7).



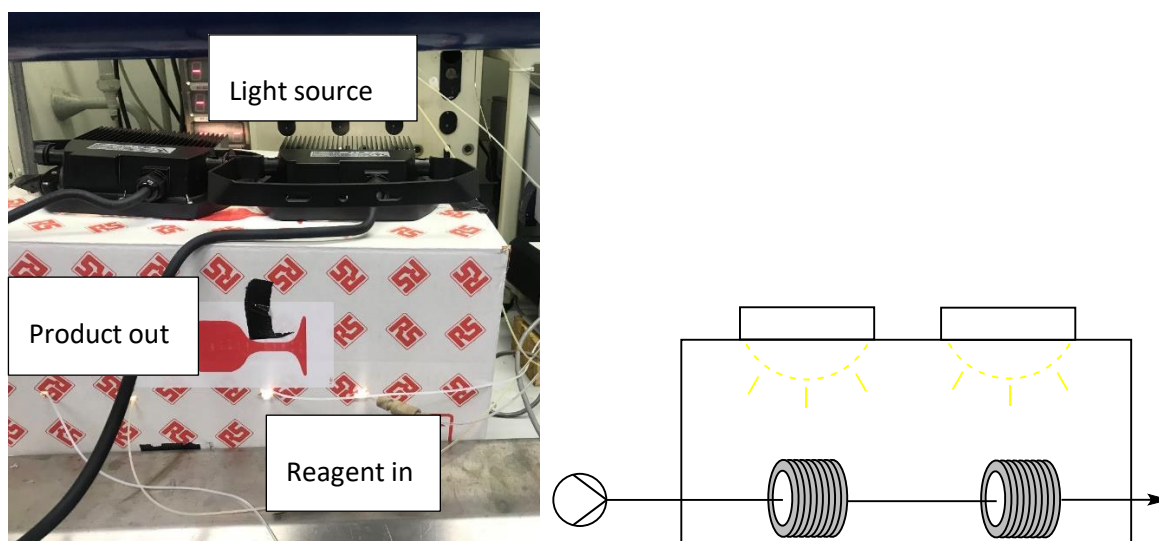


Figure 3.7: Photograph and diagram of box reactor design. On top of the box are cut-outs on which two LED lamps are placed with the outputs directed into the box. The inside of the box contains the reactors and is lined with foil to maximise light absorption. The reactors outputs and inputs are located on the side of the box.

In its current form, this design does not allow for easy cooling of the container. A design could be envisioned with a fan cut into the side providing ventilation however this could cause the release of dangerous UV radiation depending on the light source used. Additionally, this device does not scale as efficiently in terms of space occupied compared to the cylinder reactors.

### 3.2.2.2 Lamps

Due to the decrease in the required distance for light to penetrate, low power bulbs were used in place of the more traditional medium pressure mercury lamps used for photochemistry. Low power bulbs have the benefit of decreasing costs as well as increasing safety by reducing the power and thus heat output of the lamp which is near potentially flammable solvents.

As mentioned before, the choice of light source is important to ensure the reaction mixture absorbs light efficiently. There is a wide range of lamps which can be chosen covering a range of the UV and visible spectrum. Listed here are the light sources and their wavelength profiles where possible.

#### 3.2.2.2.1 UVA lamp

A 9 or 36 W bulb. Covers the wavelengths 345 to 390 nm. An emission spectrum is not provided by the manufacturer however they state a max peak emission at 350 nm.

### 3.2.2.2.2 UVB

A 9 or 36 W bulb from Philips. Covers the wavelengths 310 to 320 nm (Figure 3.8).

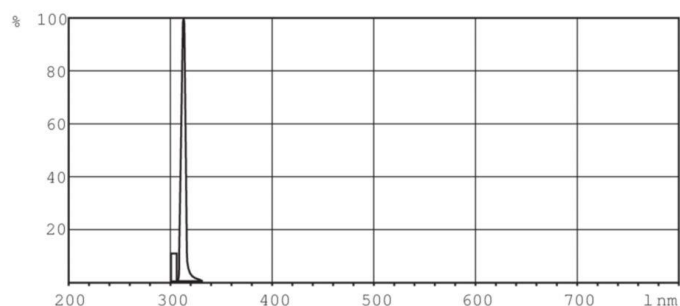


Figure 3.8: Emission spectra for the UVB lamp

### 3.2.2.2.3 UVC

A 36 W bulb from Philips. Emits the wavelength 254 nm as well as small emissions in the UVB, UVA, and visible regions (Figure 3.9)

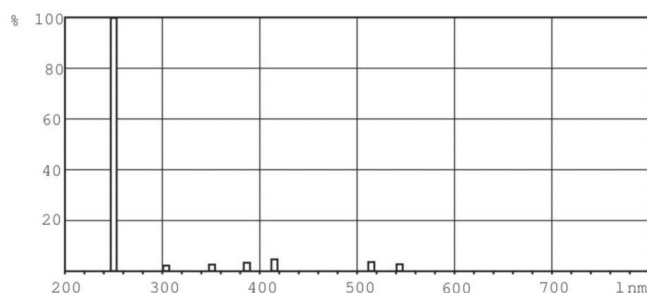


Figure 3.9: Emission spectra for the UVC lamp

### 3.2.2.2.4 Visible

A 9 W bulb from Philips. Covers the wavelengths 400 to 700 nm. No emission spectra were provided by the manufacturer.

Also used were two 20 W LED floodlights<sup>172</sup> for use with the box design.

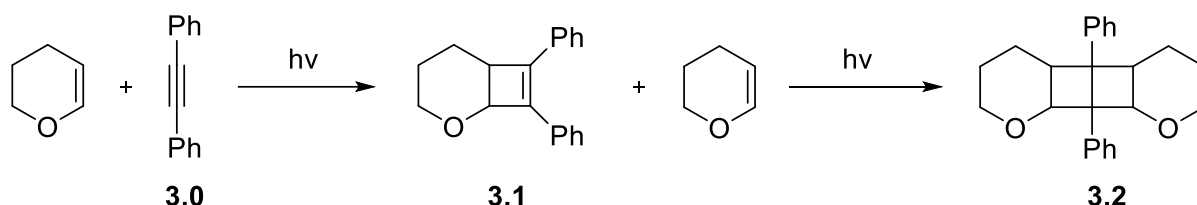
## 3.2.3 Testing the methodology: [2+2] photocycloadditions

### 3.2.3.1 Introduction

Cyclobutane and cyclobutene rings are an important structure in chemistry being used as intermediates in many syntheses<sup>173–175</sup>, being present in natural products<sup>176,177</sup> and biologically active compounds<sup>178,179</sup>. Due to this usefulness, the [2+2] photocycloaddition has been reported

by several groups in flow<sup>180–184</sup> and it was chosen as the model reaction for demonstrating the switch-off method.

The reaction chosen was the photocycloaddition of diphenylacetylene and 3,4-dihydro-2H-pyran (Scheme 3.1) due to the potential for secondary reactions between the initial product **3.1** and the pyran starting material. Therefore, there should be an optimal reaction time for the synthesis of **3.1** before yields begin to drop due to over-reaction.



Scheme 3.1: Photochemical [2+2] cyclisation between diphenylacetylene and 3,4-dihydropyran

### 3.2.3.2 Performing the method

The switch-off method is operationally simple and almost identical to a standard flow reaction:

1. Pre-warm the lamp.  
When a lamp is initially turned on, the intensity of the light output is different from when the light source is at steady state. As such, pre-warming the lamp prior to the reaction ensures uniformity across the reaction mixture.
2. Pump reaction mixture through reactor.  
The photoreactor must be full of reaction mixture at the steady state, as such a plug of 2x the size of the reactor is recommended to overcome dispersion issues. The flow rate chosen during this step depends on the maximum reaction time to be probed. At this point in time, the reactor is filled with an irradiance time gradient from 0 minutes as fresh reaction mixture enters the reactor to the irradiance time determined by the flow rate and reactor volume (Figure 3.10).

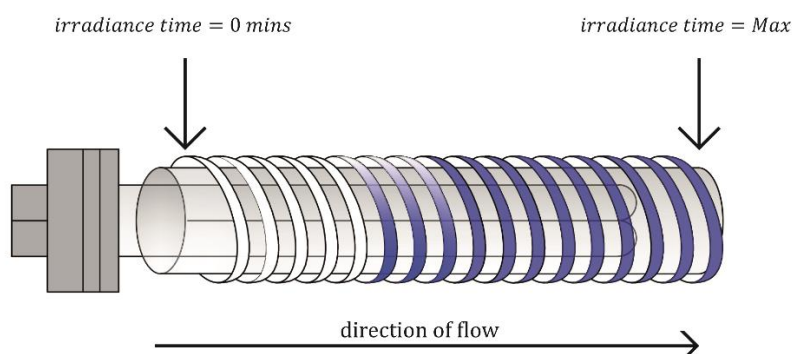


Figure 3.10: Graphical depiction of filled photochemical reactor. All irradiance times between 0 and the set max are present throughout the reactor.

3. Switch-off the light source.

Once the reactor is full the irradiance time gradient is present throughout the reactor. Switching off the light source prevents any further reaction occurring and locks in the irradiance time gradient.

4. Pump out the reaction mixture and monitor output.

### 3.2.3.2.1 UVC

Initially the 36W UVC lamp was used as the light source, with the 8 mL coiled photoreactor. A 0.056 M solution of diphenylacetylene in 3,4-dihydro-2H-pyran was pumped at 0.1 mL/min through the flow setup, giving a maximum irradiance time of 80 minutes, with analysis by GC using samples collected by a liquid handler after the reactor (Figure 3.11).

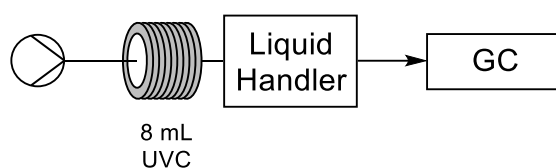


Figure 3.11: Flow setup for the photochemical reaction. Output of the reactor is a liquid handler which dispenses into GC vials which, after dilution, are immediately analysed *via* GC.

The GC results (Figure 3.12) show an increase in **3.1** up to 60 minutes irradiation after which the overall amount begins to decrease. The decrease in rate is due to the second cycloaddition to form **3.2**, overtaking the rate of the first step. Therefore, for the highest output of **3.1**, the optimal irradiance time for this setup would be 60 minutes which generates 0.43 mmol/h at this scale. However, if obtaining the highest yield is the goal, then a lower irradiance time of 10 minutes would be optimal, providing a method could be found for extraction of the product and recycling of the reaction mixture back through the photoreactor.

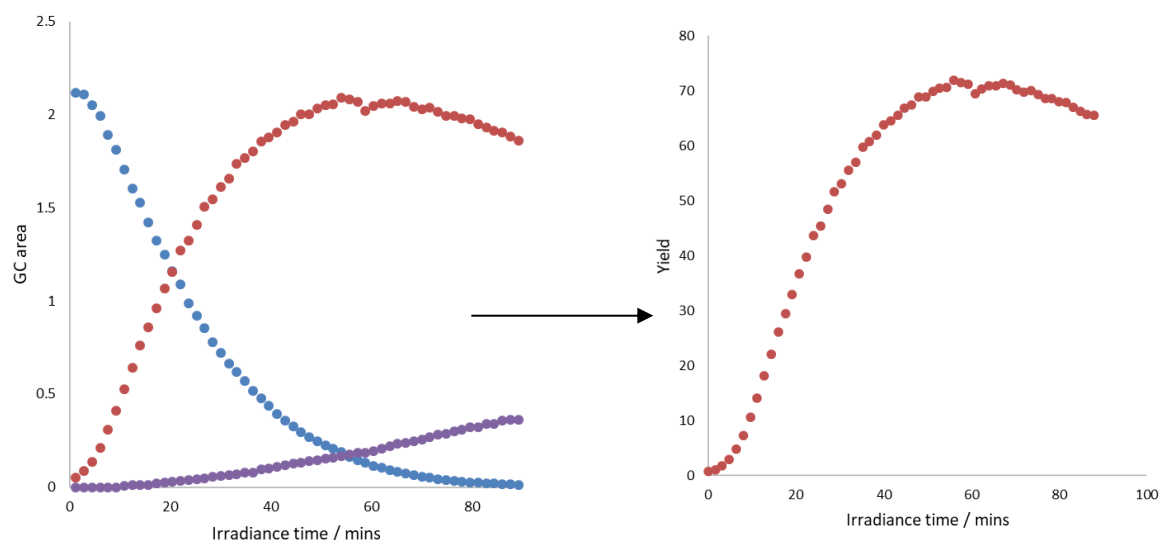


Figure 3.12: GC results from switch-off experiment using UVC irradiation. Red = **3.1** Blue = **3.0** Purple = **3.2**. GC results converted to yield with respect to **3.1**. GC is calibrated with a calibration curve relative to an internal standard.

Steady state reactions were performed using the 60 minute optimal irradiance time and a yield of 65% was obtained after purification showing good agreement with the switch-off method results.

### 3.2.3.2.2 UVB

The light source was changed to a 36 W UVB lamp and the reaction repeated with the same setup as the UVC experiment. The GC results (Figure 3.13) showed a much slower rate of reaction for the first cycloaddition, going only to an 11% yield after the maximum irradiance time, but an increased rate for the second cycloaddition. The reason for this is the low absorption of light by diphenylacetylene at the wavelengths used by the UVB lamp (305 to 315 nm) compared to **3.1** having a broad absorption across these wavelengths with  $\lambda_{\text{max}}$  of 300 nm (Figure 3.14)

## Chapter 3

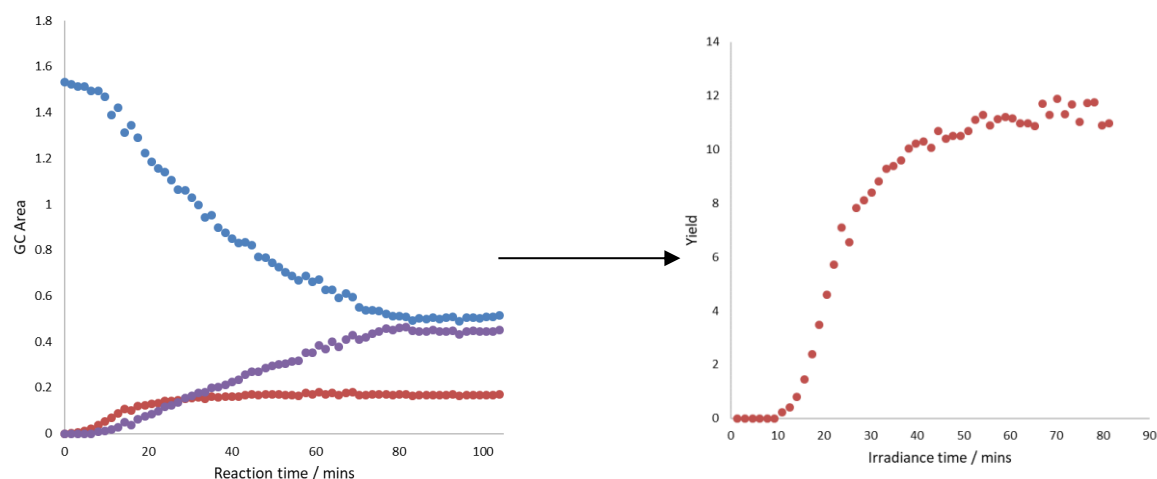


Figure 3.13: GC results from switch off experiment using UVB irradiation. Red = **3.1** Blue = **3.0** Purple = **3.2**. GC results converted to yield with respect to **3.1** GC is calibrated with a calibration curve relative to an internal standard.

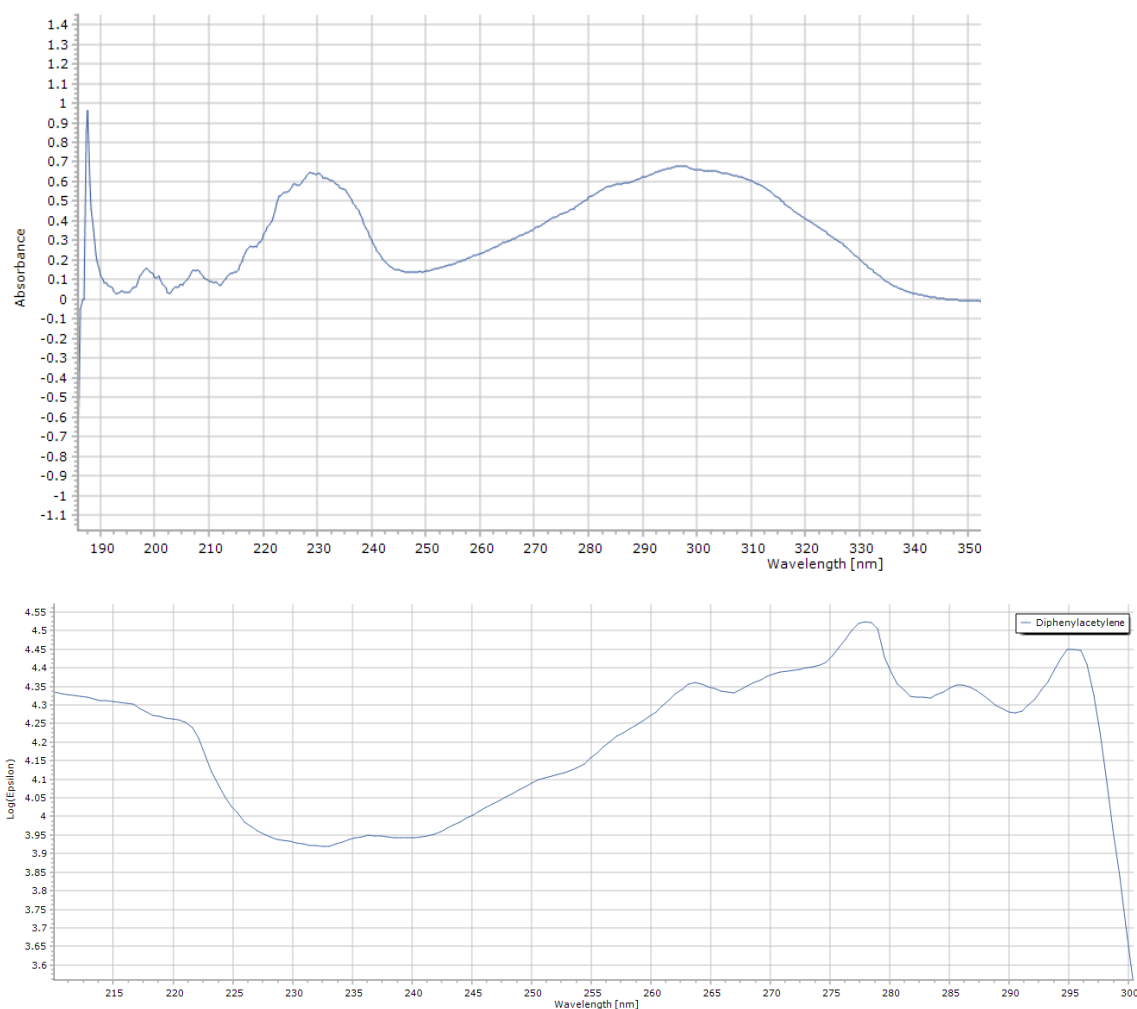


Figure 3.14: Top: UV absorbance spectrum of **3.1**. Bottom: UV spectrum of **3.0**. Absorbance drops off after 295 nm for **3.0** whereas absorbance is increasing for **3.1** at these wavelengths. UV spectra were taken in hexane.

Exchanging the reactor for a 32 mL reactor allowed access to longer reaction times and the reaction was repeated with in-line UV monitoring in addition to the offline GC monitoring. The UV and GC data overlap nicely for the monitoring of **3.1** and the increased reaction time allowed the reaction to go to completion with full conversion of the diphenylacetylene after 310 minutes. Overlaying the results from the 8 mL reactor with this (Figure 3.15) also shows a good agreement between the experiments demonstrating the transferability of the results and the excellent transmission of the PFA tubing as increasing the wall thickness by 0.25 mm did not have a measurable effect on the reaction.

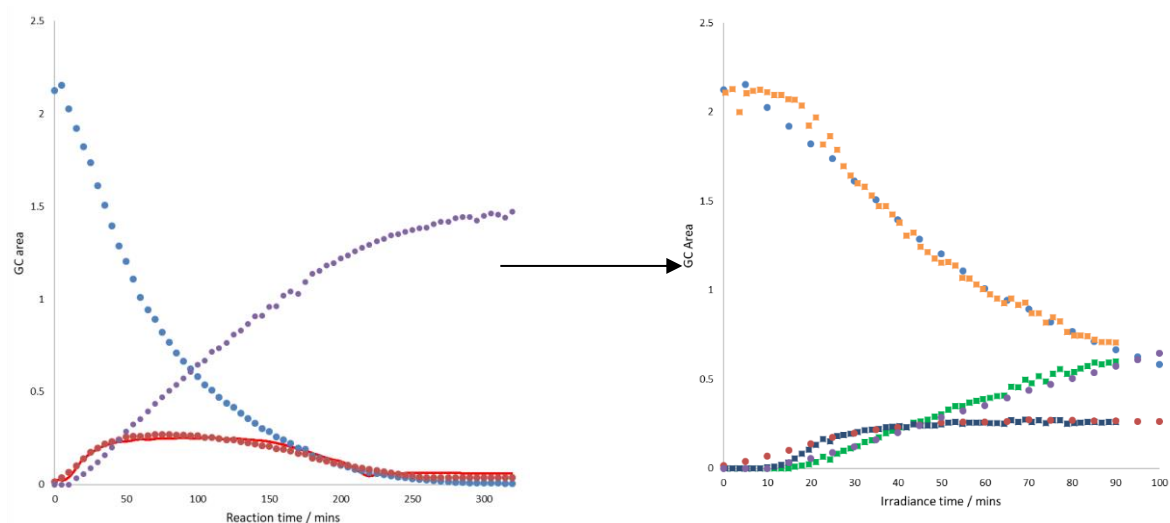


Figure 3.15: GC results relative to internal standard. Solid red = UV results for **3.1** Red = GC results for **3.1** Blue = **3.0** Purple = **3.2**. Right: Overlaid GC results from 8 mL and 32 mL reactions showing good overlap between the varying sizes of reactor.

### 3.2.4 Issues with the methodology

#### 3.2.4.1 Irregularity of the irradiation

When using the cylinder design, one factor that must be accounted for is the irregularity of the emission strength in the different areas of the bulb. Towards either end of the bulb the power output is greatly diminished compared to the centre (Figure 3.16). Also present are two plastic clips used to hold the light bulb, which cause localised areas of poor irradiance visible as two dips in efficiency at either end of the graph.

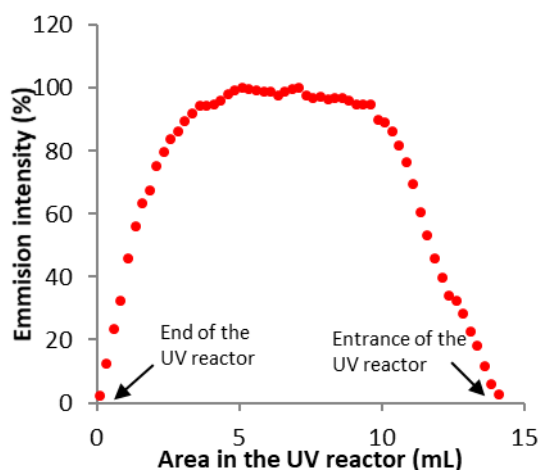


Figure 3.16: Lamp emission intensity dependant on location along reactor. Graph shows inhomogeneity of the output of the lamp.

There are three potential solutions to this problem:

1. Utilise a different reactor design.  
Designs such as the box design suffer from this less due to all the light emitted from the light source hitting every part of the reactor rather than a localised portion of the light source.
2. Only use the maximum efficiency area.  
Calculation of where the lamp has the highest efficiency allows a reactor to be built around only that portion of lamp. With this setup, the reaction mixture experiences the same light output and no variance in irradiation will be observed.
3. Correcting the irradiance time for the inefficient bulb area.  
Using the measured efficiency of the bulb it is possible to correct the observed reaction time obtained using the switch-off method to account for the variance in output using Equation 3.4.

$$\text{Corrected } rt_n = \text{Corrected } rt_{n+1} + (rt_n - rt_{n+1}) \cdot \frac{E_n}{100}$$

$rt_n$  = Reaction time at point  $n$

$E_n$  = Lamp efficiency at point  $n$

Equation 3.4: Calculation of reaction time considering areas of lower lamp output.

The first two solutions are preferable as these allow easier results transfer between systems of varying volume or lamp efficiency. Also, the third solution either assumes that the efficiency profile will stay constant as the lamp degrades over time or requires repeat experiments to monitor the efficiency of the bulb over time.



### 3.2.4.2 Maximum irradiance time and volume of reaction mixture used

The minimum flow rate achievable by most commercial mesoscale flow systems is around 0.1 mL/min. Therefore, for long reaction times (> 2 hours) you need a correspondingly large reactor (> 12 mL). As this method requires the reactor to be filled with the steady state of reaction mixture this means that twice the reactor volume will be needed to perform this methodology which could become prohibitively expensive for the longest reaction times.

Overcoming this can be achieved by utilising a smaller reactor, and after filling the reactor with steady state, stopping the flow but keeping the light source on. The reaction mixture can then be kept in the reactor for  $t_x$  mins until the wanted maximum irradiance time is reached after which, switching off the lamp will lock in a time gradient of  $t_x \rightarrow t_x + \frac{V}{u}$  which can then be pumped out and monitored as per the traditional switch-off method.

## 3.3 Summary

A simple methodology for the extraction of irradiance time data was created which utilises the continuous pumping nature of flow chemistry to access all irradiance times between 0 and the maximum irradiance time of the reactor.

In comparison to traditional methods, where several experiments are performed, both time and waste are saved when using the switch-off methodology, as only a single experiment is performed.

Additionally, when performing several steady state reactions, the true optimal irradiance time can be missed due to a smaller coverage of the reaction space. When utilising the switch-off methodology, the entire irradiance time range is covered meaning the true optimal reaction time will be found for the particular flow system.

Using the switch-off methodology, optimal irradiance times were extracted for synthesis of **3.1** and **3.2** from the photocycloaddition of diphenylacetylene and 3,4-dihydro-2H-pyran. Good consistency was seen between the switch-off results and when performing steady state experiments for the synthesis of **3.1**. Some disadvantages to the method such as inhomogeneity of the lamp output have been discussed and ways to minimise and overcome them have been presented.

## Chapter 4 The concentration gradient method

### 4.1 Introduction

We have described how the ‘push out’ and ‘switch-off’ methods restore to flow chemistry the ‘batch’ advantage of easy sampling through the reaction time (Table 4.1). In both batch and flow investigating the effect of different starting concentrations of components requires a separate reaction for each concentration. We now show how flow chemistry can be used to investigate a wide range of concentrations in a single reaction by using a concentration gradient giving it a unique advantage over batch methods (Figure 4.1).

Data obtained	Flow methodology	Batch methodology
Reaction time	Push-out, flow rate ramps	Sampling
Irradiance time	Switch-off	Sampling
Kinetics	Flow and temperature ramps, push-out	Sampling

Table 4.1: List of various obtained data and the corresponding batch and flow techniques required to obtain the data.

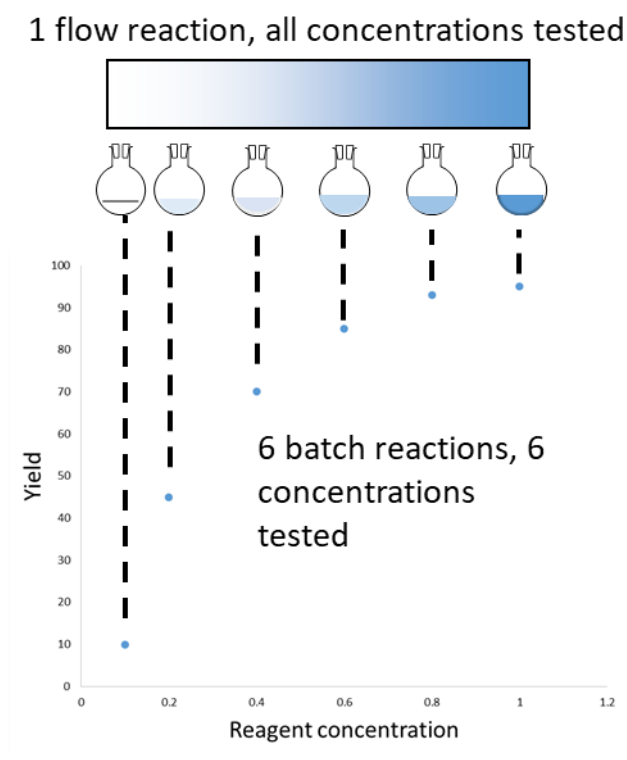


Figure 4.1: Graphical representation of how a concentration gradient could be used to obtain concentration data in a single reaction compared to several batch experiments

## 4.2 Concentration gradient method

### 4.2.1 The concept

In a typical flow reaction, two reagent streams are combined and then pumped through a reactor to the output. Monitoring this output will show identical results throughout the reaction across the steady state of the reagents (Figure 4.2).

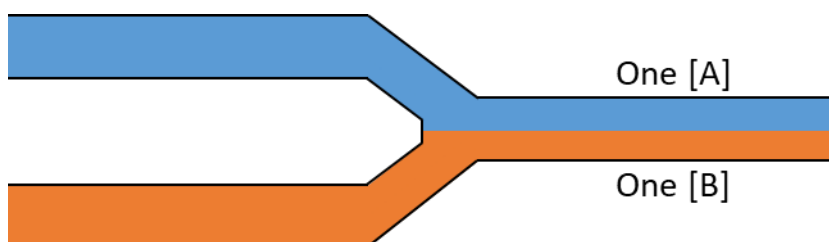


Figure 4.2: Graphical representation of a standard flow reaction where two steady state reagents react with each other.

If it were possible to replace one of the steady state reagent streams with a concentration gradient then, after mixing the streams, throughout the reactor there would be present reaction mixtures consisting of all the reagent concentrations reacting with the standard conditions (Figure 4.3). Comparatively, this is equivalent to having a virtually infinite number of small batch vessels each containing a different starting concentration of reagent, however this is being achieved with a single experiment.

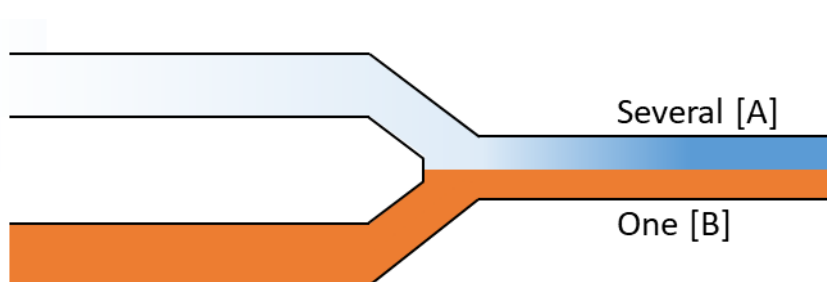


Figure 4.3: Graphical representation of a concentration gradient reaction where a gradient is reacted with a steady state reagent. Increasing intensity of blue indicates increasing concentration of reagent.

The generation of a gradient and subsequent combination with a steady state stream is the basis for the flow methodology.

### 4.2.2 Methods for generating a gradient

To utilise this concept, a concentration gradient must be formed within the flow setup, additionally this gradient generation needs to be able to selectively convert one reagent stream into a concentration gradient. Two main methods will be investigated within this thesis.

#### 4.2.2.1 Flow rate change

One method for generating a concentration gradient is to continuously vary the flow rate of a pump throughout the course of a reaction and the concentration in the reactor tubing at a set flow rate can be calculated (Equation 4.1).

$$[A]_{tube} = \frac{v_A \cdot [A]_{start}}{v_{total}}$$

$$[A]_{start} = \text{Concentration of A in reservoir}$$

$$v_A = \text{Flow rate of A}$$

$$v_{total} = \text{System total flow rate}$$

Equation 4.1: Calculation of reagent concentration after dilution by mixing with a second pump

If the setup consists of two pumps, A and B, with A being solvent and B containing a starting material, then applying a flow rate ramp from 100% A and 0% B to 0% A and 100% B will create a linear concentration gradient which will be pumped through the flow setup (Figure 4.4). A flow rate ramp procedure is identical to that used in HPLC analysis to create a gradient separation method.

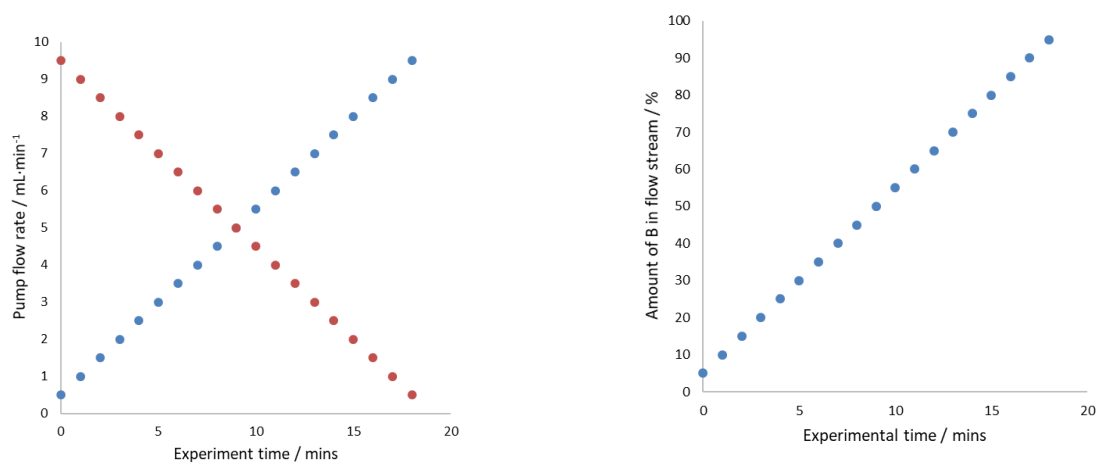


Figure 4.4: Left = Flow rates of two pumps supplying reagents A and B. Right = Amount of B after mixing at the different flow rate ratios. Demonstrates the ability of a flow rate ramp to create a concentration gradient.

Unfortunately, as with the transient flow methods, some flow equipment does not natively support flow rate changes whilst a reaction is being performed. Therefore, either manual control or programming of the flow equipment is required for this method to be functional.

#### 4.2.2.2 Dispersion

Taylor dispersion, the spreading out a plug as it travels through a tube, is a near unavoidable aspect of mesoscale flow chemistry. Typically, its effects are negative requiring the use of large plugs or slow rates to maximise the steady state with the rest of the plug disregarded. However, this discarded rest of the plug consists of a mixture of solvent and reagent in varying ratios, or a concentration gradient. That means that when a plug undergoes Taylor dispersion, a steady state plug surrounded by two concentration gradients is obtained (Figure 4.5).

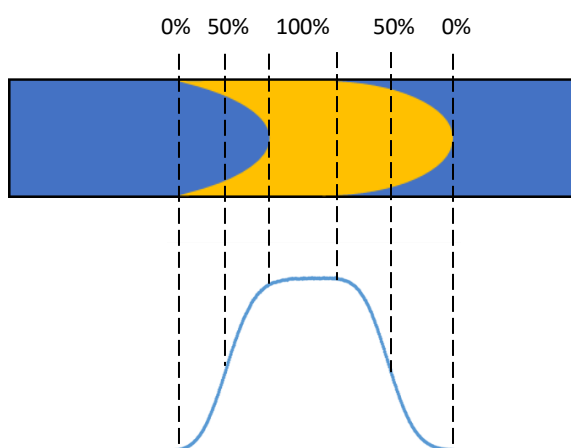


Figure 4.5: Graphical depiction of a plug after pumping through a length of tubing. Taylor dispersion has caused a spreading of the plug creating a concentration gradient along the tube.

To utilise this a reagent must be separated from the rest of the reaction mixture into a dedicated flow stream. The reagent plug must then be dispersed to convert it into a concentration gradient where it can then be combined with the steady state of the reaction mixture and sent through the flow setup. An advantage of using dispersion is that it only requires one pump rather than two additionally, the pump is only required to hold a consistent flow rate rather than changing rapidly.

Therefore, this method is applicable to all mesoscale flow systems provided that they operate within the laminar flow regime as such the dispersion method will be used for the methodology.

### 4.2.3 Gradient formation by dispersion

#### 4.2.3.1 Creation of the gradient

To force the dispersion of one reagent a dispersion coil, a length of standard tubing, is placed between the pump and the mixer (Figure 4.6). As the plug pumps through the dispersion coil it spreads out into the dual concentration gradient seen above with the slope of the gradient controlled by how much dispersion occurs.

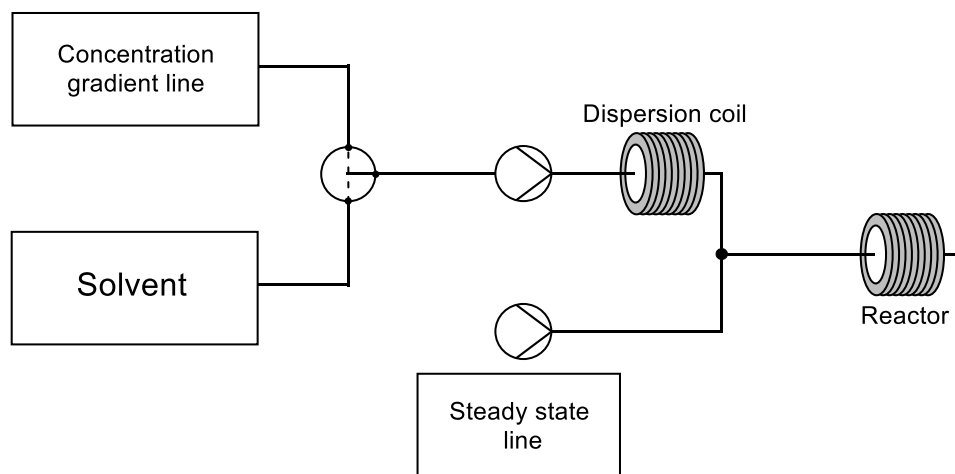


Figure 4.6: Flow setup for the generation of a concentration gradient and combination with a steady state reagent. A plug of reagent is generated by switching the T-valve from reagent to solvent mixture. The plug is then converted into a gradient by travelling through the dispersion coil.

The steepness of gradient required is determined by the analysis method used. If the time between measurements is short (in-line UV or IR), then a steep gradient will allow a shorter overall experiment time with little lost information than if a shallow gradient was used.

If there is a long wait time between measurements and a steep gradient is used, then insufficient data points could be extracted, and more than one experiment required to optimise for concentration (Figure 4.7).

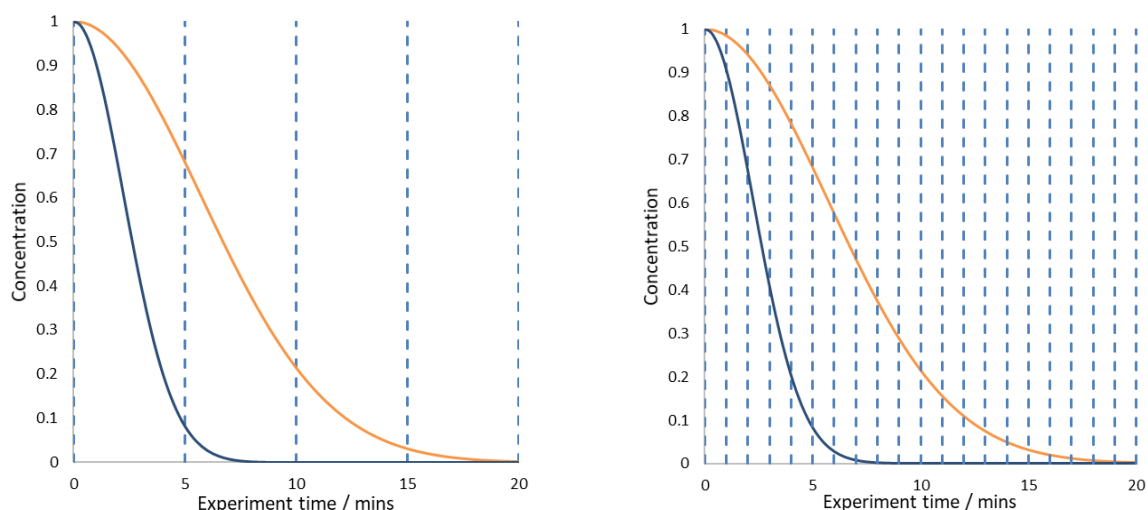


Figure 4.7: Solid lines = concentration gradient. Dashed lines = spectra obtained. Insufficient data points have been obtained on the steep gradient with slow data acquisition. Whereas enough data points are gathered on both gradients with the faster acquisition time.

The steepness can be controlled as described in section 2.2 by varying the dimensions of the dispersion coil (volume, ID, coil size, internal or external structures) or the flow rate of the system. In this chapter, a 10 mL 1.0 mm ID dispersion coil is used as it generates a 7.5 mL gradient at 0.1 mL/min which will allow for sufficient GC samples to be taken for analysis.

To minimise the experimental time and steady state reagent use, only the leading concentration gradient will be used for this chapter however, the use of both gradients will be described later.

#### 4.2.3.2 Calculating concentration from the dispersion profile

Measurement of the dispersion profile of the dispersion coil, under the same conditions to be used in an experiment, allows calculation of the concentration at a given point in the dispersion profile. Provided that the steady state is reached in the dispersion profile, the reagent concentration can be calculated from the absorbance data (Equation 4.2).

$$C_x = \frac{C_m \cdot A_x}{A_m}$$

$$C_x = \text{Concentration at time } x$$

$$C_m = \text{Maximum concentration}$$

$$A_x = \text{Absorbance at time } x$$

$$A_m = \text{Maximum absorbance}$$

Equation 4.2: Calculation of concentration from the dispersion profile

Applying this dispersion profile to in-line or offline analysis from a concentration gradient experiment requires a method for overlaying the data in the correct time point and the

positioning of the dispersion profile is important as small deviations in the placement can cause large variations in results.

There are two main methods for placement of dispersion profiles:

1. Steady state reactions.  
Performing the reaction with a single concentration of reagent can provide known results at a known concentration which can then be used to calibrate the estimated concentration results obtained from the dispersion profile.
2. Dispersion of a readily monitored test compound utilising the same flow conditions as the reaction.  
Performing a dispersion profile of the entire flow setup, using the same reaction conditions that would be used in the experiment (flow rate, mixing other lines, temperature, reactors) allows the exact time of the output of the concentration gradient to be known. Use of automated reaction conditions on both the dispersion profile and experiment ensure the placement is correct.

Performing steady state reactions allows calibration of the dispersion profile using any flow setup if reaction time and temperature are the same between setups and effects due to mass transfer are either identical between reactors or not rate limiting. The multi-reactor compatibility is due to the calibration being based on the chemical outcome of the reaction rather than the time taken to pump through the system.

However, having to perform several steady state reactions removes some of the efficiency of the methodology.

Determining the dispersion profile of the entire system does maintain the efficiency of the methodology by only having to perform one additional experiment. However, the profile must be re-performed if the reactor or flow rate is changed, for instance swapping to an equal volume but smaller ID reactor to minimise post-gradient dispersion.

Once the dispersion profile has been overlaid you can calculate the concentration present at a given reaction either by using the previous equation or by generating a trendline equation for the dispersion profile. For example, two polynomial equations can be used to describe this dispersion profile (Figure 4.8), which can then be used to calculate the concentration in a GC vial sample.



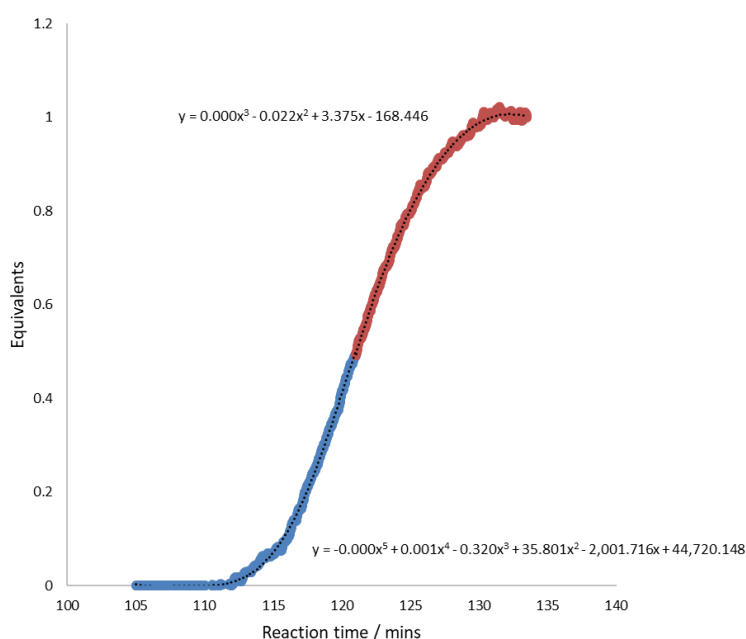


Figure 4.8: Trendline equations generated from a dispersion profile used for converting reaction time to reagent concentration.

#### 4.2.3.3 Reactor choice

After the concentration gradient has been created and combined with the other reagent streams, dispersion will continue to occur on the plug causing an averaging effect on each point on the curve which increases as dispersion increases. The averaging is a problem for the areas of the gradient which are close to the steady state and zero concentrations as these points will begin to average in these maxima and minima at an increased amount which will decrease the accuracy of the data point

For the data between the extremes, this is less of a problem as the average value will not contain a disproportionate number of maxima or minima and should stay close to the expected value. (Figure 4.9).

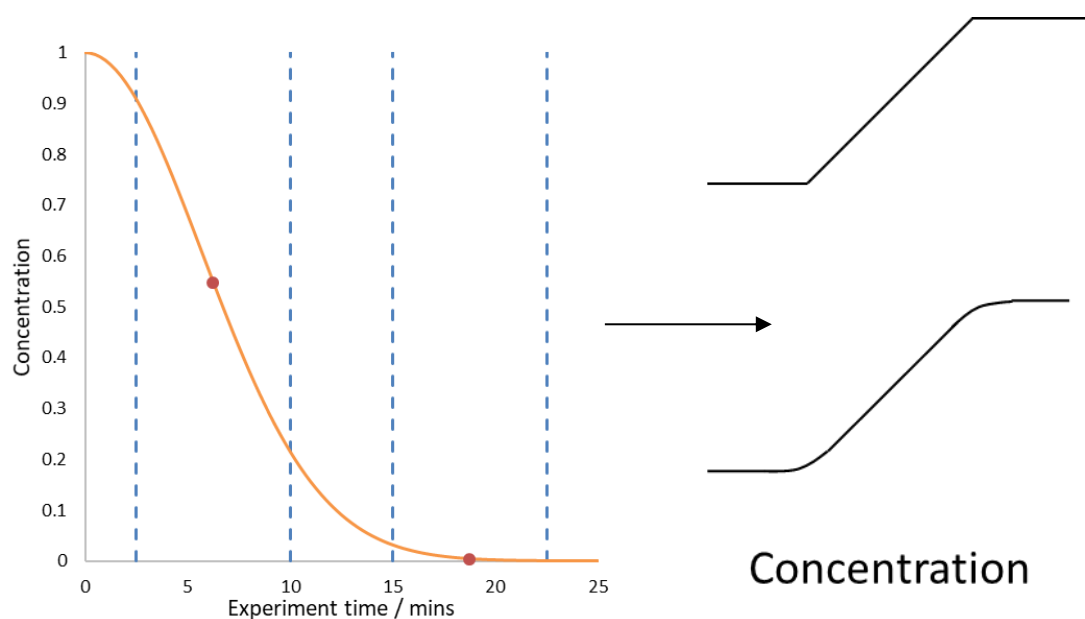


Figure 4.9: Effects of dispersion occurring post reagent mixing. Blue dashed lines show the area of averaging and the effect on concentration is shown on the right, with the top drawing being the ideal result and the bottom the result with post mixing dispersion.

To ensure the highest accuracy data possible, the minimal amount of post-mixer dispersion should be sought.

#### 4.2.4 Flow setup

After determining the location and steepness of the concentration gradient, the performing of the methodology is as simple as running a traditional flow reaction. The dispersed reagent line is connected to the reaction mixture line through a mixer, this ensures the layers of the concentration gradient are mixed as well as mixing between the reagent lines. The gradient-reaction mixture is then pumped through the reactor and into the in-line/offline analysis to extract the yield at each concentration of reagent (Figure 4.10)

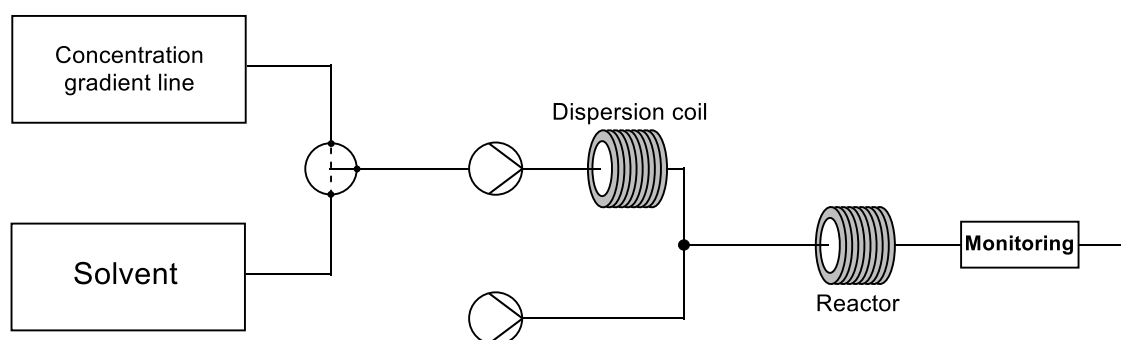


Figure 4.10: Flow setup for concentration gradient experiments. A gradient is generated and then combined with steady states of other reagents.

## 4.3 Testing the methodology: The Heck cross-coupling reaction

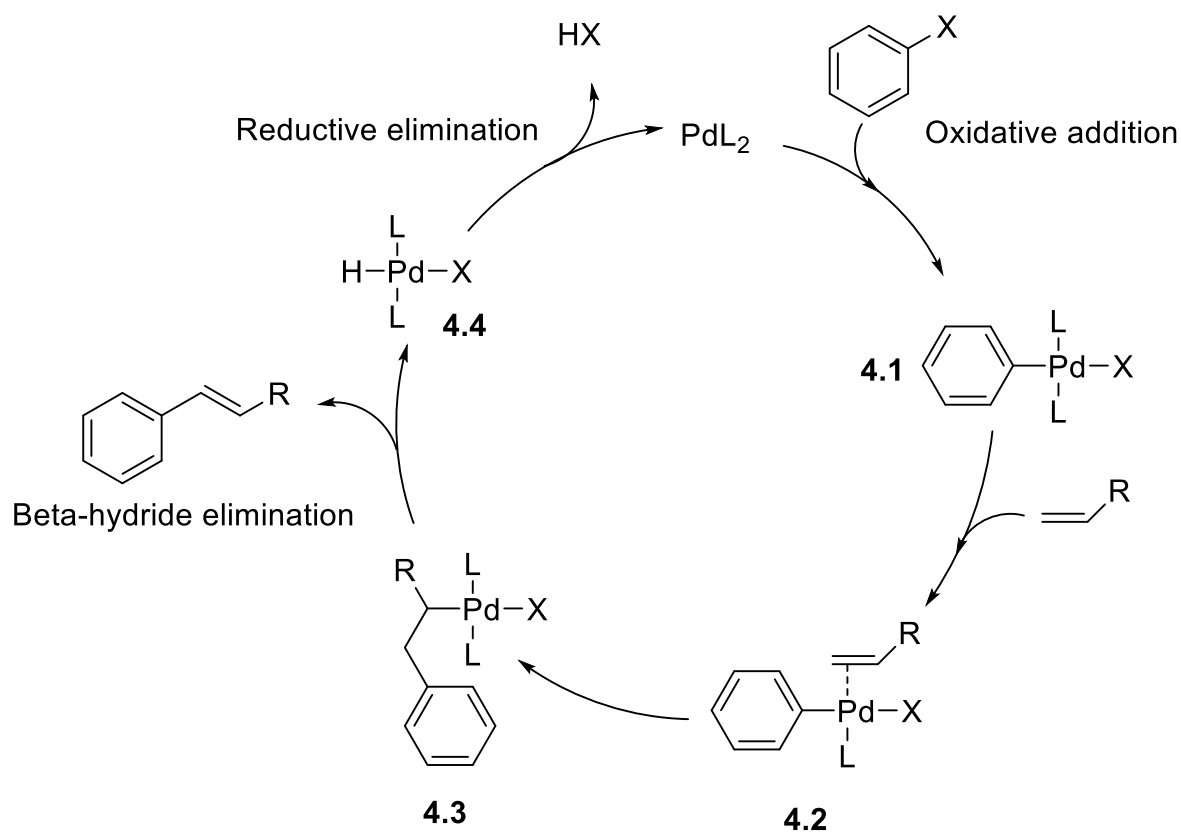
### 4.3.1 Introduction

The palladium catalysed Heck reaction<sup>185–189</sup>, the C-C coupling of alkenes with aryl or vinyl halides, is an important tool for organic synthesis used widely in both academia<sup>190–194</sup> and industry<sup>195,196</sup>. It is capable of being performed over a range of different reaction conditions with numerous different ligands, metal sources, bases, additives and ratios of these components.

#### 4.3.1.1 Mechanism

The traditional mechanism for the Heck reaction (Scheme 4.1) begins with a 14-electron species,  $\text{PdL}_2$ , formed from a Pd precursor. The  $\text{PdL}_2$  species undergoes oxidative addition with the halide to form species **4.1** after an isomerisation from the cis isomer which is less thermodynamically stable by ligand or solvent assistance<sup>197</sup>.

A vacant site is then created by loss of a ligand and the alkene coordinates to this site. The alkene then undergoes syn-addition of the C-Pd bond. The complex will then rotate about the C-C bond to ensure the  $\beta$ -hydrogen of the complex and the Pd are syn-coplanar allowing  $\beta$ -hydride elimination to occur, which releases the product, a trans substituted alkene, from the catalytic cycle. A base can then reduce the formed Pd complex back to  $\text{PdL}_2$  to restart the catalytic cycle.



Scheme 4.1: General mechanism for Heck cross coupling reaction

#### 4.3.1.2 Heck in flow: The issues

One of the main issues when attempting to perform a cross-coupling reaction in flow is the formation of insoluble palladium particles, Pd black. Formation of these solid particulates can cause blockages or restrictions in the reactor causing inconsistent flow rates and reaction times, or a complete blockage resulting in an increase in pressure causing an automated pump shutdown for safety. Particulates can also cause damage to flow equipment such as valves, back pressure regulators and in-line monitoring equipment requiring at best extensive cleaning or at worst purchasing of new expensive equipment.

There are three main ways to overcome this issue presented in the literature, which can be grouped into two categories based on the nature of the Pd source: heterogeneous and homogeneous.

##### 4.3.1.2.1 Heterogeneous Pd source

###### 4.3.1.2.1.1 Advantages

The use of a solid source of Pd contained within a packed bed prevents the release of Pd particulates into the rest of the flow setup and provides an area of high local concentration of

catalyst compared to reagents. The increase in mass transfer given by flow chemistry can also increase rates *in situations* where mass transfer has a limiting effect<sup>198</sup>.

Depending on the reaction conditions, there are several different types of support that have been reported such as, anion exchange resin<sup>199</sup>, Pd/C<sup>200</sup>, supported ionic liquid phase<sup>201</sup>, Pd/Si<sup>202</sup>.

Overall, they tend to be more cost effective than the homogeneous alternatives especially when including the cost of ligands.

#### 4.3.1.2.1.2 Disadvantages

Whilst some mechanisms for heterogeneous Pd catalysis use the surface of the immobilised Pd as the active site of catalysis<sup>203,204</sup>, there have been several papers<sup>205–214</sup> reporting that the active species is actually Pd leached from the support occurring mainly from organic halides reacting with the Pd however leaching from pure solvent has been seen<sup>215</sup>.

For batch chemistry this problem is less severe as once the reaction is complete, the leached Pd can redeposit onto the surface. However, for flow the leached Pd will flow out of the packed bed and deposit elsewhere in the flow setup or into the product through the outlet (Figure 4.11).

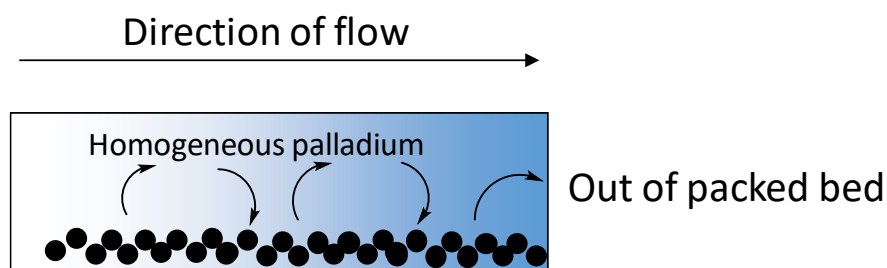


Figure 4.11: Graphical depiction of Pd leaching out of a packed bed system. Whilst some Pd will redeposit on the packed bed, some will leach into the output lowering the loading of Pd.

Leached Pd could lead to blockages or damage to the setup but will also lower the activity of the catalyst bed eventually removing all activity and requiring replacement.

The high local concentration of catalyst can also lead to a lowering in selectivity as reported by Kappe *et al*<sup>216</sup> where use of packed bed reactors gave a higher ratio of dehalogenated and homocoupled products compared to the equivalent batch reaction. However, they also note in this paper a chromatographic effect present when using Pd/C in that when passing the reaction mixture through, samples taken of the first reaction mixture through the reactor contained only NEt<sub>3</sub> and butyl acrylate indicating the aryl halide was more strongly retained to the solid support.

#### 4.3.1.2.2 Homogeneous Pd source

##### 4.3.1.2.2.1 Pd-ligand complexes

The use of ligands as either additives or preformed complexes can help stabilise the Pd(0) complex and prevent coagulation of the Pd into Pd black. Countless ligands have been created for the Heck reaction depending on the rate, stability and starting material the chemist wants to use. Phosphines<sup>217–221</sup>, palladacycles<sup>222–228</sup> and NHC<sup>229–231</sup> ligands are the main groups of compounds utilised for the Heck reaction the use of some of these catalyst-ligand combinations has been described in flow.

In the previously mentioned optimisation paper by Jensen *et al*<sup>80</sup>, *tert*-butyl-MePhos was utilised in combination with Pd(OAc)<sub>2</sub> to generate full conversion at 90 °C with no Pd black formation. However, increasing above this temperature caused precipitation to occur.

Ley *et al*<sup>232</sup> reported a two-step Heck reaction in flow with first coupling an aryl iodide to ethylene gas and then a further coupling to a second iodide. The XantPhos ligand was initially applied to minimise the formation of Pd black, which they discovered worked well in a previous paper<sup>233</sup>. However, optimisation studies showed JohnPhos to be the optimal ligand for conversion. When using JohnPhos, a small amount of precipitation was seen however a cartridge of cotton wool was added in-line after the reactor to act as a filter. They then focused on scaling up the procedure which required zero Pd black formation, for this the base was changed from NEt<sub>3</sub> to Cy<sub>2</sub>NMe and the ligand used was t-Bu<sub>3</sub>P·HBF<sub>4</sub><sup>234</sup> generating an increase in scale from 0.3 to 120 mmol.

The Wirth group reported a Heck reaction using segmented flow methods<sup>235</sup> which encountered Pd black forming with traditional loadings (5 – 10 mol%) of Pd(OAc)<sub>2</sub> and PdCl<sub>2</sub>. Lowering the loading to 1 mol% decreased the amount of precipitate but also dramatically lowered the rate of the reaction. Using 10 mol% Pd(PPh<sub>3</sub>)<sub>4</sub> removed all precipitate and also gave the highest yields of 76%.

Whilst the use of ligands does prevent the formation of Pd black, it does require an extra step at workup to remove the Pd and the ligands which can be difficult. Several papers have reported a method for recirculation of catalyst<sup>236–238</sup> back into the flow stream to minimise the workup and maximise the efficiency of the catalyst. However, these methods rely on biphasic separation methods and as such only work in specific conditions, for example highly hydrophilic product and hydrophobic Pd source.

#### 4.3.1.2.2.2 Low loadings of ligandless Pd

The other route for homogeneous catalysis is the use of very low loadings of Pd<sup>239</sup> to minimise the likelihood of precipitation of Pd black. The most common methods utilise Jeffery's conditions<sup>240</sup> which incorporate tetraalkylammonium salts which help stabilise the Pd(0).

Kappe *et al*<sup>216</sup> reported a 0.01 mol% Pd(OAc)<sub>2</sub> Heck reaction for aryl iodides which went to full conversion after 10 minutes at 170 °C. Decreasing the loading to 0.001 mol% Pd or when using bromides as the starting material required the use of Jeffrey conditions with 10 mol% TBAB added, which increased the rates of reaction in both cases.

Price *et al* also report the use of quaternary ammonium salts in combination with low loadings of Pd<sup>241</sup>. They found that at very low loadings of Pd (0.001 to 0.05 mol%) the product yield increases with the increase in Pd concentration but above that the amount of side products seen begins to increase. Using 0.05 mol% Pd(OAc)<sub>2</sub> and 150 – 200 °C, they were able to bring the reaction time down to below 20 minutes with no mention of any Pd particulates being formed.

#### 4.3.2 Initial reaction condition probing

Heterogeneous Pd sources were ruled out due to the leaching effect changing the loading of the catalyst over time leaving Pd-ligand complexes and low loadings of Pd. Reaction conditions were tested in batch to test the suitability for use in flow (short reaction time, no precipitation). The reaction studied was that of iodobenzene and butyl acrylate, initially bromobenzene was to be used however all conditions tested resulted in formation of palladium black or no reaction.

Several different conditions were tested in batch (Table 4.2). All ligands tested resulted in either Pd black formation or no reactivity after 24 hours at 150 °C. DTBPF only produced Pd black after all iodobenzene had been reacted, this is due to the Pd source being unable to undergo the oxidative addition step, and thus being stuck as a Pd(0) species which can precipitate out as Pd black. To prevent this, an excess of halide was used.

Ligand	Solvent	Pd black	Reactivity
DPPM	Toluene:DMF	×	×
Bipy	Toluene:DMF, DMF	✓	✓
TTBP.HBF <sub>4</sub>	Toluene:Methanol	✓	×
C22 <sup>242</sup>	DMF	✓	✓
DTBPF	DMF	✓	✓
Ligandless	DMF	×	✓

Table 4.2: Batch Heck reaction conditions tested for reactivity and Pd black formation

Use of similar conditions to those reported by Price, with 0.45 mol% Pd(OAc)<sub>2</sub>, resulted in full conversion after 270 minutes with no visible Pd black formation making it suitable for use in continuous flow conditions. These conditions are favourable as they allow for testing of the metal:ligand ratio as well as the concentration of metal which would not be simple using a preformed Pd-ligand complex.

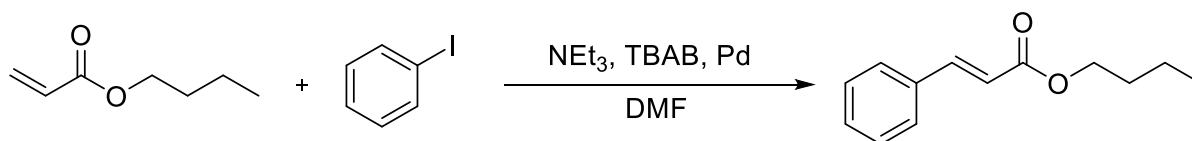
### 4.3.3 Concentration gradient of metal sources

As seen above, the Heck reaction is able to be performed at incredibly low loadings of Pd which is beneficial for two reasons:

1. Lower loadings of Pd will minimise the cost of the reaction especially at large scale.
2. Lower loadings will be easier to remove for industry<sup>243–247</sup> where there are strict rules for the Pd contamination allowed in products, especially pharmaceuticals.

The concentration gradient methodology will allow the optimal loading of Pd to be found for a set reaction time and temperature in a single reaction which will save time and resources.

The Heck reaction chosen was that of n-butyl acrylate and iodobenzene with 1 equivalent of TBAB and 1.7 equivalents of NEt<sub>3</sub> (Scheme 4.2).



Scheme 4.2: Heck reaction of n-butyl acrylate and iodobenzene to form butyl cinnamate



### 4.3.3.1 Setup

The flow setup was divided into three streams, the Pd line, a  $\text{NEt}_3$  line and the remaining reagent line. A dispersion coil was placed in-line into the Pd stream to create the concentration gradient which was then combined with the reagent line before going into the reactor. In-line IR was placed directly after the reactor for in-line measurements and sample vials for GC analysis were collected after this (Figure 4.12).

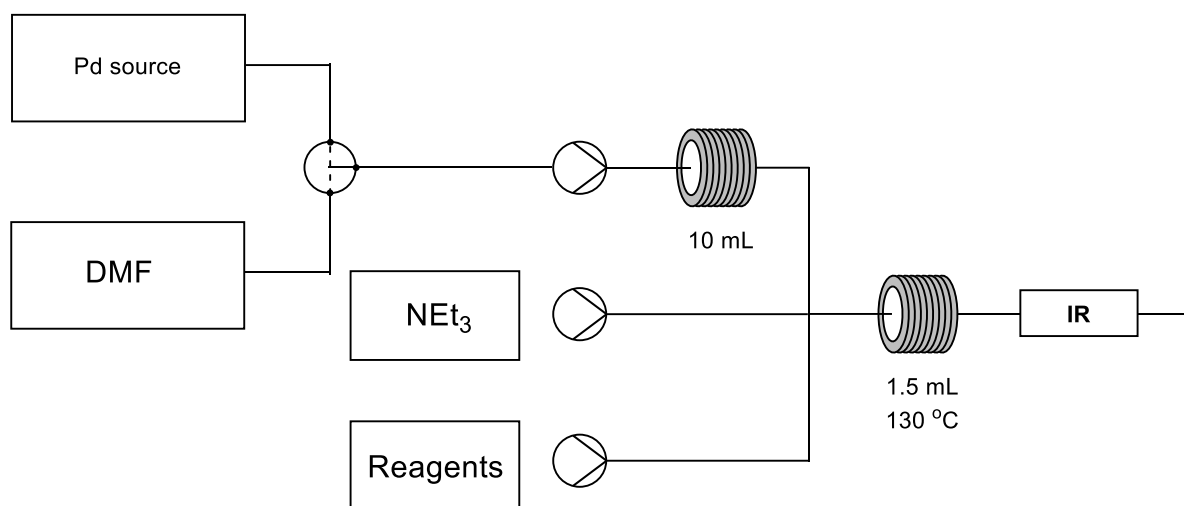


Figure 4.12: Flow setup for generation of a Pd concentration gradient before mixing with the remaining Heck reagents, pumping through a heated reactor and in-line IR monitoring

The reaction conditions chosen were 130 °C and 5 minute reaction time. These were found *via* small scale steady state reactions to ensure the concentration gradient was probing a suitable area however this is not mandatory for the methodology to work.

### 4.3.3.2 Results

Concentration gradients were performed for 4 different metal sources,  $\text{Pd}(\text{OAc})_2$ ,  $\text{PdCl}_2(\text{PPh}_3)_2$ , allylchloropalladium dimer and  $\text{Pd}(\text{dppf})\text{Cl}_2$ . Overlaying of the dispersion profile with the experimental results was achieved *via* the dispersion profile of the whole flow setup method.

Four experiments were performed changing the Pd source between each experiment with a maximum of 0.45 mol% set for the gradient. The results (Figure 4.13) show that  $\text{Pd}(\text{OAc})_2$  gave the best result reaching 98% yield at 0.2 mol% Pd. The lower rates from  $\text{Pd}(\text{dppf})\text{Cl}_2$  and  $\text{PdCl}_2(\text{PPh}_3)_2$  can be explained by the ligands providing a more stable Pd(II) complex compared to  $\text{Pd}(\text{OAc})_2$  and thus rates of oxidative addition would be slower causing an overall lower rate.

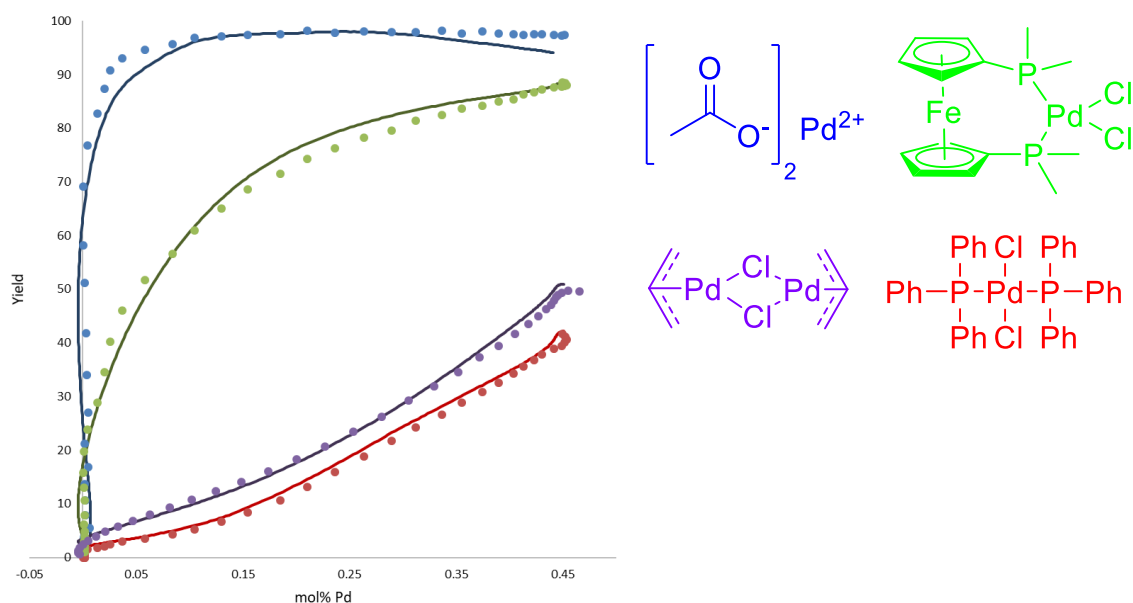
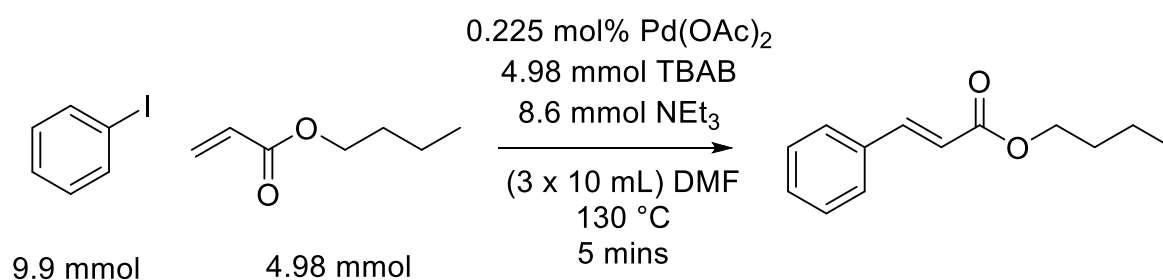


Figure 4.13 Results from 4 concentration gradient experiments. Solid lines depict IR results whereas separate points are GC data. IR data is normalised to the GC results. Reaction conditions can be found in 7.2.3.1 and 7.2.3.2

The overlap between the IR and the GC results show an acceptable overlap, with the general trends being consistent however the difference in yields at certain points can be large (7%).

An optimal metal source and concentration was found (Scheme 4.3) for these reaction conditions in 4 experiments totalling 560 minutes of experimental time. To generate a similar result using traditional steady state methods, assuming 8 data points per curve, would take 640 minutes of experimental time saving 80 minutes and generating a larger amount of data.



Scheme 4.3: Optimised reaction conditions found using the concentration gradient method. These are the reaction conditions used for future experiments.

#### 4.3.3.3 Validation

To validate the concentration gradient created, a second method for gradient generation was used, the variable flow rate method. The Pd line from the concentration gradient method was

replaced with a binary HPLC pump to deliver the variable flow rates to the same setup as before and a dispersion profile was generated for the setup (Figure 4.14). The dispersion profile consists of two straight lines of different steepness, rather than a single line. The reason for this could not be determined however this should not affect the results obtained.

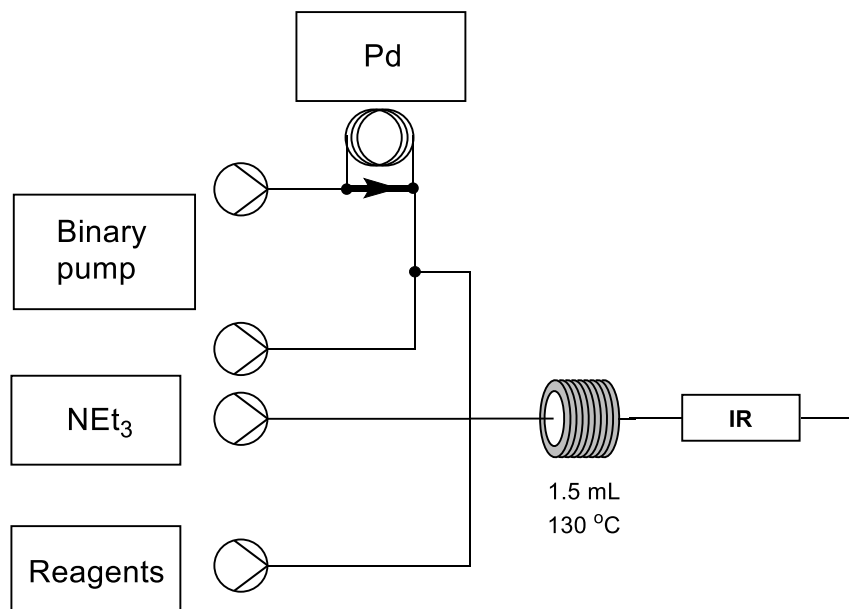


Figure 4.14: Flow setup for generating a Pd concentration gradient using a flow rate change. A gradient is generated by the ratio of flow rates between a solvent line and a line with  $\text{Pd}(\text{OAc})_2$  in DMF in a sample loop.

The experiment was performed with the same reaction conditions as the dispersion method, and a gradient of  $\text{Pd}(\text{OAc})_2$  generated. The results (Figure 4.15) display an excellent overlap between the flow rate ramp and the dispersion gradient methods with the largest difference being 3% yield.

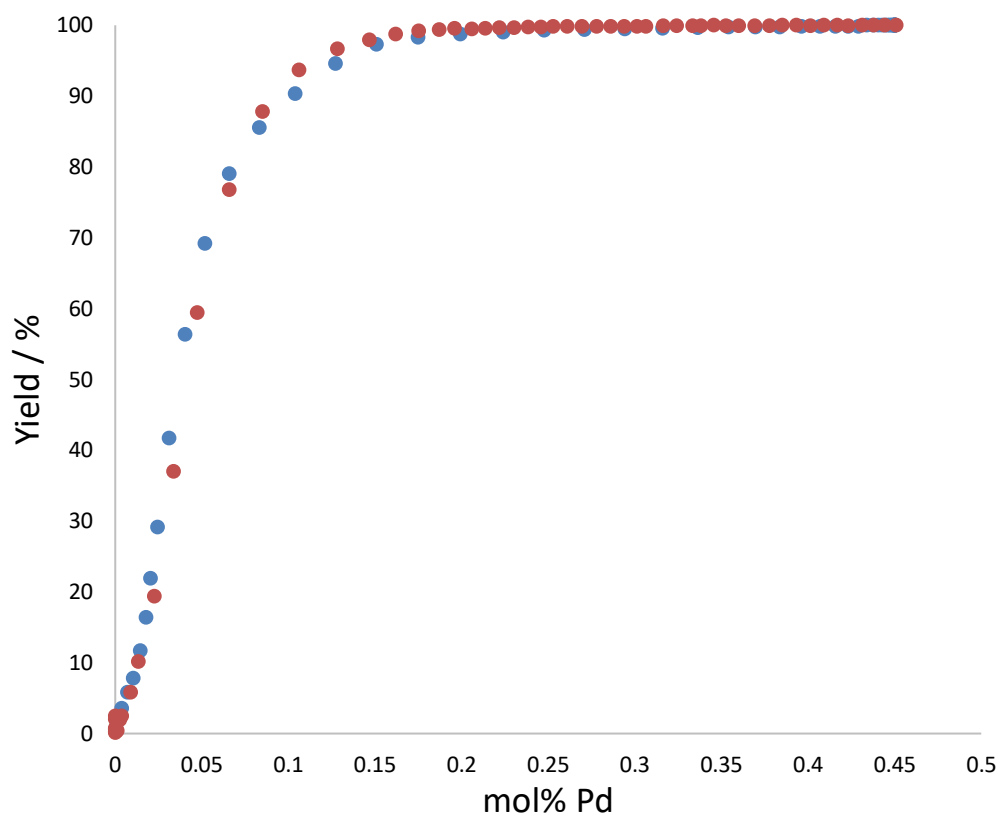


Figure 4.15: Overlap of yields generated from a dispersion and a flow rate concentration gradient reaction using reagent conditions found in 7.2.3.1 .

Red = HPLC. Blue = Dispersion.

#### 4.3.4 Probing the metal:ligand ratio

The addition of ligands can affect a reaction in many ways, the rate of reaction, selectivity, choice of starting material can all vary depending on the nature and amount of the ligand present<sup>188</sup>. As such the concentration gradient, as with optimising the metal concentration, should provide an efficient route toward ligand optimisation and analysis which is probed for the Heck reaction in this section.

##### 4.3.4.1 Setup

The flow setup consists of three lines. Two steady state lines for the Pd and reaction mixture, and one concentration gradient line for the ligand (Figure 4.16).

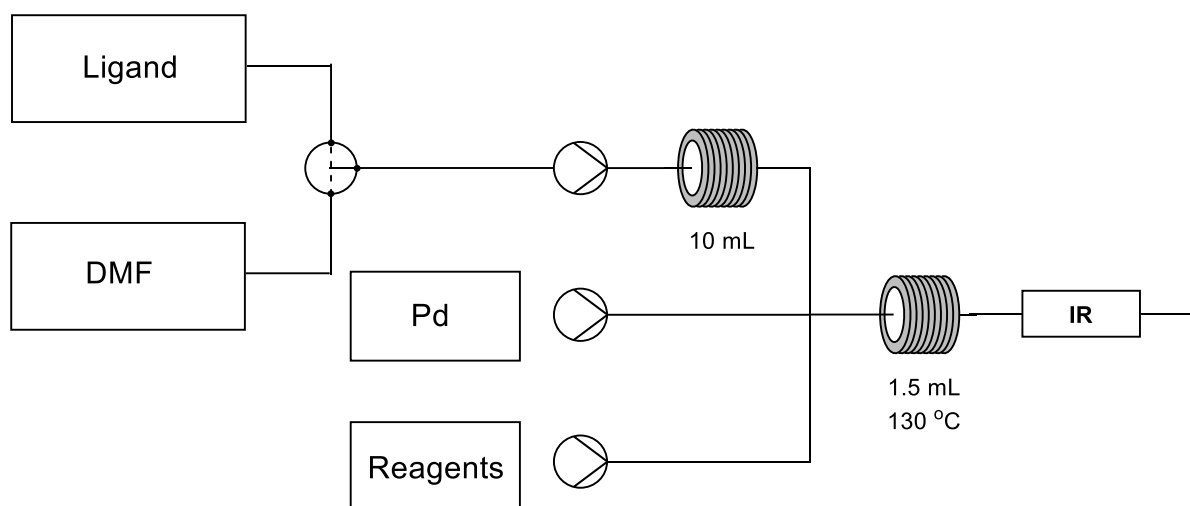


Figure 4.16: Flow setup for generating a concentration gradient of a ligand. Plugs of ligand are generated by switching of the T-valve between solvent and ligand. Concentration gradients of ligands were generated by dispersion of said plugs by passing through the dispersion coil. The gradient is then combined with  $\text{Pd}(\text{OAc})_2$  and the other reagents depicted by Scheme 4.3 before passing through the heated reactor and in-line detection before being collected using a liquid handler.

Identical reaction conditions to the metal gradient experiments were used of 130 °C and 5-minute reaction time (Scheme 4.3), the reactor size was increased to account for the additional flow rate from the third stream.

#### 4.3.4.2 Results

##### 4.3.4.2.1 $\text{PPh}_3$

As a baseline test for the addition of ligands, a gradient of  $\text{PPh}_3$  with a maximum equivalence of 35.5 that of  $\text{Pd}(\text{OAc})_2$  was performed.  $\text{PPh}_3$  was chosen due to its prevalence in the literature both in preformed catalysts and *in situ* formed intermediates. The results of the concentration gradient show a rapid decline in yield upon addition of any amount of ligand (Figure 4.17).

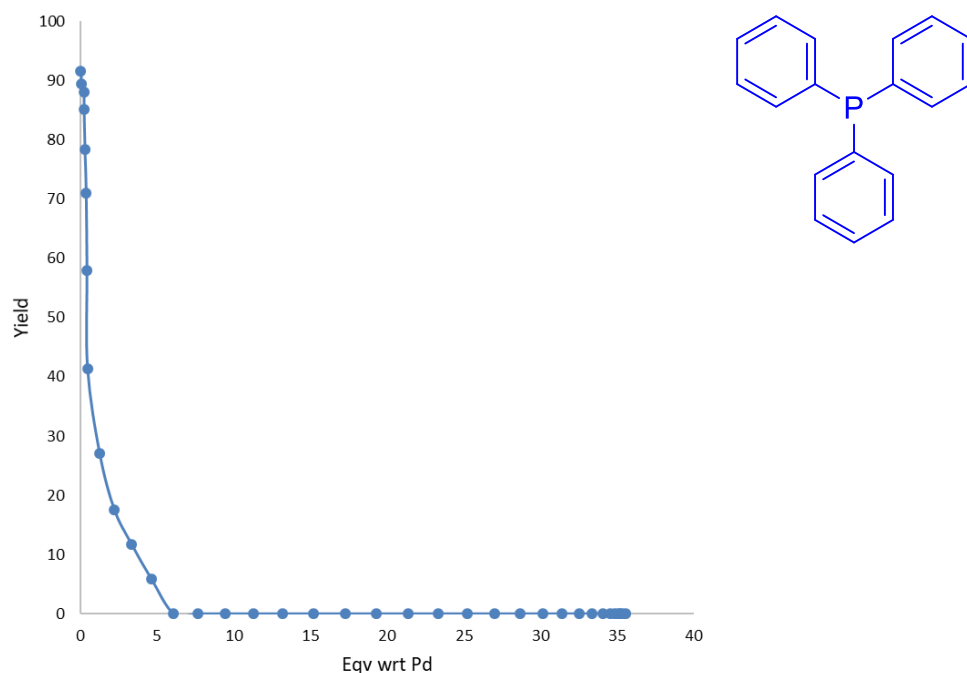


Figure 4.17: Yield from Heck reaction at varying concentration of  $\text{PPh}_3$ . Yield decreases upon addition of any amount of  $\text{PPh}_3$  with full inhibition above 5 equivalents with respect to  $\text{Pd}(\text{OAc})_2$ . Conditions are from Scheme 4.3.

The rate reduction could be due to the Pd species being formed in the reaction as  $\text{Pd}(\text{PPh}_3)_2$  is more reactive than  $\text{Pd}(\text{PPh}_3)_3$  toward oxidative addition<sup>248</sup> and the concentration of these species is controlled by the concentration of free phosphine, with higher phosphine concentrations favouring the more ligated species. As such the rate for oxidative addition is inversely proportional to the free phosphine concentration<sup>249</sup> and thus the rate would drop with increasing  $\text{PPh}_3$ .

However, it could also be due to the ligandless intermediates being more reactive than the ligated alternatives. The ligandless reaction can occur *via* a  $[\text{PdBr}_2\text{Ar}]_2^{2-}$  complex<sup>250</sup>, which in the ligand containing reaction can be formed from reaction of tetraalkylammonium salts with  $\text{Pd}(\text{L})\text{ArBr}$ . Addition of excess phosphine would drive the equilibrium toward the ligated species, lowering the rate of reaction.

When comparing the 2 equivalents result of this experiment with the result from the preformed  $\text{Pd}(\text{PPh}_3)_2\text{Cl}_2$  species, a similar yield. Which suggests minimal effect is had from either the acetate ion or the chloride as a ligand.

#### 4.3.4.2.2 Tri(ortho-tolyl)phosphine

Sterically hindered phosphines can aid in the reductive elimination<sup>234</sup> by increasing the strain in the  $\text{PdL}_2\text{HBr}$  complex left after  $\beta$ -hydride elimination. Additionally, they may help prevent Pd

precipitation by preventing access to Pd due to steric effects. To probe this tri(*o*-tolyl)phosphine was used as a sterically hindered analogue of  $\text{PPh}_3$ .

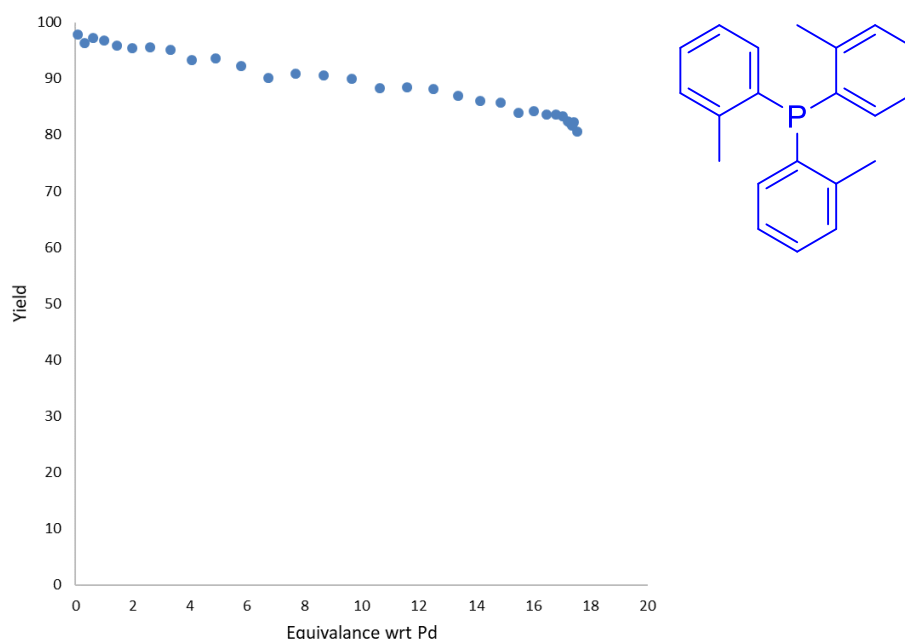
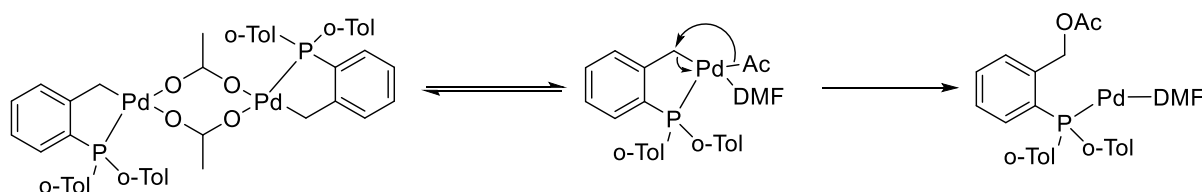


Figure 4.18: Yield from Heck reaction at varying concentration of tri(*ortho*-tolyl)phosphine.

Presence of the ligand causes an inhibition of the reaction. Reaction conditions are from Scheme 4.3.

The results (Figure 4.18) still show an inhibition from the addition of ligands, however the loss in rate is much smaller than that seen with  $\text{PPh}_3$ . The reason for this may be steric hinderance of the ligands preventing multi-ligand binding to the metal centre. Additionally, *o*-tolyl bound palladium can form dimeric palladacycles (Scheme 4.4) which can undergo reductive elimination to form a catalytically active  $\text{Pd}(0)$  species.<sup>251</sup>



Scheme 4.4: Neutral pathway to reforming  $\text{Pd}(0)$  from a dimeric Pd/ *o*-tolyl species

The reverse reaction is an intramolecular oxidative addition which will occur very rapidly and as such the dimer will be the major form of the Pd. The dimer will prevent additional ligands from bonding and forming stable, inactive compounds and keep the rate of reaction high.

#### 4.3.4.2.3 TTBP.HBF<sub>4</sub>

TTBP.HBF<sub>4</sub> has been mentioned previously as a successful ligand for a large-scale Heck reaction due to its high steric bulk which can increase the rate of reductive elimination and its high electron density aiding in oxidative addition<sup>252,253</sup>. However, when applied to this system as a concentration gradient, a similar inhibitory effect was seen (Figure 4.19).

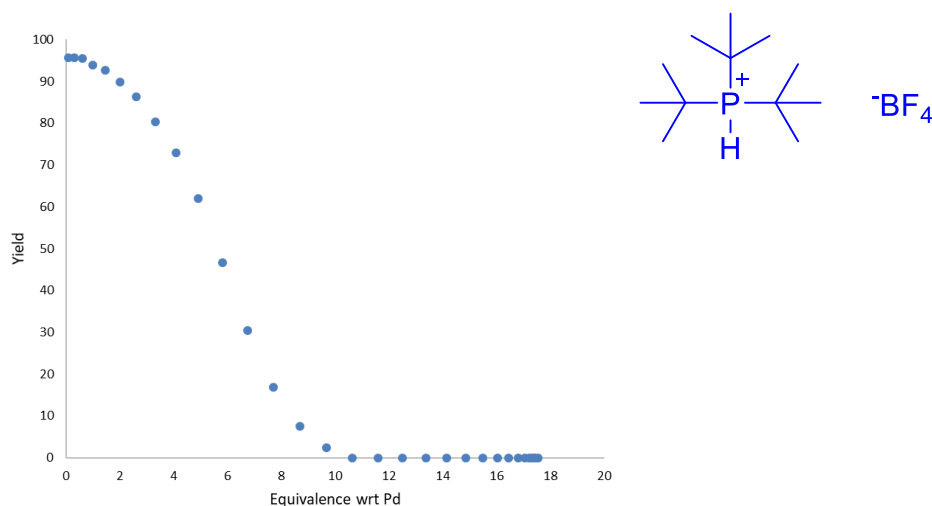


Figure 4.19: Yield from Heck reaction at varying concentration of TTBP.HBF<sub>4</sub>. Full inhibition is reached by 11 equivalents of ligand with respect to palladium. Reaction conditions are from Scheme 4.3.

The inhibitory effect is much smaller than that of PPh<sub>3</sub> suggesting that the Pd-ligand complexes formed are more reactive due to this increase in electron density and steric bulk compared to that of PPh<sub>3</sub>.

#### 4.3.4.2.4 DPPF and DTBPF

A gradient of DPPF was performed to compare the results to the preformed Pd(dppf)Cl<sub>2</sub> previously studied. DTBPF was also performed as a more sterically hindered and electron rich analogue of DPPF. At low ligand equivalence, the two curves give very similar levels of inhibition (Figure 4.20) however, as ligand equivalence is increased, the inhibition of DPPF is more pronounced with the yield reaching zero by 5 equivalents. Whereas DTBPF maintains reactivity up until 10 equivalents most likely due to the large increase in electron density and steric effects aiding in the reaction in a similar manner to TTBP.HBF<sub>4</sub>. Comparing the 2 equivalent results for DPPF obtained with the concentration gradient method to that of the preformed complex tested earlier shows a good overlap between the yields with both giving around 75% yield.



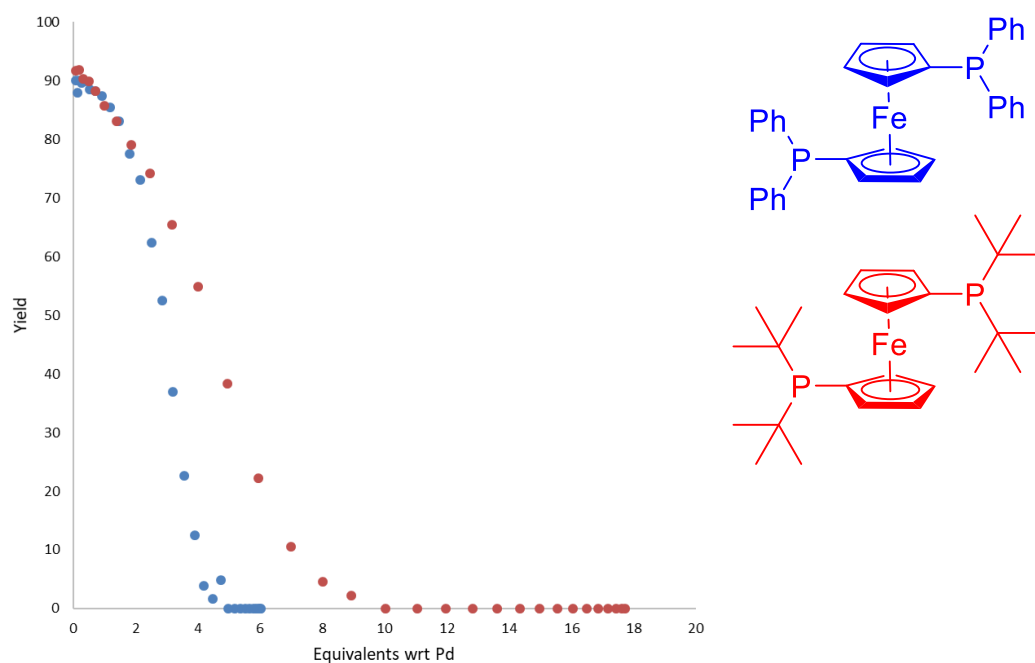


Figure 4.20: Yield from Heck reaction at varying concentration of ligand. DPPF inhibits the Heck reaction more than DTBPF, reaching full inhibition by 6 equivalents compared to 10 for DTBPF. Reaction conditions are from Scheme 4.3.

#### 4.3.4.2.5 DPPE

Bidentate ligands tend to generate more stable metal-ligand complexes<sup>190</sup>, as such it is unsurprising that when a concentration gradient of DPPE was applied to the Heck reaction conditions (Figure 4.21), strong inhibition occurred. DPPE is the most inhibiting ligand tested with zero activity seen after addition of 1.5 equivalents of ligand, due to the bidentate nature of the ligand.

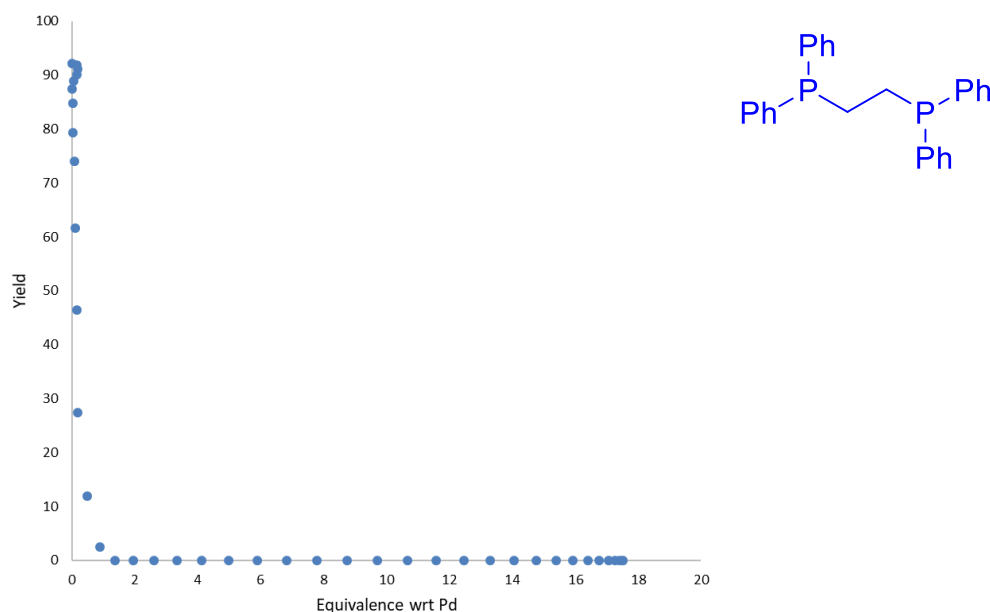


Figure 4.21: Yield from Heck reaction at varying concentration of DPPE. DPPE fully inhibits the Heck reaction by 2 equivalents added. Reaction conditions are from Scheme 4.3.

#### 4.3.4.2.6 Nitrogen-ligands

Nitrogen based ligands for the Heck reaction are much less common than the phosphine group ligands however examples of palladacycles<sup>254</sup> and free ligands<sup>255,256</sup> have been reported. As they have been known to act as ligands and it takes a small amount of time to change the flow setup for different ligands, bipy, terpy, and phen were all tested using the methodology. The results (Figure 4.22) show bipy and phen giving a very similar inhibition curve, with zero activity after 6.5 equivalents of ligand, suggesting these nitrogen ligands have poorer binding compared to  $\text{PPh}_3$ . Terpy also inhibits the reaction however to a much lower degree than the other tested ligands. Which is most likely due to the steric bulk of the ligand preventing an additional terpy from binding and blocking all the sites.

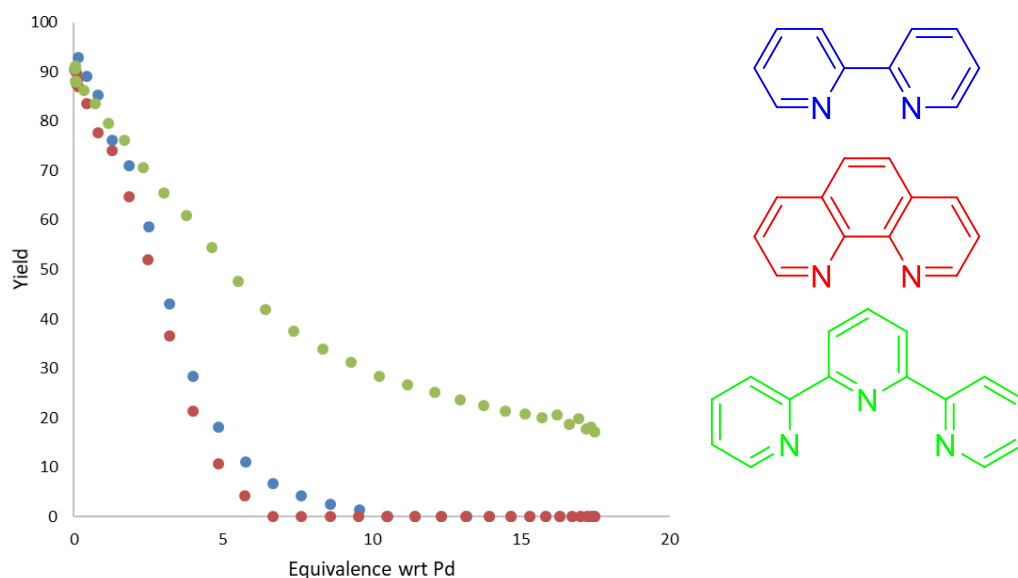


Figure 4.22: Yield from Heck reaction at varying concentration of nitrogen ligands. Ligands show a similar level of inhibition seen by phosphine ligands. Reaction conditions are from Scheme 4.3.

#### 4.3.4.3 Conclusion

Nine different ligands were tested over a range of concentrations in only nine experiments totalling 21 hours of experimental time. A productivity saving of 3 hours, assuming 5 concentrations tested per ligand, was generated over the traditional batch methods and vastly more data was generated.

All tested ligands effected a decrease in the rate of the tested Heck reaction. These results match those reported by Kadir *et al*<sup>253</sup> who found no ligand-based acceleration in rate of a Heck coupling between iodobenzene and methyl acrylate.

#### 4.3.5 Testing the effects of additives

In 2013, Collins and Glorius reported a method for the rapid assessment of a reaction robustness<sup>257</sup>. The method involved addition of additives to the tested reaction, with a particular functional group or structure, to act as surrogates for starting material with the equivalent functionalities. A much broader assessment of feasible reaction scope than is traditionally reported in the literature can be generated with much less effort than synthesising new starting materials. Whilst this is a powerful method for generating reaction data, it is limited to a single concentration at a time. As such the combination of this method with the concentration gradient method would allow a rapid robustness screen encompassing a range of concentrations.

The method could also be used as a method of screening for allowable limits of impurities in reaction mixtures from either earlier steps in a multi-step synthesis, or impurities introduced from starting materials, which is an important parameter in the chemical industry<sup>258,259</sup>.

To test this a range of additives were probed against the Heck reaction previously optimised.

#### 4.3.5.1 Setup

The flow setup required is identical to that of the ligand test with the exception of additives being dispersed rather than ligands (Figure 4.23). The identical setup allows for a rapid change from probing the effect of ligands in a reaction to testing the reaction scope.

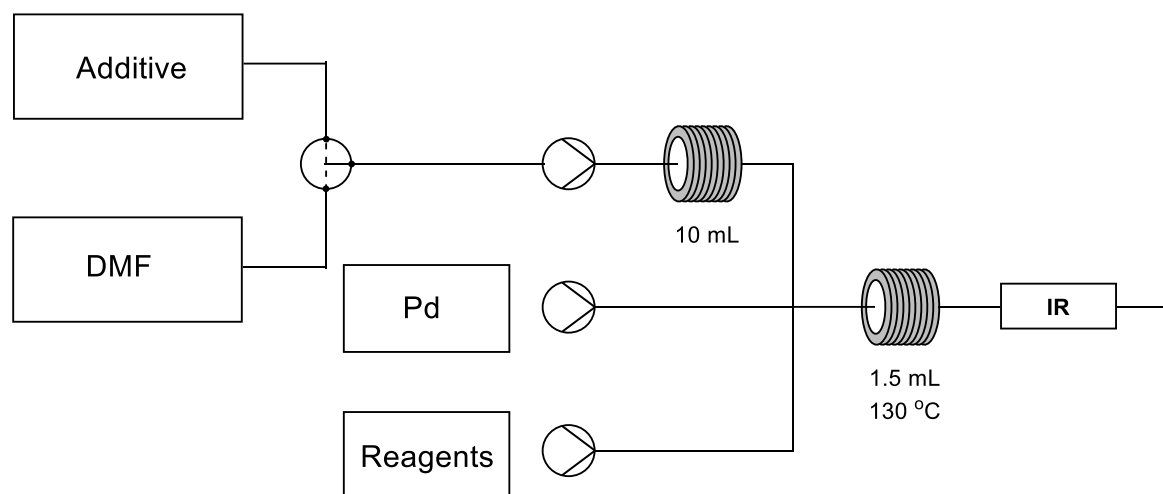


Figure 4.23: Flow setup for the generation of an additive concentration gradient. Plugs of additive are formed by switching the T-valve from additive to solvent. These plugs are then converted into concentration gradients by pumping through a dispersion coil. The concentration gradient is then combined with the other reagents from Scheme 4.3 before pumping through a heated reactor, in-line monitoring and then collection in a liquid handler.

#### 4.3.5.2 Results

##### 4.3.5.2.1 Sulfur containing compounds

Sulfur compounds are well known poisons<sup>260,261</sup> and scavengers<sup>262</sup> for metal catalysts due to their ability to form strong metal-ligand interactions<sup>263</sup>. Do to this it is important to test the scope of a reaction with respect to various sulfur containing compounds. Five sulfur containing compounds were tested using the concentration gradient method, (2-naphthalenethiol, DMSO, thiophene, diphenyldisulfide and thioanisole) encompassing a range of sulfur functional groups.

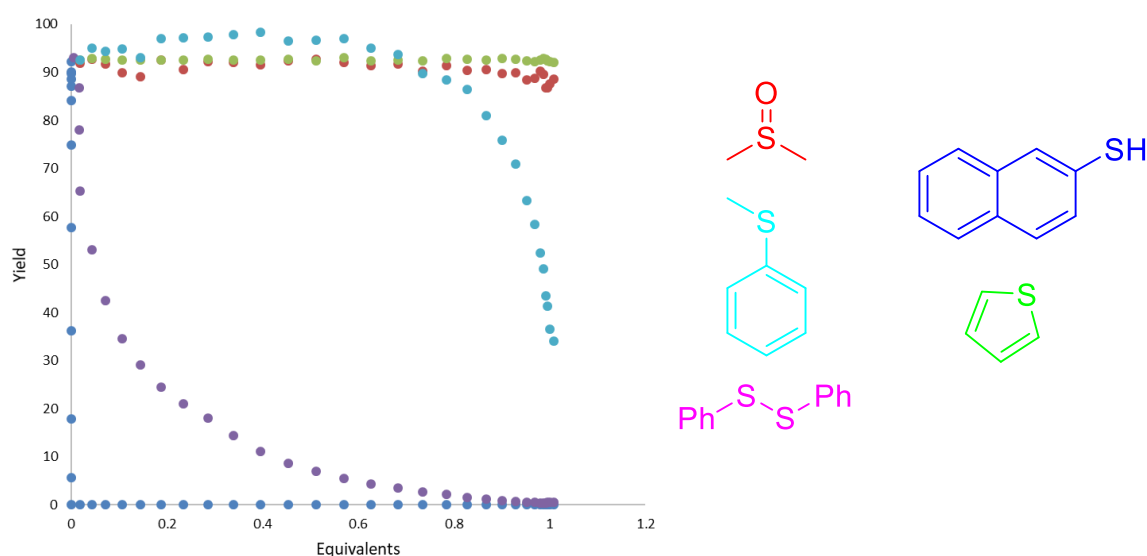


Figure 4.24: Yield from Heck reaction at various concentrations of additives. Level of inhibition is related to the nucleophilicity of the sulfur. Reaction conditions are from Scheme 4.3.

The results (Figure 4.24) show a rough dependence on sulfur nucleophilicity with an almost immediate inhibition of activity with the thiol additive. Exact values for this inhibition level cannot be obtained using this data due to the averaging effect of dispersion discussed earlier. To access these values a repeat experiment with a lower maximum concentration would need to be performed. The less nucleophilic diphenyldisulfide also acts as an inhibitor but at a much slower rate than the thiol only reaching full inhibition at 1 equivalent of additive. Thioanisole does not seem to affect the reaction until 0.6 equivalents upon which it rapidly begins to inhibit. DMSO and thiophene do not seem to have any effect on the reaction across the range of concentrations tested. These experiments show that if a thiol or disulfide group are present in the starting material of this Heck reaction, it is likely to encounter issues. However, reducing the nucleophilicity of the sulfur, such as by converting the sulfur to a sulfoxide, should allow the reaction to go unimpeded.

#### 4.3.5.2.2 Nitrogen and oxygen containing compounds

Nitrogen and oxygen based functional groups are important classes in synthetic chemistry useful in numerous chemical transformations, for increasing hydrophilicity of compounds<sup>264</sup> and increasing solubility or binding in drug molecules<sup>265–267</sup>. These functional groups are likely to be present when chemists utilise a reaction methodology, particularly in late stage synthesis, and as such knowing the scope of the various functional groups is important. Eight additives were chosen representing the alcohol, ester, aldehyde, ketone, epoxide, carboxylic acid, nitrile, amide and alkanolamine functional groups. The results (Figure 4.25) show all tested functional groups showed no effect on the progress of the reaction indicating an excellent reaction scope for

## Chapter 4

synthesis purposes. With the exception of the alkanolamine functional group which rapidly inhibited product formation.

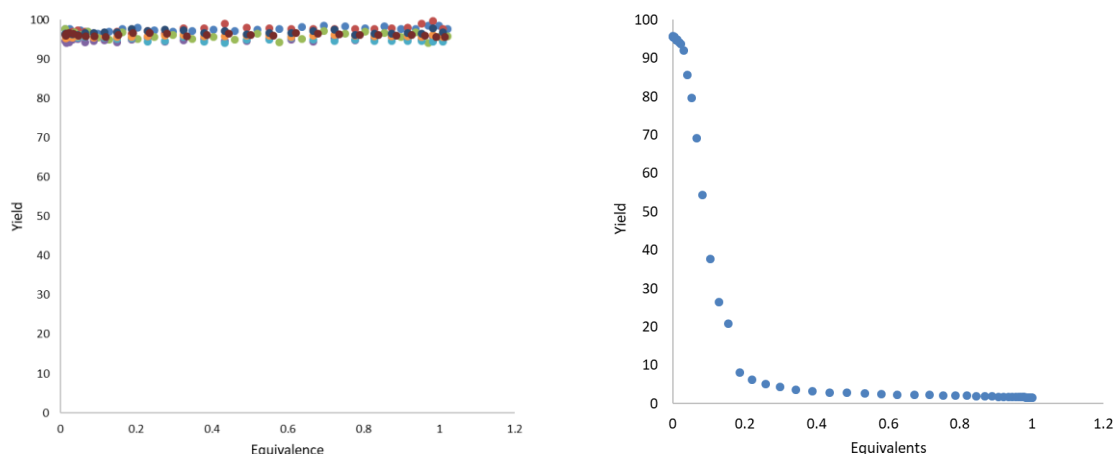


Figure 4.25: Yield from Heck reaction at varying concentration of additives. Right = 2-(methylamino)ethanol. Left = Remaining tested functional groups. All additives had no effect on the Heck reaction with the exception of the alkanolamine. Reaction conditions are from Scheme 4.3.

### 4.3.5.2.3 Heterocycles

As with oxygen and nitrogen containing compounds, heterocycles are present in the vast majority of drug compounds<sup>268,269</sup>. A series of six heterocycles were tested against the Heck reaction: furan, pyrrole, pyridine, indole, imidazole, and 3-methyl-2-oxazolidinone (MOXA) (Figure 4.26).

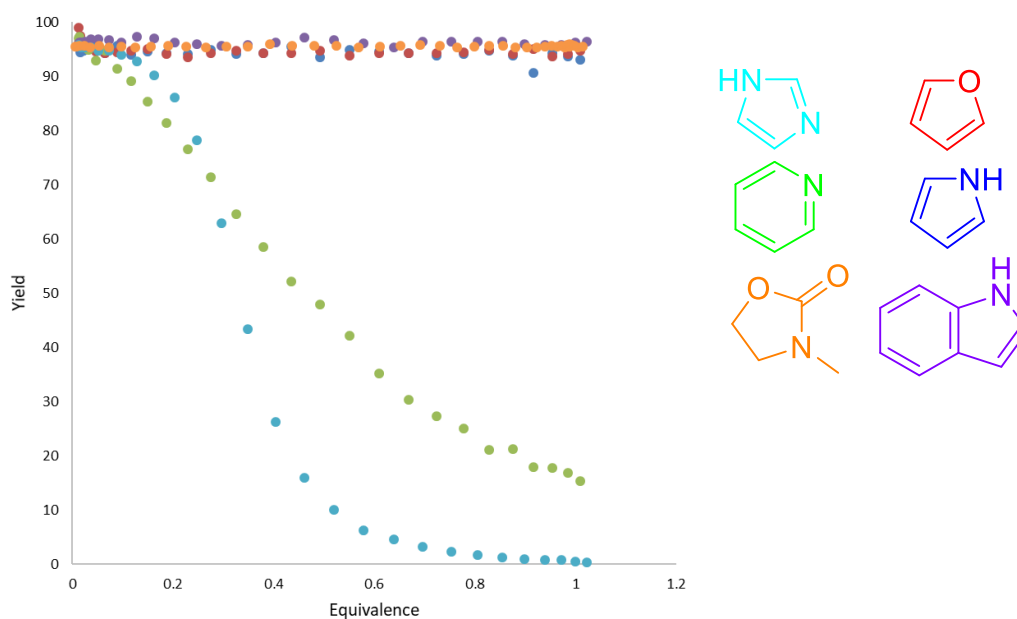


Figure 4.26: Yield from Heck reaction at varying concentration of additives. Pyridine and imidazole show inhibition of the Heck reaction, no effect is seen with the other additives.

Reaction conditions are from Scheme 4.3

MOXA, furan, pyrrole and indole all show no inhibition across the tested range. Pyridine causes a linear decrease in yield as the concentration increases, to a minimum of 15% yield at 1 equivalent. Whereas imidazole reaches full inhibition by 1 equivalent of additive however has a more sigmoidal shape curve. These curve shapes tend to appear in negative cooperative binding where the binding of a ligand is hindered by the presence of other ligands<sup>270</sup>, which may be the case here with small clusters of nanoparticulate Pd.

#### 4.3.5.2.4 Alkenes and alkynes

As Pd reacting with an alkene is an important step in the Heck reaction, and alkenes and alkynes are common groups occurred during product synthesis, testing the reaction scope in the presence of various alkenes and alkynes is necessary. Norbornene, 1-hexene, 1-octyne and 1,5-cyclooctadiene were all tested using the methodology (Figure 4.27).

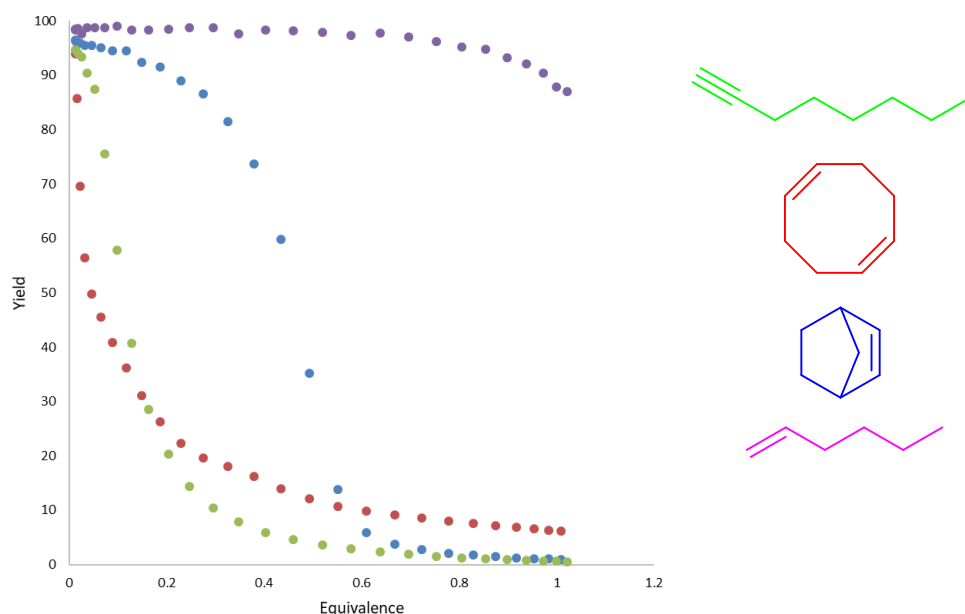


Figure 4.27: Yield from Heck reaction at varying concentration of additives. All additives showed an effect on the Heck reaction, with 1-octyne and 1,5-cyclooctadiene inhibiting more than norbornene and 1-hexene. No reaction between these additives and iodobenzene was observed by GC. Reaction conditions are from Scheme 4.3

1-octyne and 1,5-cyclooctadiene both initially inhibit with a strong dependence on equivalence however this dependence begins to decrease as the amount of additive increases, which could be due to steric interactions preventing additional additive-metal interactions from forming.

Norbornene appears to behave in the opposite manor with an initial slow rate of inhibition which then increases at higher amounts of additive perhaps due to the sterics lowering the stability of the Pd-ligand complex thus only forming when there is a high concentration of ligand present.

1-hexene shows no inhibition until 0.7 equivalents upon which a very small amount of inhibition occurs. To probe this further two repeat experiments were performed with 3 and 10 equivalents of hexane and the results combined (Figure 4.28)



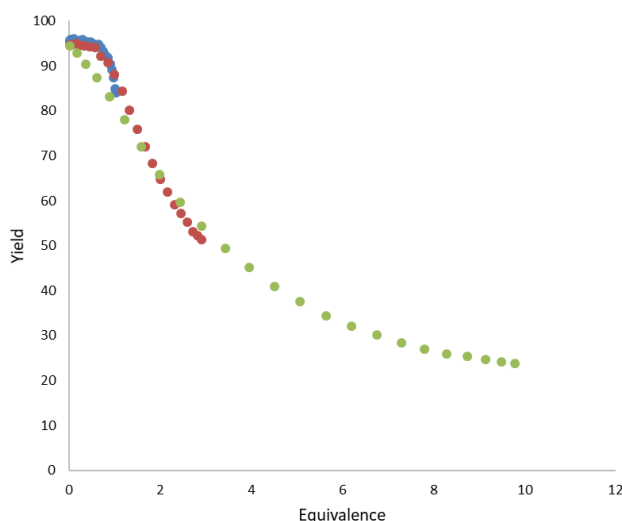


Figure 4.28: Combined yield graphs from 3 1-hexene concentration gradient experiments with 1, 3, and 10 as the maximum equivalents. The effect of averaging can be seen below 2 equivalents when comparing the lines, with more averaging occurring in the green line, compared to the blue and red, causing an inaccurate result.

Of note in the combined graph is the difference between the lines below 1 equivalent, this difference is caused by the averaging in of the steady states mentioned earlier when the plug disperses in the reactor. Therefore, if a high maximum concentration gradient is performed, to have confidence in the values obtained for low concentration data, repeat experiments must be performed with a lower starting concentration for the gradient.

Throughout these reactions, no products were observed via GC of the additive coupling with the iodobenzene, either through a new peak appearing or the iodobenzene level remaining unchanged. The lack of reaction suggests that the additive was binding to the palladium inhibiting the reaction but not undergoing its own reaction cycle.

#### 4.3.5.3 Conclusion

The concentration gradient method allows the evolution of the rapid scope assessment procedure by Collins and Glorius, including inhibition data at various concentrations. 24 compounds were tested in an equivalent number of experiments and an insight into the scope of the Heck reaction was obtained.

As well as improving the knowledge of the reaction scope, the methodology can also be used to screen for known impurities in reaction starting material. For example, if 2-(methylamino)ethanol was an known impurity in a starting material for this Heck reaction then, from one experiment, an upper limit for that impurity of 0.1 equivalents can be set. The limit can then be used to screen stocks of starting material to ensure the reaction is always below this limit.

The ability to overlay several concentration gradients with different maximum concentrations was also demonstrated with three 1-hexene reactions allowing the method to show the broad trends but also enhance the resolution at lower concentrations with repeat experiments.

### 4.4 Copper-free Sonogashira

The Sonogashira reaction, much like the Heck reaction, has become an important tool for synthetic chemists for C-C bond formation<sup>271–274</sup> enabling the coupling of terminal alkynes and aryl or vinyl halides. A typical procedure for this coupling involves both a Pd source and a cocatalyst, usually Cu<sup>275–278</sup>. The inclusion of a Cu cocatalyst produces a major issue for the Sonogashira which is undesired Glaser coupling, the Cu catalysed homocoupling of alkynes<sup>279,280</sup>. To prevent this the system needs to be strictly under an inert atmosphere otherwise homocoupling will occur which will lower yields, increase waste and potentially consume expensive starting materials. As such a methodology for the Sonogashira which does not utilise Cu would be beneficial.

#### 4.4.1 Literature

Several heterogeneous Cu-free Sonogashira reactions have been reported<sup>281–285</sup> however due to the previously mentioned issues when performing heterogeneous cross-coupling reactions in flow, homogeneous catalysis will be the main focus with a brief overview representative of the current literature is presented.

##### 4.4.1.1 Homogeneous

The Sonogashira coupling of aryl iodides has been reported<sup>286</sup> in the synthesis of kinase inhibitors utilising 1 mol% Pd(OAc)<sub>2</sub>, 2 mol% PPh<sub>3</sub> and NEt<sub>3</sub> in MeCN providing 98% yield of an intermediate product. Later in the synthesis they employed another reported Sonogashira utilising Bu<sub>4</sub>NOAc in a “ligand, copper, and amine free” Sonogashira coupling<sup>287</sup>. However, given the potential for tetraalkylammonium salts to act as a stabilising ligand under Jeffrey conditions, the “no-ligand” inclusion is debatable.

A procedure utilising water as a solvent has also been reported<sup>288</sup> which coupled electron poor and electron rich aryl iodides with phenyl acetylene in above 82% yield, using 1 mol% PdCl<sub>2</sub> with pyrrolidine as the base.

For bromides substrates in the Sonogashira, the use of 2.5 mol% (AllylPdCl)<sub>2</sub> and P(tBu)<sub>3</sub> as a ligand with DABCO or piperidine as a base<sup>289</sup> proved effective. These conditions gave high reaction yields at room temperature over > 11 hours reaction time.

The coupling of aryl bromides functionalised with carboxylic acids has also been reported<sup>290</sup> which utilised 4 mol% of  $\text{PdCl}_2(\text{PPh}_3)_2$  with 10 equivalents of piperidine as the base, heated to 70 or 85 °C for 10-20 mins giving excellent yields

The use of bulky ligands for the bromide coupling was reported again for the C-6-alkynylation of protected 2'-deoxyadenosine.<sup>291</sup> JohnPhos was used in addition to 6 mol%  $\text{Pd}(\text{PPh}_3)_4$  and 2.4 equivalents  $\text{Cs}_2\text{CO}_3$  to react various electron poor and rich bromides in good yield over several hours. The only bromide which failed to react was 2,4,6-tri-*tert*-butylbromobenzene due to steric hindrance.

Similarly to bromides, when using chlorides bulky electron rich ligands are required. A microwave heated method was reported<sup>292</sup> which utilised the rapid direct heating allowed by the microwave to bring reaction times down to 10 minutes for aryl chlorides. 2 mol%  $\text{PdCl}_2(\text{PPh}_3)_2$ , 4 mol%  $\text{P}(\text{tBu})_3$ , 10 mol% DBU and 1 equivalent  $\text{Cs}_2\text{CO}_3$  were used allowing coupling between electron-poor and rich chlorides.

Buchwald *et al* also reported<sup>293</sup> a Cu-free alternative consisting of 1 mol% of the Pd source, 3 mol% XPhos, and 2.6 equivalents of  $\text{Cs}_2\text{CO}_3$  which allowed reaction of electron-deficient aryl chloride at 70 °C and electron neutral and rich at 90 °C.

The coupling of 1-chloroisoquinolines with alkynes has also been reported<sup>294</sup> again utilising a bulky electron rich ligand, RuPhos. A combination of 2.5 mol%  $\text{Pd}(\text{OAc})_2$ , 10 mol% RuPhos, 2 equivalents  $\text{NEt}_3$ , heated at 70 °C for 45 minutes in a 1:10 ratio of  $\text{H}_2\text{O}$ :THF provided the coupled product in greater than 65% yield.

#### 4.4.1.2 Cu-free Sonogashira in flow

Fukuyama *et al* reported<sup>295</sup> an efficient Sonogashira reaction using 5 mol%  $\text{PdCl}_2(\text{PPh}_3)_2$ , 3.6 equivalents of diisopropylamine and an ionic liquid  $[\text{BMIm}][\text{PF}_6]$  as the solvent. Heating at 110 °C for 10 minutes allowed for yields of 93% however the catalyst could be recycled easily by extraction of the coupling products by addition of hexane or ether. After recycling the yield decreased to 83% suggesting inefficiency in the separation method or losses due to precipitation and deactivation.

Buchwald *et al* demonstrated a flow version of the previously mentioned Sonogashira<sup>296</sup> conditions with KOH used instead of  $\text{Cs}_2\text{CO}_3$ . To prevent clogging from the inorganic bases and bromide precipitates a 4:3 mixture of dioxane: $\text{H}_2\text{O}$  was used. The reagents were pumped through a stainless steel packed bed reactor heated to 110 °C for 1-7 minutes generating good yields with a variety of starting organobromides.

The use of a step by step rapid mixing and heating system has been reported<sup>297</sup> in which water and the reaction substrates are combined in a stream and rapidly mixed to form substrate particles spread throughout the water layer. The system is then rapidly heated to 250 °C and the substrate dissolves forming a homogeneous mixture. For the Sonogashira they tested (2 mol% PdCl<sub>2</sub>, 2M NaOH) quantitative yields were obtained after 4 seconds reaction time and extraction was aided by the formation of a biphasic system of water and product after the temperature had decreased. The majority of the Pd was deposited as Pd black which does not make this method suitable for all systems as well as the high pressures needed (160 bar).

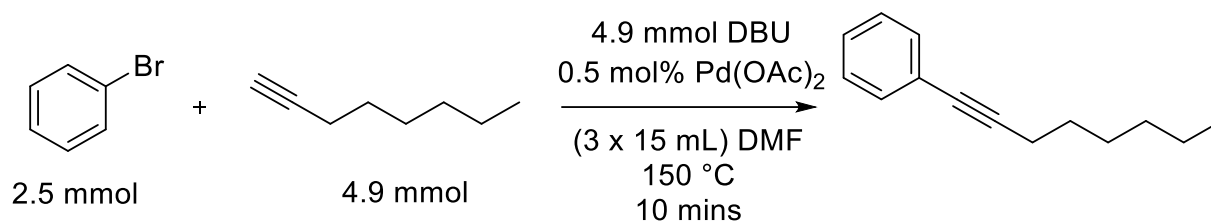
#### 4.4.2 Reaction conditions and flow setup

For the reaction of bromides in the Cu-free Sonogashira reaction, the use of large bulky ligands, or inorganic bases is prevalent. Additionally, the only procedures for the reaction in flow utilise ionic liquids which not every flow system is setup for easily or a heavily water based solvent mixture which may not be suitable for organic substrates. To this end, the aim for this section was to use the concentration gradient method to probe a flow methodology for the Cu-free Sonogashira.

The initial conditions chosen were first tested within the group using traditional batch methods to ensure suitability for flow.

0.5 mol% Pd(OAc)<sub>2</sub>, 2 equivalents DBU, 4 equivalents of PPh<sub>3</sub>, 1 equivalent aryl bromide, 2 equivalents alkyne heated at 150 °C gave no visible precipitation in batch and initial steady state reactions in flow indicated a reaction time of 10 minutes with an adequate starting point of 46% conversion. Additionally, no efforts were taken to ensure the reaction was dry or operated under inert conditions minimising the effort of reaction setup.

The test reaction chosen was the coupling between bromobenzene and 1-octyne (Scheme 4.5) with 2 equivalents of DBU and the flow setup for the concentration gradient reactions is shown below (Figure 4.29)



Scheme 4.5: Reaction conditions used for the Sonogashira reaction of bromobenzene and octyne in this thesis. Yields are calculated using the product peak by GC calibrated with respect to an internal standard.

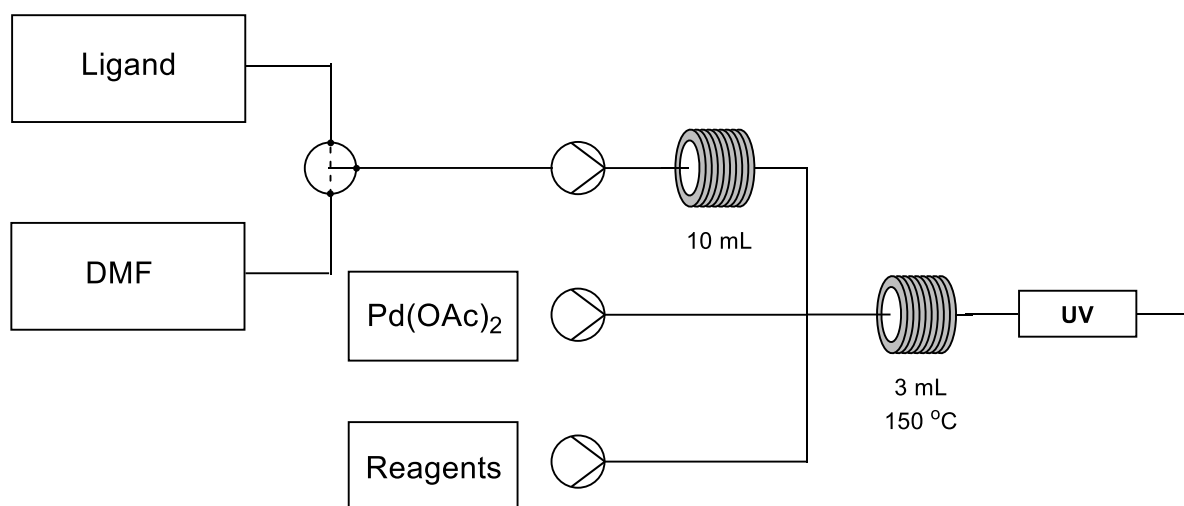


Figure 4.29: Flow setup for the generation of a ligand concentration gradient for combination with the Sonogashira reagents. Plugs of ligand are generated by switching the T-valve between solvent and ligand. The plugs are then converted into concentration gradients by pumping through a dispersion coil. Gradients are then combined with the reagents described in Scheme 4.5 and pumped through a heated reactor, inline monitoring and collected by a liquid handler.

#### 4.4.3 Ligands

From the literature above, the choice of ligand has an important effect on this reaction, with bulky, electron rich ligands necessary for the use of chloride whereas iodides can react under ligand free conditions. Therefore, a ligand screen was an important first step to be taken.

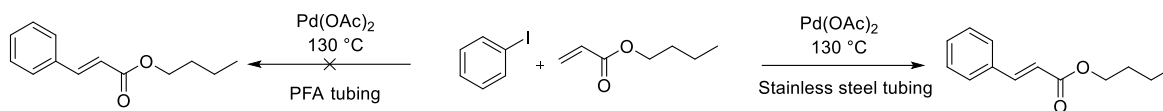
##### 4.4.3.1 $\text{PPh}_3$

The initial ligand chosen for the concentration gradient methodology was  $\text{PPh}_3$  due to its cost and its wide use in other cross coupling reactions and preformed catalysts and its success in the batch prescreening.

##### 4.4.3.1.1 Steel effect

Initial attempts at a concentration gradient experiment generated significantly lower conversions than expected (6% to 46%). The effect of mixing was probed by changing the design of the mixer however no change was seen. Premixing of the metal and ligand was also tested to no avail. The difference in reactivity was eventually found to have been caused by the material of construction (Scheme 4.6). The initial steady state tests were performed using a stainless-steel reactor and this was exchanged for a PFA reactor for the concentration gradient experiments. The increase in

reactivity was not due to deposited Pd from previous reactions as a new reactor gave an equivalent reactivity to the old reactor.



Scheme 4.6: Sonogashira reaction effected by the choice of reactor material. Reaction performs well when the reactor is made of stainless steel, but no reaction is seen when the reactor is made of PFA.

To probe the effect a packed column of steel wool was made and placed at various locations throughout the flow setup with a PFA reactor placed after the mixer (Figure 4.30). Placing the steel column in-line with any of the reagents (position A, B and C) but before the mixer showed no increase in conversion, this rules out any potential leaching effect from the steel.

Placing the column after the mixer (position D) showed a small increase in conversion (3%) at room temperature, heating the column to  $150\text{ }^\circ\text{C}$  caused the conversion to increase to 47%. Repetition of this reaction without the PFA reactor gave a conversion of 40% suggesting that nearly all the reaction is occurring within the steel column. The combination of this data and the leaching experiments suggests that the reaction is occurring on the surface of the steel. After a successful reaction, a repeat was performed with the exclusion of the  $\text{Pd}(\text{OAc})_2$ . A small conversion (3%) was observed which potentially suggests a small amount of depositing on the surface of the steel however, the majority of the reactivity was due to Pd in the reaction mixture.

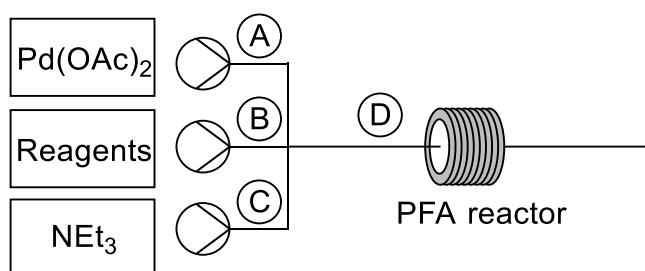


Figure 4.30: Reactor scheme for the packed bed of steel reactions. A, B, C, and D are positions where the packed bed can be placed. No reaction is seen unless the bed is in position D suggesting that the reaction is performed on the surface of the steel.

The experiments were repeated using a stainless-steel packed column and consistent results were obtained.

Exchanging the steel for glass wool, also showed a positive effect on the reaction. The conversion was increased by 33% when the glass wool column was added post mixer. Direct comparisons between the glass and steel are difficult due to the variance in packing and surface area.

However, when the reaction was repeated using a glass-lined stainless-steel reactor, only 20% conversion was observed. The variance between the reactor types increases the likelihood of the surface catalysis hypothesis as the glass will have a smoother surface than the steel reactor, allowing for less sites for Pd deposition.

The method chosen for overcoming this issue was to only utilise stainless-steel reactors for the concentration gradient method.

#### 4.4.3.1.2 Concentration gradient

The typical loading of a ligand is 2-4 equivalents with respect to the metal, as such the maximum concentration initially chosen was 16 equivalents as it was assumed the optimal amount would be contained within that range. The results (Figure 4.31) however show a continuous increase in the yield as the concentration of  $\text{PPh}_3$  increase with the maximum highly likely to be above 16 equivalents.

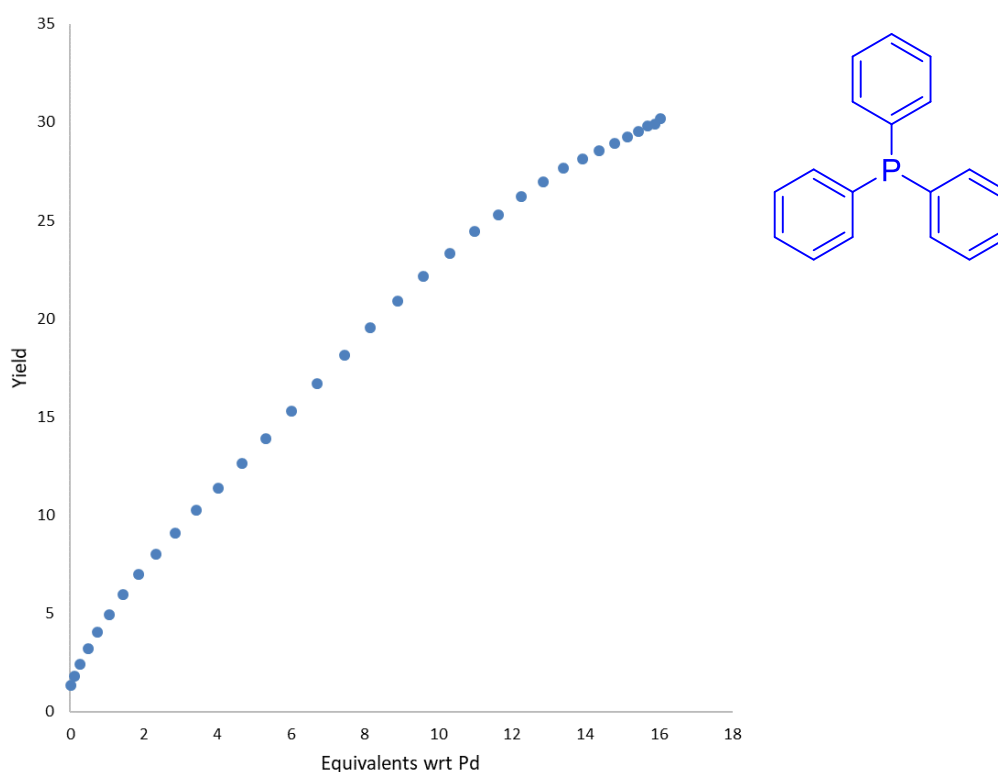


Figure 4.31: Yield from Sonogashira reaction at varying concentration of  $\text{PPh}_3$ . Presence of ligand increases the overall yield of the reaction to 30% at 16 equivalents. Reaction conditions are from Scheme 4.5.

A second reaction was performed with 160 equivalents as the new maximum and under these conditions (Figure 4.32), the optimal loading of  $\text{PPh}_3$  was found to be 47 equivalents with respect to the Pd, which is far in excess of the traditional amounts.  $\text{PPh}_3\text{O}$  is formed during the reaction

## Chapter 4

suggesting that the ligand plays a continuous role in reducing the Pd aiding in returning it back to a catalytically active species, otherwise a linear relationship would be expected. Interestingly the rate of formation of the oxide decreases after the reaction has reached its optimal concentration further supporting the hypothesis.

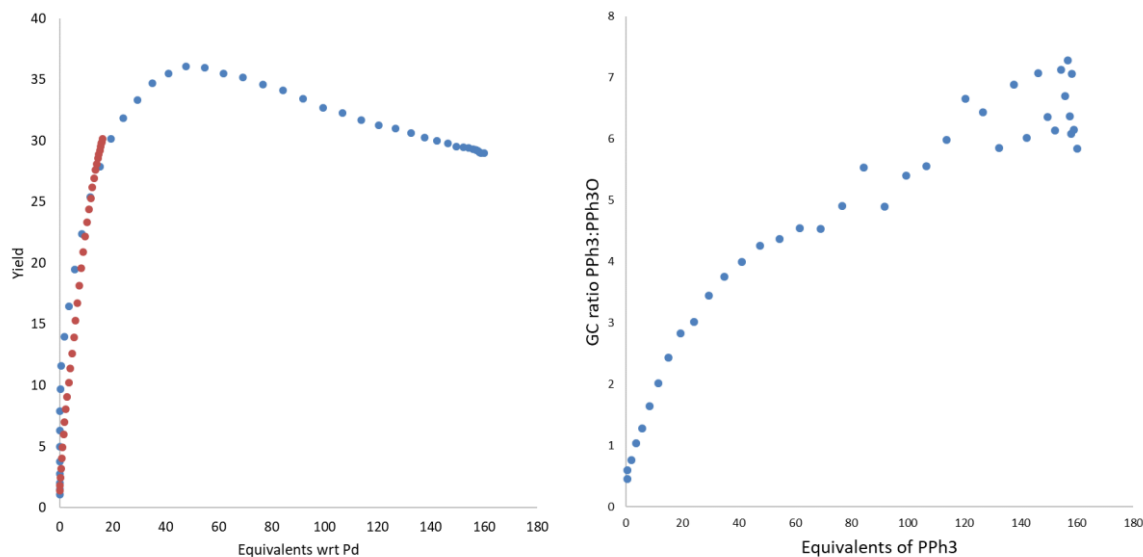


Figure 4.32: Left = Overlay of two concentration gradient experiments varying the maximum equivalents of  $\text{PPh}_3$ . Maximum yield is reached at 47 equivalents of  $\text{PPh}_3$ . Reaction conditions are from Scheme 4.5.  
Right = Uncalibrated GC ratio of  $\text{PPh}_3$ : $\text{PPh}_3\text{O}$ . There is always an excess of  $\text{PPh}_3$  compared to the oxide.

As seen with the hexane overlaps for the Heck coupling, overlap between the beginning of the 160-equivalent curve with the 16-equivalent gradient is representative of the correct trend however it is lacking in accuracy.

### 4.4.3.1.3 Validation

The 160-equivalent gradient was repeated utilising a slight variant in the flow rate ramp method described earlier. Rather than the pumps directly pulling from a reservoir of starting material, the  $\text{PPh}_3$  is introduced *via* a sample loop on one of the HPLC lines (Figure 4.33).



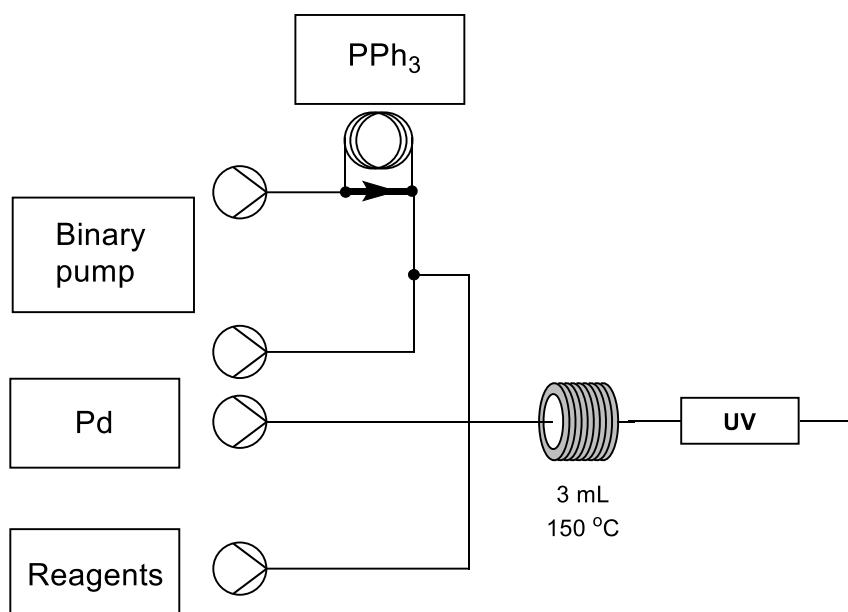


Figure 4.33: Flow setup for generating a  $\text{PPh}_3$  concentration gradient using a flow rate change. The ratio of flow rates on the binary pump lines vary to create a concentration gradient of  $\text{PPh}_3$  analogous to the one created by the dispersion methodology.

The overlap between the flow rate ramp method and the dispersion method (Figure 4.34) is good however the differences here are larger than with the Heck reaction (5% yield differences) this is most likely due to a small deposition of Pd onto the walls of the stainless steel reactor, as whilst all efforts were made to clean the reactor, it is difficult to ensure all of the Pd has been removed without causing damage to the reactor or flow system.

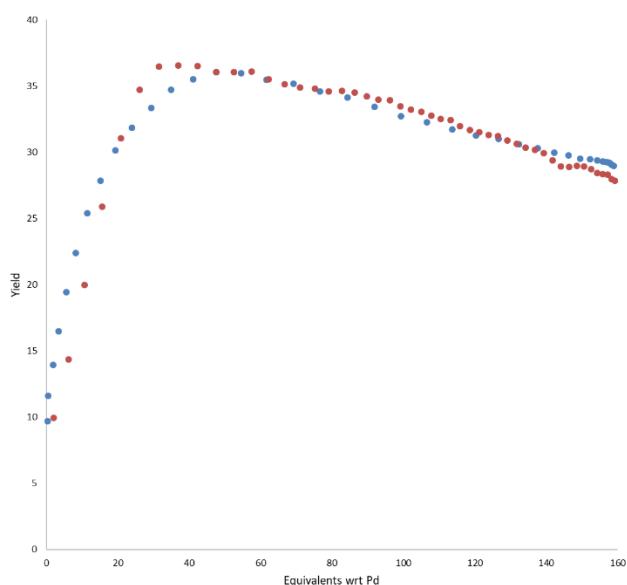


Figure 4.34: Overlap of yield generated from a dispersion and a flow rate concentration gradient reaction. Curves show same overall trend of increasing yield with increasing amounts

of ligand until a maximum is reached near 40 equivalents. Reaction conditions are from Scheme 4.5. Red = HPLC. Blue = Dispersion

#### 4.4.3.2 Modification to the phenyl ring: tolyl and alkyl phosphines

Tri(o-tolyl), tri(p-tolyl) phosphine, methyldiphenylphosphine and ethyldiphenylphosphine were all tested using the concentration gradient method. The results (Figure 4.35) show only a small increase in reactivity for o-tolyl suggesting that the palladacycles formed when using this ligand, are unreactive under these reaction conditions. The p-tolyl example does generate a slightly higher yield than  $\text{PPh}_3$  and at a slightly lower equivalents (47 to 44) perhaps due to the small increase in steric bulk and the increased electron density from the additional methyl group. Methyl and ethyl diphenylphosphine both give lower yields than  $\text{PPh}_3$  with the latter generating the higher yield of the two, which also suggests the positive influence of bulk and electron density. The optimal equivalence is much lower with these ligands, 26 and 31 for methyl and ethyl respectively, and the rate of inhibition after the optimum is much faster than with any of the other tested ligands.

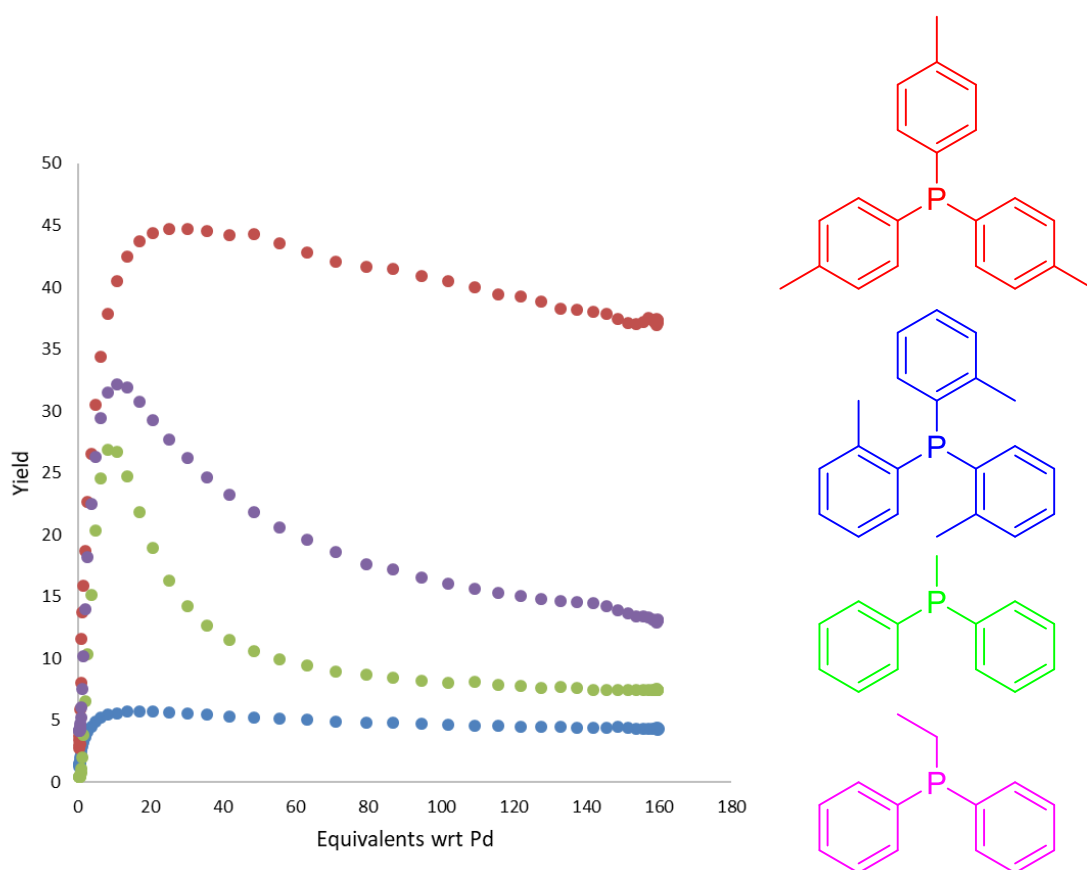


Figure 4.35: Yield from Sonogashira reaction at varying concentration of ligands. Reaction conditions are from Scheme 4.5.

#### 4.4.3.3 Bulky and electron rich: RuPhos and TTBP.HBF<sub>4</sub>

To probe the effect of steric bulk and electron density, RuPhos and TTBP.HBF<sub>4</sub> were tested as both TTBP.HBF<sub>4</sub> and RuPhos have been utilised in the Cu-free Sonogashira coupling as mentioned above. However, despite the literature precedence TTBP.HBF<sub>4</sub> only provided a maximum yield of 3% at 3 equivalents, initial concerns were whether the base was strong enough to form the TTBP ligand *in situ* however the pK<sub>a</sub> is 11.4<sup>298</sup> and other sources in the literature have used DBU to activate the ligand<sup>299</sup> so this was not the issue. The issue appears to arise from the Pd source used, as the previously mentioned paper<sup>292</sup> only saw increased yields with TTBP when using PdCl<sub>2</sub>(PPh<sub>3</sub>)<sub>2</sub> as the Pd source, and <5% yield when using Pd(OAc)<sub>2</sub> which matches with the results seen here (Figure 4.36).

RuPhos generates a higher yield than TTBP.HBF<sub>4</sub> however falls far below the maximum achieved by p-tolyl and triphenylphosphine. The point of maximum inhibition was not reached with RuPhos due to poor solubility prohibiting experimentation at the high concentration needed.

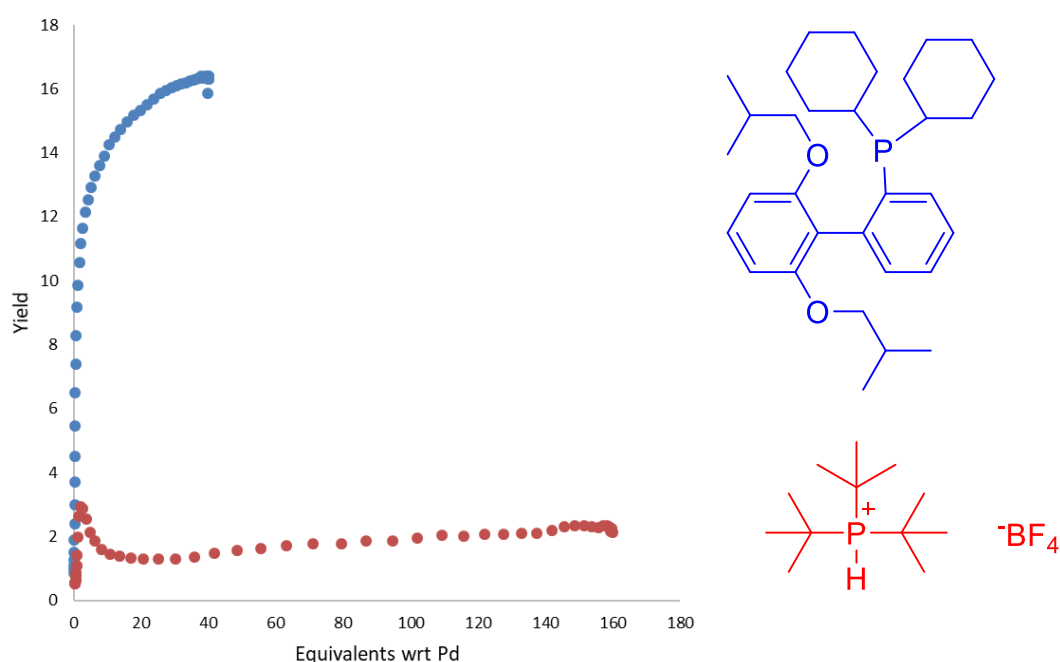


Figure 4.36: Yield from Sonogashira reaction at varying concentration of ligands. RuPhos was not taken to as high a concentration as the other tested ligands due to solubility issues in DMF. Reaction conditions are from Scheme 4.5.

The difference in activity between the literature and the results found here could also be due to the reaction occurring on the surface of the steel changing the optimal ligand requirements.

#### 4.4.3.4 Heterocycle containing ligands

By changing the nature of the group attached to the phosphine, it is possible to dramatically vary the electronics of the phosphine ligand. Exchanging phenyl groups for 2-furyl groups decrease the sigma bond donating capability of the phosphine<sup>300</sup> but increasing the  $\pi$ -accepting ability of the phosphine. Which can lead to stronger binding to Pd(0) complexes compared to PPh<sub>3</sub> but weaker to Pd(II) which may aid the reactivity<sup>301</sup>.

Similarly exchanging a phenyl group for a pyridyl will affect the sterics of the ligand and allow the ligand to act as both a monodentate and bidentate ligand<sup>302</sup> with the pyridyl group acting as a labile ligand.

Concentration gradients of bis(2-furyl)phenylphosphine and tri(2-furyl)phosphine show an overall lower yield than that of PPh<sub>3</sub>, with tri(2-furyl)phosphine having a slightly higher yield than bis(2-furyl)phenylphosphine (Figure 4.37). However, the optimal equivalents for both compounds is much higher than that of PPh<sub>3</sub> suggesting that increased  $\sigma$ -bond character lowers the maximum concentration needed to reach the optimum of the reaction. Additionally there is a lack of a distinct peak with tri(2-furyl)phosphine which may also be caused by this decrease in  $\sigma$ -bond character.

Diphenyl-2-pyridyl phosphine was also tested and showed an increased yield over PPh<sub>3</sub> reaching a maximum of 44% at 72.5 equivalents. The increase in equivalents needed to reach maximum yield is somewhat surprising as if the ligand were acting as a bidentate ligand, it should take a lower concentration to occupy the ligand binding sites compared to the monodentate PPh<sub>3</sub>. Therefore, the nitrogen is likely very labile in this system if it acts at all as a ligand.

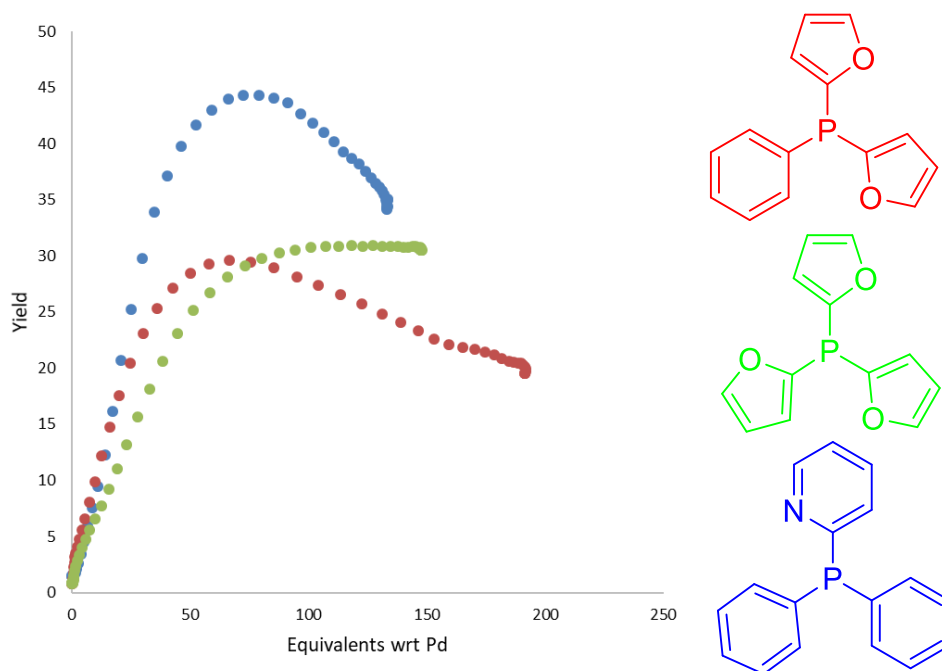


Figure 4.37: Yield from Sonogashira reaction at varying concentration of ligands. Diphenyl-2-pyridyl phosphine reaches the highest yield seen in these groups of gradient experiments. Reaction conditions are from Scheme 4.5.

#### 4.4.3.5 Bidentate ligands

With the surprising result obtained from the bidentate diphenyl-2-pyridyl phosphine ligand, a series of traditional bidentate ligands were tested. Dppm, dppe, dppp, dppb, dppf and XantPhos were all tested using the concentration gradient method (Figure 4.38). As expected, the optimum equivalents for these ligands is much lower than the monodentate ligands with dppm, dppe, dppp and dppb all reaching their maximum below 5 equivalents.

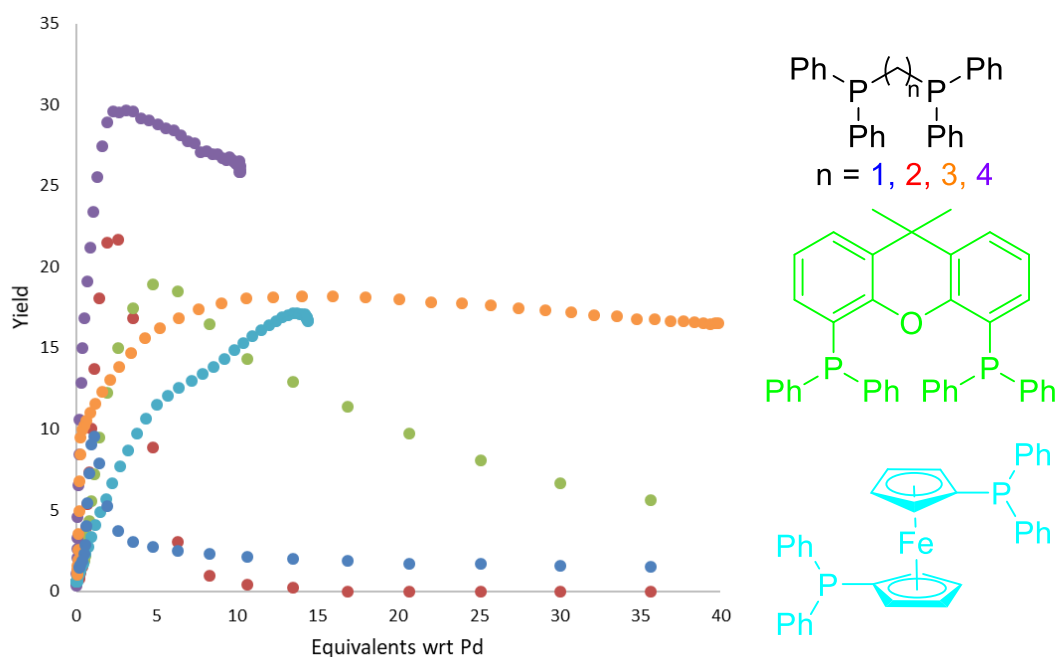
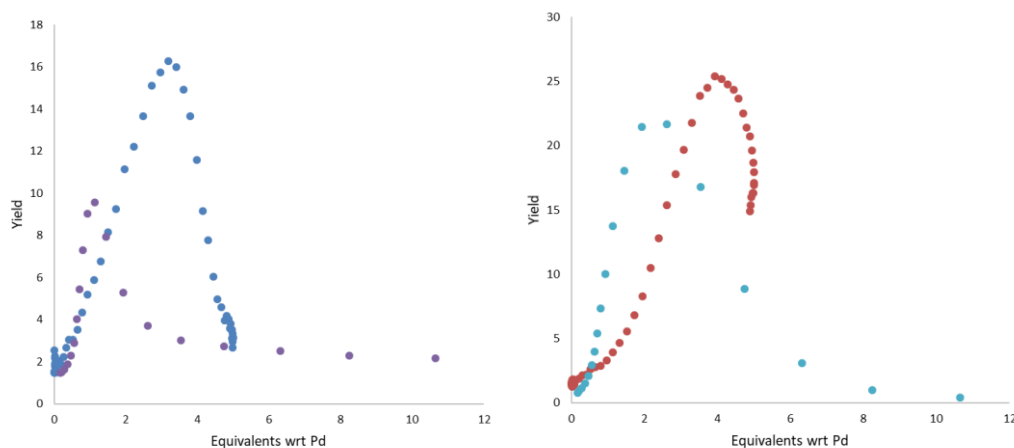


Figure 4.38: Yield from Sonogashira reaction at varying concentration of ligands. General trend of increasing chain length and increasing yield. Reaction conditions are from Scheme 4.5.

As the dppx type ligands reach their optimal concentrations at very low equivalents where the error from dispersion is the highest, the concentration gradients for dppm, dppe, and dppp were all repeated with a low maximum concentration of 5 equivalents (Figure 4.39). The similarities between the two gradients for dppe and dppp are good with an expected level of variance from the averaging in of steady states from the higher concentration gradient. However, the results for dppm are quite different with the lower concentration gradient appearing closer to a bell shape curve, where the previous experiment had an exponential inhibition curve after the optimal concentration. The difference may be due to the averaging effects however as this large difference is not seen on any of the other examples, another effect must also be present, however this is not currently known.



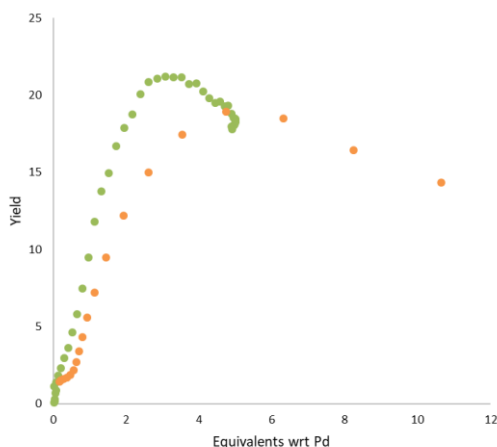


Figure 4.39: Overlay of initial ligand concentration gradients with 5-equivalents maximum repeat experiments. Reaction conditions are from Scheme 4.5. Top left = DPPM. Top right = DPPE. Bottom = DPPP

A plot of the ligand bite angles<sup>303–305</sup> against yield (Figure 4.40) shows a curve with a maximum of around 90°. All tested ligands follow this general trend with the exception of dppp. Different structural geometries of the metal complex prefer different bite angles of ligands<sup>306</sup>, the optimal bite angle of 90° seen here suggests either an octahedral or square-planar complex<sup>303</sup> is a major part of the catalytic cycle. A similar bite angle effect has been previously reported<sup>307</sup> for the palladium coupling of sec-butyl magnesium chloride with bromobenzene, which had an optimal bite angle of 102.7°.

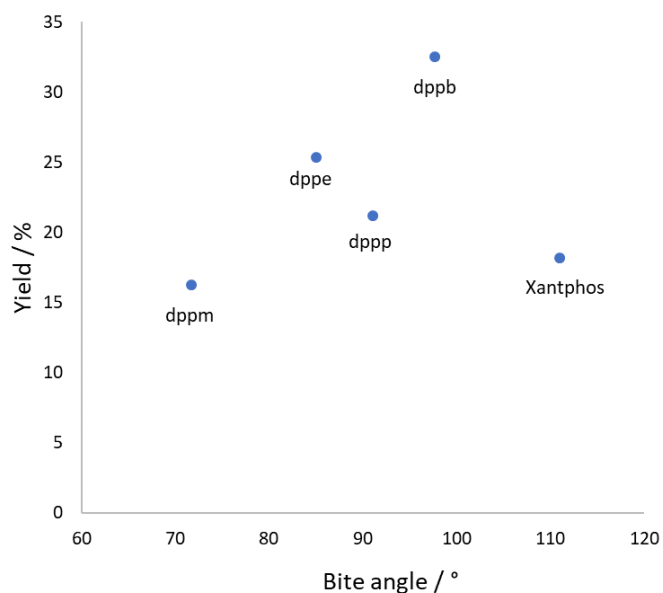


Figure 4.40: Bite angle of the tested ligands against maximum yields obtained from concentration gradient reactions. DPPF removed as maximum yield was not reached during the reaction.

If the same plot is made using the cone angles<sup>300,308,309</sup> of the monodentate ligands (Figure 4.41), there appears to be less of an obvious effect compared to the bidentate ligands. However, the results are grouped into two vertical groups, the bulky electron rich ligands and the remaining ligands, suggesting that a low cone angle, electron poor ligand may perform well in this reaction.

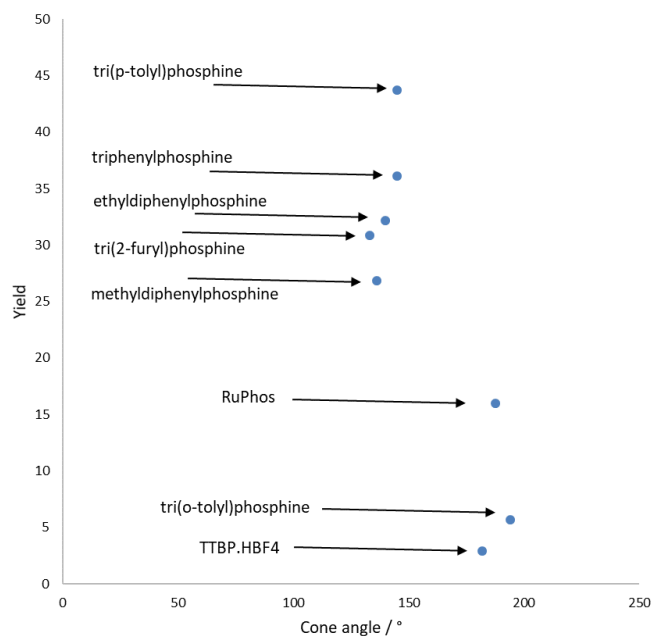


Figure 4.41: Cone angle of tested ligands against maximum obtained yield from concentration gradient experiments.



#### 4.4.4 Increasing yield

Whilst the data obtained currently is useful, the maximum yield obtained is quite low. Thus, a method to increase the yield was sought which would be compatible with the concentration gradient method to investigate whether the excess ligand effects seen above accelerate the rate of the reaction or if the excess is necessary to reach the higher yields.

There are two main methods for increasing the yield of a reaction in flow. Increasing the reaction temperature and increasing the residence time. For this reaction, increasing the temperature above the current 150 °C is not possible due to decomposition of starting materials which leaves increasing the residence time as the best option.

The residence time is dependent on the flow rate and the volume of the reactor use however if the flow rate is changed, then the amount of dispersion which occurs in the dispersion coil will also change and dispersion profiles will have to be reperformed for each time point. Whilst this is possible, it will increase the time taken to obtain results.

Changing the reactor volume will not affect the gradient generation but will affect the overlaying of the dispersion profile with the reaction data. So new steady state reactions or a total flow setup dispersion profile will need to be performed for each reaction time point.

For this reaction, the pump flow rate was already set at the minimum acceptable value of 0.1 mL/min for each of the pumps, so reactor volume was the only option.

The reactor volume was doubled from 3 to 6 mL corresponding to an increase to 20 minutes reaction time.

##### 4.4.4.1 $\text{PPh}_3$

Increasing the reaction time when using  $\text{PPh}_3$ , causes a corresponding increase in yield (Figure 4.42) bringing the maximum obtained up to 72% from 36% yield, with the same maximum equivalents. Interestingly, this increase is not uniform across the equivalents tested as above 24 equivalents there is a constant 2x increase in the obtained yield, but below 24 equivalents, there is a linear decrease until almost no benefit is seen at the very low loadings of  $\text{PPh}_3$ .

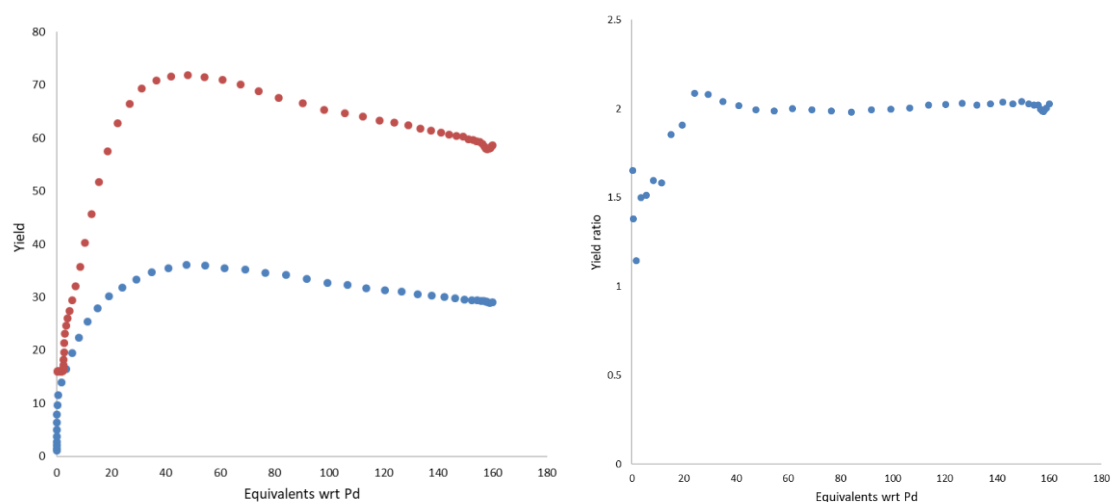


Figure 4.42: Reaction conditions are from Scheme 4.5 apart from varying reaction time.

Left = Overlay of initial 10 minute and 20 minute reactions. Right = Ratio of yields from the two experiments at different concentrations of ligand

#### 4.4.4.2 Tri(o-tolyl)phosphine

A similar result is seen with tri(o-tolyl)phosphine (Figure 4.43) with a nearly constant 2x increase in yield above a set concentration (6 equivalents in this case). However, where this varies is that below this level, there is an increase in the ratio of yields rather than the decrease seen for  $\text{PPh}_3$ , this may be due to dispersive effects generating error in the low values, equally at these low values of yield, a small error will have a larger effect.

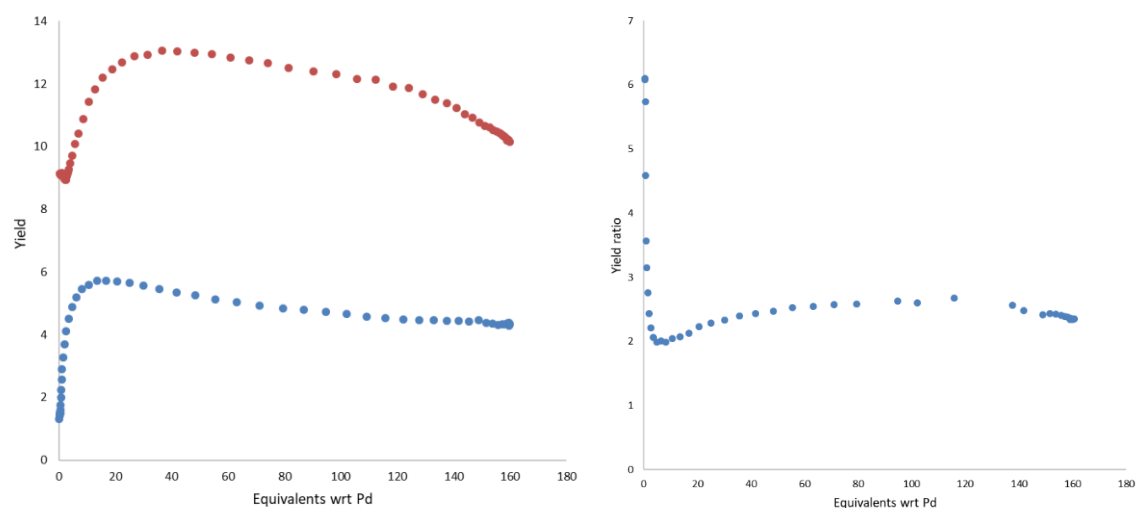


Figure 4.43: Reaction conditions are from Scheme 4.5 apart from varying reaction time.

Left = Overlay of initial 10 minute and 20 minute reactions. Right = Ratio of yields from the two experiments at different concentrations of ligand. The large increase in the ratio of yields at low equivalents of ligand is most likely due to the averaging effect caused by dispersion.

#### 4.4.4.3 Tri(p-tolyl)phosphine

Tri(p-tolyl)phosphine again shows the same trend as  $\text{PPh}_3$  of around 2x yield improvement above 70 equivalents with a linear decrease below that (Figure 4.44). Of note is that again at very low concentrations the yield ratio increases dramatically suggesting that if it is an error it is a systematic one. The equivalents needed for optimal concentration increases by a factor of 5 to 100 equivalents, suggesting that the higher amounts are needed to reach the highest yields in this setup rather than just increasing the rate. Before 40 equivalents, the longer reaction time generates a lower yield than the shorter reaction. The reason for this could be due to instability of the product at the longer reaction time however, as this does not occur with every experiment, it is unlikely to be the cause.

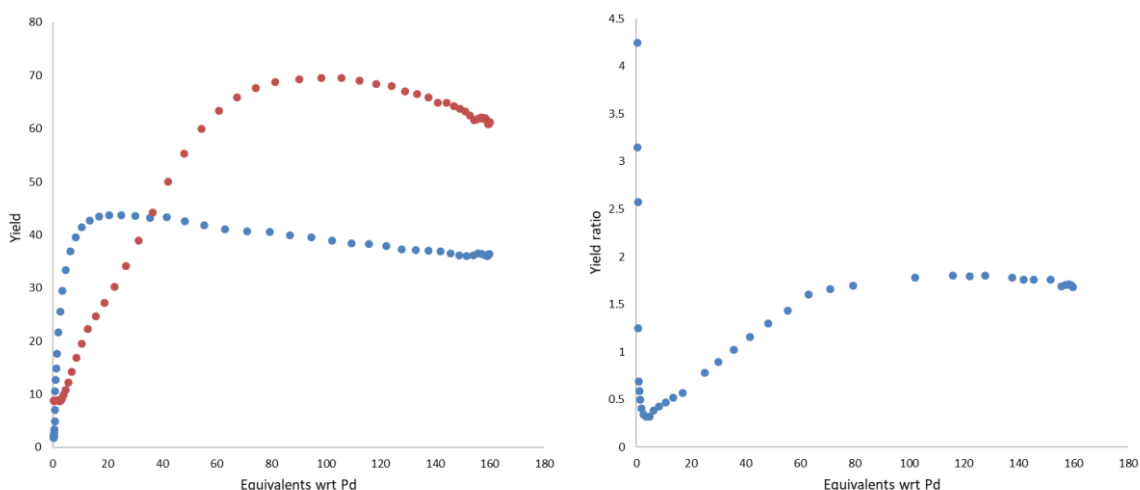


Figure 4.44: Reaction conditions are from Scheme 4.5 apart from varying reaction time.

Left = Overlay of initial 10 minute and 20 minute reactions. Right = Ratio of yields from the two experiments at different concentrations of ligand. The large increase in the ratio of yields at low equivalents of ligand is most likely due to the averaging effect caused by dispersion.

#### 4.4.4.4 DPPB

DPPB gives an almost identical trend to that of tri(p-tolyl)phosphine with a linear decrease in reactivity below 8 equivalents and 2x the yield of the 10 minute reaction above (Figure 4.45). The increase in the optimal equivalents is also seen with a 4x increase to 8 equivalents needed.

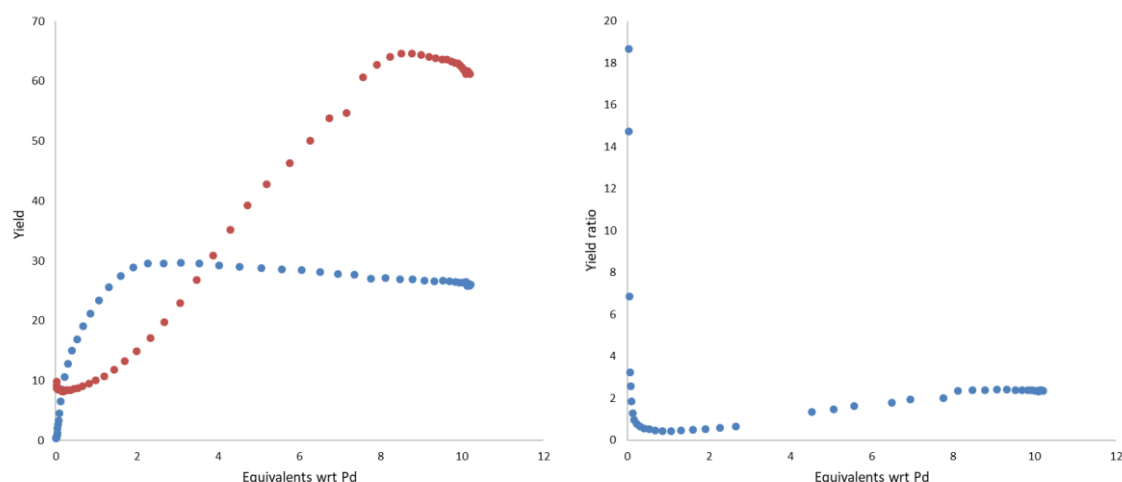


Figure 4.45: Reaction conditions are from Scheme 4.5 apart from varying reaction time.

Left = Overlay of initial 10 minute and 20 minute reactions. Right = Ratio of yields from the two experiments at different concentrations of ligand. The large increase in the ratio of yields at low equivalents of ligand is most likely due to the averaging effect caused by dispersion.

Whilst the yield is still not as high as it could be, further increases in reaction time will present more problems due to averaging errors caused by dispersion. As such, finding the optimal yield at this point would be more suited to traditional steady state methods and thus will not be pursued in this thesis.

## 4.5 Summary

Taylor dispersion has been utilised to create in-line concentration gradients of reagents for the rapid optimisation and probing of reaction conditions.

The use of this methodology allows a large amount of concentration information to be extracted in a single experiment. To extract an equivalent amount of data using traditional steady state would take tens to hundreds of experiments, demonstrating a saving of a large portion of time and resources when using the concentration gradient methodology.

The data extracted using this technique can be utilised in the optimisation of reagent concentration, ligand and additive testing, impurity probing, acid/base stability of compounds, and the extraction of kinetic data.

The use of dispersion, rather than a flow rate ramp, to generate concentration gradients allows access to this methodology at a low cost, as it only requires additional tubing rather than an additional pump capable of changing flow rate automatically.

The validity of the dispersion generated concentration gradients were tested by comparison with gradients generated using traditional flow rate ratio changes common with HPLC methodologies. A maximum of 5% difference in generated yield was observed between the two gradient generation techniques.

In this thesis, the methodology was tested on two examples:

1. The Heck cross coupling reaction.  
The Pd source and the effect of ligands were probed. Additionally, the methodology was combined with a rapid reaction scope method to probe inhibition by various functional groups.
2. The copper-free Sonogashira cross coupling reaction.  
The effect of various ligands on the reaction was tested and it was found that a large excess of monodentate ligands was required to reach the maximum yield for the reaction. Two reaction times were tested which began to introduce a limitation in the methodology, in that in order to change reaction time, re-calibration of the dispersion profile is necessary for each time point wanted.

## Chapter 5 Multi time point generation

### 5.1 Introduction

In the previous chapter, a method to obtain reaction information on the effect of varying concentration in a single experiment using a concentration gradient was detailed. However, the information could only be obtained for a single time point. In this chapter, multiple time points are obtained in one reaction by continuously circulating the reaction mixture through a detector (Figure 5.1).

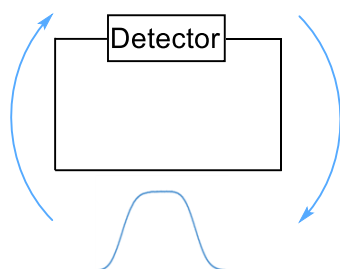


Figure 5.1: Simplified graphical depiction of plug circulation to generate multiple time points with in-line detection. The plug is repeatedly pumped through an in-line monitoring device to generate several time points.

The circulation of the reaction mixture could be accomplished easily using a peristaltic pump, however these pumps tend to only be capable of low pressure operation<sup>41</sup> which can limit the range of conditions able to be tested. Additionally, as most commercial flow systems utilise the HPLC style pumps, a universal method which could work on any flow system would be preferred.

The circulation was achieved through the use of a continuously pumped solvent stream to drive the circulation, with 2-position valves to manipulate the direction of the plug. Two main designs were created which will be discussed here.

### 5.2 Reciprocating flow

The first method directs the plug through the detector and then reverses the flow direction sending the plug back through the detector generating an additional time point. These steps can then be repeated until the desired reaction time is reached removing the flow rate dependence from the reaction time.

### 5.2.1 Method

To achieve this a 10-port, 2 position valve was used setup as shown below (Figure 5.2) with two reactors placed either side of a detector. The plug initially flows through the system as in a traditional flow reaction but after the plug has passed through the detector, the valve switches to the other mode which reverses the overall direction of the flow, passing the plug back through the detector generating another time point. The process can then be repeated.

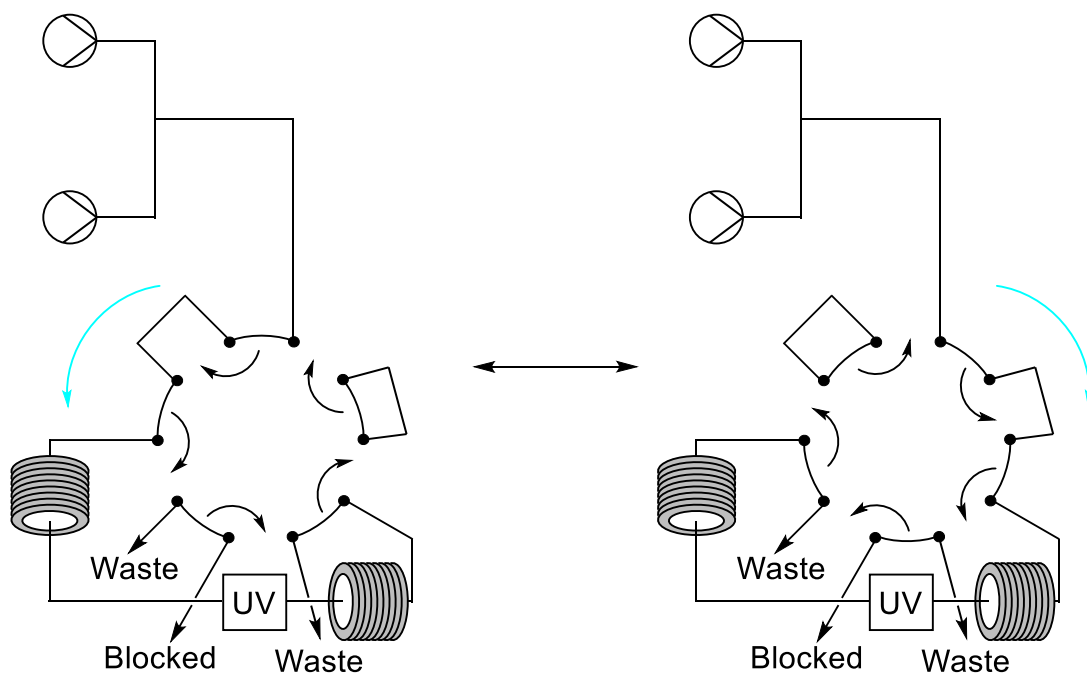


Figure 5.2: Valve setup for reciprocating a plug through a detector by changing the direction of the flow. The blue line indicates the direction of the flow. Valve is switched after the plug has passed through the detector which has the effect of reversing the direction of flow of the plug.

The reactors on either side of the detector must be larger than the starting reaction plug as they will have to contain the entire plug before the flow direction is flipped.

### 5.2.2 Results

#### 5.2.2.1 Cancelling dispersion

As the plug travels through the reactor it will undergo dispersion. It was hypothesised that when the direction of the flow is reversed, the dispersion will occur in the opposite direction to that of the initial dispersion, cancelling it out and reverting to the starting plug.

## Chapter 5

To test this a dispersion profile was performed on the reciprocating system for a set reaction time and then comparing to a dispersion profile of correct volume to generate an equal maximum reaction time.

Unfortunately, upon overlaying the two dispersion profiles it was clear that no cancelling out of dispersion was happening (Figure 5.3). The lack of difference means that the speed of reversing the flow is much slower than the speed at which the laminar flow layers are mixed, through diffusion and Dean circulation. The mixing of layers results in dispersions that are additive resulting in the same result as if the plug had passed through an equivalent reactor normally.

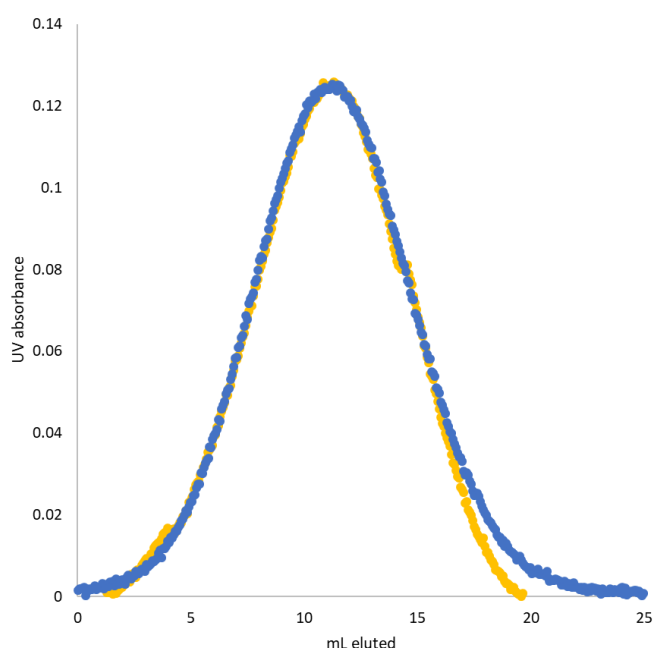


Figure 5.3: Overlap of final pass through of a reciprocating flow method with an equivalent length standard reactor. Both methods overlap showing there is no cancelling out of dispersion when the flow direction is reversed.

### 5.2.2.2 Reactor and condition choice

For this methodology, the first time point collected, and the rate of time point collection, are related to the flow rate. Increasing the flow rate decreases the time for the first monitoring and increases the rate of collection. As such obtaining a high as flow rate as possible is important for this methodology.

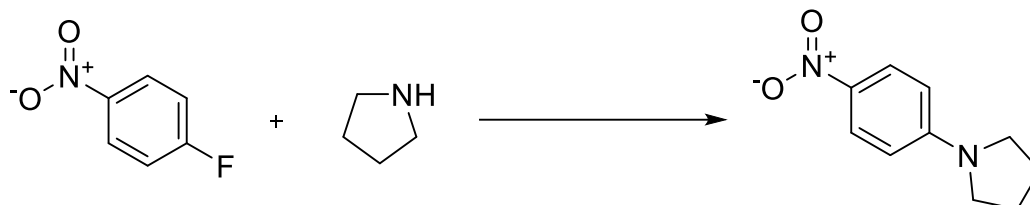
For this section, 2 mL/min is used which means that a low dispersion reactor must be used in order to maintain the steady state of the reaction mixture for as long as possible, in this case 11.1 mL of glass bead filled reactor were placed either side of the detector.



A larger starting plug could also be used with a traditional reactor to 'brute force' the maintaining of the steady state however, this would then require larger reactors for the setup which would increase the time before the first data point and also increase dispersion.

### 5.2.2.3 Reaction test: Steady state

To test the methodology, the  $S_NAr$  reaction of 1-fluoro-4-nitrobenzene and pyrrolidine (Scheme 5.1) was used due to the ease of monitoring *via* UV-Vis spectroscopy.



Scheme 5.1:  $S_NAr$  reaction of 1-fluoro-4-nitrobenzene and pyrrolidine

### 5.2.2.4 Manual control

#### 5.2.2.4.1 Dispersion profile

Initially a dispersion profile was performed to measure when the plug had completely passed through the detector in order to time the switching of the valves correctly. A 5 mL plug was used and the dispersion profile was passed through the system for 2 hours after which it was allowed to flow to waste. The steady state at this point was still significantly large and the profile could have been continued, however as it was being obtained manually it was stopped here. The reaction was then tested with the valves being switched at the time points obtained from the dispersion profile.

#### 5.2.2.4.2 Data handling and results

When looking at the raw UV data, it is separated into each time the plug passes through the detector and consists of the steady state portion of the plug and the non-steady state portions either side.

The non-steady state portions are removed by overlaying the previously recorded dispersion profile with the in-line data. The areas on the experimental data which do not line up with the steady state of the dispersion profile are deleted leaving only the steady states of the plug. (Figure 5.4)

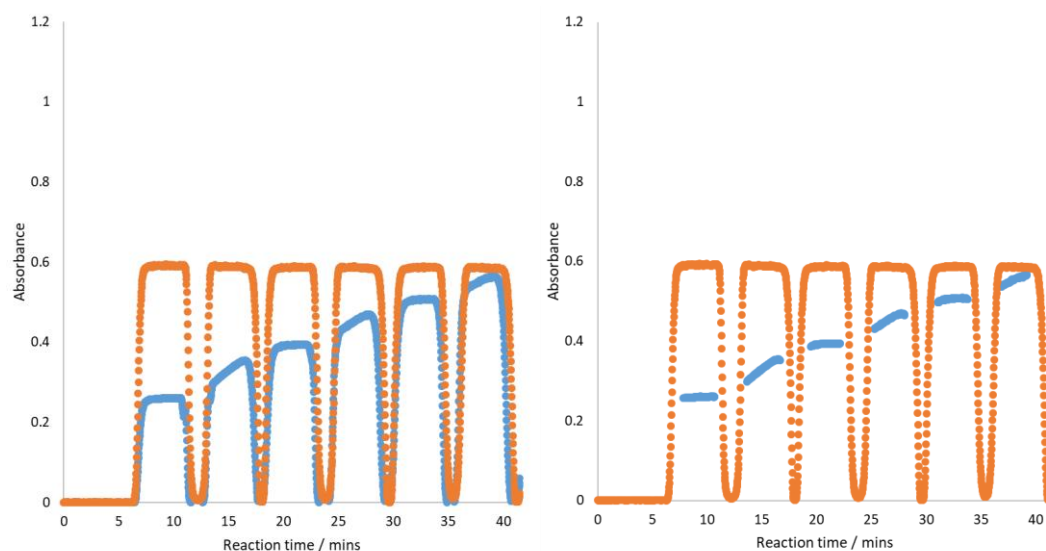


Figure 5.4: Left = Raw UV data from  $S_NAr$  reaction overlaid with the dispersion profile. Right = UV data post data manipulation. The alternating gradient and steady state reaction time measurements are caused by the reversal of plug flow direction causing a varying residence time in the reactor across the length of the plug. Reaction conditions are from 7.2.4.1

For the first pass through, the entire plug has spent the same amount of time in the reactor when it travels through the detector. However, on reversal of the flow, the first reaction mixture through will have only had one reactor's worth of reaction time, whereas the last through will have had two. Therefore, a residence time gradient is monitored for the reverse flow pass throughs.

Once the flow is returned to its original direction, a single time point is monitored for the entire plug again, which is seen in the above figure as every other pass through has a single absorbance whereas the others have absorbance ramps corresponding to the increasing reaction time monitored.

The reaction time for each pass through must then be calibrated by either calculating when the plug should be entering the detector using the volume and flow rate. Otherwise by taking the first time point when the plug is detected as the first time point for that pass through. For the non-time gradient pass throughs, this time point is the same for the whole plug but for the time gradient pass throughs, the time increase measured from the in-line monitoring can be used. The absorbance can then be converted to yield using a calibration curve generating the reaction time/yield graph (Figure 5.5)

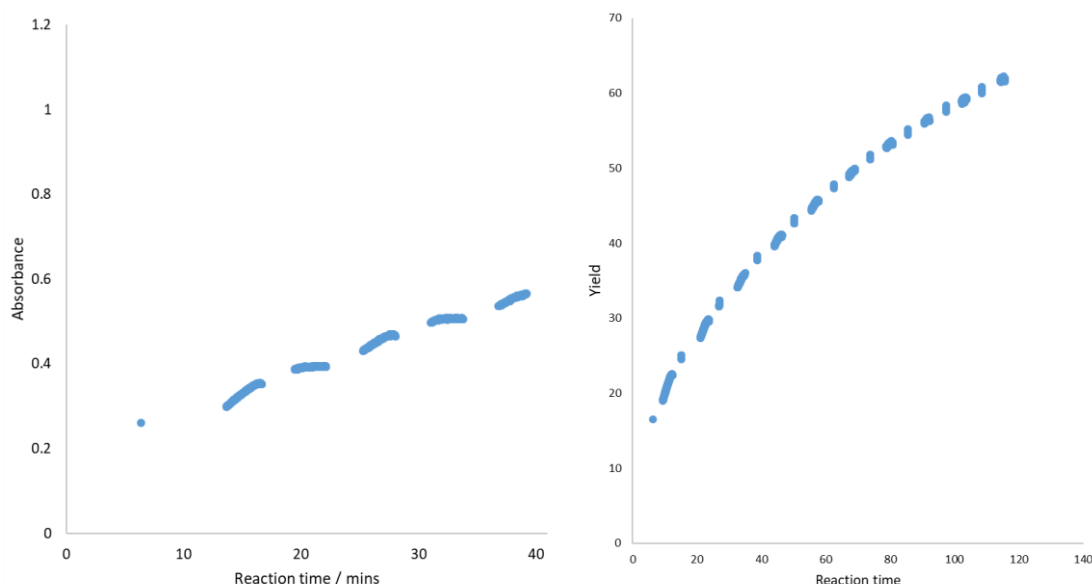


Figure 5.5: Left = UV data post data manipulation. Right = Absorbance converted to yield and reaction time calculated for pass throughs. Yield is calculated from a UV calibration curve. Reaction conditions are from 7.2.4.1

For the non-time gradient pass throughs, all the points do not give the same yield. The reason for this is due to error in the UV measuring and inclusion of non-steady state portions of the pass through due to inaccurate removal. However, a good curve is still obtained with a maximum yield of 61% after 115 minutes of reaction time, with all data obtained from a single experiment.

#### 5.2.2.4.3 Automated control

To overcome this, flow chemistry's ease of automation was applied, and a simple Python script was created to automate the switching of the valves. The switching times calculated from the manual dispersion profile were used to automate a second longer dispersion profile, and then perform the experiment.

The data handling was also automated, with a Python script looking at the difference between the absorbance values of the dispersion profile. When the difference increased above a set value, the dispersion profile would no longer be in the steady state and the Python script started the removal of that data, leaving only the steady state data behind. The yield could then be calculated as before generating the reaction time/yield graph (Figure 5.6).

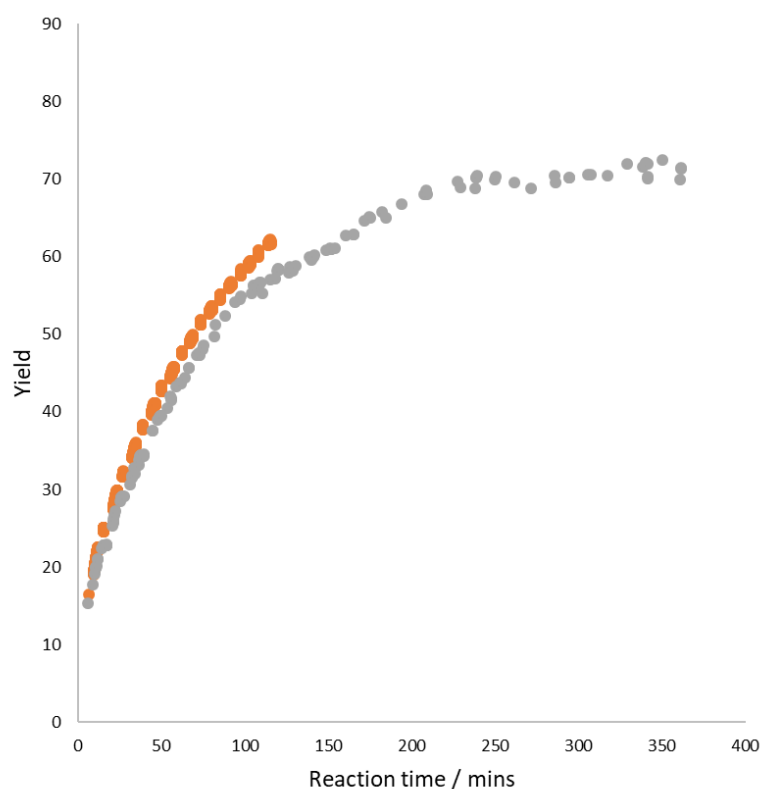


Figure 5.6: Overlaid results from manual and automated reciprocating experiments. Reaction conditions are from 7.2.4.1. Orange = manual. Grey = automated

There is a difference between the manual and automated graphs, however this is due to either differences in temperature between the reactions or errors in the set-up of the reaction rather than differences caused by the change in methodology. Overall switching to the automated methodology saved 6 hours of experimental time which could be utilised elsewhere and 1 hour of data handling time.

### 5.2.3 Disadvantages

In its current design, the methodology relies on the use of in-line monitoring to function, this means that it will only work on reactions capable of being monitored by the devices that you own. Whilst a design could be envisaged which collects samples for offline HPLC or GC monitoring before recirculating the remaining reaction mixture, this is limited in that it will remove portions of the steady state lowering the maximum reaction time for the system.

Additionally, whilst it is possible to combine this method with the concentration gradient method, the time gradients generated every other pass through complicate the data handling significantly compared to if it were a single time point each time.

The methodology is also limited in that the first time point comes after the reaction mixture has passed through a reactor which means that no  $t_0$  time point is generated which can be useful in kinetics. The use of two switching valves can allow for  $t_0$  measurements (Figure 5.7) however this increases the cost of the methodology.

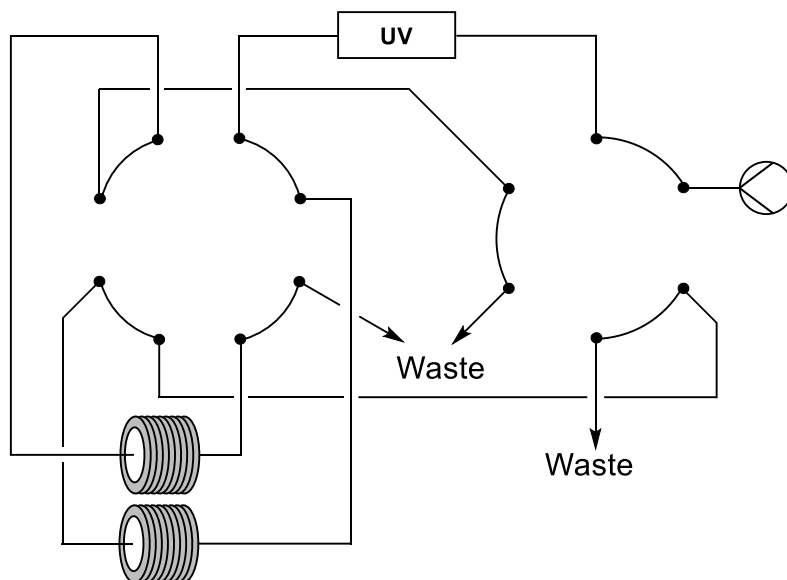


Figure 5.7: Valve setup for obtaining a  $t_0$  time point using the reciprocating flow. The additional 6-port valve allows the plug to initially be pumped directly into the monitoring device generating the  $t_0$  data point.

#### 5.2.4 Summary

The reciprocating flow methodology is a simple method which allows the generation of a reaction time/yield graph in a single flow experiment. It achieves this without the use of changing flow rates, making it a universally applicable methodology requiring only an in-line monitoring device and a monitorable reaction.

### 5.3 Non-reciprocating flow

The time gradient generation originates from the reversal of the flow direction. Therefore, a method which recirculates the flow repeatedly through a detector without reversing the direction would generate the multiple time points required but with no time gradients on any pass throughs.

To accomplish this, 2-position valves were again utilised this time with a 6-port valve in addition to the 10-port valve seen previously.

The plug initially enters the 6-port valve and is directly channelled through the detector and into a reactor, this generates a  $t_0$  time point (Figure 5.8).

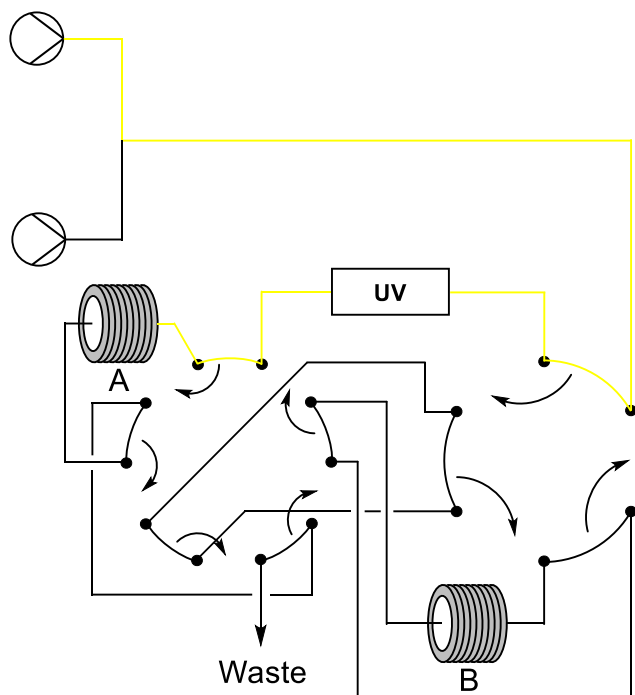


Figure 5.8: Initial valve setup for non-reciprocating multi time point methodology. The yellow lines indicates the path the plug takes from the starting round bottom flask, through the in-line detector and into reactor A.

Both valves are then switched and the plug is pumped through the detector again before entering into the second reactor generating the second time point (Figure 5.9).

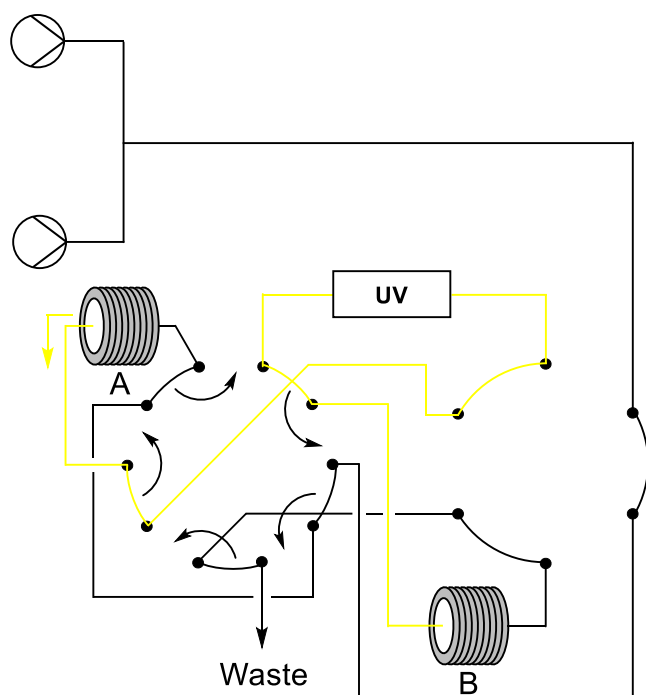


Figure 5.9: Second position for valve setup for non-reciprocating multi time point methodology.

The plug is pumped from A, through the in-line detector, and into reactor B. The yellow line indicates the plug travel path and direction.

The 10-port valve is then switched again, and the plug is directed through the detector and into the first reactor generating an additional time point. The 10-port can then be switched again which directs the plug back through the detector and into the second reactor generating another time point (Figure 5.10). These final two steps can then be repeated for the necessary reaction time, or until dispersion has spread the plug to an unusable level.

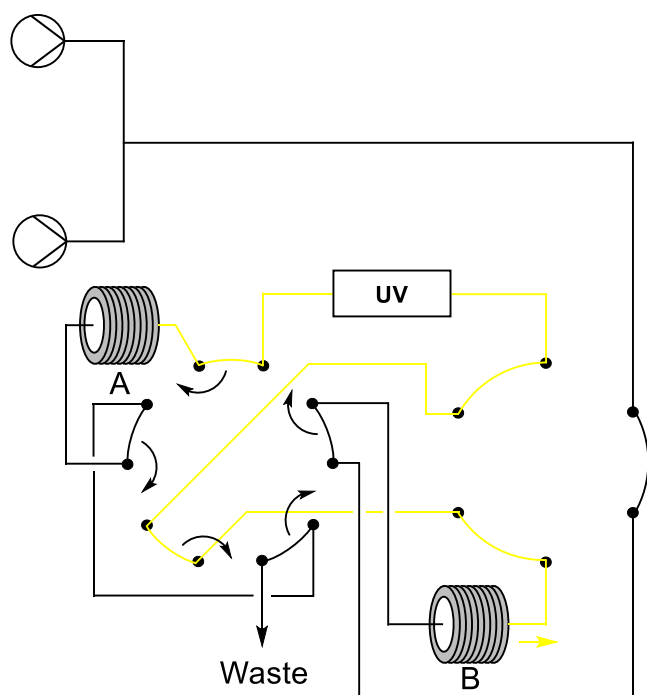


Figure 5.10: Third position for valve setup for non-reciprocating multi time point methodology.

The plug is pumped from reactor B, through the in-line detector, and into pump A. Throughout these valves switching, the plug is being pumped in a single direction maintaining the reaction time steady state across the plug. The yellow line indicates the plug travel path and direction.

### 5.3.1 Steady state reaction

The same  $S_NAr$  reaction used for the reciprocating methodology was utilised here as a test reaction with all valves controlled automatically. Data handling was identical to that of the reciprocating method however all pass throughs have consistent reaction times throughout the plug which is shown in the raw UV data having all flat steady state tops rather than the alternating ramps seen before (Figure 5.11).



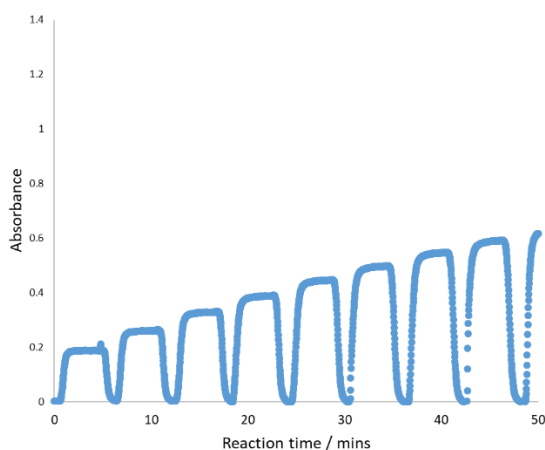


Figure 5.11: Raw UV data from non-reciprocating methodology. Every pass through has a steady state whereas the reciprocating method had alternating gradients and steady states.  
Reaction conditions from 7.2.4.2

Conversion of absorbance to yield and comparison to the reciprocating method shows a good overlap with a maximum difference of 3% yield (Figure 5.12).

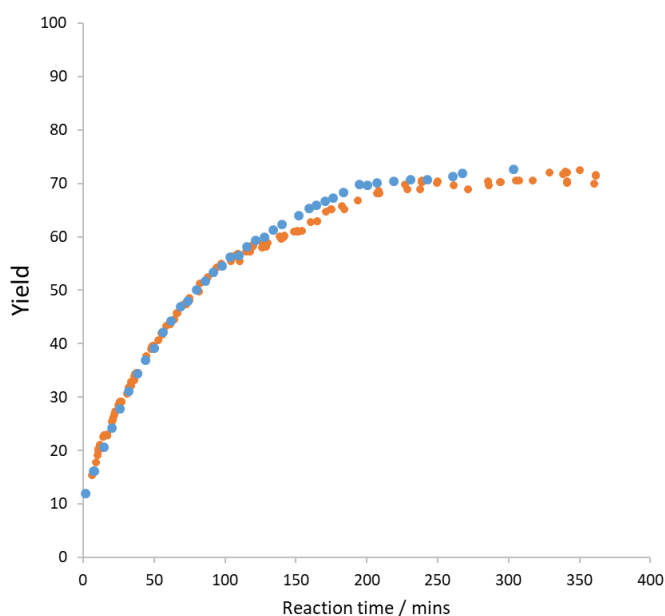


Figure 5.12: Overlay of reciprocating and non-reciprocating multi time point methods for the  $S_NAr$  reaction. Yields calculated from a UV calibration curve. Orange = reciprocating. Blue = Non-reciprocating

As the overlap between the methodologies is good and the time gradients observed in the reciprocating method are not present here, this demonstrates the usability of the non-reciprocating methodology for the combination with the concentration gradient method.

### 5.3.2 Single gradient multi time point

#### 5.3.2.1 Gradient generation and clipping

As with the standard concentration gradient method, a reagent must be dispersed in order for it to be converted from a steady state plug to a concentration gradient which means the addition of a dispersion coil to a reagent line. However, where the methods differ is that the size of the gradient is now limited to the size of one of the reactors. To minimise the averaging effects caused by post gradient dispersion, a shallow gradient is preferred so for this system filling one of the reactors with a single concentration gradient with a small amount of steady state is optimal. Unfortunately, due to the nature of Taylor dispersion, a front and back gradient are created when converting to a concentration gradient. The dispersion means that in the ideal situation, the overall plug size will be much larger than the reactor size which will cause averaging issues when the valves start switching as the front of the gradient plug will begin to mix with the back end of the plug.

To overcome this a steeper gradient or smaller plug size could be used, however this would minimise the maximum reaction time achievable and maximise the averaging errors. A better solution would be to separate the front gradient from the rest of the plug (Figure 5.13) and use that to generate the multi time points.

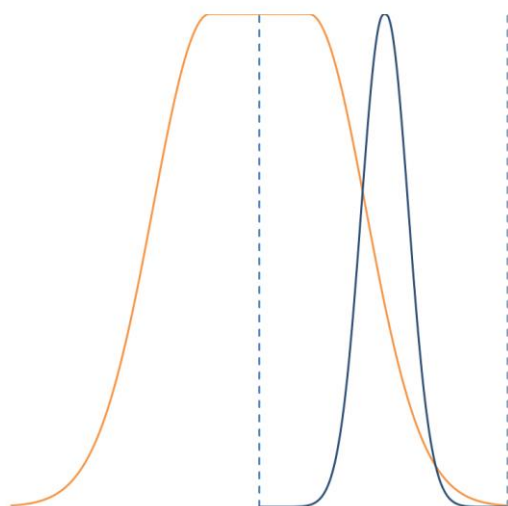


Figure 5.13: Graphical depiction of two methods for including a complete gradient in the multi time point setup. The small amount of steady state and overall plug size mean that the blue line would give averaging errors from dispersion quicker than the larger yellow plug. Blue dashed lines represent the volume of the reactor.

To accomplish this, a gradient clipping valve was introduced into the flow setup. The valve is configured with a 10 mL dispersion coil to generate the concentration gradient and once the front gradient has exited the valve (as measured by a dispersion profile), the valve is switched and the remainder is sent to waste but the front gradient can continue to the multi-time point setup (Figure 5.14).

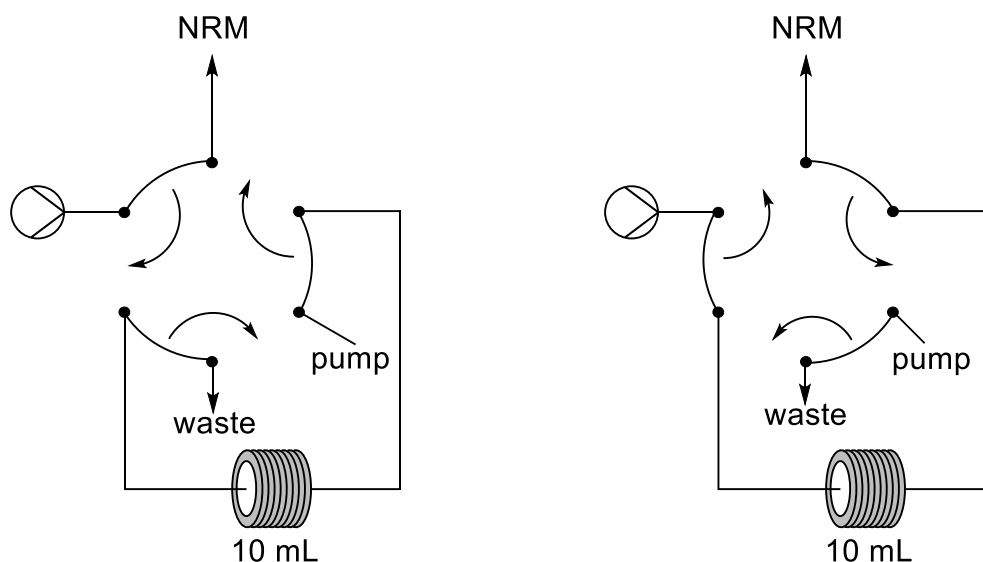


Figure 5.14: Valve setup for generation of a gradient and clipping of the front gradient from the remainder of the plug. By switching the valves at different times when the plug is exiting the dispersion coil, it is possible to change how much of the gradient is clipped and sent to waste.

Another important factor is ensuring a good overlap between the concentration gradient and the steady state reagents line. A delay will need to be placed on the steady state line related to the flow rate of the system and the volume of the dispersion coil. The system used for these experiments has a 10 mL dispersion coil and each pump is pumping at 1 mL/min, this requires a 3 mL delay to ensure a good overlap (Figure 5.15) which was determined experimentally by dispersion profiles.

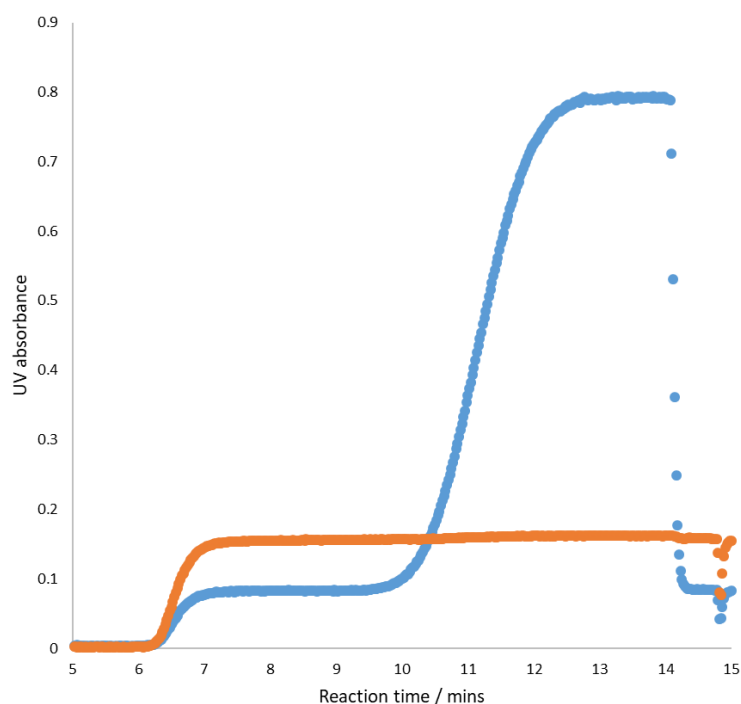


Figure 5.15: Dispersion profile demonstrating the overlap of clipped gradient (blue) and steady state reagent (orange).

Using these conditions, the reaction can be monitored for 180 minutes after which the steady state portion of the plug has completely dispersed into the gradient and the solvent (Figure 5.16). Monitoring can continue after this point however the data at the edges of the gradient must be discarded due to the averaging effect, with an increasing amount discarded as the reaction time increases.

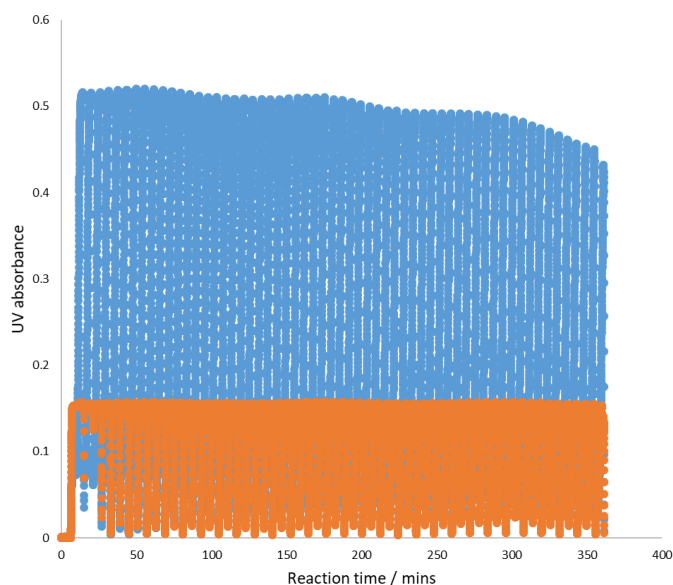


Figure 5.16: Automated dispersion profile. Steady state begins to decrease after 180 minutes due to dispersion of the gradient.

### 5.3.2.2 Results

The methodology was tested on the same  $S_NAr$  reaction with a gradient of pyrrolidine tested with a maximum of 15 equivalents. As before the valves were controlled automatically *via* a Python script with timings determined *via* a short dispersion profile. A raw UV output was generated in a manner similar to the steady state output however a concentration gradient of pyrrolidine is present across the top rather than a steady state (Figure 5.17)

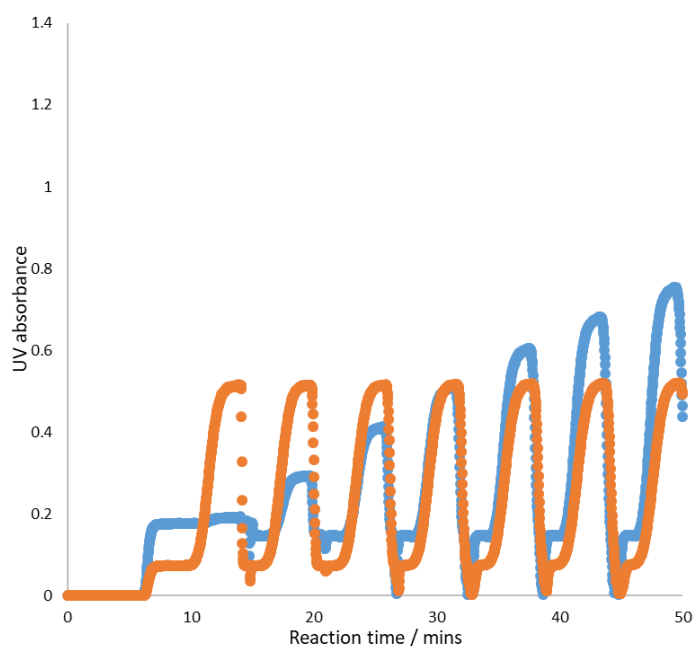


Figure 5.17: Raw UV data from the  $S_NAr$  experiment overlaid with the dispersion profile. Reaction conditions are from 7.2.4.3. Orange = Dispersion profile of the gradient. Blue = Raw UV data from experiment.

The data analysis is handled by a Python script, again looking at the differences between the absorbance on the dispersion profile however this time the script is removing data where the difference between the values is small and the absorbance itself less than 0.4, which removes the data which is not part of the concentration gradient or the maximum concentration steady state. The reaction time for each pass through can then be calibrated by equating each pass through times to that of the first time point in which the plug is detected and subtracting the time taken for the reagents to travel through the dispersion coil. Doing so generates a reaction time/yield graph containing all the tested concentrations of pyrrolidine at each time point which can be better interpreted as a contour plot (Figure 5.18). Whilst the data obtained is unsurprising, increasing concentration and reaction time increases yield, the amount of data is vast with every black point on the graph, a single data point from the reaction. Of note is the decreasing information at high reaction times due to the averaging effects.

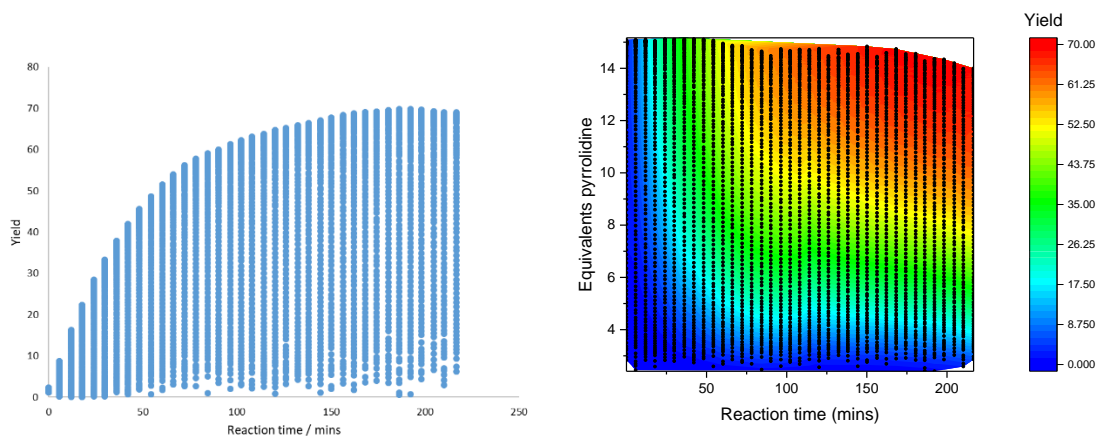


Figure 5.18: Left = Reaction UV data post data manipulation. Right = Contour plot of equivalents of pyrrolidine against reaction time and yield. Reaction is from 7.2.4.3 Contour plot is generated using Origin. Black points = unique data points

### 5.3.3 Multi gradient

As stated previously, the steepness of the gradient depends upon the analysis method used. For this reaction in-line UV spectroscopy is used which can perform a scan on average every 0.02 mins therefore, a steep concentration gradient can be used. However, for the multi-time point concentration gradient above, a large a gradient as possible was used to fill the reactor, far above the minimal size required for the fast scan rate of the UV spectrometer. With the use of smaller, steeper gradients, it should be possible to fit several concentration gradients inside the multi-time point reactor setup (Figure 5.19), effectively optimising three reagents, across a range of concentrations, and at several time points in a single reaction.

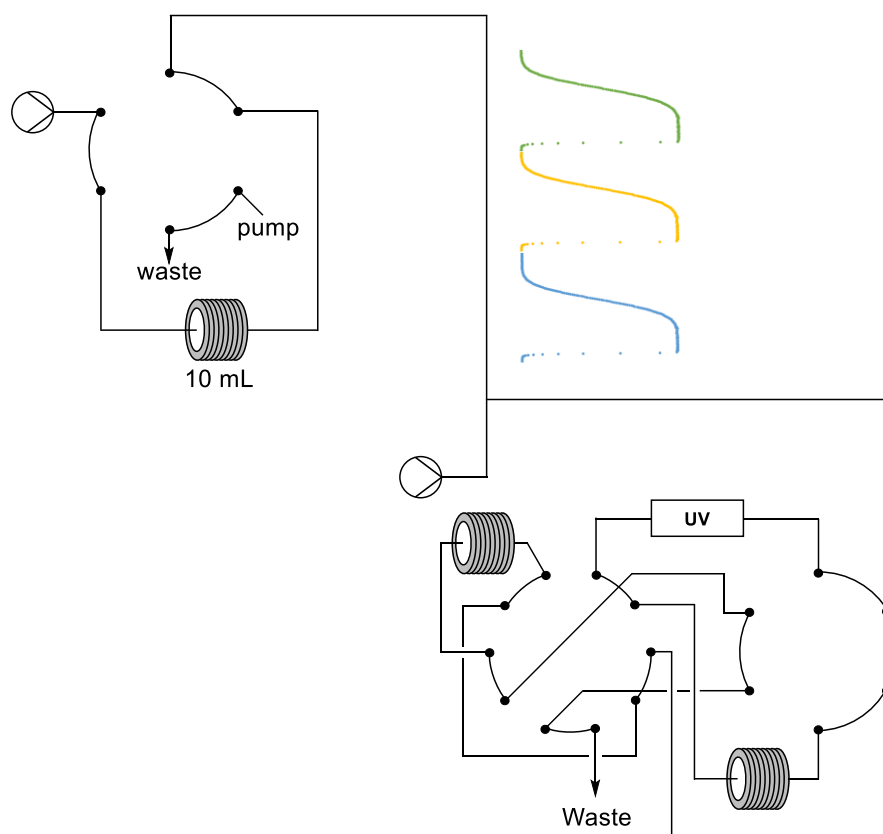


Figure 5.19: Graphical depiction of valve setup for a multi-gradient, multi-time point methodology. Several plugs are sent into the multi-time point system by switching of the 6-port sample loop valve and refilling the loop with an additional reagent plug.

### 5.3.3.1 Method

#### 5.3.3.1.1 How many gradients

The number of gradients that can be performed at the same time depends on several factors based around the volume of the reactor.

1. The maximum needed reaction time.  
The longer a reaction time needed, the larger a gradient required to minimise the averaging effects. The larger a gradient, the less can be fit into the reactors.
2. Viscosity of solvent.  
An increase in viscosity of solvent will increase the post-gradient generation dispersion which means larger gaps between gradients will be required as well as larger gradients minimising the maximum number capable.
3. Reactor volume and system pressure.  
As all the gradients must fit within the reactor, simply increasing the reactor size will allow for more to be included. However, depending on the reactor chosen, this can cause an issue with back pressure of the system. For the examples here, a glass bead filled reactor at high flow rates is used to minimise the post-gradient generation dispersion, this comes at the cost of a large pressure increase (>20 bar) and increasing the volume more will risk

hitting the pressure limit of the system or of the PFA tubing itself. As such for certain reactors, the number of gradients possible is limited to the back pressure capabilities of the pump and the reactor.

### 5.3.3.1.2 Generation and clipping

Two valve setups were created for this methodology, using smaller plugs and dispersion coils to minimise the size of the gradient plugs.

#### 5.3.3.1.2.1 Variable plug, minimal dispersion gradients

The first setup is for minimal dispersion to create the steepest and smallest gradients possible.

Two 6-port valves are added to the multi-time point setup with the first acting as a sample loop and the second acting as the gradient clip (Figure 5.20).

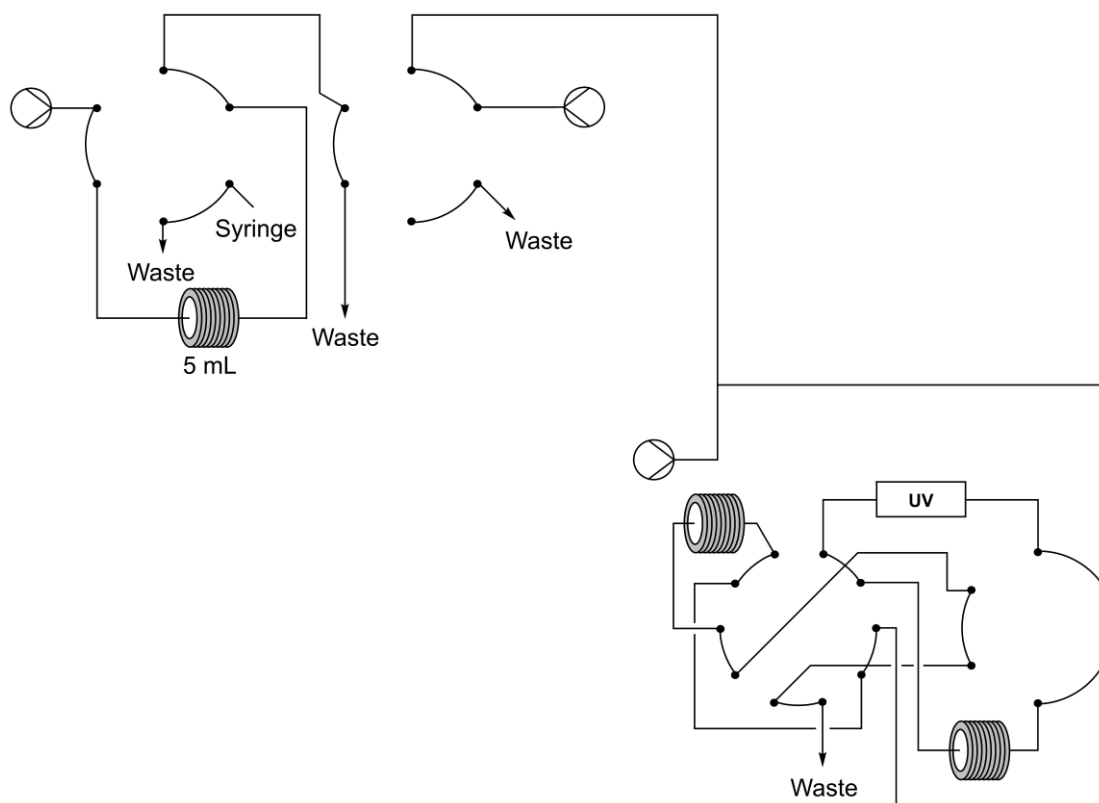


Figure 5.20: Valve setup for multi-gradient, multi-time point methodology. Reaction plugs are syringed into the sample loop 6-port valve before being pumped into the 2<sup>nd</sup> valve for gradient clipping. Gradient generation occurs when pumping through the sample loop and clipping tubing.

The reagent mixture is added to the sample loop *via* a syringe however, the size of the plug to be sent to the multi-time point setup is determined by the switching of the sample loop valve allowing for several samples of varying size to be added. The dispersion occurs as the reagent



mixture is pumped out of the sample loop and through the clipping valve resulting in a minimal amount of dispersion and thus a very steep gradient and small overall plug size.

The clipping valve can then be switched to clip the back gradient off the plug however, when utilising small gradients, there is only a small gain from doing so. Its second purpose is to continue the pumping of the gradient whilst the sample loop is refilled with the next reagent for gradient generation (Figure 5.21).

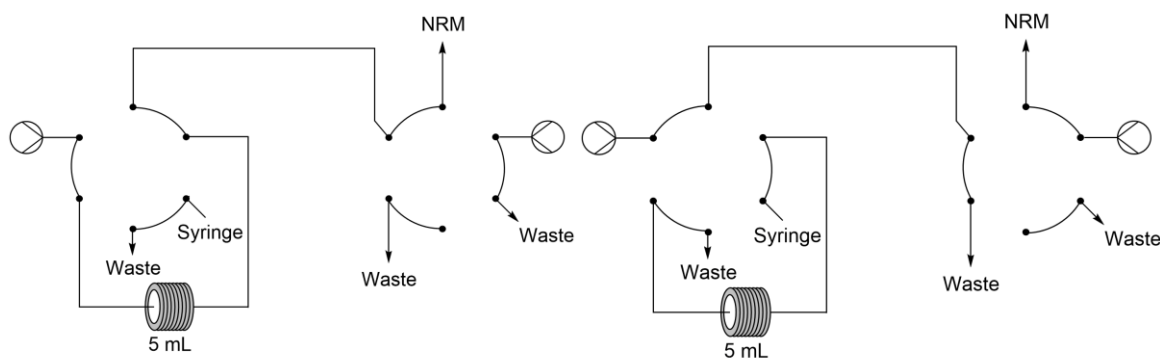


Figure 5.21: Valve setup for introduction of multiple plugs of variable sizes. Left = Generation of the gradient and clipping. Right = Refilling the sample loop and gradient is pumped into the multi-time point setup.

The process can then be repeated for the number of gradients required. The clipping valve in this setup could be replaced with a 4-port valve for maximum port efficiency, however none were available in the lab, so a 6-port was used.

The valve setup allows for simple variation of plug size by varying the timing of the first valve switch and generates minimal amounts of dispersion as the plug passes through only the sample loop.

#### 5.3.3.1.2.2 Variable dispersion, minimal plug gradients

The second setup again utilises two additional 6-port valves with a sample loop setup as the first valve. However, the changes appear in the setup of the second valve which in this case is the joint gradient generation and clipping valve (Figure 5.22).

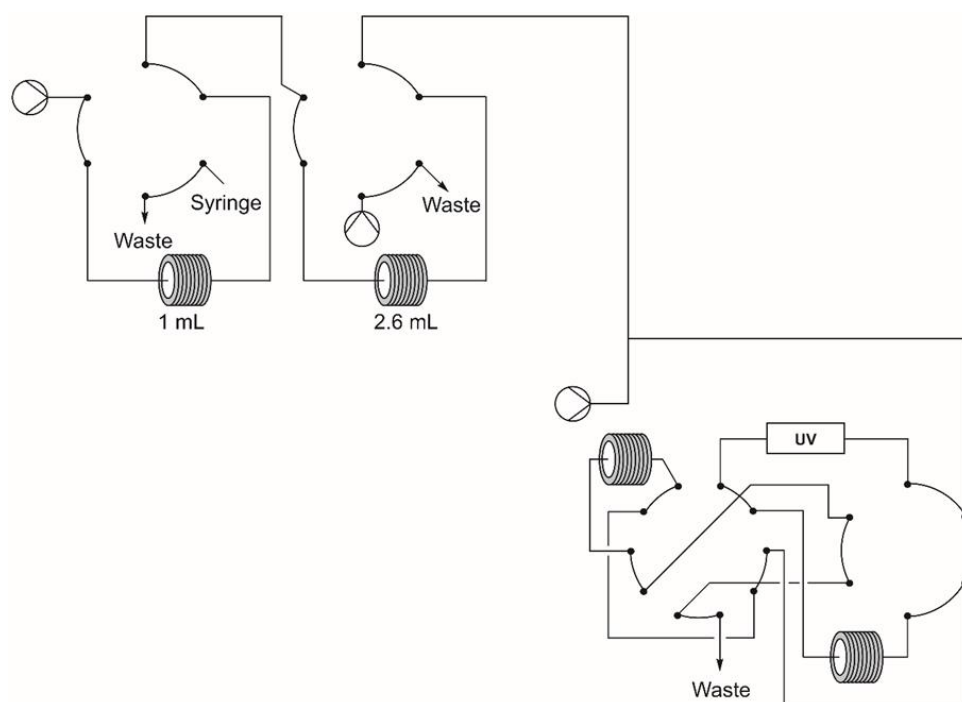


Figure 5.22: Valve setup for varying the amount of dispersion with minimal plug size. Gradient generation and clipping is controlled by the second 6-port valve and can be varied by changing the flow rate of the connected pump.

The sample loop is initially filled with the reagent mixture *via* syringe and then switched to begin pumping into the second valve. The plug then undergoes dispersion to convert it into a concentration gradient whilst the sample loop is refilled. The sample loop valve is then switched, and the second plug enters the dispersion coil. The switching is timed so that the first plug is exiting the valve after the second has completely entered which allows the second valve to act as a clipping valve for the first gradient (Figure 5.23). The switching also allows an increase in the separation between the plugs as the flow rate of the pump attached to the second valve can be adjusted so the plugs either become closer or further away depending on the flow rate compared to the first pump.

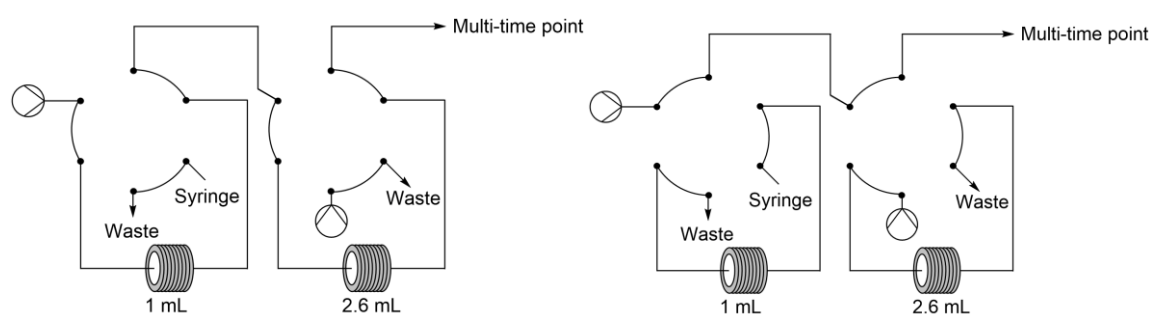


Figure 5.23: Valve setup for gradient clipping and plug separation. Left = Pumping plug into dispersion coil. Right = Generation of gradient and refilling of sample loop.

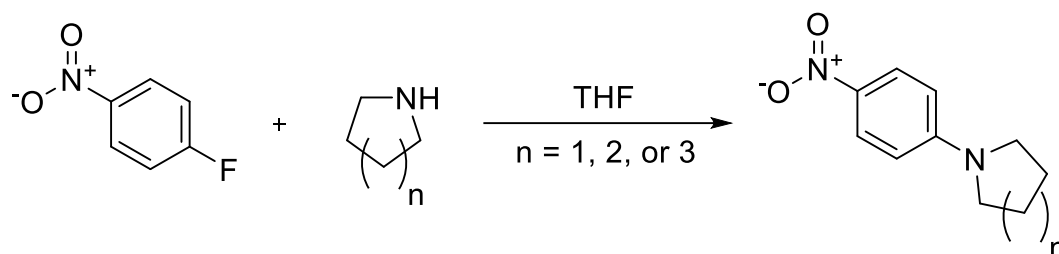
These steps can then be repeated as needed. The steepness of the concentration gradient can be controlled by varying the size of the dispersion coil present on the second valve.

The valve setup allows for simple variation of the amount of dispersion by varying either the flow rate or the dispersion coil size.

### 5.3.3.2 Reaction test

With the current glass bead filled reactor set-up with 11 mL reactors, a maximum of three gradients could be performed in the same experiment. 1 mL sample

The  $S_NAr$  reaction of 1-fluoro-4-nitrobenzene with pyrrolidine, piperidine and azepane tested as the three gradients (Scheme 5.2)



Scheme 5.2:  $S_NAr$  of amine heterocycles with 1-fluoro-4-nitrobenzene. 1.3 mmol of 1-fluoro-4-nitrobenzene in 10 mL THF is the steady state reagent line. 3.3 mmol of amine in 5 mL THF is the concentration gradient stock solution.

Performing a dispersion profile of this setup shows a retention of steady state for three pass throughs, or 15 minutes reaction time and then the plugs start overlapping after 40 minutes (Figure 5.24). Compared to the single gradient method, this is a much lower reaction time due to the smaller concentration gradients used. Therefore, the reaction above will need to be performed at 75 °C to demonstrate the method sufficiently. Additionally, as the gradient plugs are small, no clipping of the back gradient was performed, and as such information from two gradients of a reagent can be obtained.

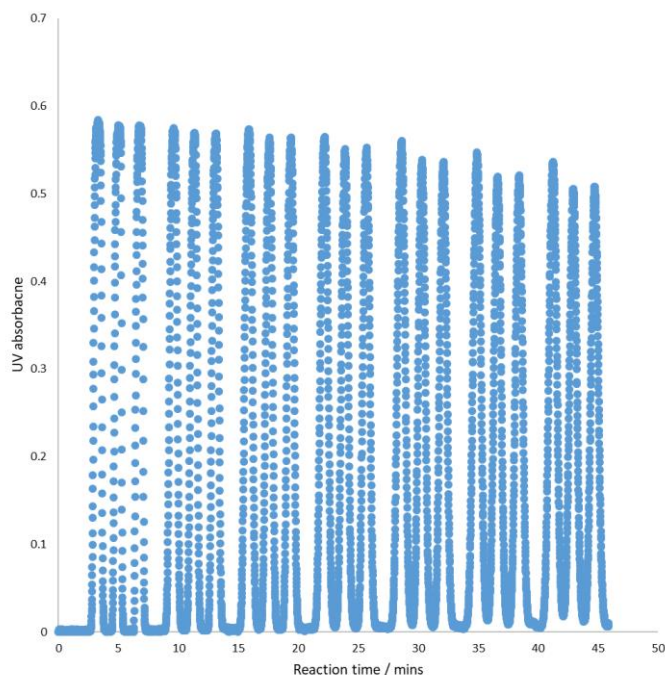


Figure 5.24: Dispersion profile for multi-gradient multi-time point method. Each peak in a triplet would be a separate reagent. Reaction conditions are from Scheme 5.2

The methodology was performed with manual valve switching and sample loop refilling however, it would be trivial to automate this with a Python script and a liquid handler. The steady state reagent was kept as one large plug encompassing all three gradients however this could be adjusted to have separate steady state reagent for each gradient by addition of a sample loop to the steady state reagent line.

From the raw UV data it is possible to see the three gradients of each reagent at each time point. The data handling is identical to that of the single gradient however all three of the reagent gradients get identical reaction times. The only variance in the methods is when the gradients begin to overlap, at which time the Python script does not delete these data points accurately so manual removal is necessary (Figure 5.25).

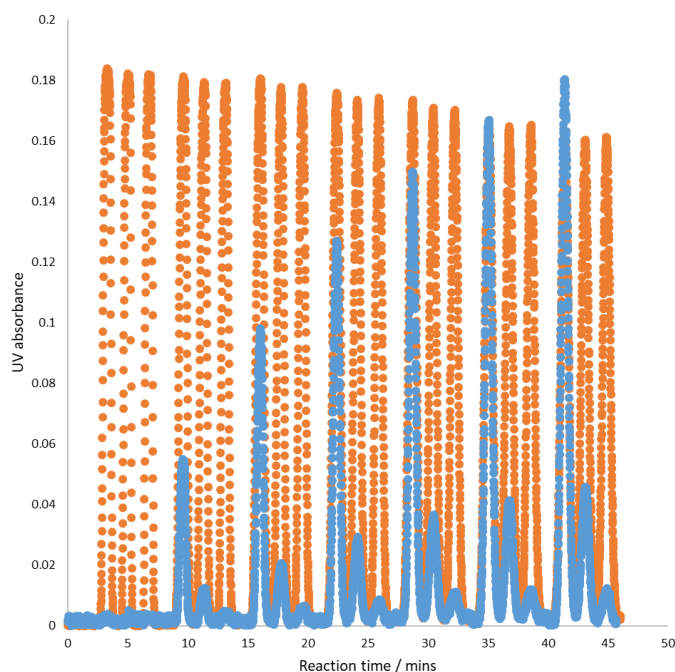


Figure 5.25: Peaks are pyrrolidine, piperidine and azepane from left to right in each triplet.

Reaction conditions are from Scheme 5.2. Blue = Raw UV data from experiment.

Orange = Dispersion profile

Conversion of the absorbances to yield allows creation of three contour plots demonstrating the effect of varying the concentration of amine on the yield at various reaction times (Figure 5.26). The data shows a general decrease in reactivity as the ring size increases which matches with the trend in decreasing nucleophilic parameter<sup>310</sup> for pyrrolidine and piperidine<sup>311</sup>. Unfortunately, no literature value could be found for azepane in MeCN.

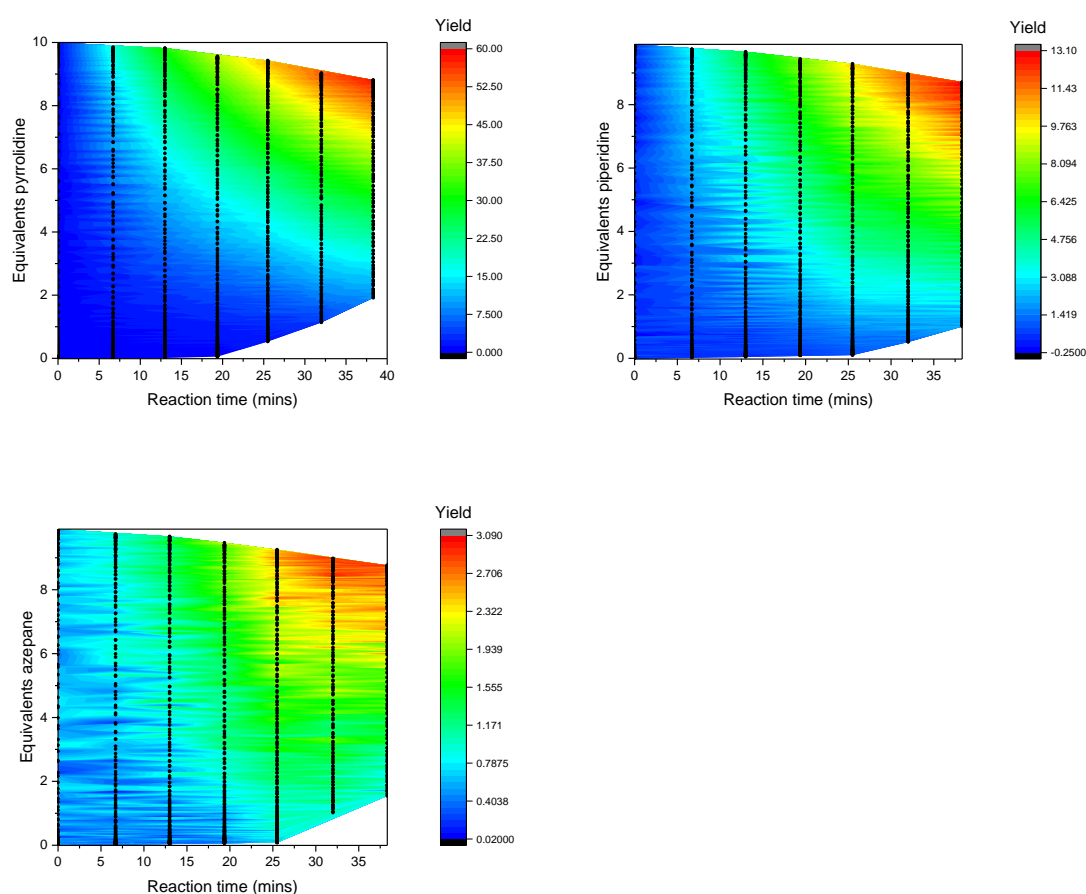


Figure 5.26: Contour plots extracted from multi-gradient multi-time point experiment. Top left = pyrrolidine. Top right = piperidine. Bottom = azepane. The scale of the yield varies between graphs.

As two concentration gradients are measured using this methodology, there exists a method for checking the dispersion profile overlaying with the reaction data. If concentration against yield is plotted for each reaction time, the resulting graph should be a straight line, as equivalent concentrations should give the same yield regardless of whether it is the front or back gradient. An example from the pyrrolidine plug is shown below for the 36 minute time point (Figure 5.27). The two lines differ by only a small amount of yield and appear to be almost a single line meaning a good overlap between the dispersion profile and experimental data.

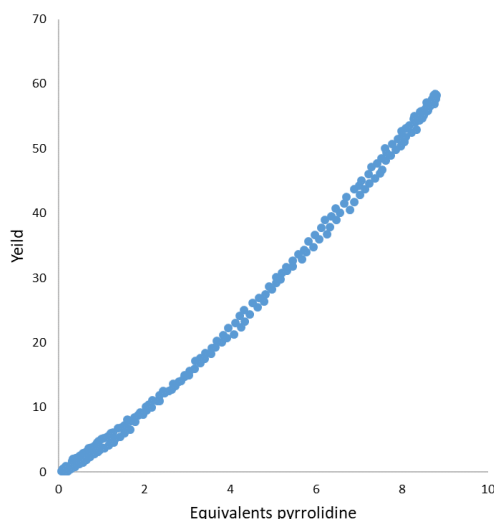


Figure 5.27: Overlaid front and back edge of a pyrrolidine gradient resulting from good dispersion profile overlay

### 5.3.3.3 Validation against steady state

For methodology validation, the pyrrolidine reaction was chosen because the large differences between the various equivalents and reaction times will provide an excellent test of method accuracy compared to the lower yielding amines.

Initial attempts using traditional steady state methods and 8 equivalents of pyrrolidine were generating a much higher yield than that given by the multi-gradient multi-time point method. The effect of mixing, pressure and accuracy of reactor volumes were all tested however, none caused the increase in yield. The problem was due to poor heat transfer in the multi-gradient, multi-time point method. As a high flow rate was used and there is poor heat transfer given by the Vapourtec air heater, the reaction mixture was not reaching the expected temperature in the multi-gradient, multi-time point method. Whereas the traditional method was using a much slower flow rate, allowing a higher temperature to be reached thus generating a larger yield.

To overcome this, an oil or water bath heater could be used to increase the heat transfer to the reactors. However, this would take up a large space in a fume hood with already limited space from the Vapourtec system, the switching valves, the in-line monitoring devices, and the liquid handler. As such, the steady state experiments were repeated using identical conditions to that of the multi-gradient, multi-time point methodology (high flow rates, air heated), and this generated yields within 5% of those obtained by the methodology across 2, 5 and 8 equivalents and several time points (Figure 5.28).

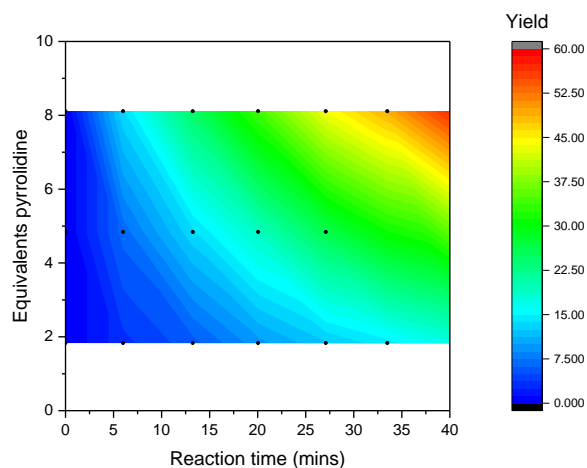


Figure 5.28: Contour plot from steady state pyrrolidine  $S_NAr$  experiments. Comparison between these results and the results from the multi-gradient, multi-time point experiments show good overlap.

### 5.3.4 Variations

The multi-time point system is not limited to the setup shown above and several different designs for various uses can be constructed, some of which are listed here.

#### 5.3.4.1 Vapourtec integration

The Vapourtec R2+ series comes with four 6-port sample loop valves preinstalled onto the system for reagent addition. These can be reconfigured to act as a single gradient multi-time point system (Figure 5.29) minimising the cost of entry to use of this methodology for laboratories which have already purchased this flow system.



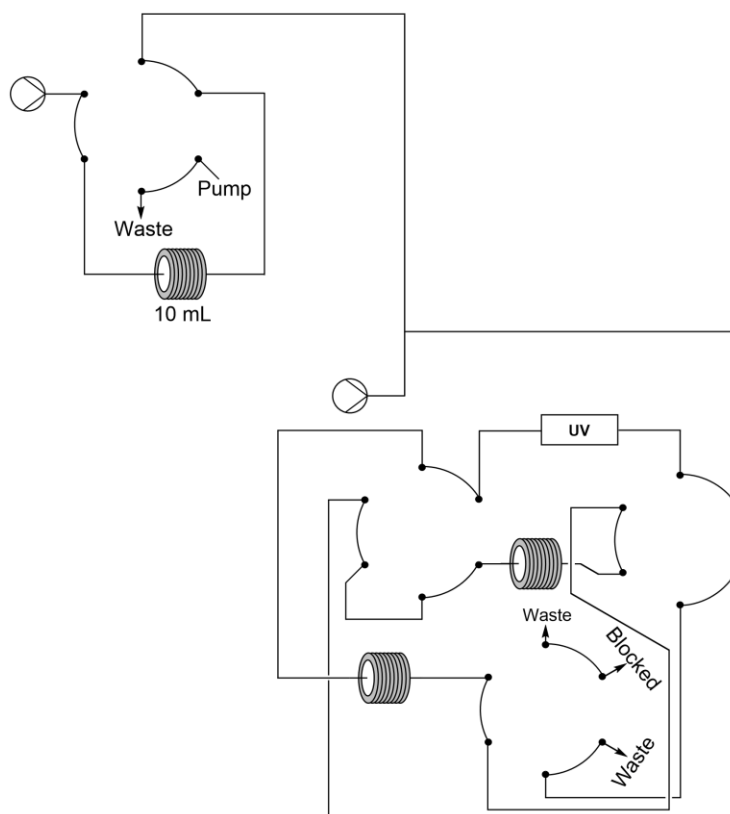


Figure 5.29: Valve setup for Vapourtec integrated gradient multi-time point system. The Vapourtec system comes with several 6-port valves allowing for concentration gradient multi-time point reactions to be performed natively.

#### 5.3.4.2 HPLC in-line with quench

Whilst in-line UV and IR are powerful techniques for monitoring a reaction, they are incapable of monitoring small impurities or enantiopurity in the reaction mixture. As such being able to utilise a monitoring method such as HPLC would be ideal. A design for this can be achieved by addition of a small volume switching loop in the setup (Figure 5.30). The loop transfers a small amount of reaction mixture into the HPLC stream where it is diluted to the correct concentration by a quench line which can then be monitored.

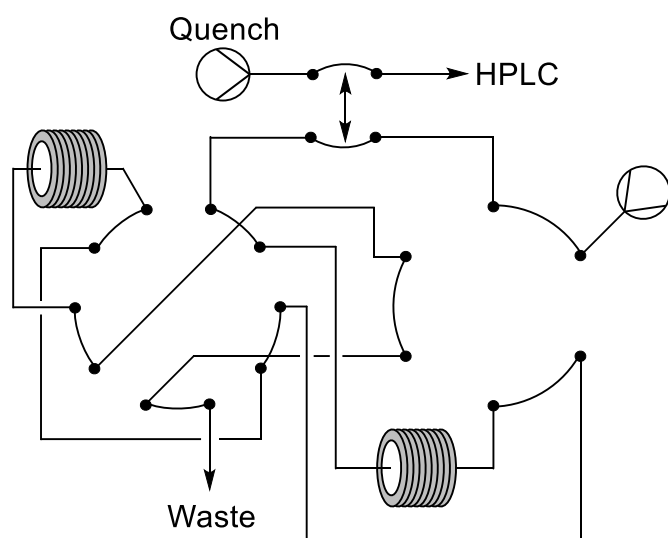


Figure 5.30: Valve setup for in-line HPLC monitoring within the multi-time point system.

For steady state reactions, this is all that is required. However, for concentration gradient reactions, several samples would need to be taken at each time point so after quenching, the different samples would need to be held in a holding loop whilst the first sample gets analysed. A holding loop system can be implemented in three ways:

1. A 4-port valve set up as a sample loop which can either send the plug directly to the HPLC for monitoring or if the HPLC is currently running a method, send the plug into a small holding loop where it can be stored until the HPLC is ready (Figure 5.31).

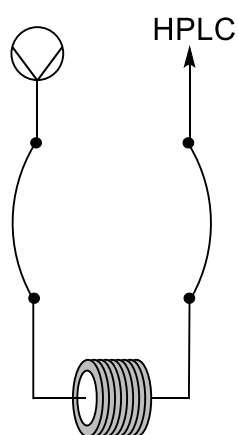


Figure 5.31: Valve setup for storage of a plug for future HPLC analysis. The plug can remain in the reactor until the HPLC is ready to analyse it, whilst the reaction continues in the multi-time point system.

2. A multi position valve which can direct each sample to its own small holding loop, which can then be pumped out as required (Figure 5.32).

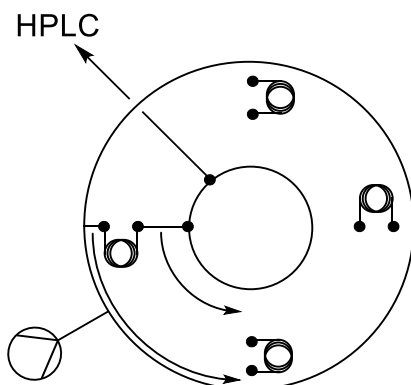


Figure 5.32: Multi position valve with attached storage loops for plugs for future HPLC analysis.

Valve allows for the easy storage and access of several plugs.

3. Addition of a liquid handler removes the need for a holding loop entirely by adding each individual sample into its own vial. However, a liquid handler has the downside of requiring manual relocation of the vials to the HPLC if the system is not preconfigured for vial addition directly to the HPLC.

The multi position valve is the preferred setup due to the minimised dispersion which would occur compared to the first method, meaning less risk of plugs overlapping and small peaks being invisible by HPLC due to dilution. Each of these methods will have a slightly decreased maximum time due to the removal of reaction mixture. Additionally, results at the higher reaction times will be less accurate due to dilution with solvent added through the sampling process.

#### 5.3.4.3 Two gradients, two conditions, multi-time point

When performing the single gradient, multi-time point methodology, at the gradient clipping process the back gradient is sent to waste. Instead this second gradient can be pumped into its own multi-time point setup under different conditions, such as a higher temperature, and the amount of data obtained can be doubled (Figure 5.33). Otherwise the back gradient could go through a standard reactor to generate a single time point at multiple concentrations as a reference guide for the multi-time point method.

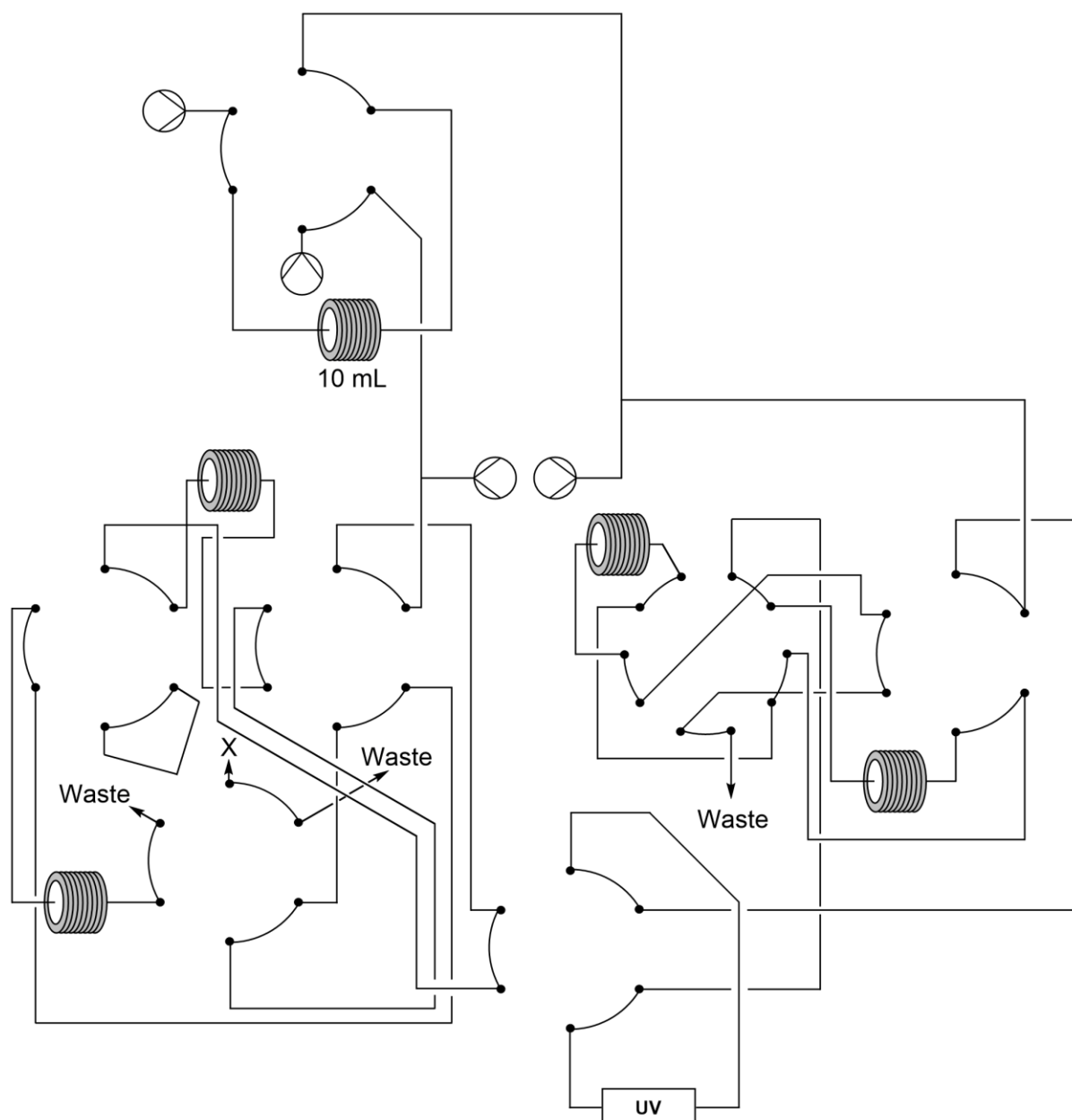


Figure 5.33: Valve setup for separating the front and back gradients from a plug and sending both into individual multi time point setups. Two different conditions could be tested this way from a single batch of starting material, such as varying the reagents in the steady state or the reactor temperature.

#### 5.3.4.4 Single syringe pump, non-reciprocating multi time point

The syringe pump is one of the most common pumps in the standard organic laboratory due to their relatively low cost and their use in traditional batch chemistry for timed addition of reagents to a reaction. As such, a multi time point method which can utilise these pumps will have the largest potential impact. The design shown here (Figure 5.34) can operate with a single syringe pump and utilises the pumps ability to push and pull the flow.

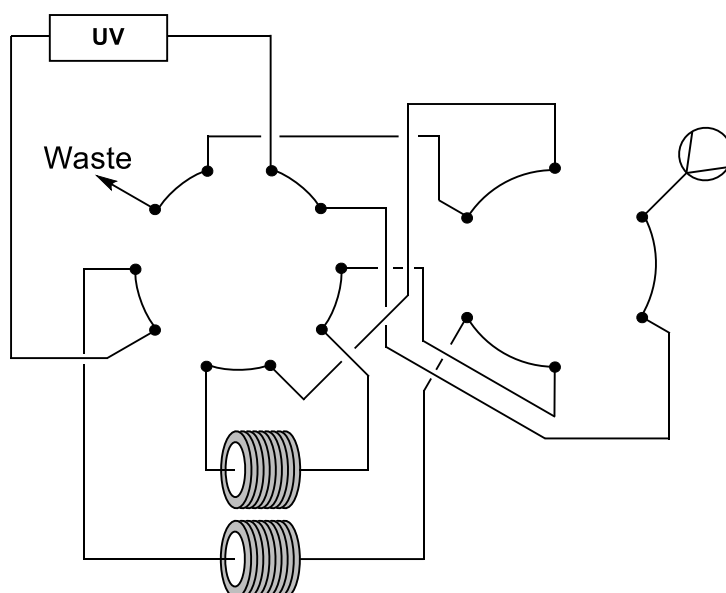


Figure 5.34: Valve setup for accessing multi time points with non-reciprocating flow by use of a single syringe pump.

Initially the plug is pushed through the setup which generates the  $t_0$  time point and loads the plug into the reactor. Both valves are then switched, and the syringe is set to pull, generating a second time point and loading the second reactor. The 10-port valve is then switched, and the syringe is set to push the plug generating another time point and reloading the first reactor. The 10-port valve can then continually be switched along with a corresponding change in the push/pull of the syringe pump to generate the desired number of time points. As well as generating a  $t_0$  time point, this design benefits from never changing the direction of the reaction mixture, thus the whole plug experiences the same reaction time rather than the time gradient seen before.

#### 5.3.4.5 Summary

Many configurations other than the previously detailed setups can be created depending on the exact needs of a project. Additionally, the valves can be exchanged between configurations as the project evolves and the requirements change.

## 5.4 Case study: Triazole formation

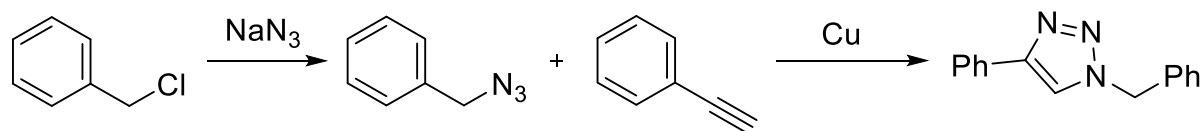
### 5.4.1 Introduction

One of the main benefits of flow chemistry is the ability to easily perform multi step reactions to form complex molecules due to the ease of addition of reagents at the correct reaction times.

However, each step requires optimisation which can take a large amount of time. Therefore, if the

gradients at multi-time points method can be used to accelerate the optimisation for each step, a large time saving will be achieved.

To test the hypothesis a suitable reaction was chosen which could be easily monitored by in-line IR spectroscopy, the formation of 1-benzyl-4-phenyl-1,2,3-triazole (Scheme 5.3).



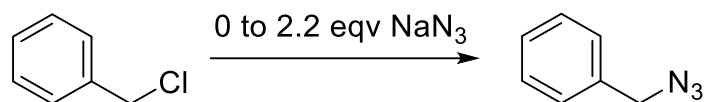
Scheme 5.3: Synthesis of 1-benzyl-4-phenyl-1,2,3-triazole from benzyl chloride

The reaction can be separated into two steps:

1. The formation of benzyl azide from benzyl chloride and sodium azide
2. The copper-catalysed azide-alkyne cycloaddition between phenylacetylene and the benzyl azide formed in the first step.

#### 5.4.2 Optimisation of step 1

The initial conditions tested were adapted from literature and a 0.25 M solution of benzyl chloride in DMSO at room temperature was used with a gradient of sodium azide for optimisation (Scheme 5.4)



Scheme 5.4: Synthesis of benzyl azide from benzyl chloride. A gradient of  $\text{NaN}_3$  is probed against a steady state of 2.5 mmol benzyl chloride in 10 mL DMSO.

##### 5.4.2.1 Flow setup: in-line IR monitoring

The single gradient, multi-time point setup was used as only a single reagent needed to be tested and in-line IR was used as a monitoring device due to the ease of monitoring the appearance of the azide peak.

Initial attempts at obtaining a dispersion profile generated peculiar results, the plugs appeared to decrease in size rapidly as the dispersion profile ran and in different valve modes, the maximum absorbance and solvent signal was different. The decrease in plug size and reaction time is due to a limitation in the software used to monitor the IR signal. Rather than equal time between scans seen with the in-line UV and set by the IR software, for IR, the time between scans increases as

reaction time increases (Figure 5.35). The additional time can easily be accounted for by using a Python script to extract the exact time of the scan rather than estimating with the scan time set in the software.

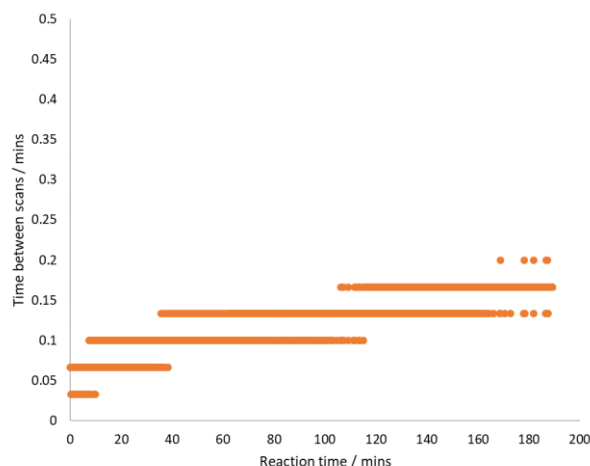


Figure 5.35: Rate of IR spectra acquisition decreases as reaction time increases.

Additionally, there is a difference in solvent signal and maximum absorbance between the different valve modes. The reason for the difference is due to the design of the IR flow cell. It consists of two windows separated by a small washer, with o-rings on either side of the windows and the system is zeroed in one of the valve modes. However, depending on the valve mode, the IR flow cell can be in three different environments: Before all reactors, after reactor 1 or after reactor 2. Each of these locations experiences a different system pressure and this difference in pressure changes the gap between the cell windows allowing more solvent or reaction mixture in and changes the solvent signal and maximum absorbance. To overcome this the system was zeroed in the “after reactor 1” mode as the difference between this and “after reactor 2” is minimal and these modes are where the majority of the reaction data is created.

Applying these fixes allows generation of a dispersion profile in which a maximum reaction time of 60 minutes can be reached before the steady state begins to decline (Figure 5.36). The viscosity of DMSO results in much lower maximum reaction time than the experiments listed above for two reasons. The increase in viscosity causes an increase in back pressure, as such a slower flow rate (0.4 mL/min) has to be used in order to remain within safe pressure ranges. The decrease in flow rate has the side effect of increasing the amount of dispersion across the same volume. The increased viscosity also directly increases the dispersion according to the equations mentioned in section 2.2.

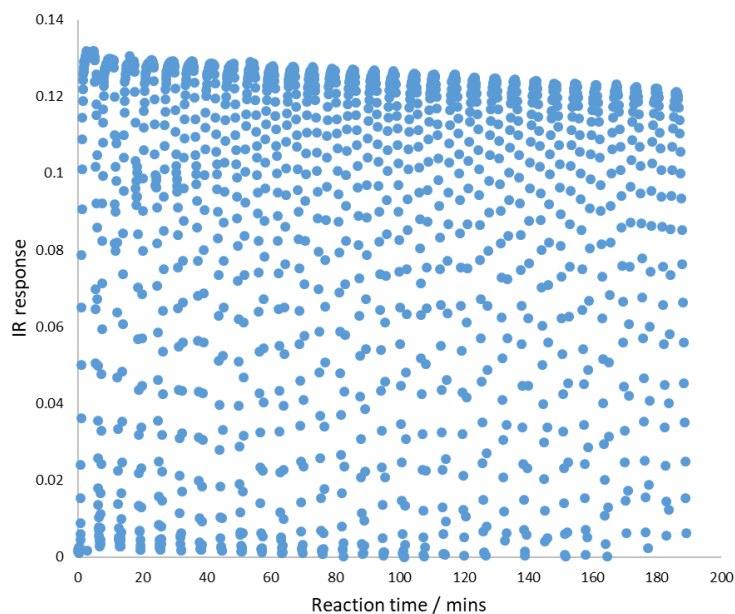


Figure 5.36: Dispersion profile for multi time point setup. Steady state lowers after 60 minutes, much sooner than previously observed due to the increased viscosity of the solvent.

#### 5.4.2.2 Room temperature reactivity: increasing the maximum reaction time

The gradient methodology was performed with the maximum concentration of sodium azide determined by the solubility limit.

Initially the reaction was performed at room temperature with the valves switching automatically, and the data handled as above. However, the results (Figure 5.37) show only a maximum of 80% yield after 60 minutes which is below the ideal target.



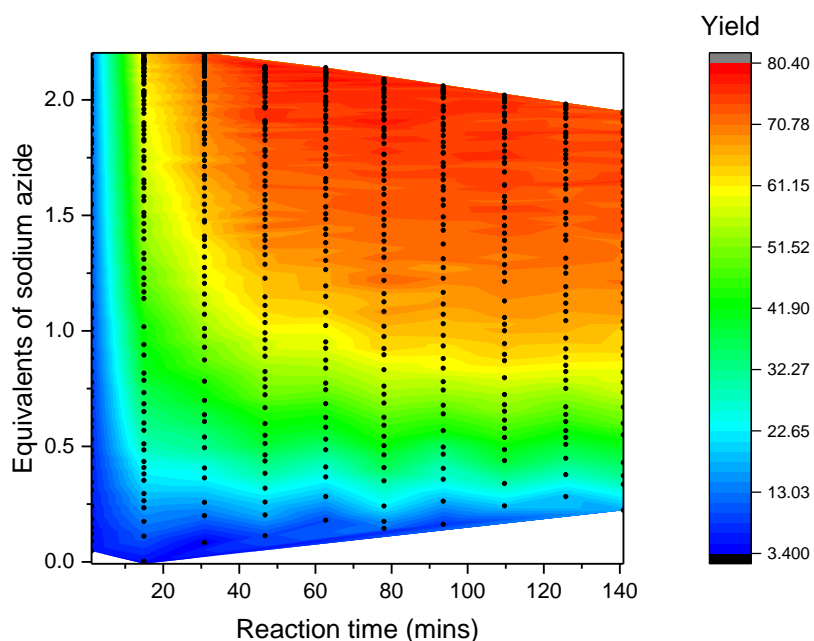


Figure 5.37: Contour plot for benzyl azide single gradient multi time point reaction. Reaction conditions are from Scheme 5.4.

To probe whether this is just due to slow reactivity or an issue with the setup, a longer reaction time was needed. To increase the maximum reaction time using this methodology there are two main options.

1. Decrease the flow rate
2. Increase the overall plug size

Decreasing the flow rate is not an ideal solution here as the system is already at a low flow rate and only a small gain in maximum reaction time will be seen.

Increasing the plug size to allow for more steady state and a shallower gradient would be a better solution however, this would require a larger reactor which would increase the back pressure of the system and in this setup the system is already close to the maximum of 40 bar. As such a different method was needed. The method chosen is the “stop-flow” method which utilises the relatively slow rate of axial molecular diffusion. In previous work<sup>113</sup> it was shown that axial molecular diffusion has no effect on the overall shape of a plug after an hour. Therefore, if the flow is stopped after the concentration gradient is fully contained in the reactor of the multi-time point setup, then any time gap can be applied before restarting the flow allowing access to longer reaction times than were previously possible with continuous flow, whilst still preserving the concentration gradient. With this methodology the reaction is now limited to the number of pass throughs possible before the averaging effect becomes too great.

The stop-flow method was tested on the reaction with 60 minute gaps between the flow restarting (Figure 5.38), after an initial wait of three hours generating a maximum reaction time of 360 minutes. Full conversion was reached with 1.5 equivalent after 180 minutes showing that the reaction yield was limited by the low reactivity rather than any other potential issue with the reaction, such as product degradation and reaction stalling, or the flow setup. Unfortunately, the time taken is far too high to be considered useful in a continuous process however, the data generated could be utilised to create a batch process for this reaction.

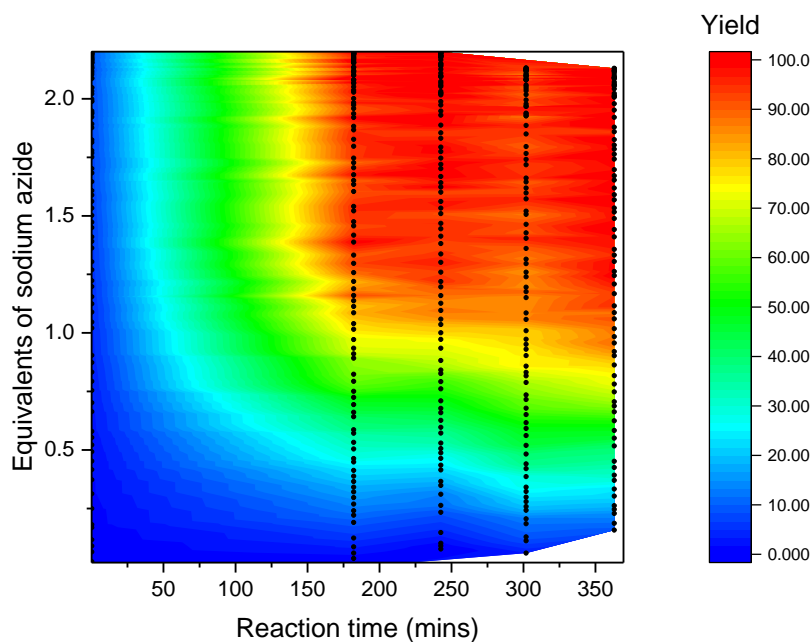


Figure 5.38: Contour plot from stop flow, single gradient, multi time point for benzyl azide formation. Reaction conditions from Scheme 5.4

#### 5.4.2.3 Decreasing the reaction time needed

To overcome this the reaction was repeated with the Vapourtec air reactor set at 75 °C. Increasing the temperature lowered the reaction time needed for full conversion, with 1.1 equivalents, to 18 minutes (Figure 5.39), with the latter being an acceptable reaction time for the eventual combination with the second step. Of note is that the reaction most likely finishes prior to this time however this is the first time point obtained using this setup and to get earlier time points would require a fast flow rate which is currently impossible due to the pressure limits.

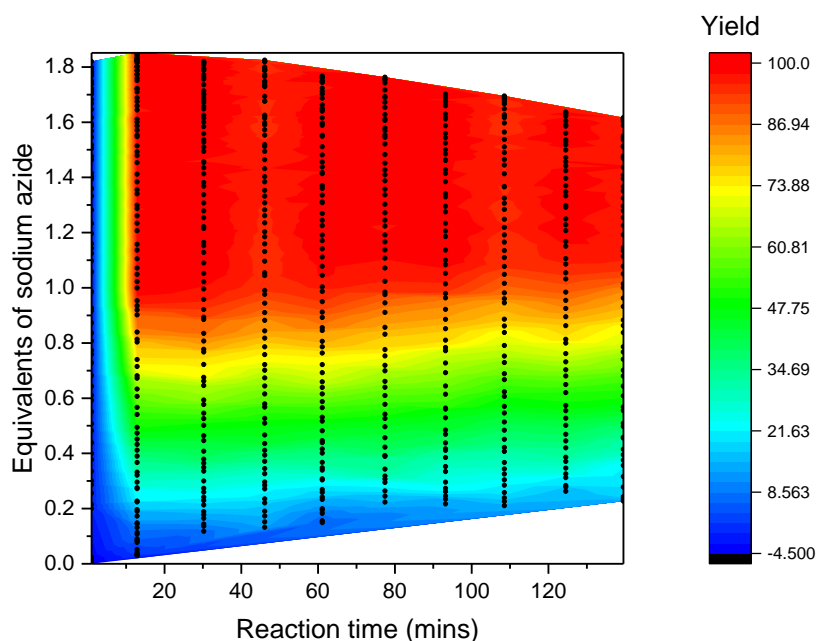


Figure 5.39: Contour plot for benzyl azide single gradient multi time point reaction at 75 °C.

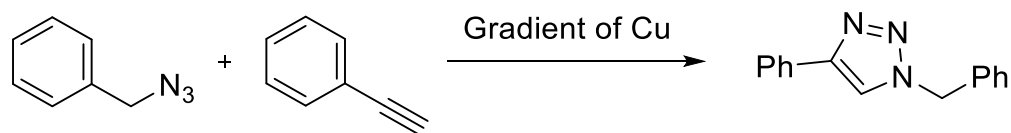
Reaction conditions from Scheme 5.4.

Unfortunately, this increased reactor temperature does introduce problems particularly with the glass bead filled reactors. The combined temperature and pressure causes an expansion of the tube which allows the glass balls to move and readjust changing the packing of the system. The majority of the time this has very little effect on the reaction, however the balls can align themselves in a way that restricts or entirely blocks the flow causing a rapid increase of pressure which can cause the system to stop pumping or cause a leak in the reactor.

Use of a different low dispersion reactor design or using a stronger wall material such as stainless steel for the glass bead filled reactor would solve this however at the time of the experimentation no other designs were available in the laboratory and stainless steel tubing is not compatible with the method used for making the reactors due to not being able to see any blockages or gaps when packing.

#### 5.4.3 Optimisation of step 2

For the CuAAC reaction, the starting materials and solvent are predetermined by the first step. As such the main unknown to be found is the source of Cu (Scheme 5.5)



Scheme 5.5: Formation of 1-benzyl-4-phenyl-1,2,3-triazole from benzyl azide and phenylacetylene. 1.25 mmol of benzyl azide and 1.25 mmol of phenylacetylene are reacted against a gradient of different Cu sources at 0.088 mmol.

#### 5.4.3.1 Multi-gradient, multi-time point attempts

Three different copper sources were taken from the literature<sup>312–314</sup> (CuI, CuBr(PPh<sub>3</sub>)<sub>3</sub>, and [Cu(phen)(PPh<sub>3</sub>)<sub>2</sub>]NO<sub>3</sub>) due to their success in similar conditions and their commercially availability, at low cost.

Initially this appeared to be a perfect setup for the multi-gradient, multi-time point system. However, when a dispersion profile was performed using the variable gradient size method described above, the plugs were overlapping almost immediately. The system was then swapped to the minimal gradient layout but even this caused plug overlap after only 2 pass throughs (Figure 5.40). The low number of possible pass throughs is due to the high dispersion caused by the viscous solvent as mentioned previously, and as such cannot easily be solved using this setup. Therefore, only single-gradient multi-time point reactions were performed.

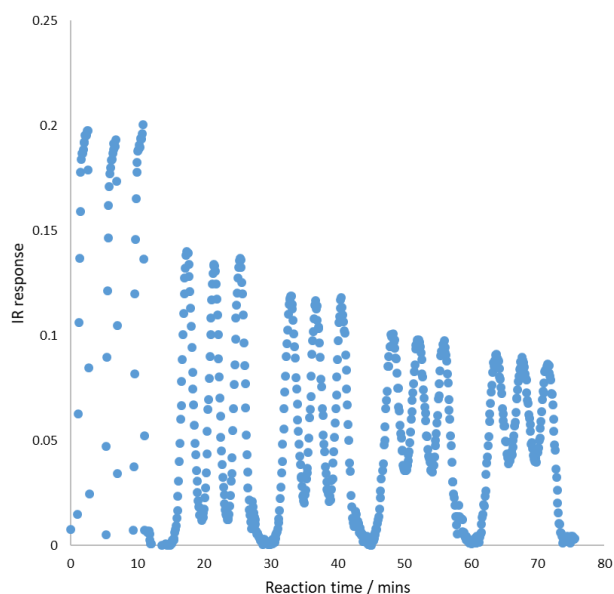


Figure 5.40: Dispersion profile for multi gradient, multi time point experiment in DMSO. Only one pass through was achieved before plugs began to overlap

#### 5.4.3.2 Single gradient, multi-time point

The initial optimisation occurred using  $\text{CuBr}(\text{PPh}_3)_3$  with the aim to achieve as high a yield as possible whilst using a minimal amount of Cu with a short reaction time. Three temperature set points were tested using the Vapourtec air heater: 50, 75 and 100 °C. A maximum concentration of 14 mol% Cu source was utilised (Figure 5.41). A 50 °C reaction temperature, showed full conversion by 60 minutes for above 12 mol%, with a 6 mol % loading reaching full conversion at 90 minutes and 4 mol% takes 120 minutes to reach the final yield. At 75 °C, the reaction takes less time to hit full conversion with above 10 mol% reaching completion by 15 minutes, 6 mol% taking 45 minutes and 4 mol% after 60 minutes. 100 °C improves on the lower mol% conditions taking 30 minutes for 6 mol% and 45 minutes for 4 mol%. Whilst these conditions do give the best outcome in terms of lowest reaction time, there is a higher potential for decomposition of the azide, as such the 75 °C conditions were taken as the optimal for testing the other Cu sources.

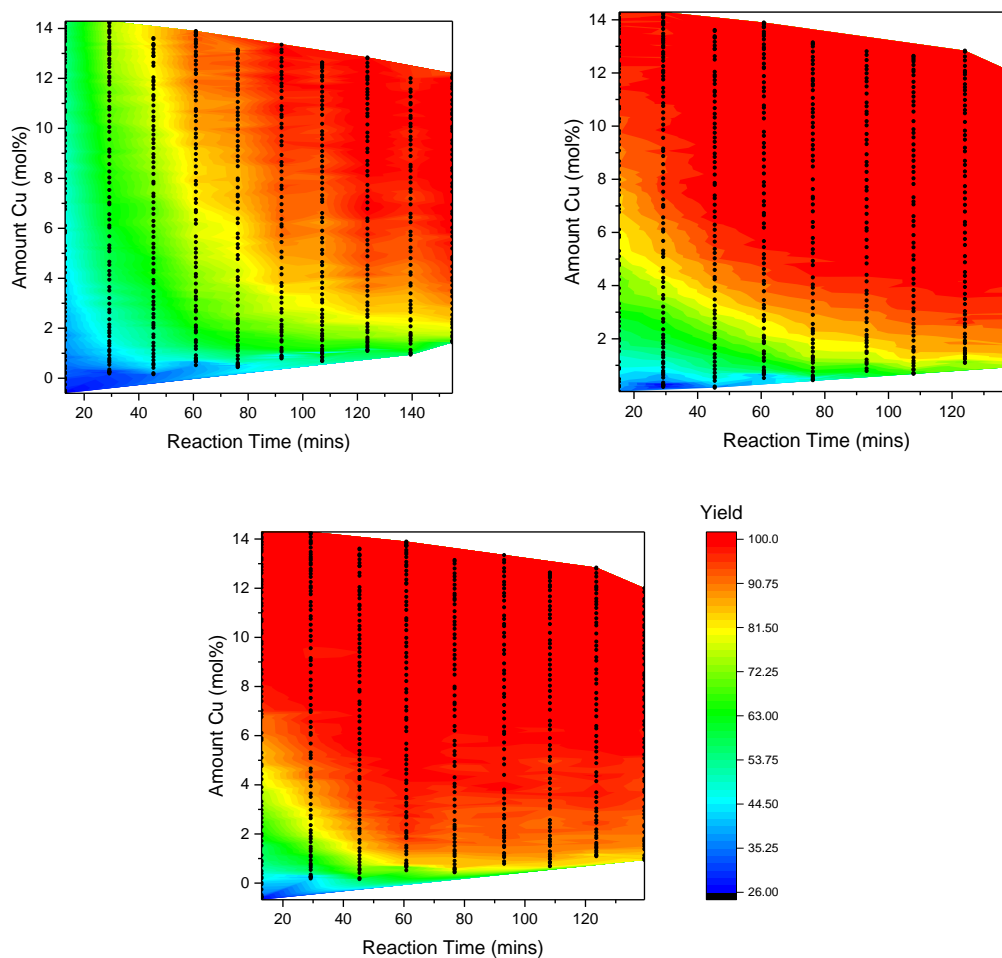


Figure 5.41: Contour plots from formation of 1-benzyl-4-phenyl-1,2,3-triazole using  $\text{CuBr}(\text{PPh}_3)_3$ .

Reaction conditions from Scheme 5.5. Top left = 50 °C. Top right = 75 °C. Bottom = 100 °C

$[\text{Cu}(\text{phen})(\text{PPh}_3)_2]\text{NO}_3$  and  $\text{CuI}$  were tested under the optimal conditions and both showed almost identical results to each other (Figure 5.42) but showed an increase in reactivity compared to  $\text{CuBr}(\text{PPh}_3)_3$  reaching 100% yield at 4 mol% after only 30 minutes.

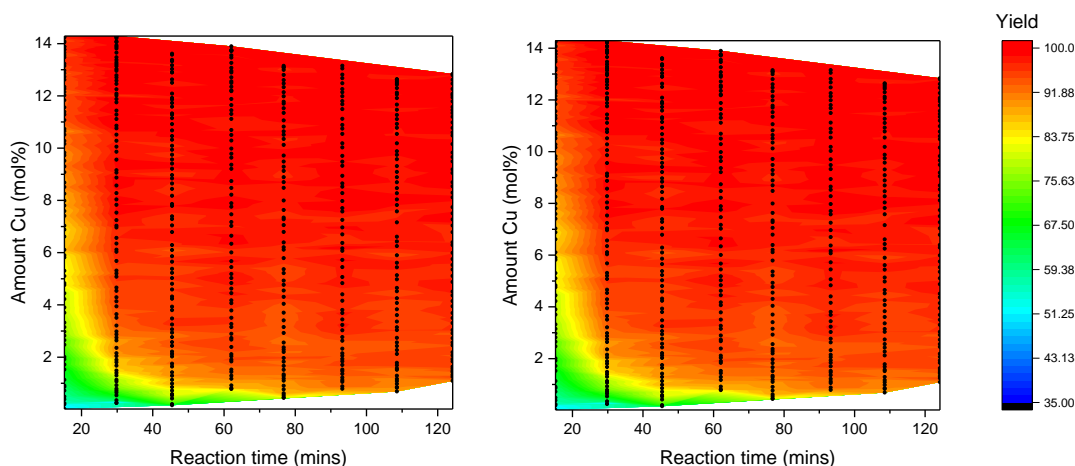
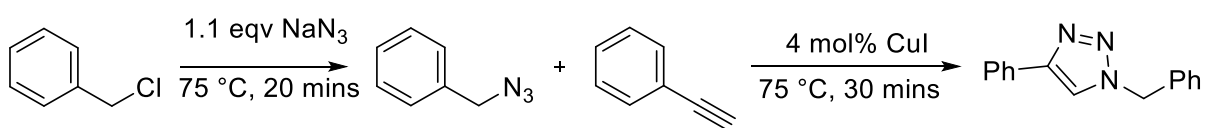


Figure 5.42: Contour plot from formation of 1-benzyl-4-phenyl-1,2,3-triazole. Reaction conditions from Scheme 5.5. Left =  $[\text{Cu}(\text{phen})(\text{PPh}_3)_2]\text{NO}_3$ . Right =  $\text{CuI}$

$\text{CuI}$  was chosen as the optimal source of copper due to costing only 24p/g compared to £13.14/g for  $[\text{Cu}(\text{phen})(\text{PPh}_3)_2]\text{NO}_3$  at similar purities<sup>315,316</sup>.

#### 5.4.4 Combination of step 1 and step 2

The combined reaction scheme is given below (Scheme 5.6) obtained from the multi-time point optimisation as well as the flow setup required to combine the steps (Figure 5.43). Initially the  $\text{CuI}$  and the acetylene were combined within the same reservoir, however this caused a yellow precipitate to form, attributed to unreactive phenyl copper acetylide<sup>317</sup> necessitating the need for two separate streams for the second step.



Scheme 5.6: Optimised formation of 1-benzyl-4-phenyl-1,2,3-triazole. Conditions generated from Concentration gradient multi-time point reactions.

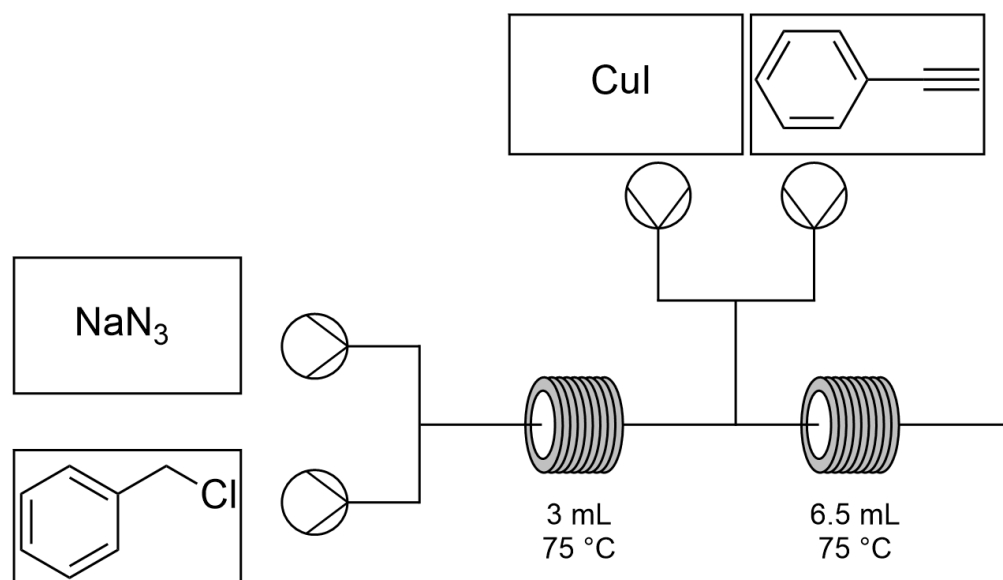


Figure 5.43: Flow setup for continuous formation for 1-benzyl-4-phenyl-1,2,3-triazole. Reaction conditions are from Scheme 5.6.

Unfortunately, upon attempting the continuous reaction, no triazole product was observed. In-line IR placed between the two reactors and post-reaction GC analysis showed excellent conversion to benzyl azide but again no triazole product could be seen.

#### 5.4.4.1 Troubleshooting using gradients

There are two major differences between the combined synthesis and the optimisation process.

1. There is sodium azide present in the second step due to the slight excess in the first step which was not present during the optimisation.
2. An equivalent of chloride ions is also present in the second step from the benzyl chloride starting material.

To test the effect of these, the second step was set up as a standard flow reaction and the concentration gradient method was used to test the robustness of the reaction to different concentrations of sodium azide and chloride ions (Figure 5.44).



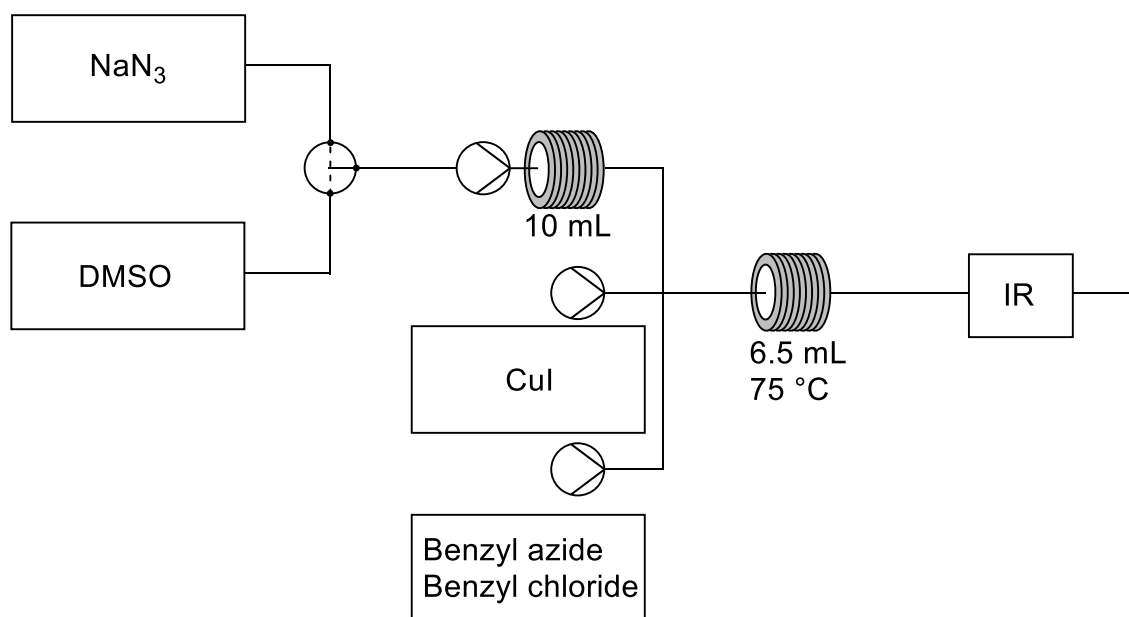


Figure 5.44: Flow setup for the use of gradient troubleshooting. A gradient of  $\text{NaN}_3$  is tested against the steady state conditions from Scheme 5.6.

The concentration gradient with maximum 1 equivalent sodium azide showed an inhibition of the CuAAC reaction reaching full inhibition by 1 equivalents of azide presumably because the azide is acting as a ligand toward the Cu. However the result for the amount present in the two-step synthesis, 0.1 equivalents, inhibits to 55% conversion suggesting that another effect is also inhibiting the reaction. Even so the inhibition by sodium azide can be overcome by lowering the equivalents of sodium azide to 1 during the first step. In practise under these conditions, the reaction still provides zero conversion to the triazole meaning another problem must also be occurring.

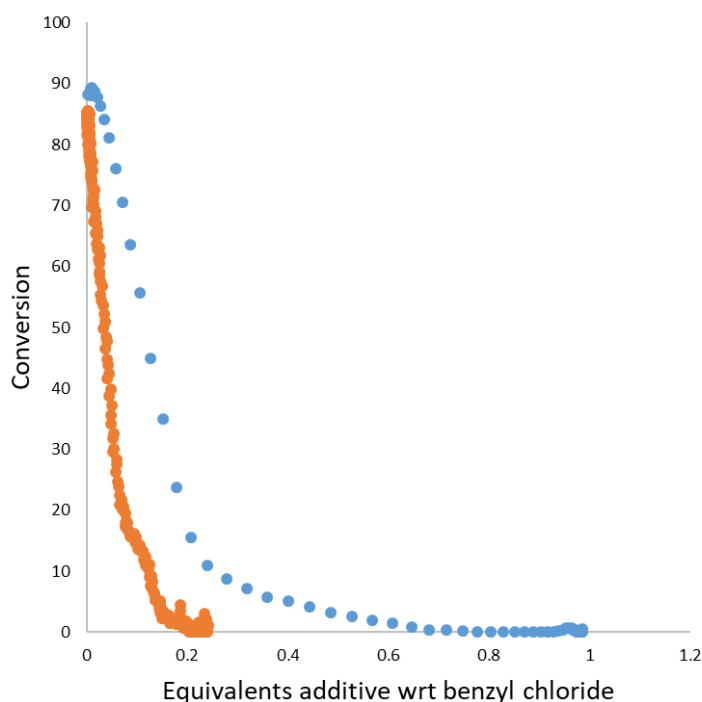


Figure 5.45: Effect of sodium azide (blue) and sodium chloride (orange) on conversion of benzyl azide to 1-benzyl-4-phenyl-1,2,3-triazole. Reaction conditions are from Scheme 5.6. Both additives inhibit the cyclisation reaction.

Testing a gradient of sodium chloride again shows inhibition of the cyclisation however at a much higher rate than that of sodium azide with full inhibition occurring at only 0.2 equivalents of chloride (Figure 5.45). Similar inhibition results have been reported by Moorman *et al*<sup>318</sup> who found that presence of a halide inhibited the CuAAC reaction in water, with iodide fully inhibiting after 5 mol% loading, and bromide and chloride reaching 25 and 20% inhibition at 100 mol% respectively.

#### 5.4.4.2 Testing solutions

To solve this issue, the chloride ions must be removed from the system, or conditions must be found which protect the Cu from the chloride.

The excess halide may be inhibiting the reaction by causing the formation of unreactive polynuclear acetylide complexes<sup>317,319</sup>. As such, protecting the Cu with ligands may prevent the formation of these complexes.

Two commonly used amines were tested DIPEA<sup>320,321</sup> and triethylamine<sup>322</sup> using the concentration gradient additive setup used above. Unfortunately, both showed no effect across the range of concentrations tested, 1 equivalent of triethylamine and 0.5 equivalents of DIPEA.

Phenanthroline has also been reported<sup>323</sup> as a ligand for the CuAAC reaction and testing its effect on the CuAAC reaction did show a small increase in the amount of product seen by GC, and a corresponding decrease in azide (Figure 5.46). However, the results are very erratic and the effect is too small to be useful in the complete reaction setup.

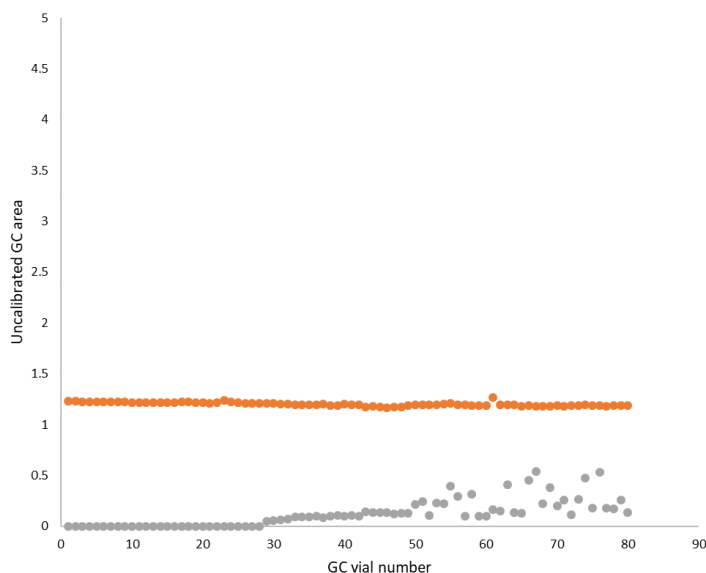


Figure 5.46: Uncalibrated GC showing effect of increasing phenanthroline on formation of 1-benzyl-4-phenyl-1,2,3-triazole. Reaction conditions are from Scheme 5.6. Orange = benzyl azide. Grey = 1-benzyl-4-phenyl-1,2,3-triazole

Ascorbic acid and sodium ascorbate<sup>324</sup> are commonly used in this reaction as reducing agents to convert Cu(II) species into active Cu(I) species. Its presence in this particular reaction condition could be beneficial if the reason for inactivity is the formation of a Cu(II) species. Additionally the ascorbic acid can act as weak bidentate ligand toward the Cu<sup>325</sup> perhaps preventing the formation of the polynuclear acetylide complexes but still allowing the addition of the azide to form the triazole product. Unfortunately, upon testing with a gradient of 1 equivalent ascorbic acid, no beneficial effect is seen.

If the issue is the presence of chloride ions, then removing or exchanging the chloride for a different ion, should alleviate the problem. The inclusion of a packed bed of anion exchange resin in-line prior to the addition of Cu should allow for exchange of the chloride ion preventing the inhibition by the halide. For this purpose, Amberlite IRA-420 was used to exchange the chloride for a hydroxide ion. Calculations based on the resin capacity<sup>326</sup> suggested that 0.789 g per reaction would suffice therefore a packed bed consisting of 2 g of the resin was made. As there was no gradient to test with this setup, the packed bed was placed in-line in a non-dispersed stream of 1 equivalent of chloride ions. Upon pumping of solvent through the resin, the colour changed from a brown-orange to a deep black due to removal of water from the resin. GC of the

reaction mixture again showed no product formation suggesting that the removal of water is affecting the ability to exchange the anions.

Lal *et al* also reported<sup>312</sup> halide inhibition when utilising organic solvents and NaBr as an additive. However, when switching to water as the solvent, no inhibition was seen. Whilst changing solvents between the two steps is feasible, the acetylene and potentially the product would not be soluble, presenting potential problems for continuous flow production. As such a water:DMSO mixture was attempted to see if an improvement in yield would occur. A gradient of water was tested against the optimal second step conditions as well as with  $\text{CuBr}(\text{PPh}_3)_3$  as the source of Cu. The result for CuI shows no impact from moving to a mixed solvent system. Whereas when using  $\text{CuBr}(\text{PPh}_3)_3$  a conversion of 20% is reached based upon the azide GC peak (Figure 5.47). Whilst this is the best result obtained, it is still far below the expected yield.

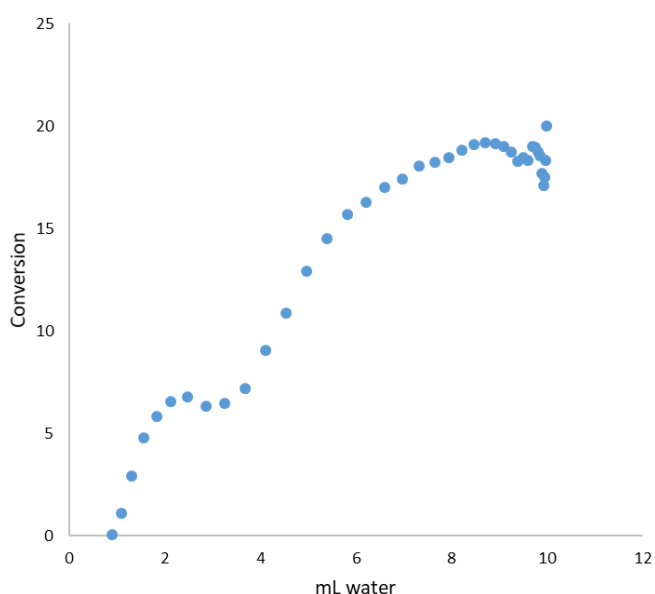


Figure 5.47: Effect of increasing amount of water on formation of 1-benzyl-4-phenyl-1,2,3-triazole. A gradient is created from a solution of 10 mL water in 5 mL DMSO and pumped against the steady state conditions from Scheme 5.6.

There are several potential solutions for the removal of chloride ions including in-line extraction or solvent switch, changing starting material to avoid the halide by-product and use of a different ion exchange material. However, implementing these would be costly and fall outside of the goal of demonstrating the concentration gradient method and the multi-time point method. As such the reaction optimisation was concluded with a need for two separate steps with a work-up in between.

## 5.5 Summary

Two different methodologies have been created for generating multiple time point data in a single reaction without the need for varying flow rate. The first method, the reciprocating time point methodology, utilises valves to reverse the direction of flow repeatedly passing a reaction plug through an in-line detector. The method creates single time points and a time gradient across the steady state of the plug depending on which direction the plug is travelling.

The dual gradient/steady state time point generation allows for added confidence in the measurements obtained as the steady state time points show how much averaging from dispersion has occurred over the plug. However, the time gradient generated made it difficult to incorporate other methodologies with the reciprocating multi-time point methodology.

As such, the second methodology was created, the non-reciprocating multi time point methodology, which again utilises valves to direct a plug repeatedly through a detector. However, this method allows the plug to remain traveling in a single direction ensuring that only single time points are generated each time. The methodology was combined with the concentration gradient methodology to generate vast amounts of both concentration and reaction time data in a single experiment. The combined methodology was used to optimise an  $S_NAr$  reaction with respect to the concentration of pyrrolidine at multiple time points.

These methodologies generate a time and resource saving over traditional steady state methods for obtaining reaction time data as only a single experiment is required rather than the several it would take for steady state methods.

When compared to transient methods such as the push-out method, the transient methods generate more reaction data than the multi-time point methodologies and require less additional equipment to perform. However, the transient methodologies cannot easily be combined with the concentration gradient methodology which means that in order to match the data output of the multi-time point methodologies, tens to hundreds of reactions must be performed.

The combined methodology was taken further by the inclusion of several gradients in a single reaction, allowing for the optimisation of several different reagents in a single reaction. Pyrrolidine, piperidine, and azepane were tested using the multi-gradient methodology in the aforementioned  $S_NAr$  experiment.

The combined methodology was then utilised to optimise the two-step synthesis of 1-benzyl-4-phenyl-1,2,3-triazole from benzyl chloride and phenylacetylene. The concentration of sodium azide was optimised in the first step and three different Cu sources and their concentrations were probed for the second step. In this, a methodology for allowing increased reaction times was

created called the stop flow method which stops the flow whilst the reaction mixture is inside the reactor. The flow is restarted once the needed reaction time is reached with no visible change to the plug due to diffusion.

Unfortunately, the combination of the two optimised steps was unsuccessful. The reaction was troubleshooted using the concentration gradient method and it was found that the presence of excess sodium azide and chloride ions both inhibited the reaction. Several additives were tested using this method however none were successful apart from introducing a mixed solvent system of H<sub>2</sub>O:DMSO however this required switching the Cu source and only generated 20% conversion. Whilst this was not the desired outcome it did effectively show the concentration gradient and multi-time point methodologies usefulness in optimising and troubleshooting a reaction.

## Chapter 6 Conclusion

An investigation was performed into fluid mechanical effects on the meso scale including Dean circulation, the Bodenstein number, the Dean number, tubing internal diameter, molecular radius, flow rate and their effects on Taylor dispersion.

A technique was designed to enable the rapid optimization of irradiance time in flow photochemical reactions using a single experiment by generation of a time gradient. The technique was demonstrated on the [2+2] photocyclisation of diphenylacetylene and 3,4-dihydro-2H-pyran using UVC and UVB irradiation and the robustness of the method was demonstrated by repetition of the reaction with two varying reactors.

A second technique was reported which enabled the investigation of a range of concentrations of a reagent in a single reaction. This was achieved by the generation of concentration gradients by two methods, dispersion and flow rate change. The gradients were utilised in concentration optimisation, ligand screening, functional group scoping and impurity screening for a Sonogashira and Heck cross coupling reaction. Additionally, reaction troubleshooting was performed for a Cu-catalysed triazole formation by screening a range of concentrations of NaCl and NaN<sub>3</sub>. The concentration gradient methodology also has uses in kinetic data extraction, base/acid stability, work-up optimisation, catalyst poisoning studies, and any situation where a range of concentrations needs to be tested. The use of the methodology generates a large time and resource saving over traditional steady state methods with tens to hundreds of steady state experiments needed to match the data output of a single concentration gradient experiment.

A multi-port valve setup was constructed for the generation of multiple time points in a single reaction. Several different designs were shown and two of these setups were used, a reciprocating method which generated a time gradient, and a non-reciprocating method which generated multiple steady state time points. These methodologies in isolation, generate less information than transient flow methodologies such as the push-out methodology. However, these methodologies can be used in combination with other methodologies such as the concentration gradient methodology.

The non-reciprocating time point was used in combination with the concentration gradient method to generate both reagent concentration and reaction time data in a single experiment which was demonstrated in the rapid optimisation of a triazole formation reaction. The methodology was taken a step further and multiple concentration gradients were utilised in the same experiment to optimise three different starting materials in a S<sub>N</sub>Ar reaction. These methodologies can rapidly cover a large portion of a reaction space and optimise several reaction

## Chapter 6

conditions in a single experiment by varying the conditions in each of the concentration gradients. The combination of these methodologies generates a vast amount of information which would require tens of transient reactions to match the output and hundreds of steady state reactions. These methodologies can rapidly cover a large portion of a reaction space and optimise several reaction conditions in a single experiment by varying the conditions in each of the concentration gradients.



## Chapter 7 Experimental

Experimental information	Section
Instrumentation, techniques and data interpretation	7.1
Procedures	7.2
Data from fluid mechanics characterisation	7.2.1
Data from switch-off methodology	7.2.2
Representative data handling and calibration curve for switch-off experiments.	7.2.2.1
Data from concentration gradient experiments	7.2.3
Representative data handling, calibration curve and GC for concentration gradient experiment.	7.2.3.1
Data from multi-time point experiments.	7.2.4
Python scripts and RS232 commands	7.3

### 7.1 Instrumentation and techniques

#### 7.1.1 NMR

NMR spectra were obtained on a Bruker AV300 or DPX400 MHz spectrometer as stated.  $^1\text{H}$  chemical shifts are reported as values in ppm referenced to  $\text{CHCl}_3$  impurity present. The following abbreviations are used to assign multiplicity: s = singlet, d = doublet. Coupling constants, J, are measured in Hertz (Hz).  $^{13}\text{C}$  spectra are proton decoupled and referenced to solvent.  $^{13}\text{C}$  resonances are reported as C, CH,  $\text{CH}_2$  or  $\text{CH}_3$  depending on the number of directly attached protons (0, 1, 2, 3 respectively) as determined by DEPT experiments.

#### 7.1.2 Mass Spectrometry

Low resolution mass spectrometry samples were analysed using a Waters (Manchester, UK) TQD mass spectrometer equipped with a triple quadrupole analyser. Samples were introduced to the mass spectrometer *via* an Acquity H-Class quaternary solvent manager (with TUV detector at

254nm, sample and column manager). Ultra-performance liquid chromatography was undertaken *via* a Waters BEH C18 column (50 mm x 2.1mm 1.7µm). Gradient 20% acetonitrile (0.2% formic acid) to 100% acetonitrile (0.2% formic acid) in five minutes at a flow rate of 0.6 mL/min. Low resolution mass spectra were recorded using positive ion electrospray ionisation.

### 7.1.3 Chromatography

Thin layer chromatography was carried out on Merck silica gel plates, which were visualised under UV irradiation of 254 nm and/or by staining with aqueous KMnO<sub>4</sub>, methanolic H<sub>2</sub>SO<sub>4</sub>, PMA or iodine. Column chromatography was performed with Merck silica gel 60 using solvent ratios as volumes before mixing described in the method.

### 7.1.4 Solvents and reagents

3,4-Dihydro-2H-pyran, pyrrolidine, piperidine, azepane and DBU were distilled over CaH<sub>2</sub> prior to use. Otherwise reagents were used as received from suppliers.

### 7.1.5 Inert atmosphere

If the use of inert atmosphere was reported, reactions were performed under a N<sub>2</sub> atmosphere using standard Schlenk equipment and techniques. Glassware was oven dried at 150 °C overnight prior to use.

### 7.1.6 Flow equipment

Flow chemistry reactions were performed using a Vapourtec R2/R4 system. Flow rates below 0.1 mL/min were provided *via* two V6 Kloehe syringe pumps.

Reaction heating was provided *via* the Vapourtec air heater or *via* submersing in an oil bath placed on a hot plate with heating controlled *via* a probe submersed in the bath. Reactors used were synthesised from PFA or stainless steel depending on the required reaction conditions.

Photochemical reactions were performed using the equipment described in section 3.2.2.

In-line UV spectra were collected using an Ocean Optics DH-2000-BAL spectrometer integrated into the flow with Starna® fluorimeter flow cells type 584.4 with a path length of 0.1, 0.01 or 1 mm.

In-line IR spectra were obtained using an alpha transmission FT-IR from Bruker combined with a Harrick DLC2™ demountable liquid flow cell with sodium chloride plates.

Samples for offline GC analysis were collected using a Gilson Prep FC fraction collector. GC analysis was performed on a Hewlett Packard HP 6890 series GC system, using a HP-5, 30 m column, consisting of a film thickness of 0.25  $\mu\text{m}$  and 0.32 mm internal diameter. The carrier gas was helium and the flow rate was 2.7  $\text{mL min}^{-1}$ . The injector is maintaining at 300  $^{\circ}\text{C}$  with 1  $\mu\text{L}$  injection. The run start at 80  $^{\circ}\text{C}$  with a gradient of 25  $^{\circ}\text{C/min}$  until 275  $^{\circ}\text{C}$  which is held for 4 minutes.

### 7.1.7 Data interpretation

In-line UV and IR data was interpreted using the Bristol Online Reaction Investigation Software (BORIS). Spectra were either interpreted *via* peak picking or orthogonal projection approach. Data extracted using BORIS was exported to an excel spreadsheet. Off-line GC data was collected using a gradient method starting from 80  $^{\circ}\text{C}$  and increasing by 25  $^{\circ}\text{C/min}$  to a maximum of 275  $^{\circ}\text{C}$ . Areas of peaks were normalised to an internal standard and if necessary, a calibration curve was created to extract yields from the data.

Multi-time point data was manipulated using custom Python scripts (See section 6.3.3).

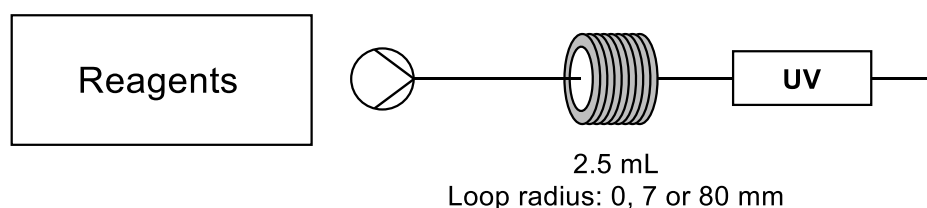
### 7.1.8 Data storage

Processed data and python scripts used in this thesis are stored in the University of Southampton institutional repository<sup>327</sup>. On request, raw data can be obtained by emailing Richard Whitby (R.J.Whitby@soton.ac.uk) or Stephen Alston (S.Alston@soton.ac.uk).

## 7.2 Procedures

### 7.2.1 C1: Fluid mechanics

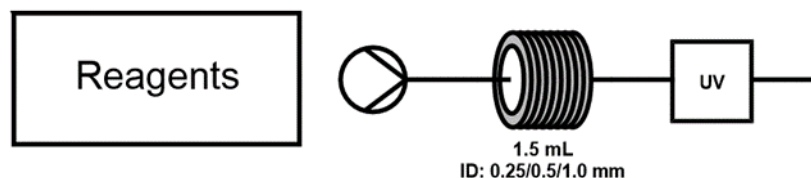
#### 7.2.1.1 Measuring the effects of Dean circulation



Methyl orange (0.035 g, 0.107 mmol) was dissolved in 10 mL DMSO. 0.3 mL plugs of this stock solution were syringed into a 0.1 mL sample loop attached to the flow setup above. Three 2.5 mL reactors were tested with 7 and 80 mm coil radius and a linear tube with flow rates of 0.1, 2 and

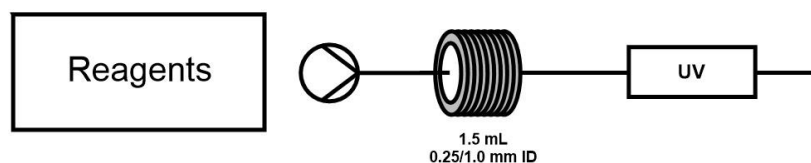
10 mL/min. In-line UV spectra was obtained with a 1 second delay between spectra. Data obtained was compared to a standard 'zero dispersion' run consisting of no reactor to obtain percentage dispersion values.

### 7.2.1.2 Measuring the effect of internal diameter



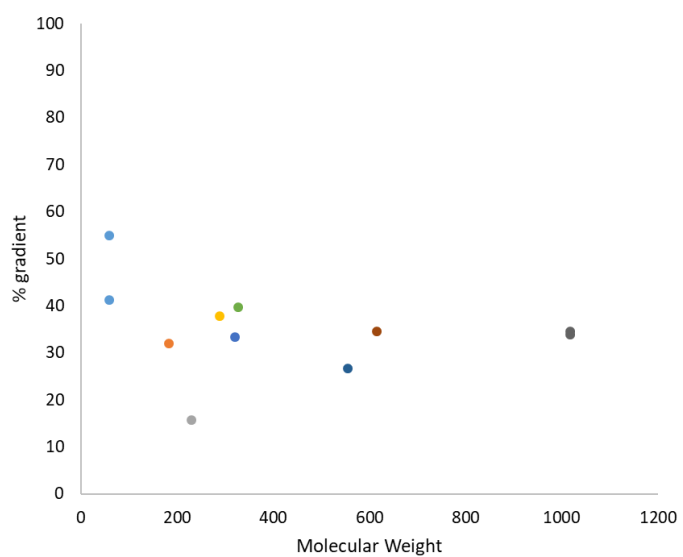
Rose Bengal (0.004 g, 0.004 mmol) was dissolved to 10 mL MeCN. 0.1 mL plugs of this solution were pumped into the flow setup above with different loop ID (0.25, 0.5, 1.0 mm) and different flow rates (0.1, 0.5, 1.0, 2.0, 5.0, 10.0 mL/min). In-line UV analysis was used with a 1 second delay between spectra. Data was manipulated as with 6.2.1.1.

### 7.2.1.3 Measuring the effect of molecular weight

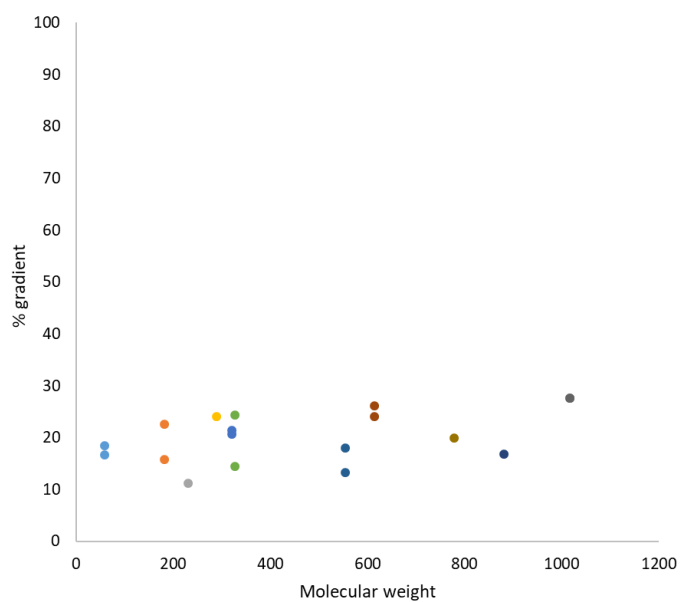


The reagent was dissolved in 20 mL MeCN and 0.3 mL plugs of this stock solution were syringed into a 0.1 mL sample loop attached to the flow setup above. The plug was pumped at various flow rates and reactor dimensions used to vary the Dean number. In-line UV spectra was obtained with a 1 second delay between spectra. Data was manipulated as with 6.2.1.1.

Data from 0.1 mL/min using a 1.0 mm ID reactor:

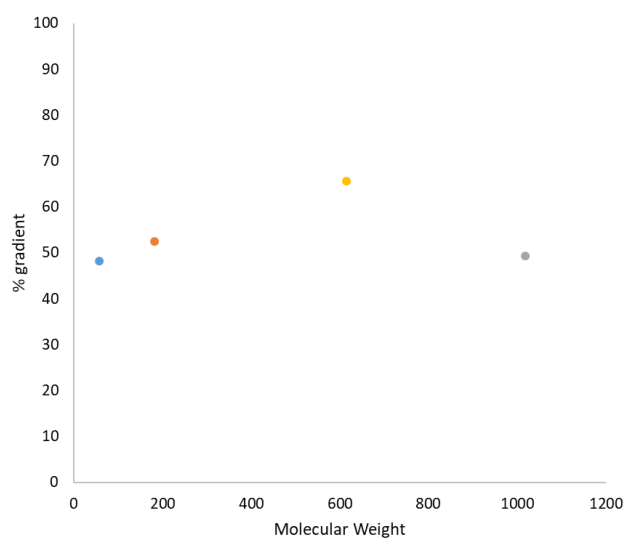


Data from 0.5 mL/min using a 1.0 mm ID reactor:

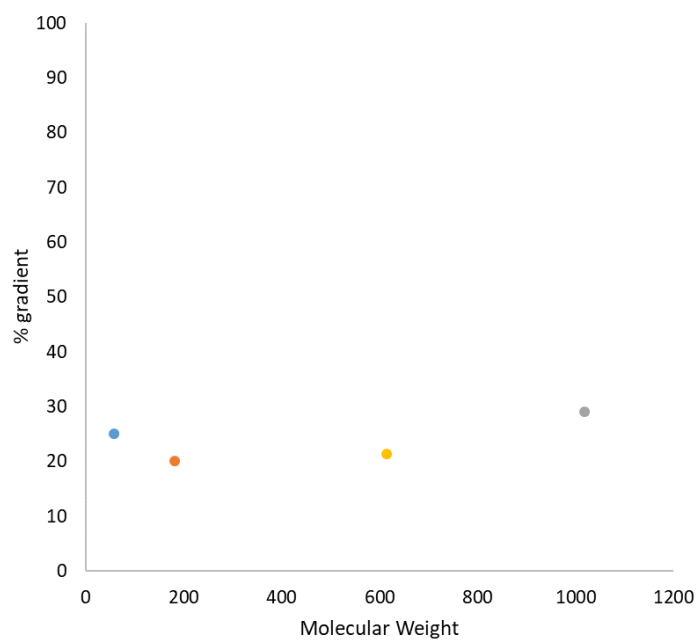


Data from 0.01 mL/min using a 0.25 mm ID reactor:

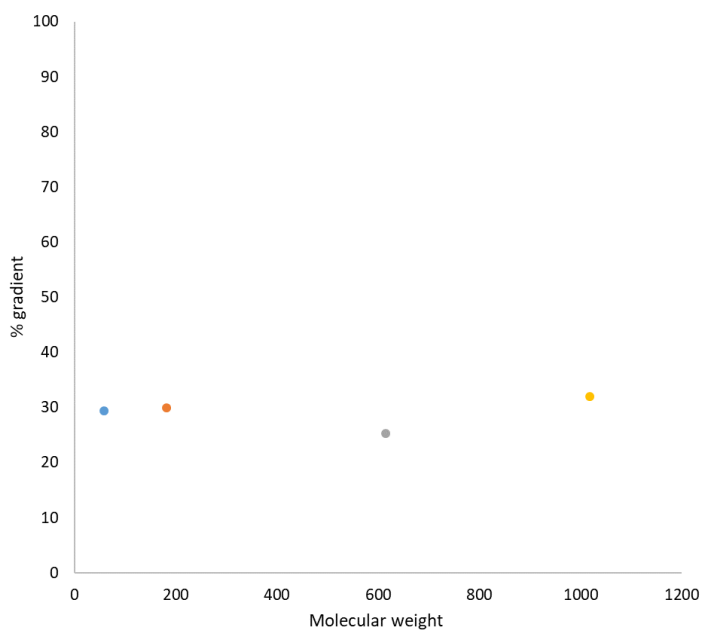
## Chapter 7



Data from 0.1 mL/min using a 0.25 mm ID reactor:

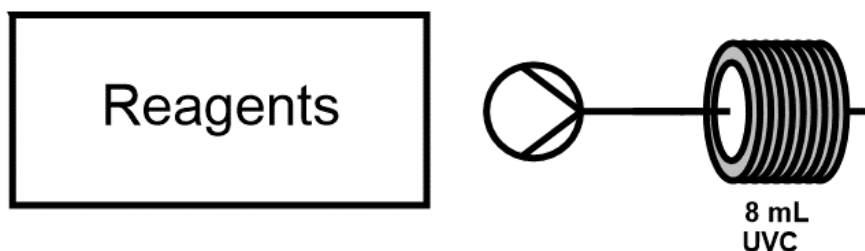


Data from 0.01 mL/min using a 1.0 mm ID reactor:



## 7.2.2 C2: Switch-off

### 7.2.2.1 Switch-off reaction of 3,4-dihydro-2H-pyran and diphenylacetylene



UVC:

Diphenylacetylene (0.200 g, 1.12 mmol) was dissolved in 20 mL 3,4-dihydro-2H-pyran in a round bottom flask. The UVC lamp was prewarmed 30 minutes prior to the reaction start. After this, the solution was pumped into the reactor at 0.1 mL/min until 2x reactor volumes had been pumped through. At this point the light source is turned off and collection *via* fraction collector is started.

Raw GC data is converted into yield *via* use of a calibration curve and internal standard and irradiance time is calculated using the maximum irradiance time calculated from the reactor volume and flow rate.

Irradiance time	Diphenylacetylene	Mono addition	Bis addition	n(Pdt)	Yield
118	0	0.901352	0.18934	5.20068E-06	59.09865

## Chapter 7

116.4	0	0.901064	0.200532	5.19902E-06	59.07973
114.8	0	0.90567	0.203498	5.2256E-06	59.38176
113.2	0	0.909398	0.206747	5.2471E-06	59.62614
111.6	0	0.929807	0.212556	5.36486E-06	60.96433
110	0	0.926533	0.210576	5.34597E-06	60.74962
108.4	0	0.92957	0.211788	5.3635E-06	60.94881
106.8	0	0.925725	0.214221	5.34131E-06	60.69665
105.2	0	0.935241	0.205823	5.39621E-06	61.32061
103.6	0	0.935423	0.208236	5.39727E-06	61.33257
102	0	0.946303	0.205546	5.46004E-06	62.0459
100.4	0	0.950976	0.20699	5.487E-06	62.3523
98.8	0	0.945902	0.202459	5.45772E-06	62.01959
97.2	0	0.952441	0.202862	5.49546E-06	62.44836
95.6	0	0.963109	0.198946	5.55701E-06	63.14784
94	0	0.972775	0.199919	5.61278E-06	63.78161
92.4	0.005637	0.970078	0.19948	5.59722E-06	63.60476
90.8	0.006287	0.976111	0.195725	5.63203E-06	64.00029
89.2	0.006891	0.975498	0.190658	5.62849E-06	63.96011
87.6	0.007471	0.987023	0.190326	5.69499E-06	64.71579
86	0.007978	0.999202	0.186677	5.76526E-06	65.51433
84.4	0.009864	1.002466	0.178381	5.78409E-06	65.72833
82.8	0.010501	1.011712	0.177706	5.83744E-06	66.33458
81.2	0.01207	1.022677	0.168617	5.90071E-06	67.05352
79.6	0.013271	1.035519	0.168618	5.9748E-06	67.89551
78	0.015106	1.038142	0.161254	5.98994E-06	68.06748
76.4	0.017256	1.04616	0.156169	6.0362E-06	68.59323
74.8	0.019139	1.045237	0.1505	6.03088E-06	68.53268
73.2	0.021647	1.057725	0.147284	6.10293E-06	69.35147
71.6	0.025996	1.068763	0.141719	6.16662E-06	70.0752
70	0.028771	1.062885	0.134813	6.1327E-06	69.68982



68.4	0.032743	1.070493	0.12943	6.1766E-06	70.18863
66.8	0.037879	1.083694	0.123377	6.25277E-06	71.05418
65.2	0.043231	1.08722	0.121729	6.27311E-06	71.28538
63.6	0.047951	1.08082	0.115623	6.23618E-06	70.86572
62	0.054823	1.080791	0.108409	6.23602E-06	70.86386
60.4	0.060525	1.072707	0.102398	6.18937E-06	70.33376
58.8	0.067969	1.060156	0.096094	6.11696E-06	69.51088
57.2	0.076745	1.085676	0.096924	6.26421E-06	71.18416
55.6	0.086085	1.091021	0.091947	6.29504E-06	71.5346
54	0.09922	1.097348	0.087363	6.33155E-06	71.94941
52.4	0.108319	1.077419	0.082852	6.21656E-06	70.64277
50.8	0.118483	1.075491	0.079892	6.20544E-06	70.51632
49.2	0.129612	1.066047	0.075659	6.15094E-06	69.89709
47.6	0.140887	1.050246	0.07225	6.05978E-06	68.86112
46	0.155634	1.050897	0.06855	6.06353E-06	68.90381
44.4	0.171352	1.028112	0.065261	5.93207E-06	67.40988
42.8	0.186897	1.019655	0.06069	5.88327E-06	66.85536
41.2	0.205334	0.999679	0.056877	5.76801E-06	65.54557
39.6	0.229242	0.984055	0.052046	5.67787E-06	64.5212
38	0.249338	0.97351	0.049007	5.61702E-06	63.82977
36.4	0.270556	0.945586	0.041717	5.45591E-06	61.99893
34.8	0.298697	0.926829	0.039759	5.34768E-06	60.76908
33.2	0.323362	0.910559	0.037092	5.2538E-06	59.70232
31.6	0.348198	0.868357	0.033293	5.0103E-06	56.93523
30	0.378067	0.84641	0.030597	4.88367E-06	55.49627
28.4	0.409077	0.809794	0.028068	4.6724E-06	53.09547
26.8	0.44832	0.788437	0.024225	4.54917E-06	51.69514
25.2	0.482781	0.738931	0.023286	4.26353E-06	48.44921
23.6	0.516955	0.693218	0.019834	3.99977E-06	45.45199
22	0.571386	0.665378	0.016657	3.83914E-06	43.62658

20.4	0.608247	0.605891	0.014138	3.49591E-06	39.72624
18.8	0.655084	0.559385	0.012532	3.22757E-06	36.67698
17.2	0.694063	0.502813	0.01	2.90116E-06	32.96773
15.6	0.74413	0.449039	0.00667	2.5909E-06	29.44201
14	0.801037	0.397926	0.006481	2.29598E-06	26.09068
12.4	0.840526	0.336394	0.005204	1.94095E-06	22.05624
10.8	0.893889	0.275768	0.003649	1.59114E-06	18.08116
9.2	0.950311	0.215025	0	1.24067E-06	14.09848
7.6	0.990849	0.160709	0	9.2727E-07	10.53716
6	1.044302	0.110883	0	6.39783E-07	7.270257
4.4	1.076017	0.071981	0	4.15322E-07	4.719563
2.8	1.104599	0.045149	0	2.60501E-07	2.960244
1.2	1.110236	0.026247	0	1.5144E-07	1.720909

Table 7.1: GC data obtained vials collected during switch-off experiment. Data is relative to an internal standard. Yield is calculated via a calibration curve. Reaction conditions in Section 7.2.2.1.

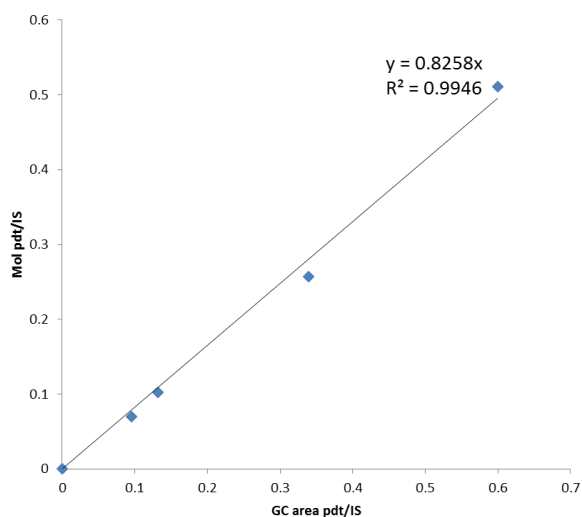


Figure 7.1: GC calibration curve for calculating yield of 7,8-diphenyl-2-oxabicyclo[4.2.0]oct-7-ene

UVB:

Diphenylacetylene (0.200 g, 1.112 mmol) was dissolved in 20 mL 3,4-dihydro-2H-pyran in a round bottom flask. The solution was used as with UVC method except with a UVB lamp for irradiation.

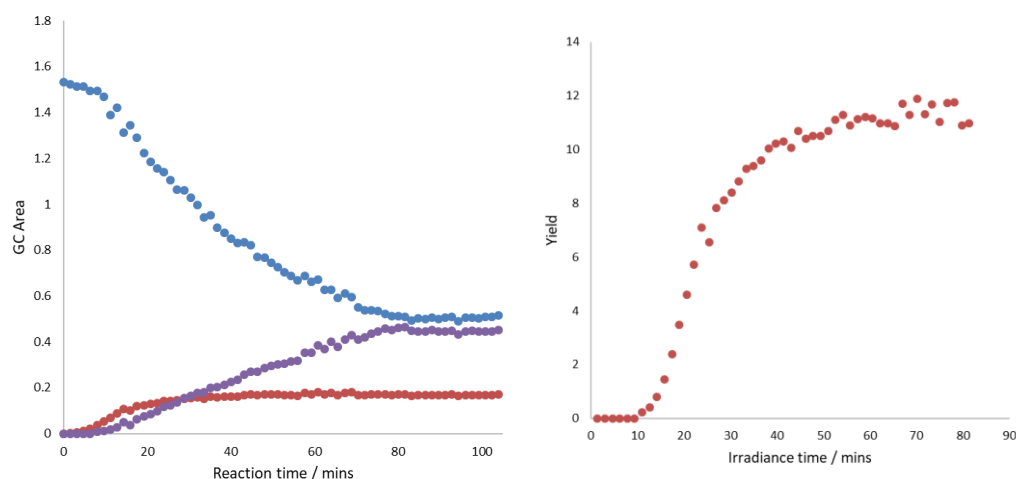
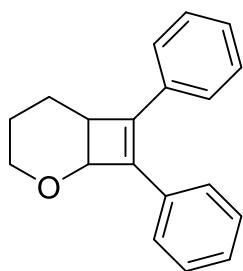


Figure 7.2: Left: GC data from switch off experiment relative to an internal standard. Right = Yield calculated from GC data. Blue = Diphenylacetylene. Red = **7.2.2.2** Purple = **7.2.2.3**

### 7.2.2.2 Synthesis of 7,8-diphenyl-2-oxabicyclo[4.2.0]oct-7-ene



Diphenylacetylene (1.01 g, 5.66 mmol) was dissolved in 132 mL of 3,4-dihydro-2H-pyran. The solution was pumped into an 8 mL UV reactor at 0.16 mL/min, using a UVC lamp for irradiation. The steady state of the reaction was collected according to FlowCommander. The solution was concentrated and purified *via* column chromatography (toluene) giving a white solid of title compound (0.811 g, 54.6 % yield)

Addition of methanol to a yellow oil obtained from the column and leaving in a freezer overnight resulted in the formation of further title compound as a white solid (0.148 g, 9.97% yield, 64.6% total yield).

NMR is consistent with the literature<sup>328</sup>

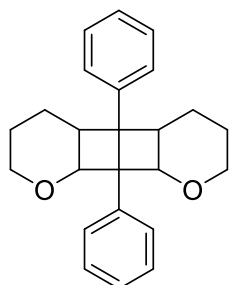
<sup>1</sup>H NMR (400 MHz, CDCl<sub>3</sub>): δ 7.57-7.20 (m, 10H), 4.75 (d, 1H), 3.74 (m, 2H), 3.21 (m, 1H), 2.1-1.5 (m, 4H) ppm.

<sup>13</sup>C NMR (101 MHz, CDCl<sub>3</sub>): δ 143.75, 140.69, 134.91, 134.64, 129.12, 128.59, 128.40, 127.96, 126.94, 126.67, 70.67, 61.90, 40.48, 23.01, 21.53 ppm.

UV (MeCN):  $\lambda_{\text{max}}$ : 300 nm,  $\varepsilon = 9481.67 \text{ M}^{-1} \cdot \text{cm}^{-1}$

MS: LRMS (ESI)  $m/z$  263.3  $[\text{M}+\text{H}]^+$

**7.2.2.3 Synthesis of 4b,8b-diphenyldecahydro-2H,4bH-pyrano[2'',3'':3',4']cyclobuta[1',2':3,4]cyclobuta[1,2-b]pyran**



7,8-Diphenyl-2-oxabicyclo[4.2.0]oct-7-ene (0.131 g, 0.499 mmol) was dissolved in 8.95 mL 3,4-dihydro-2H-pyran. The solution was pumped into a 32 mL UV reactor at 0.1 mL/min giving an irradiance time of 320 minutes, using a UVB lamp for irradiation. The steady state of the reaction was collected according to FlowCommander. The solution was concentrated and purified *via* column chromatography (9:1 toluene:EtOAc) giving a colourless oil of title compound (0.037 g, 21.4 % yield)

$^1\text{H}$  NMR (400 MHz,  $\text{CDCl}_3$ ):  $\delta$  7.56-6.88 (m, 10 H), 4.49 (d,  $J=5.4$  Hz, 2 H), 3.49 - 3.34 (m, 2 H), 3.28 - 3.14 (m, 2 H), 2.69 (td,  $J=7.5, 5.5$  Hz, 2 H), 1.69 -1.11 (m, 8 H) ppm.

$^{13}\text{C}$  NMR (101 MHz,  $\text{CDCl}_3$ ):  $\delta$  138.65 (C), 136.49 (C), 129.54 (CH), 127.29 (CH), 125.86 (CH), 125.81 (CH), 74.98 (CH), 63.98 (C), 63.14 ( $\text{CH}_2$ ), 59.27 (C), 42.73 (CH), 21.42 ( $\text{CH}_2$ ), 20.34 ( $\text{CH}_2$ ) ppm.

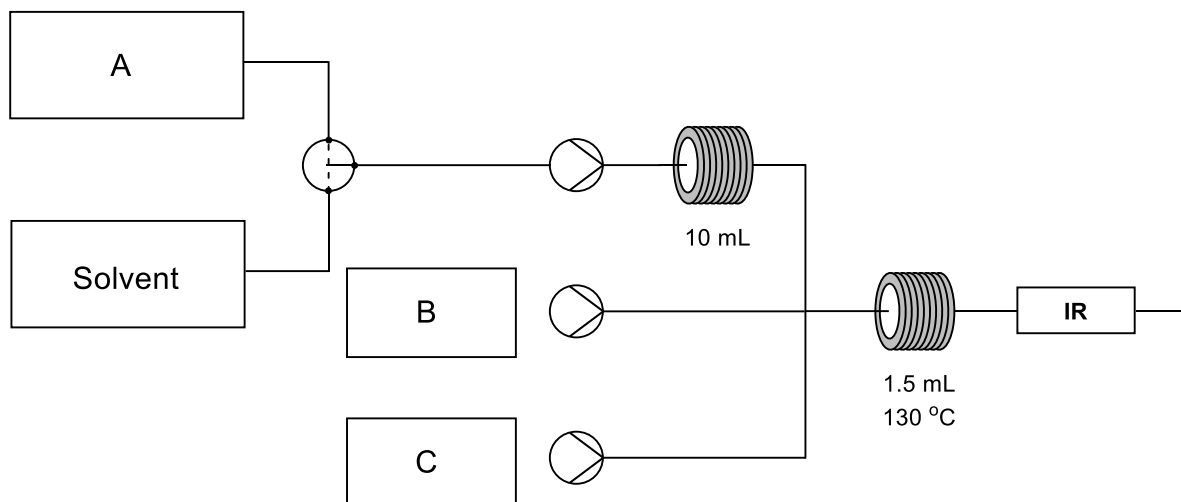
IR:  $\nu_{\text{max}}$  (neat)/ $\text{cm}^{-1}$  2948.94 (M), 2844.95 (M), 1494.80 (S), 1129.00 (S), 1087.93 (S), 1061.61 (S), 760.65 (M), 731.16 (M), 701.57 (S)

MS: LRMS (ESI)  $m/z$  347.3  $[\text{M}+\text{H}]^+$

HRMS (ESI) Found 369.1821  $[\text{M}+\text{Na}]^+$  Calculated 369.1825

### 7.2.3 C3: Concentration gradient

#### 7.2.3.1 Concentration gradient of $\text{Pd}(\text{OAc})_2$



Dispersion profile:

A dispersion profile was created of the flow setup above using diphenylfulvene (0.010 g, 0.043 mmol) in 20 mL DMF pumped at 0.1 mL/min using in-line UV to monitor. The UV was then replaced with IR for the reaction.

Reaction:

0.055 g  $\text{Pd}(\text{OAc})_2$  was dissolved in 15 mL DMF.

In a rbf, 2.06 mL of this solution was added to 12.94 mL DMF in line A.

In a second rbf, (2.41 g, 7.48 mmol) TBAB, 0.95 mL veratrole, (1.66 mL, 9.68 mmol) iodobenzene, (1.08 mL, 7.53 mmol) n-butyl acrylate were added to 15 mL DMF and attached to line B

In a third rbf, 1.8 mL  $\text{NEt}_3$  was added to 15 mL DMF and attached to line C.

15 mL plugs were pumped from the solutions into the flow setup at 0.1 mL/min, giving a reaction time of 5 minutes. Lines B and C had a delay of 4.7 mL.

Reaction progress was monitored by in-line IR, 4 sec delay and offline GC *via* 0.2 mL samples taken from 95.13 minutes after pumping is started.

Time	Acrylate	Iodobenzene	Product	mol prod	Yield
95.13	0.811465	1.747881	0	0	0
95.81	0.811625	1.748445	0	0	0
96.48	0.820263	1.756265	0	0	0

## Chapter 7

97.16	0.820072	1.756781	0	0	0
97.83	0.825785	1.76071	0	0	0
98.51	0.821979	1.762101	0	0	0
99.18	0.822466	1.759293	0	0	0
99.86	0.822513	1.759579	0	0	0
100.53	0.830629	1.77083	0	0	0
101.21	0.81667	1.758836	0	0	0
101.88	0.834418	1.777449	0	0	0
102.56	0.834359	1.778618	0	0	0
103.23	0.833129	1.779955	0	0	0
103.91	0.82716	1.775781	0	0	0
104.58	0.838013	1.781433	0	0	0
105.26	0.835836	1.782299	0	0	0
105.93	0.842013	1.787213	0	0	0
106.61	0.83596	1.778788	0.003434	3.05E-07	0.190881
107.28	0.834447	1.783445	0.00554	4.93E-07	0.307922
107.96	0.831698	1.779171	0.009451	8.4E-07	0.525293
108.63	0.829354	1.774756	0.015362	1.37E-06	0.853834
109.31	0.831318	1.779258	0.027055	2.41E-06	1.503702
109.98	0.818284	1.762645	0.043462	3.86E-06	2.415616
110.66	0.80287	1.749238	0.068341	6.08E-06	3.798382
111.33	0.789871	1.730783	0.099318	8.83E-06	5.520068
112.01	0.775601	1.716835	0.140807	1.25E-05	7.826043
112.68	0.74525	1.681055	0.191293	1.7E-05	10.63207
113.36	0.725795	1.65983	0.245381	2.18E-05	13.63826
114.03	0.695463	1.627926	0.304123	2.7E-05	16.90314
114.71	0.659792	1.588489	0.380475	3.38E-05	21.14682
115.38	0.613645	1.538873	0.485125	4.31E-05	26.96324
116.06	0.553885	1.475845	0.61098	5.43E-05	33.95825
116.73	0.485355	1.394732	0.752506	6.69E-05	41.82431

117.41	0.409621	1.318435	0.921738	8.2E-05	51.23017
118.08	0.333617	1.236014	1.04557	9.3E-05	58.11281
118.76	0.25807	1.152666	1.244694	0.000111	69.1801
119.43	0.194597	1.08621	1.382525	0.000123	76.84072
120.11	0.143557	1.027984	1.488696	0.000132	82.7417
120.78	0.103961	0.979069	1.571873	0.00014	87.36472
121.46	0.075866	0.952172	1.634598	0.000145	90.85094
122.13	0.056398	0.925561	1.674348	0.000149	93.06027
122.81	0.040361	0.908479	1.702248	0.000151	94.61095
123.48	0.029502	0.895139	1.720575	0.000153	95.62954
124.16	0.022996	0.887599	1.743606	0.000155	96.90964
124.83	0.016667	0.874561	1.74807	0.000155	97.15774
125.51	0.01229	0.869149	1.753118	0.000156	97.43828
126.18	0.008233	0.858053	1.755145	0.000156	97.55098
126.86	0.007603	0.853185	1.766853	0.000157	98.20166
127.53	0.004082	0.844421	1.759147	0.000156	97.7734
128.21	0.003556	0.845867	1.763022	0.000157	97.98878
128.88	0	0.839939	1.760676	0.000157	97.8584
129.56	0	0.834379	1.762054	0.000157	97.93497
130.23	0	0.83315	1.765385	0.000157	98.12008
130.91	0	0.830594	1.757145	0.000156	97.66212
131.58	0	0.826971	1.763961	0.000157	98.04093
132.26	0	0.827118	1.756624	0.000156	97.63317
132.93	0	0.823936	1.755144	0.000156	97.55089
133.61	0	0.82203	1.752845	0.000156	97.42311
134.28	0	0.817636	1.753979	0.000156	97.48613
134.96	0	0.8162	1.754639	0.000156	97.52285
135.63	0	0.81891	1.751048	0.000156	97.32327
136.31	0	0.816234	1.750067	0.000156	97.26872
136.99	0	0.813013	1.751082	0.000156	97.32513

## Chapter 7

137.66	0	0.814495	1.747886	0.000155	97.14751
138.34	0	0.815304	1.750435	0.000156	97.28917
139.01	0	0.817033	1.752381	0.000156	97.39733
139.69	0	0.812424	1.7442	0.000155	96.94265
140.36	0	0.816842	1.748134	0.000155	97.16129
141.04	0	0.818182	1.743992	0.000155	96.93106
141.71	0	0.815058	1.749161	0.000156	97.21838

Table 7.2: GC data from the Heck reaction with a concentration gradient of  $\text{Pd}(\text{OAc})_2$ . GC areas are relative to an internal standard. Yield is calculated using a calibration curve. Reaction conditions in Section 7.2.3.1

GC data is converted to yield *via* a calibration curve relative to an internal standard.

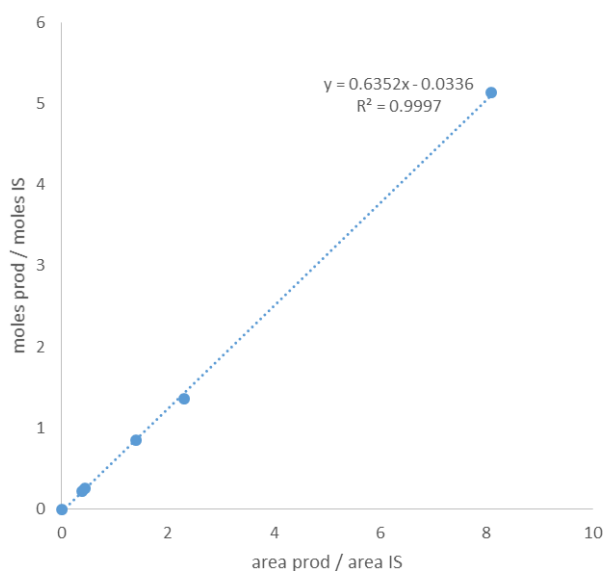


Figure 7.3: Calibration curve for calculating yield of butyl cinnamate

Sample GC trace:



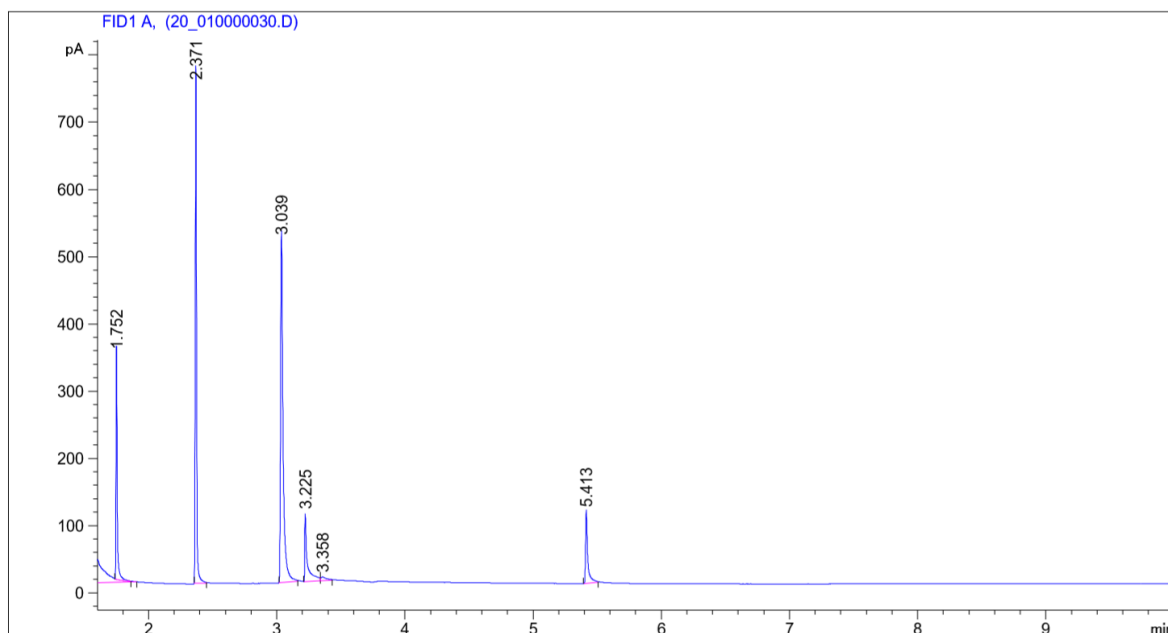
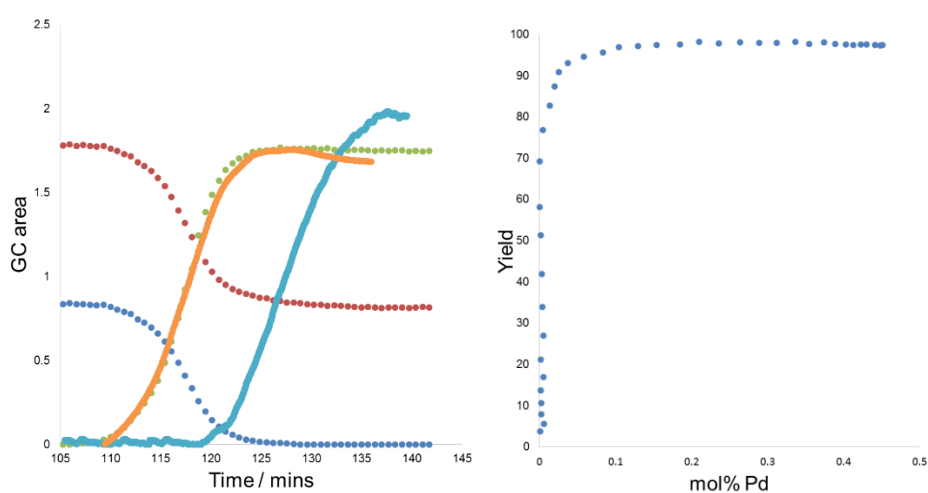
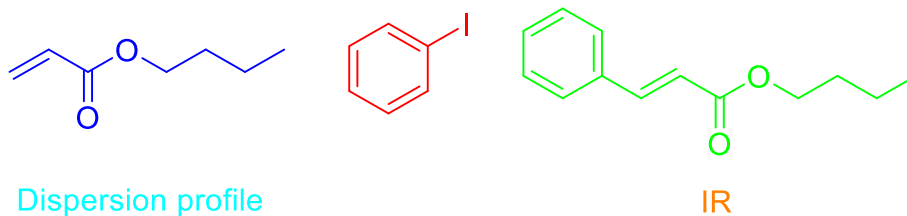


Figure 7.4: Representative GC of Heck reaction. 1.752: Butyl acrylate. 2.371: Iodobenzene. 3.039: Veratrole. 5.413: Butyl cinnamate

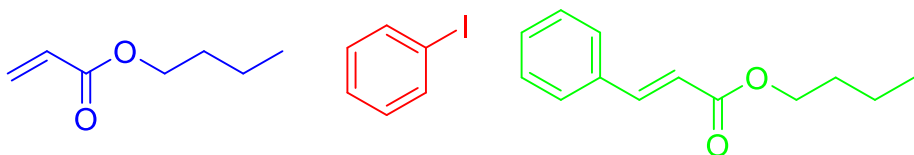
The dispersion profile was overlaid with the GC data lining up the experimental time from both experiments. Trend lines for the dispersion profile were then used to calculate the concentration at set experimental time which was then combined with the GC data to generate yield at each concentration.



### 7.2.3.2 Concentration gradient of Pd sources

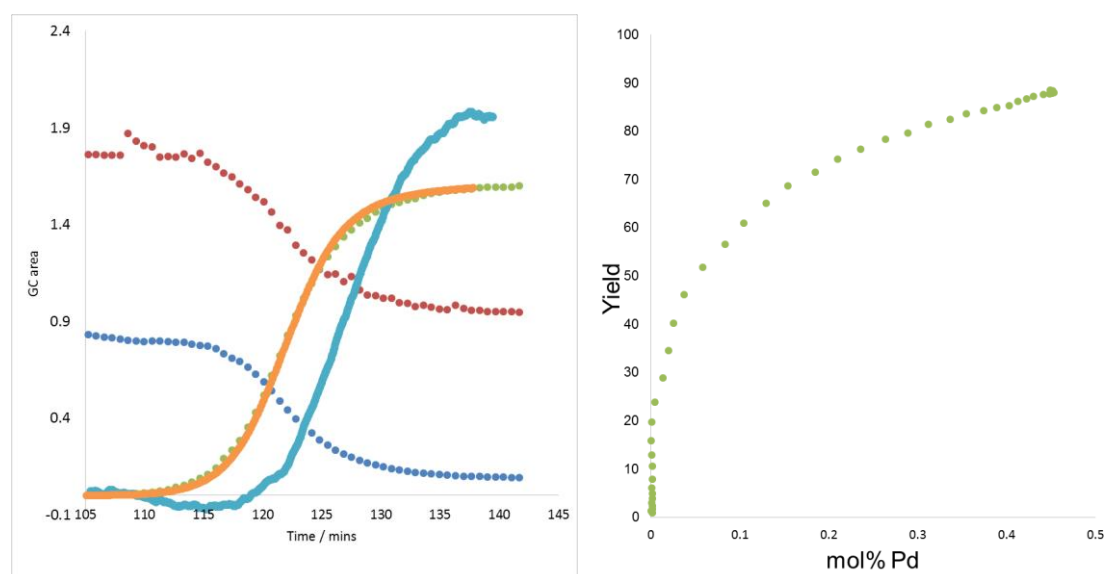
#### 7.2.3.2.1 Pd(dppf)Cl<sub>2</sub>

(0.024 g, 0.033 mmol) Pd(dppf)Cl<sub>2</sub> was dissolved in 15 mL DMF and same procedure as Pd(OAc)<sub>2</sub> was followed.



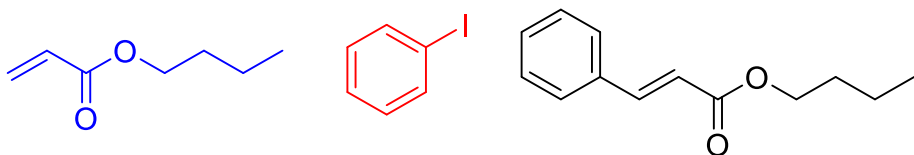
Dispersion profile

IR



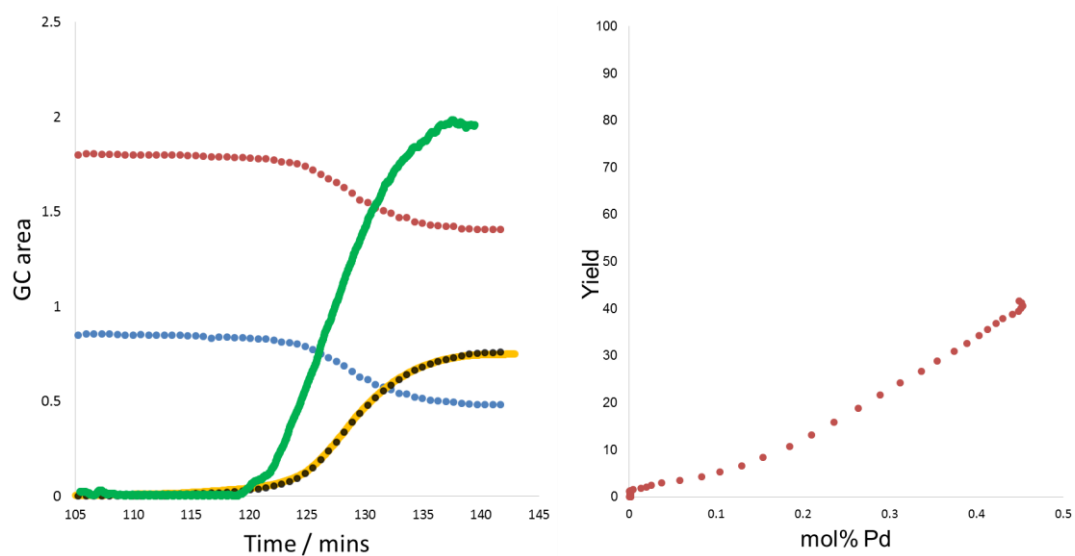
#### 7.2.3.2.2 PdCl<sub>2</sub>(PPh<sub>3</sub>)<sub>2</sub>

(0.023 g, 0.033 mmol) PdCl<sub>2</sub>(PPh<sub>3</sub>)<sub>2</sub> was dissolved in 15 mL DMF and same procedure as Pd(OAc)<sub>2</sub> was followed.



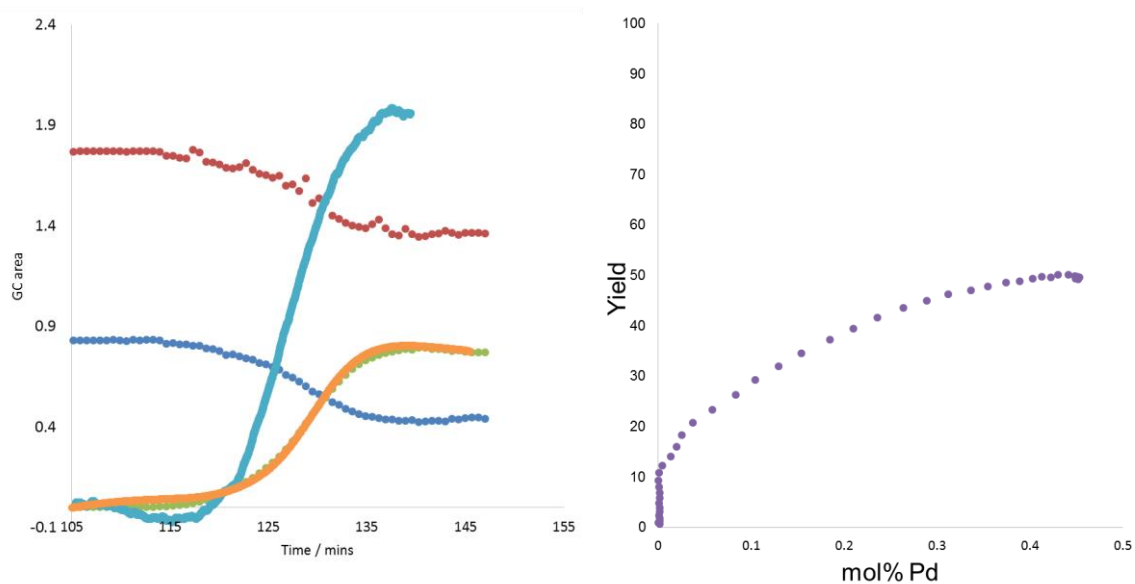
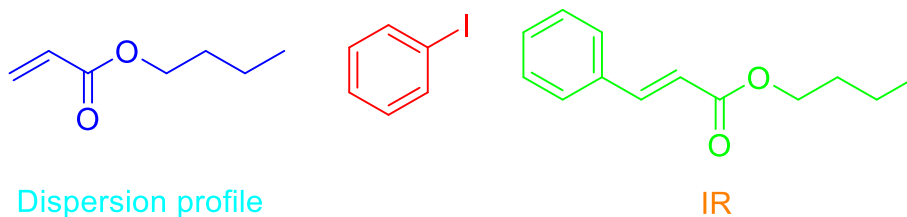
Dispersion profile

IR



### 7.2.3.2.3 Allylchloropalladium dimer

(0.006 g, 0.016 mmol) allylchloropalladium dimer was dissolved in 15 mL DMF and same procedure as  $\text{Pd}(\text{OAc})_2$  was followed.



## 7.2.3.3 Concentration gradient of ligands

7.2.3.3.1  $\text{PPh}_3$ 

In a rbf, (0.104 g, 0.397 mmol)  $\text{PPh}_3$  was dissolved in 10 mL DMF and attached to line A.

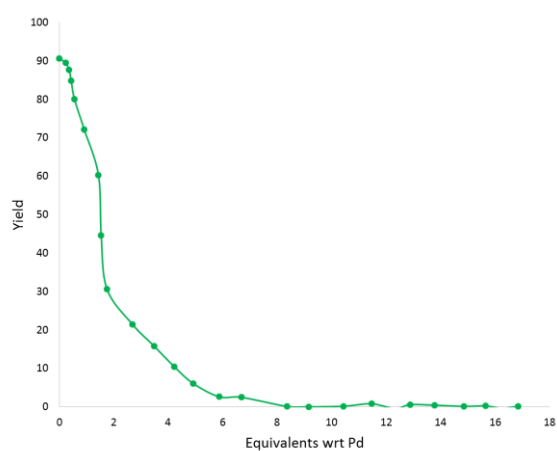
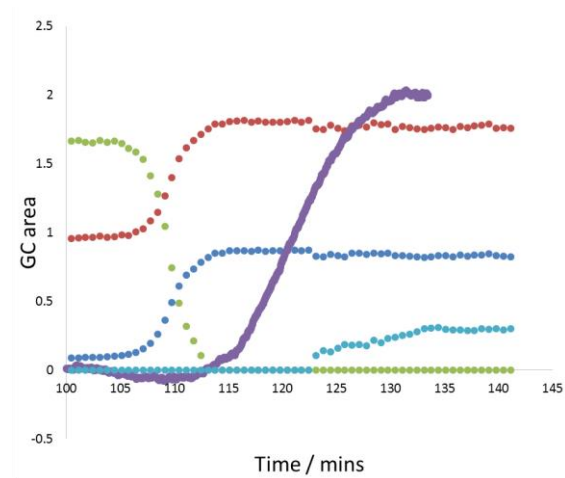
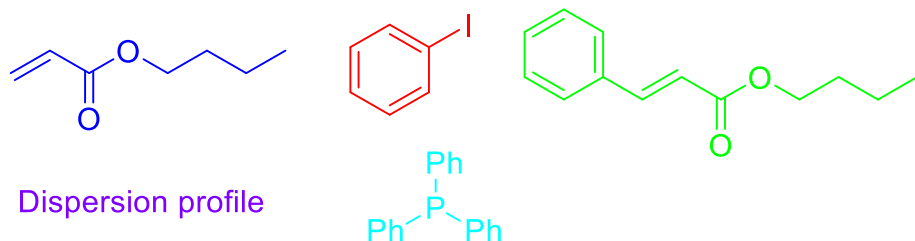
In a second rbf, (1.61 g, 4.98 mmol) TBAB, 0.63 mL veratrole, (1.10 mL, 9.90 mmol) iodobenzene, (0.72 mL, 4.98 mmol) n-butyl acrylate, and 1.2 mL  $\text{NEt}_3$  were added to 10 mL DMF and attached to line B

0.055 g  $\text{Pd}(\text{OAc})_2$  was dissolved in 15 mL DMF. 0.69 mL of this solution was added to 9.31 mL DMF and this solution was attached to line C.

10 mL plugs were pumped from the solutions into the flow setup at 0.1 mL/min, giving a reaction time of 5 minutes. Lines B and C had a delay of 4.7 mL.

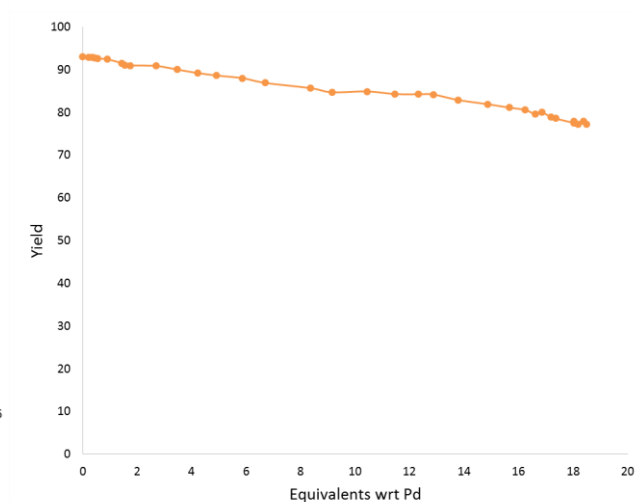
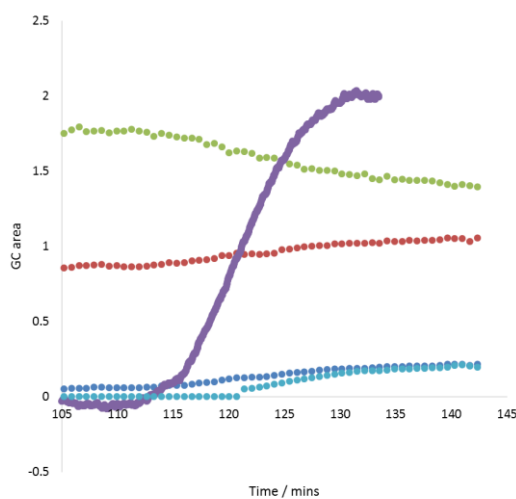
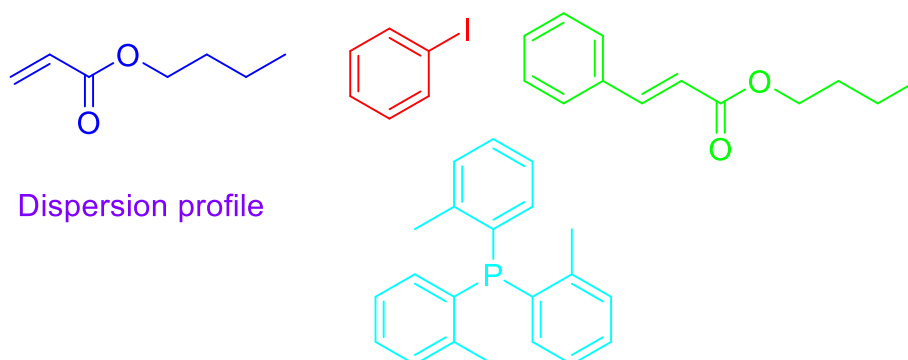
Reaction progress was monitored by offline GC via 0.2 mL samples taken at 95.13 mins experiment time.

Data was interpreted as with  $\text{Pd}(\text{OAc})_2$  gradient.



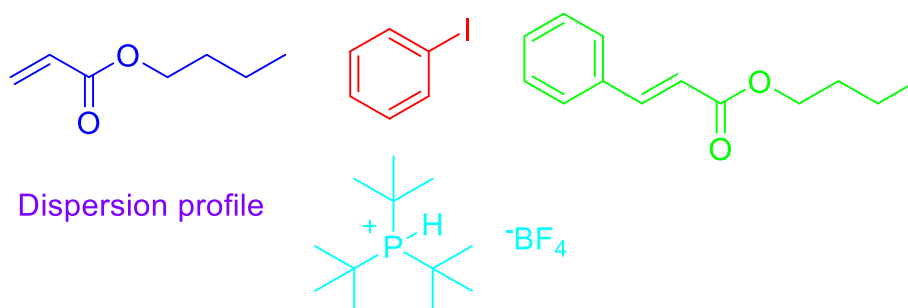
### 7.2.3.3.2 Tri(o-tolyl)phosphine

(0.061 g, 0.200 mmol) Tri(o-tolyl)phosphine was dissolved in 10 mL DMF and the same procedure as  $\text{PPh}_3$  was followed.

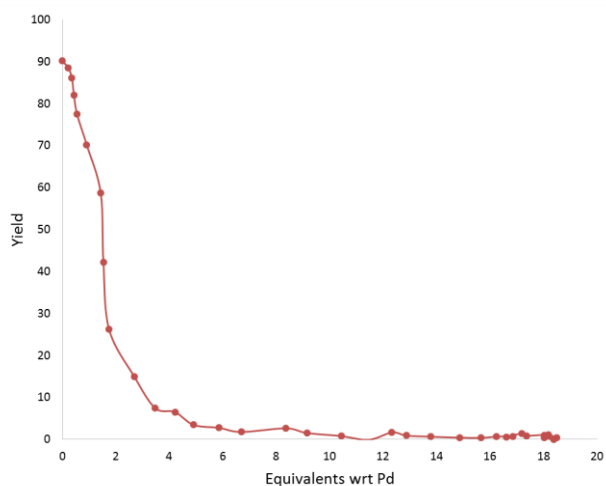
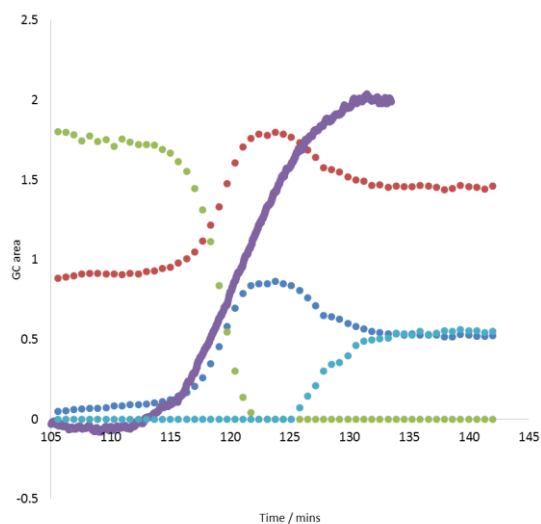


### 7.2.3.3.3 TTBP.HBF<sub>4</sub>

(0.057 g, 0.196 mmol) TTBP.HBF<sub>4</sub> was dissolved in 10 mL DMF and the same procedure as  $\text{PPh}_3$  was followed.

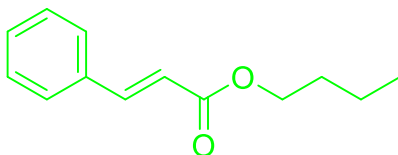
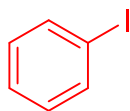
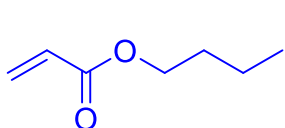


## Chapter 7

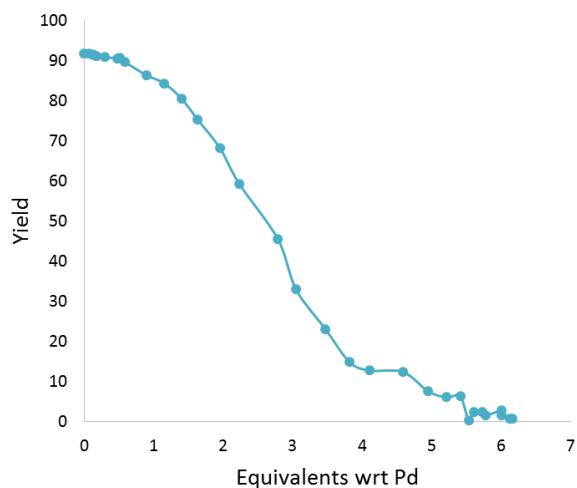
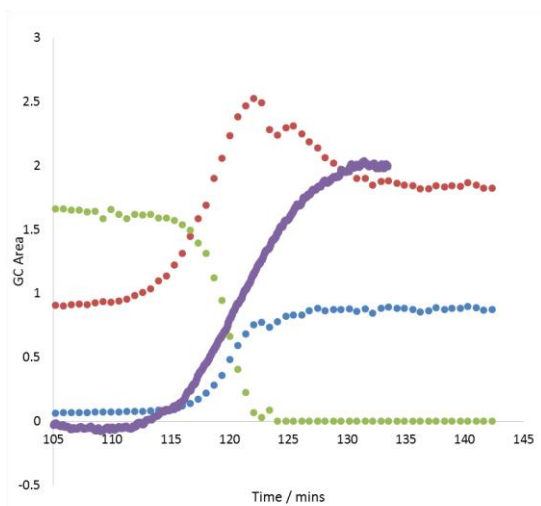


### 7.2.3.3.4 DPPF

(0.036 g, 0.065 mmol) Dppf was dissolved in 10 mL DMF and the same procedure as  $\text{PPh}_3$  was followed.

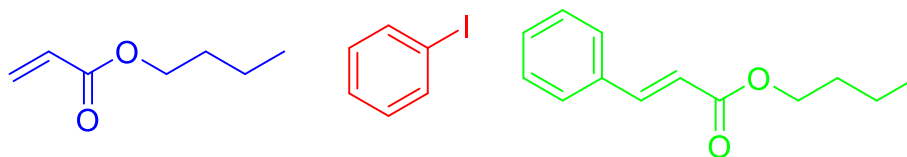


### Dispersion profile

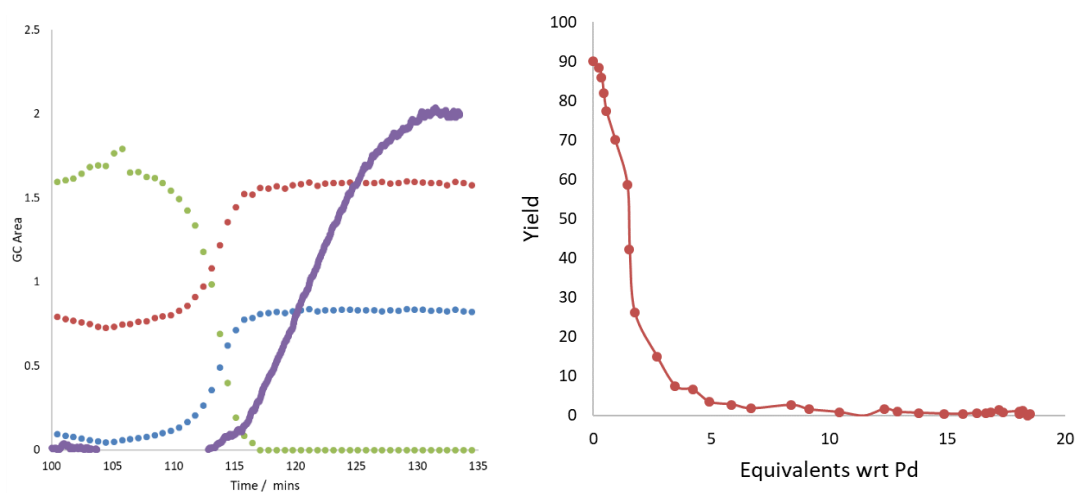


### 7.2.3.3.5 DTBPF

(0.094 g, 0.198 mmol) DTBPF was dissolved in 10 mL DMF and the same procedure as  $\text{PPh}_3$  was followed.

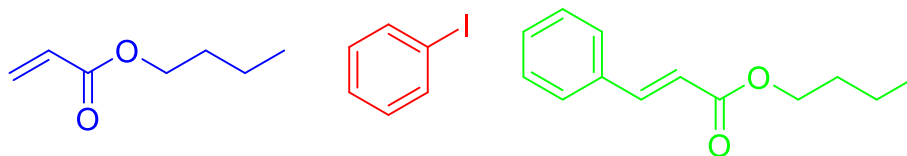


## Dispersion profile

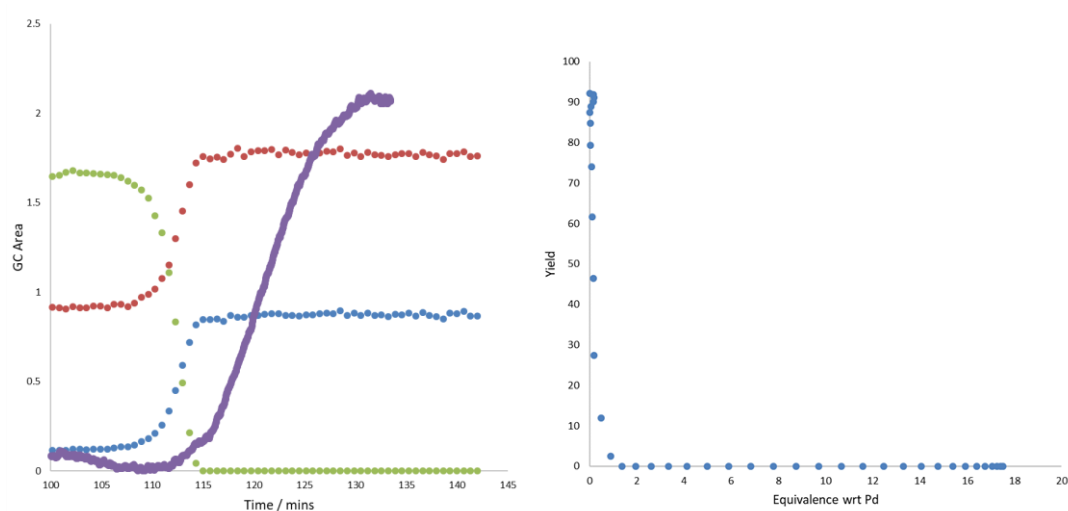


## 7.2.3.3.6 DPPE

(0.079 g, 0.198 mmol) DPPE was dissolved in 10 mL DMF and the same procedure as  $\text{PPh}_3$  was followed.

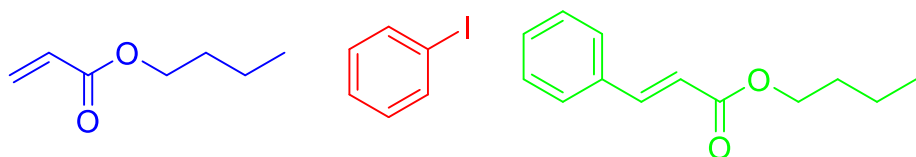
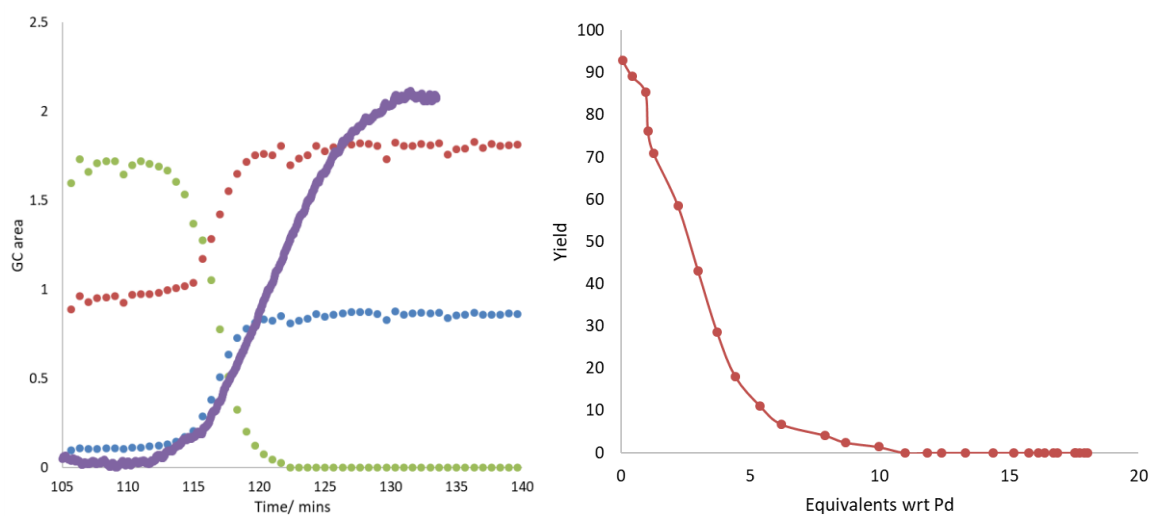


## Dispersion profile

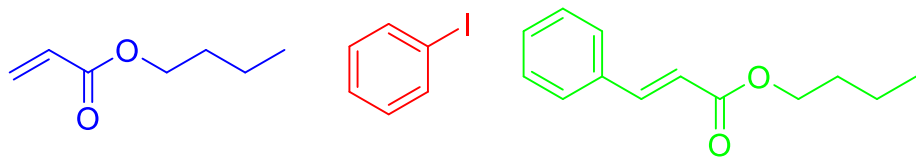


**7.2.3.3.7 Bipy**

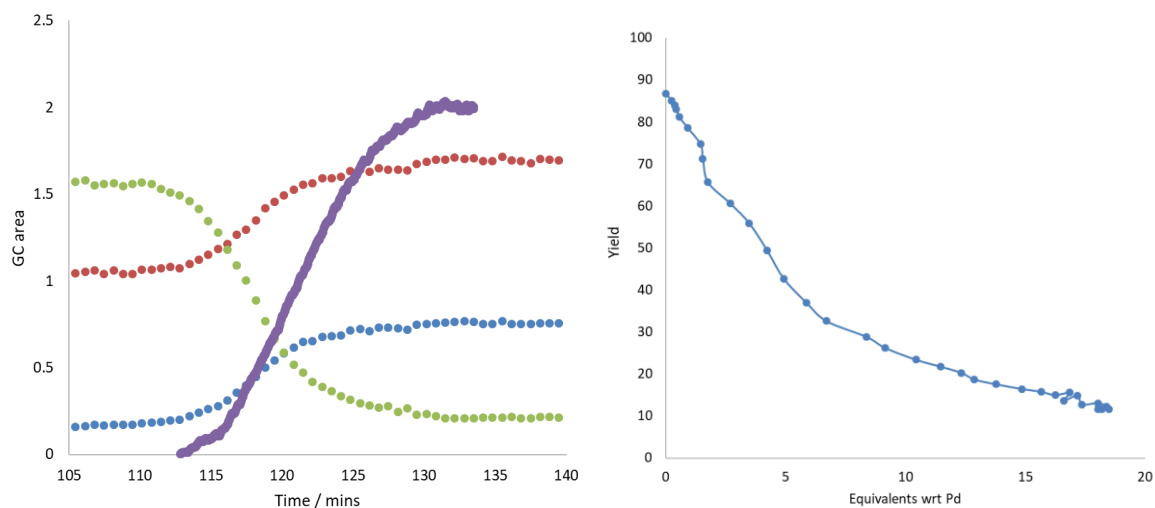
(0.031 g, 0.198 mmol) Bipy was dissolved in 10 mL DMF and the same procedure as  $\text{PPh}_3$  was followed.

**Dispersion profile****7.2.3.3.8 Terpy**

(0.046 g, 0.198 mmol) Terpy was dissolved in 10 mL DMF and the same procedure as  $\text{PPh}_3$  was followed.

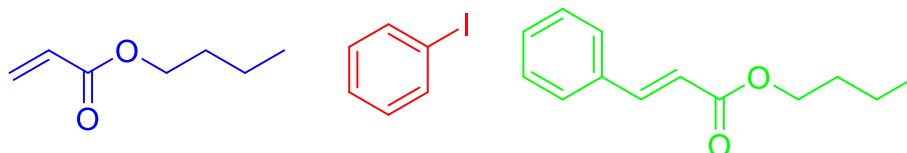
**Dispersion profile**



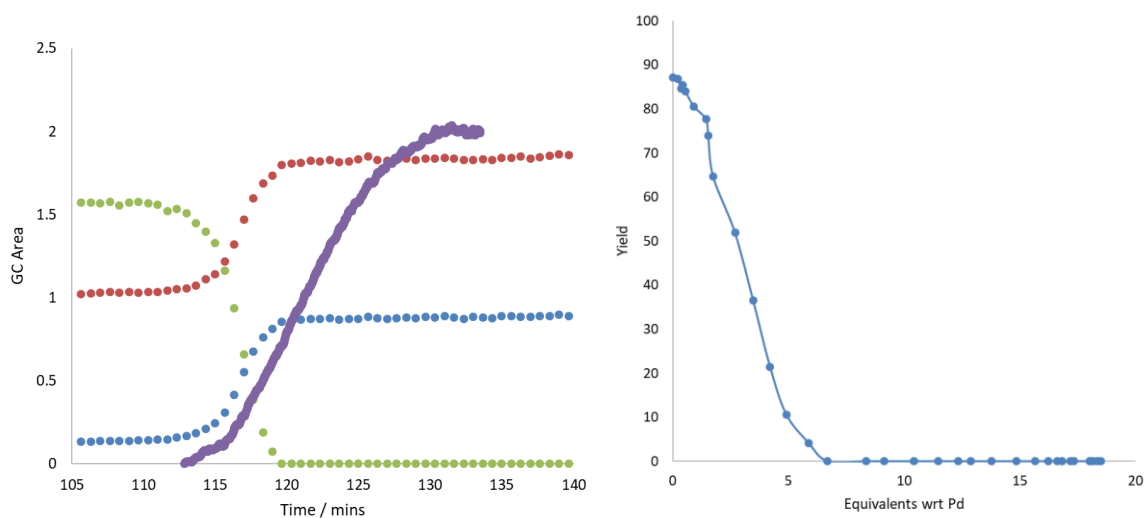


### 7.2.3.3.9 Phen

(0.036 g, 0.198 mmol) Phen was dissolved in 10 mL DMF and the same procedure as  $\text{PPh}_3$  was followed.



### Dispersion profile

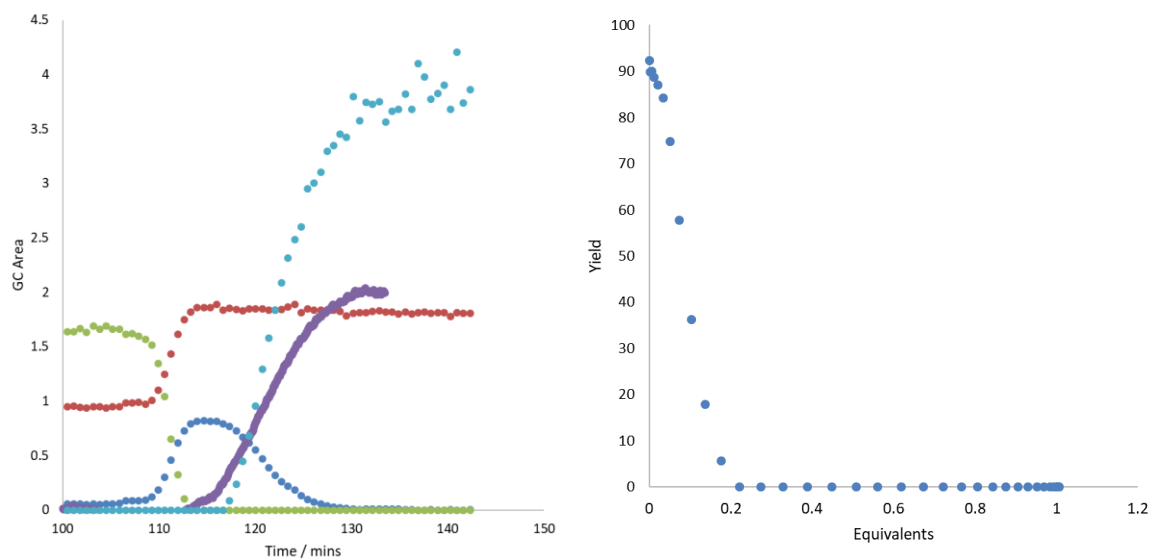
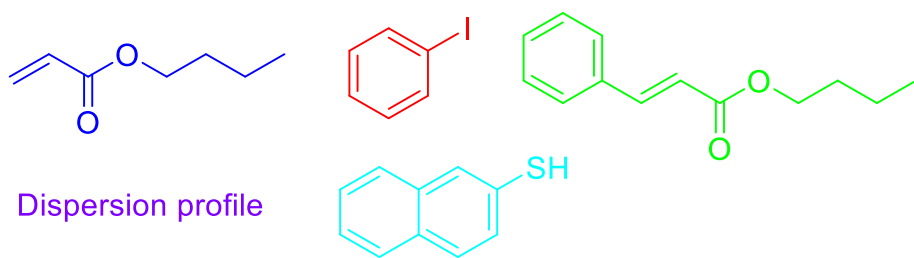


### 7.2.3.4 Concentration gradient of additives

#### 7.2.3.4.1 2-Naphthalenethiol

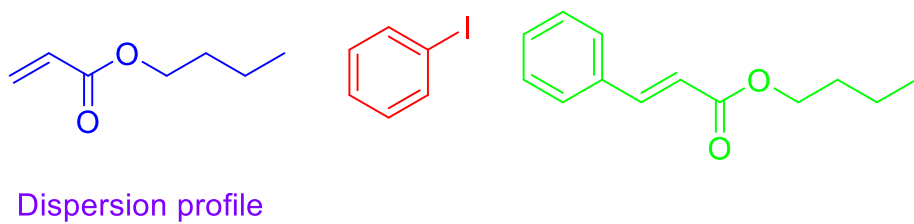
(0.801 g, 4.98 mmol) 2-naphthalenethiol was dissolved in 10 mL DMF and the same procedure as  $\text{PPh}_3$  was followed.

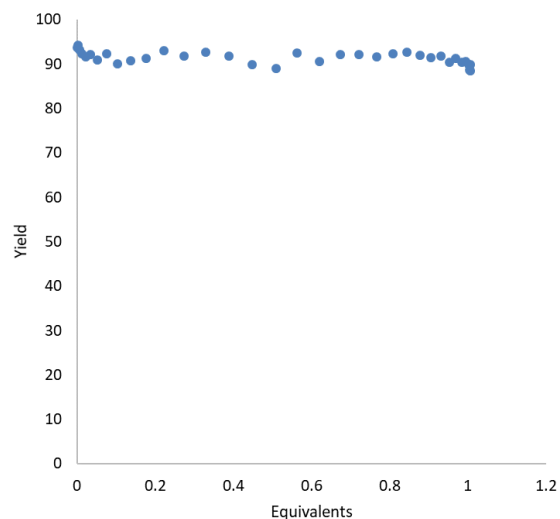
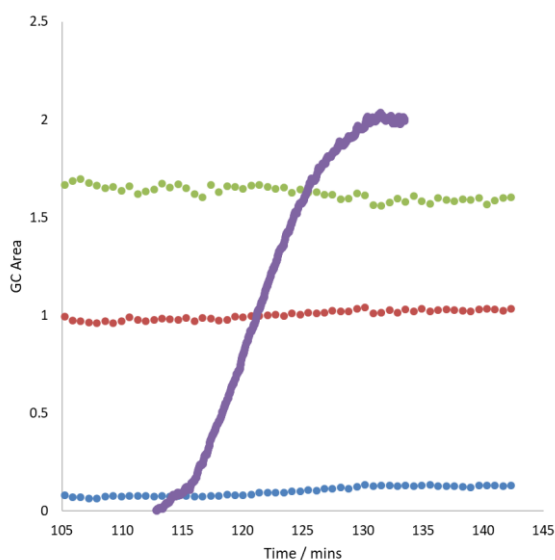
## Chapter 7



### 7.2.3.4.2 DMSO

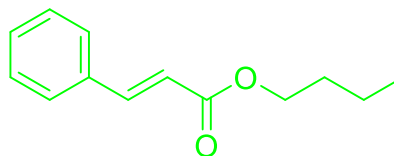
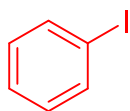
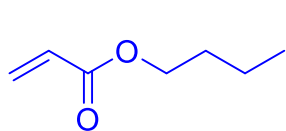
(0.391 g, 4.98 mmol) DMSO was dissolved in 10 mL DMF and the same procedure as  $\text{PPh}_3$  was followed.



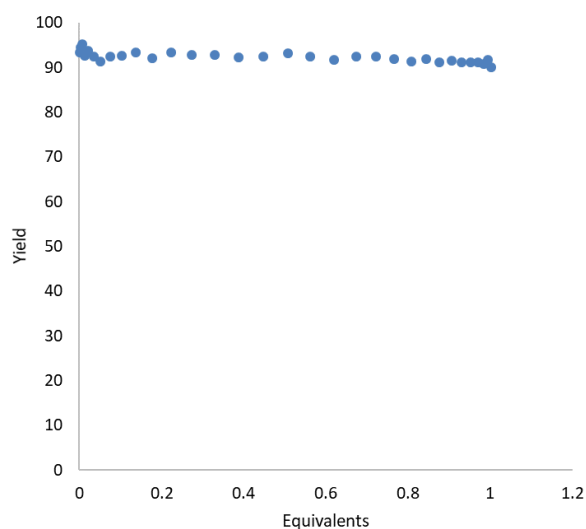
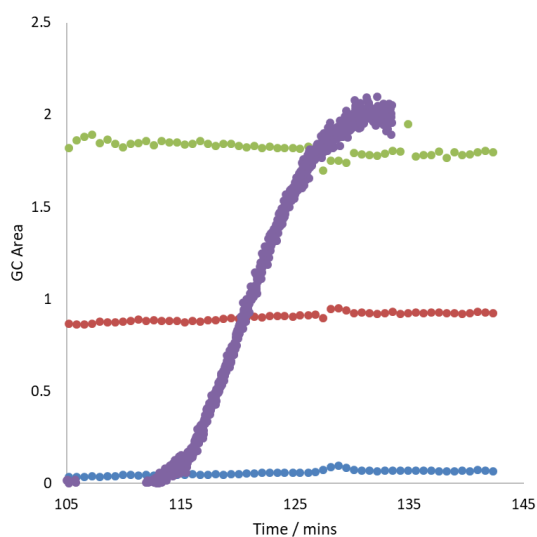


### 7.2.3.4.3 Thiophene

(0.421 g, 4.98 mmol) Thiophene was dissolved in 10 mL DMF and the same procedure as  $\text{PPh}_3$  was followed.

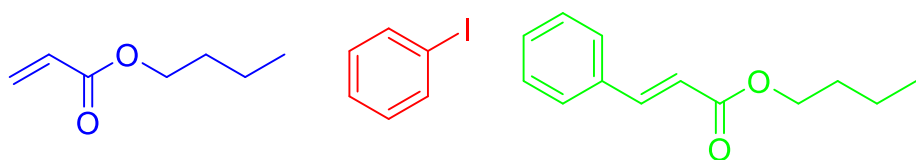


### Dispersion profile

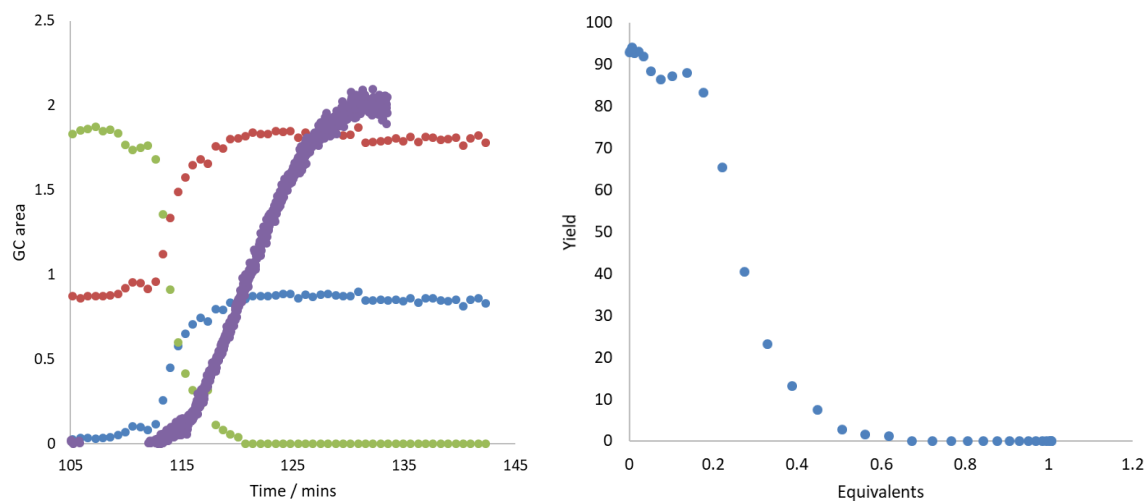


### 7.2.3.4.4 Diphenyldisulfide

(1.09 g, 4.98 mmol) Diphenyldisulfide was dissolved in 10 mL DMF and the same procedure as  $\text{PPh}_3$  was followed.

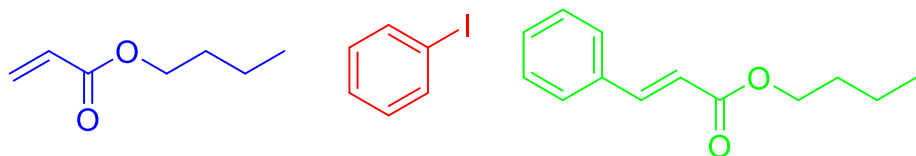


## Dispersion profile

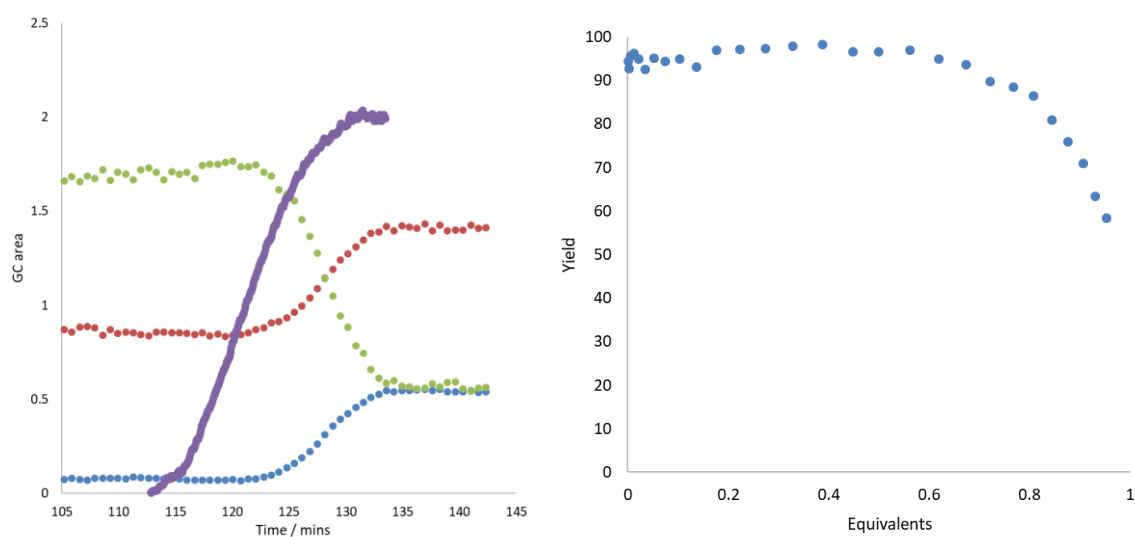


## 7.2.3.4.5 Thioanisole

(0.620 g, 4.98 mmol) Thioanisole was dissolved in 10 mL DMF and the same procedure as  $\text{PPh}_3$  was followed.

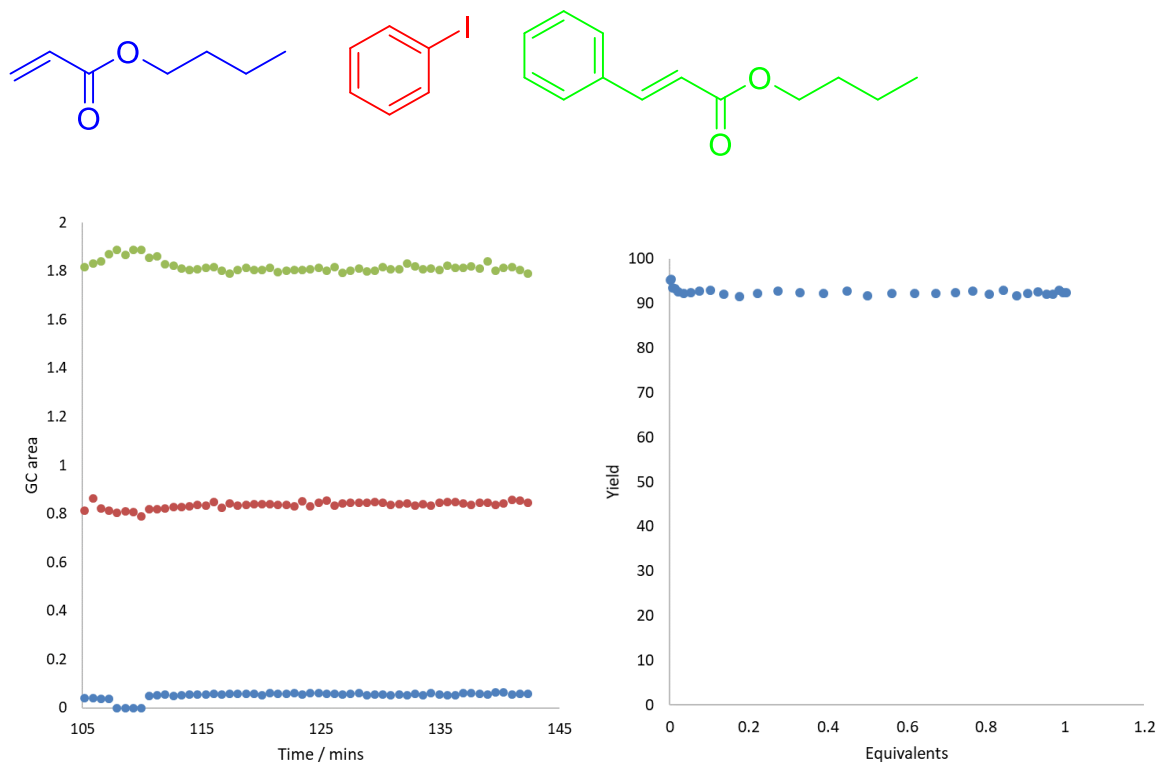


## Dispersion profile



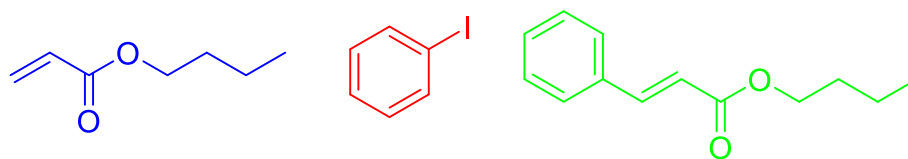
## 7.2.3.4.6 Pyrrole

(0.336 g, 4.98 mmol) Pyrrole was dissolved in 10 mL DMF and the same procedure as  $\text{PPh}_3$  was followed.



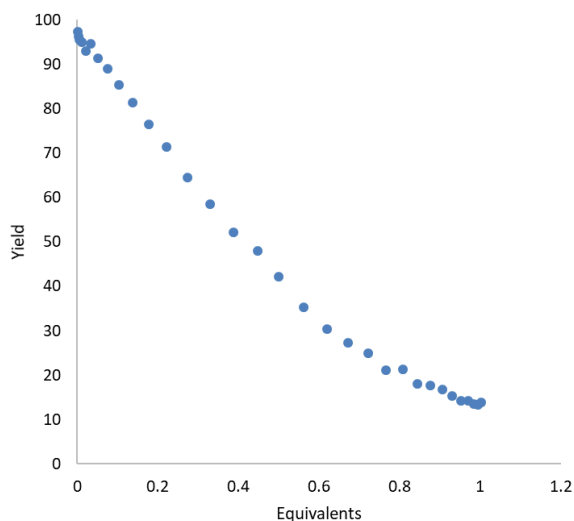
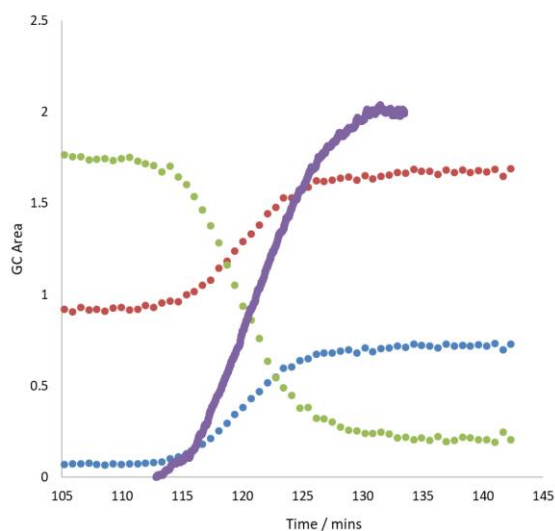
## 7.2.3.4.7 Pyridine

(0.396 g, 4.98 mmol) Pyridine was dissolved in 10 mL DMF and the same procedure as  $\text{PPh}_3$  was followed.



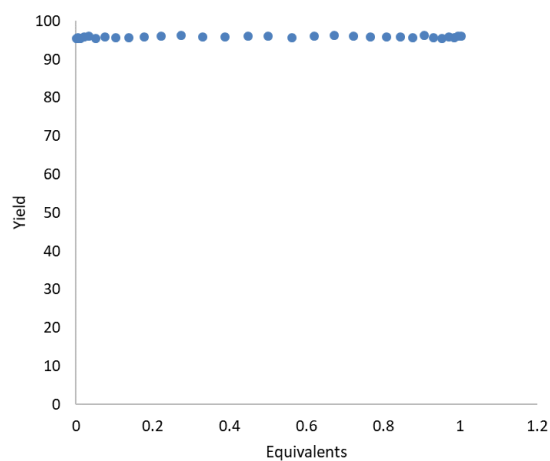
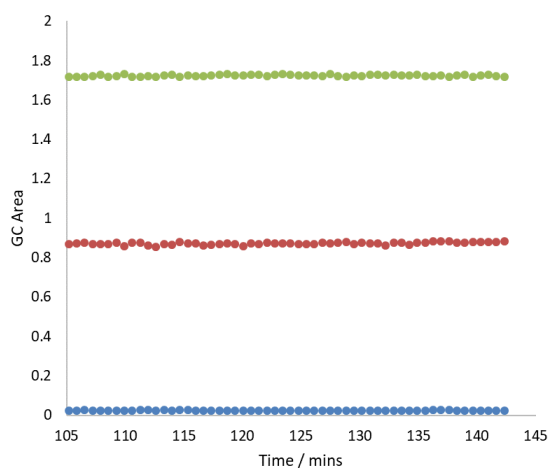
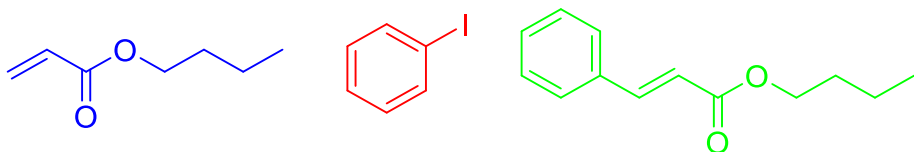
Dispersion profile

## Chapter 7



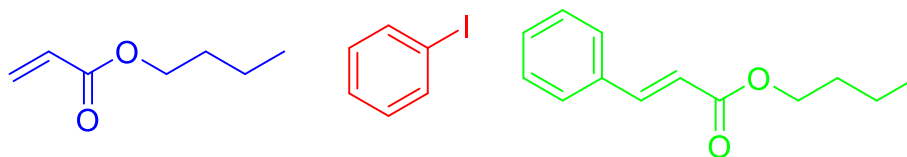
### 7.2.3.4.8 Acetonitrile

(0.205 g, 4.98 mmol) Acetonitrile was dissolved in 10 mL DMF and the same procedure as  $\text{PPh}_3$  was followed.

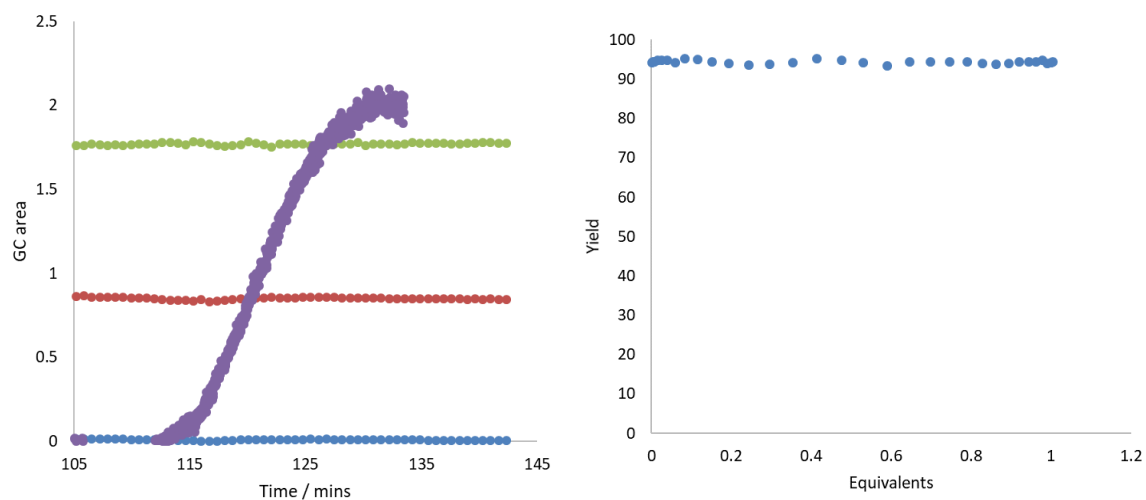


### 7.2.3.4.9 Indole

(0.585 g, 4.98 mmol) Indole was dissolved in 10 mL DMF and the same procedure as  $\text{PPh}_3$  was followed.

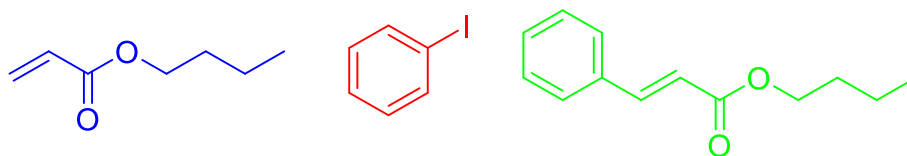


## Dispersion profile

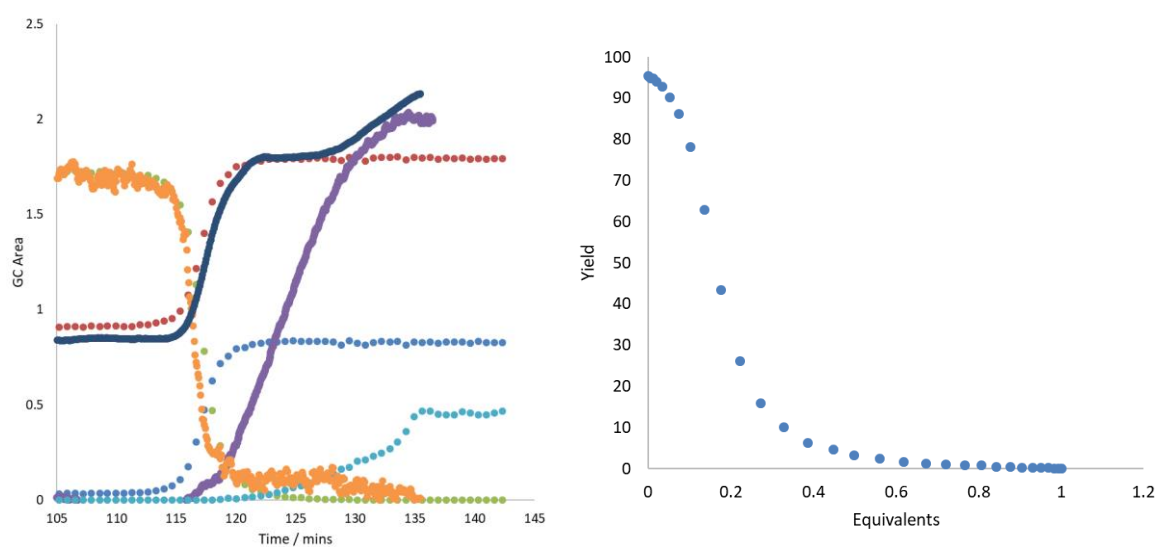


## 7.2.3.4.10 Imidazole

(0.340 g, 4.98 mmol) Imidazole was dissolved in 10 mL DMF and the same procedure as  $\text{PPh}_3$  was followed.

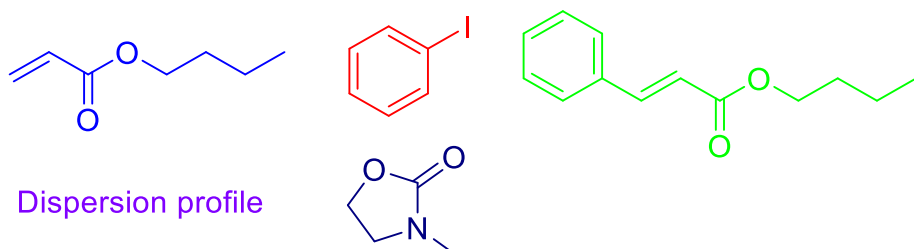


## Dispersion profile

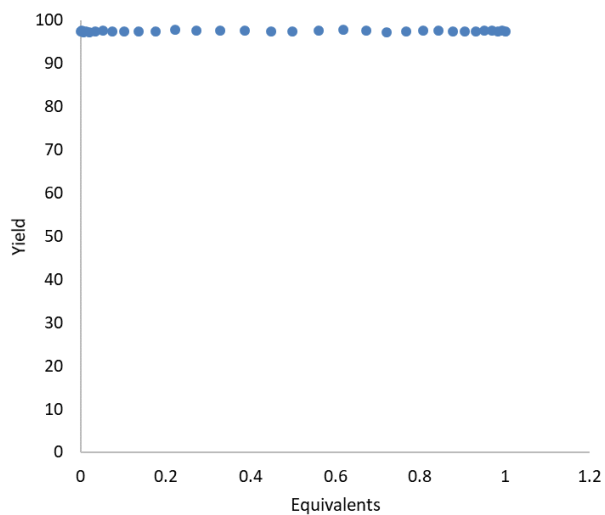
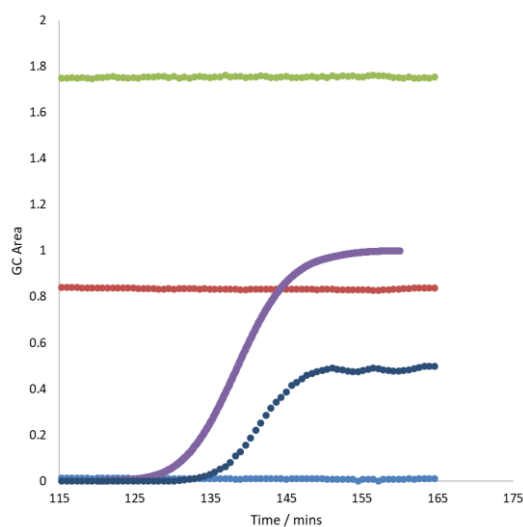


**7.2.3.4.11 3-methyl-2-oxazolidinone**

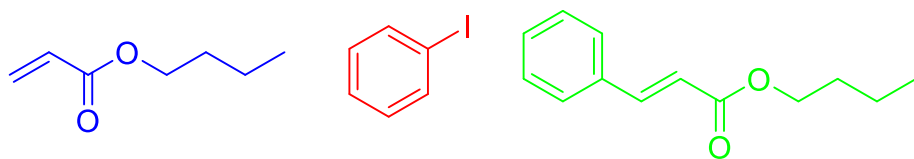
(0.504 g, 4.98 mmol) 3-Methyl-2-oxazolidinone was dissolved in 10 mL DMF and the same procedure as  $\text{PPh}_3$  was followed.



Dispersion profile

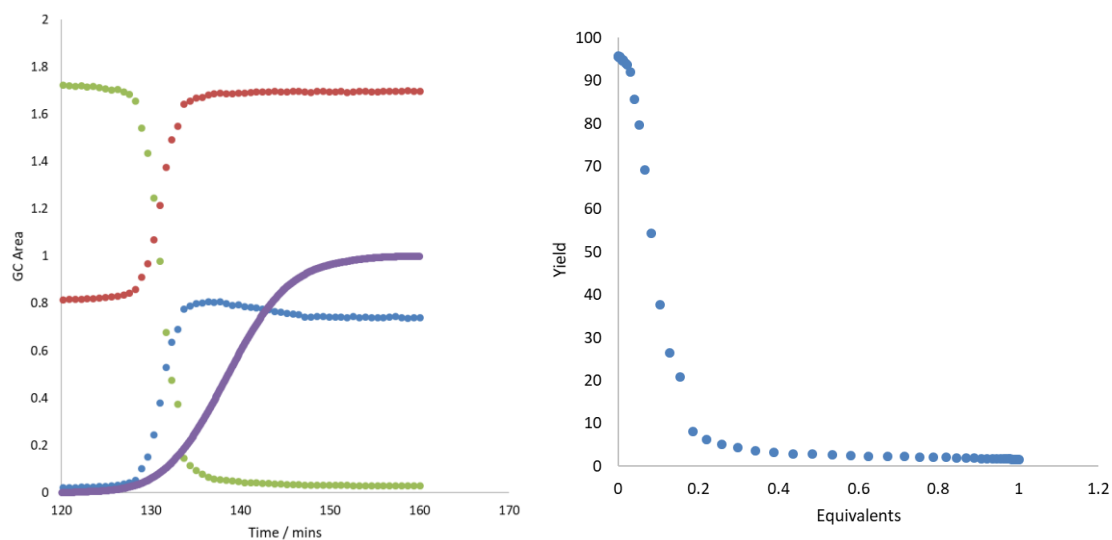
**7.2.3.4.12 2-(methylamino)ethanol**

(0.374 g, 4.98 mmol) 2-(methylamino)ethanol was dissolved in 10 mL DMF and the same procedure as  $\text{PPh}_3$  was followed.



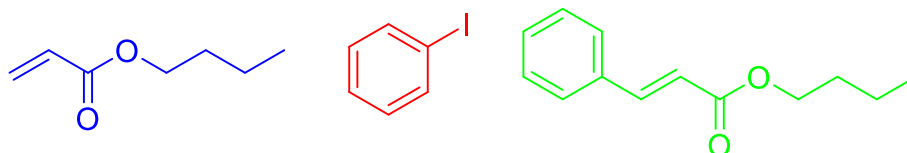
Dispersion profile



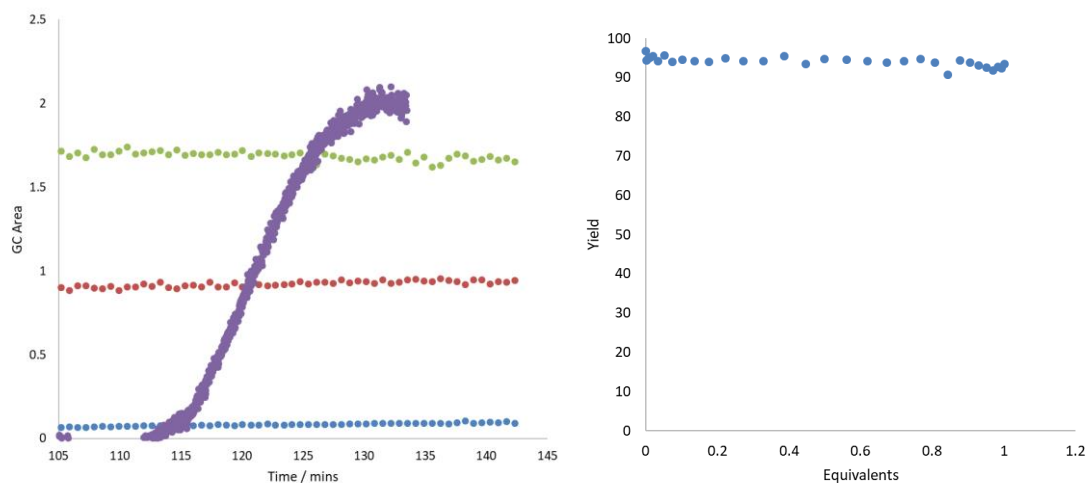


#### 7.2.3.4.13 Furan

(0.341 g, 4.98 mmol) Furan was dissolved in 10 mL DMF and the same procedure as  $\text{PPh}_3$  was followed.



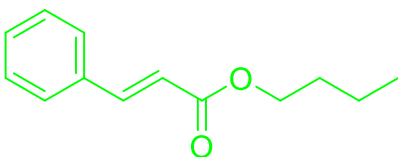
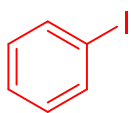
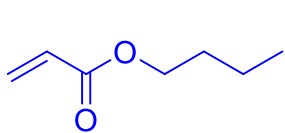
#### Dispersion profile



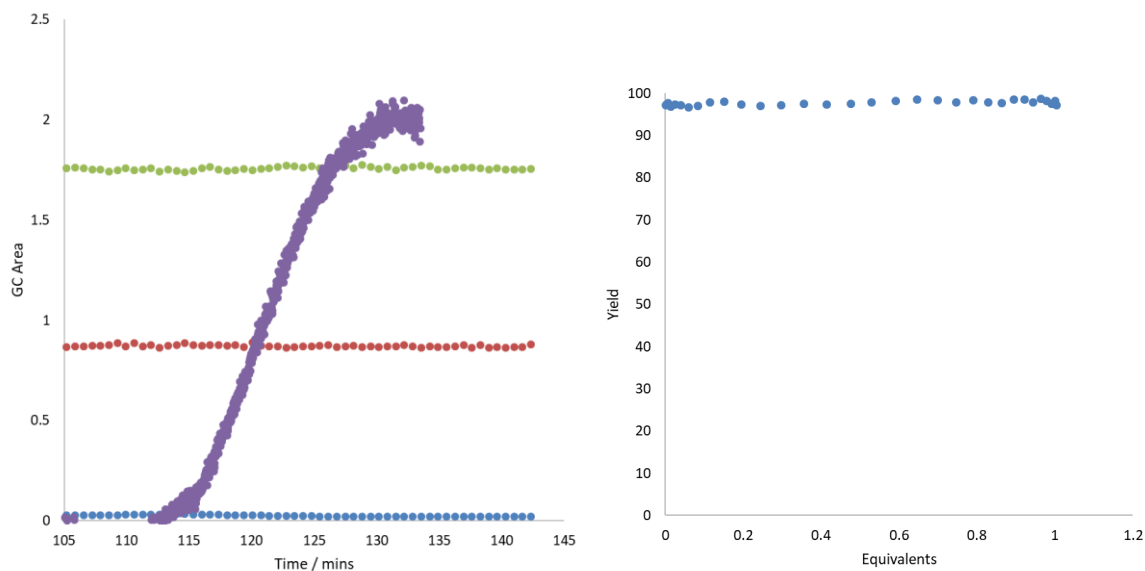
#### 7.2.3.4.14 Isovaleraldehyde

(0.430 g, 4.98 mmol) Isovaleraldehyde was dissolved in 10 mL DMF and the same procedure as  $\text{PPh}_3$  was followed.

## Chapter 7

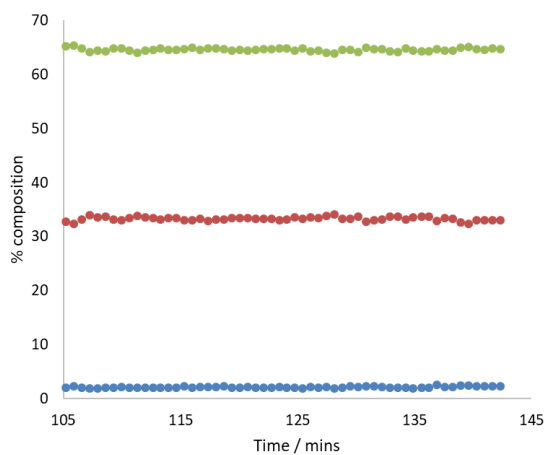
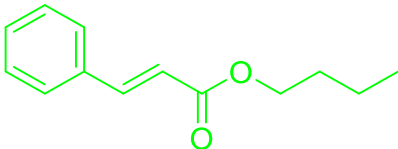
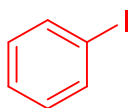
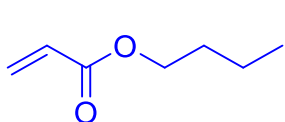


### Dispersion profile



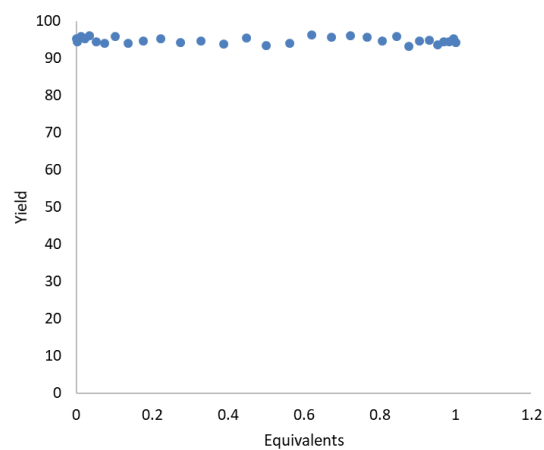
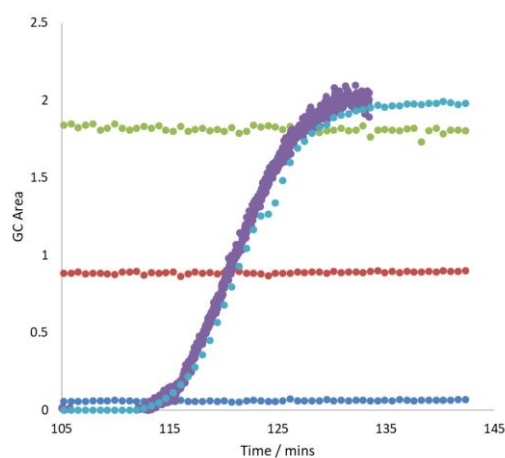
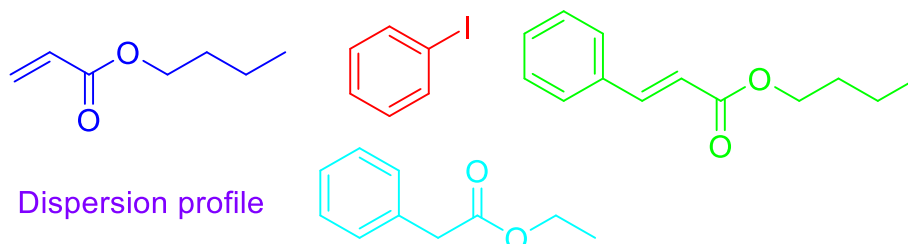
### 7.2.3.4.15 2-Methylacetophenone

(0.671 g, 4.98 mmol) 2-methylacetophenone was dissolved in 10 mL DMF and the same procedure as  $\text{PPh}_3$  was followed. Yield was not calculated for this experiment due to overlap of the GC signals of the internal standard and the additive.



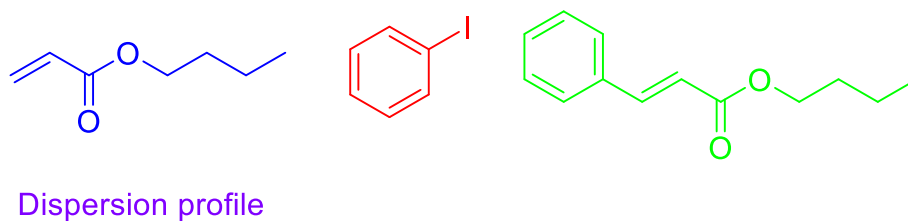
#### 7.2.3.4.16 Ethyl phenylacetate

(0.821 g, 4.98 mmol) Ethyl phenylacetate was dissolved in 10 mL DMF and the same procedure as PPh<sub>3</sub> was followed.

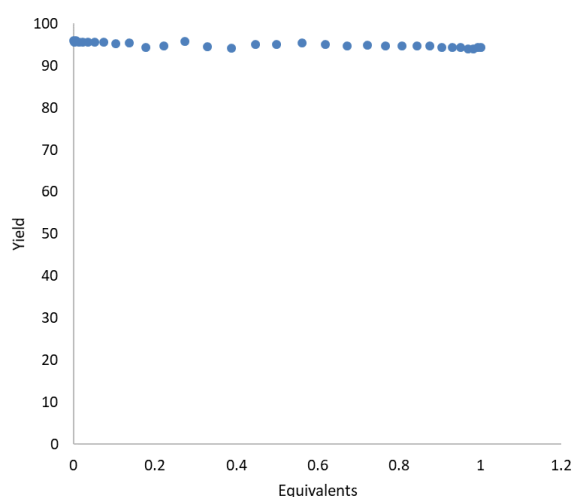
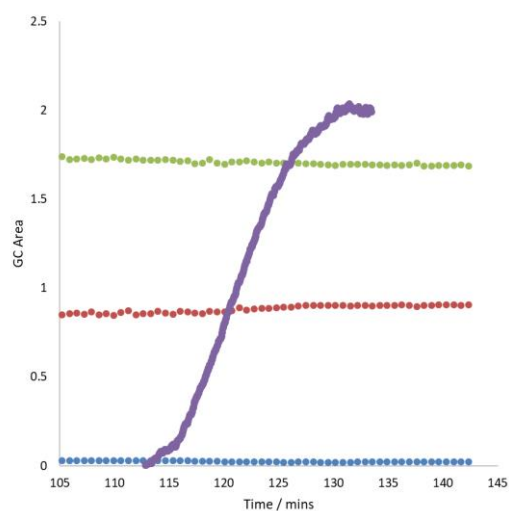


#### 7.2.3.4.17 Styrene oxide

(0.601 g, 4.98 mmol) Styrene oxide was dissolved in 10 mL DMF and the same procedure as PPh<sub>3</sub> was followed.

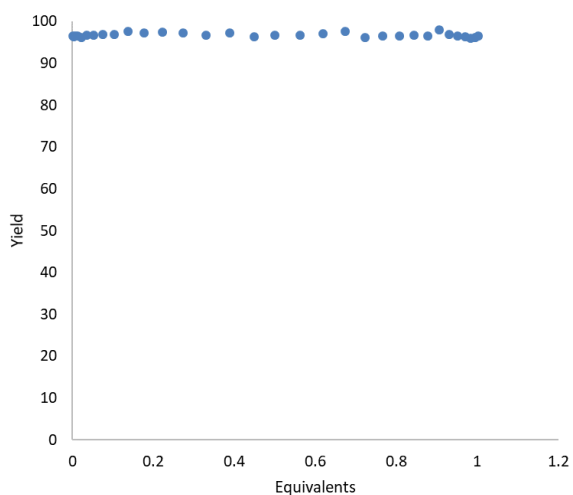
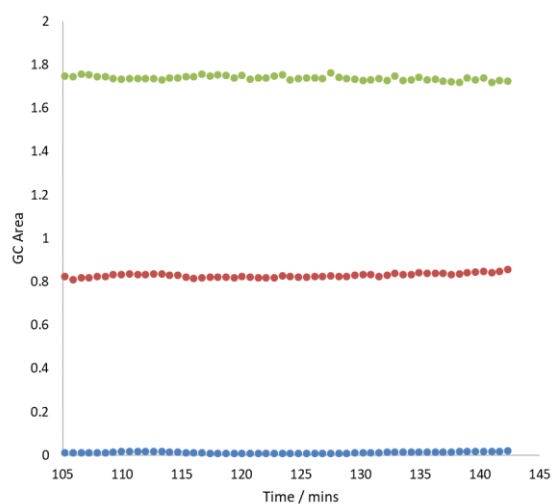
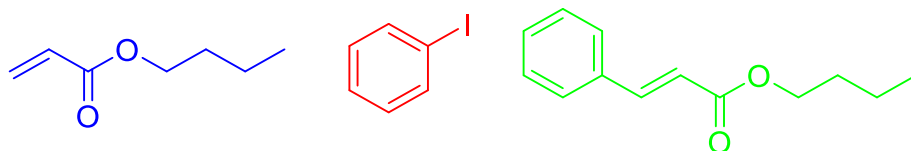


## Chapter 7



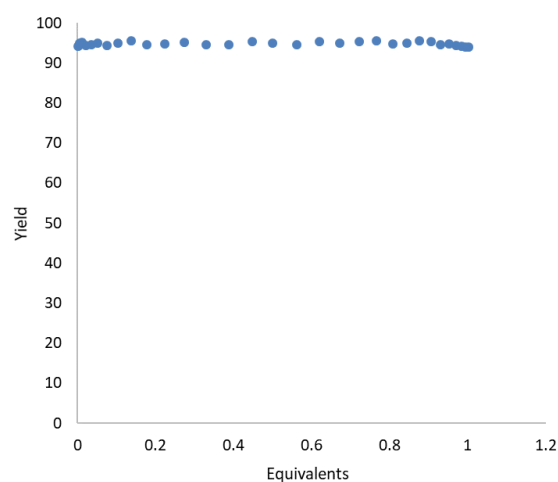
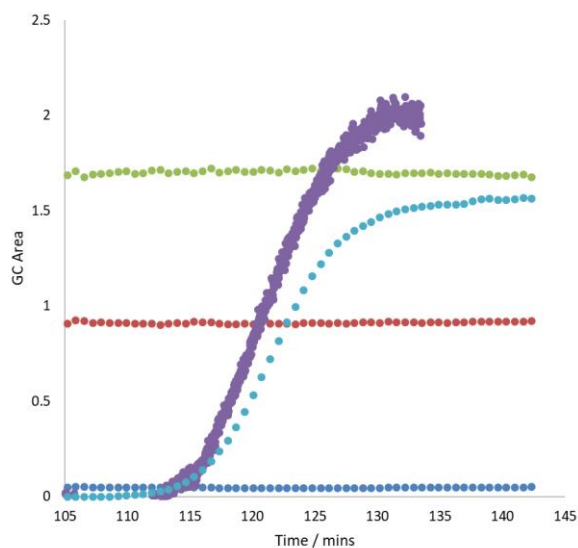
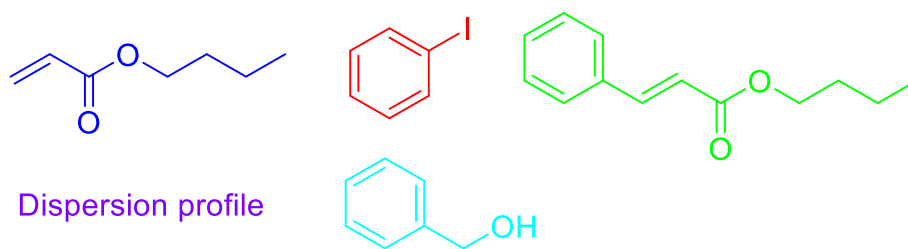
### 7.2.3.4.18 Acetic acid

(0.300 g, 4.98 mmol) Acetic acid was dissolved in 10 mL DMF and the same procedure as  $\text{PPh}_3$  was followed.



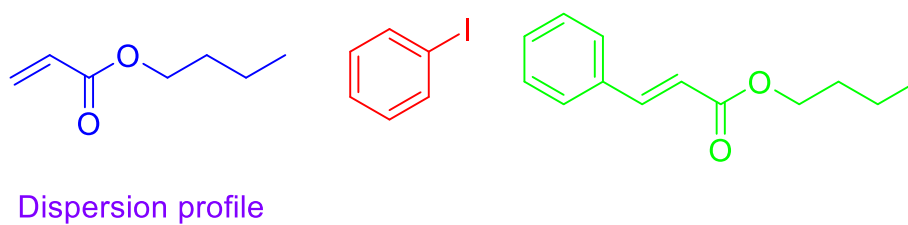
### 7.2.3.4.19 Benzyl alcohol

(0.541 g, 4.98 mmol) Benzyl alcohol was dissolved in 10 mL DMF and the same procedure as  $\text{PPh}_3$  was followed.

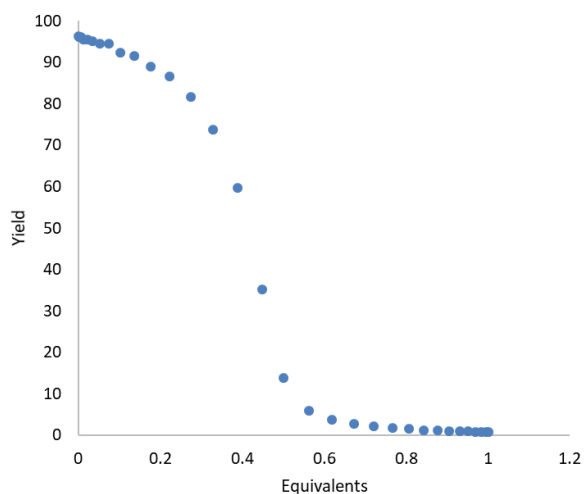
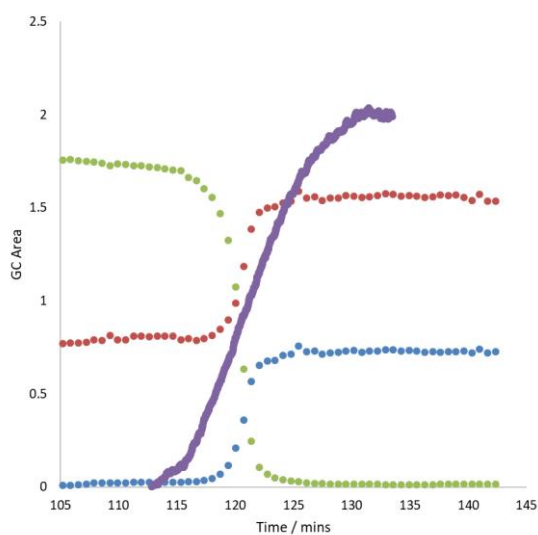


#### 7.2.3.4.20 Norbornene

(0.470 g, 4.98 mmol) Norbornene was dissolved in 10 mL DMF and the same procedure as  $\text{PPh}_3$  was followed.

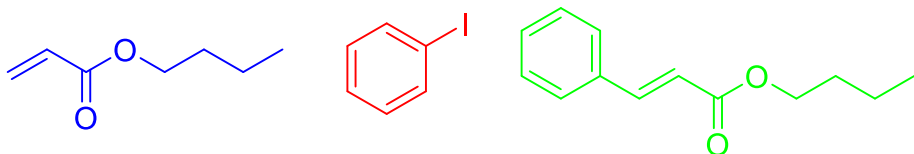


## Chapter 7

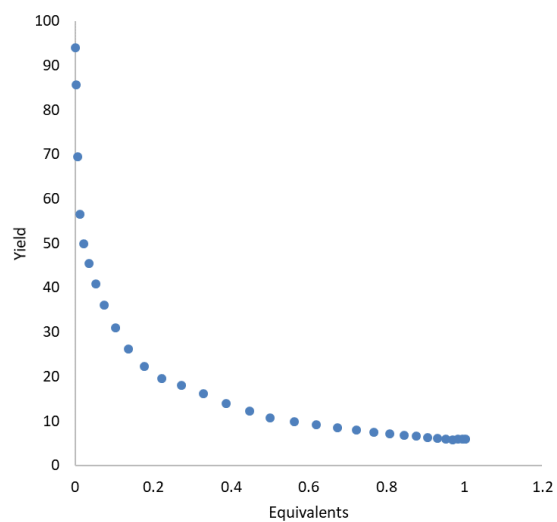
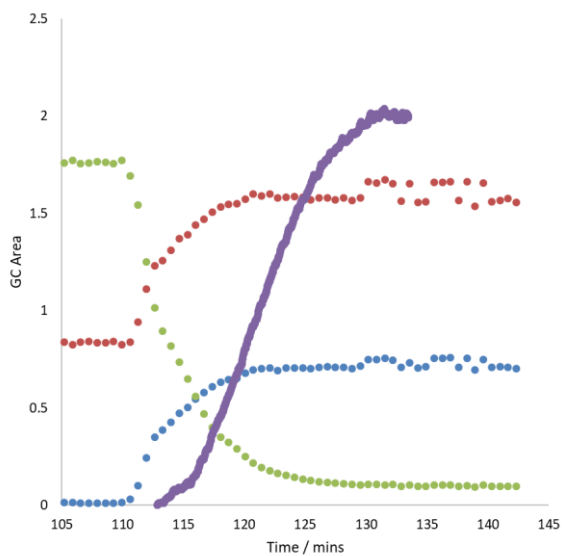


### 7.2.3.4.21 1,5-Cyclooctadiene

(0.540 g, 4.98 mmol) 1,5-Cyclooctadiene was dissolved in 10 mL DMF and the same procedure as PPh<sub>3</sub> was followed.

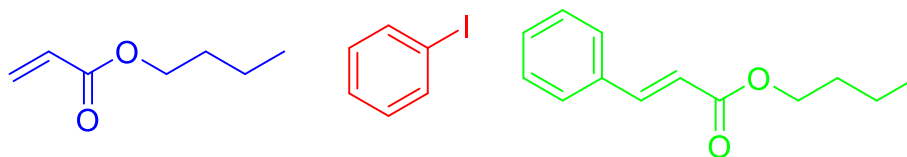


#### Dispersion profile

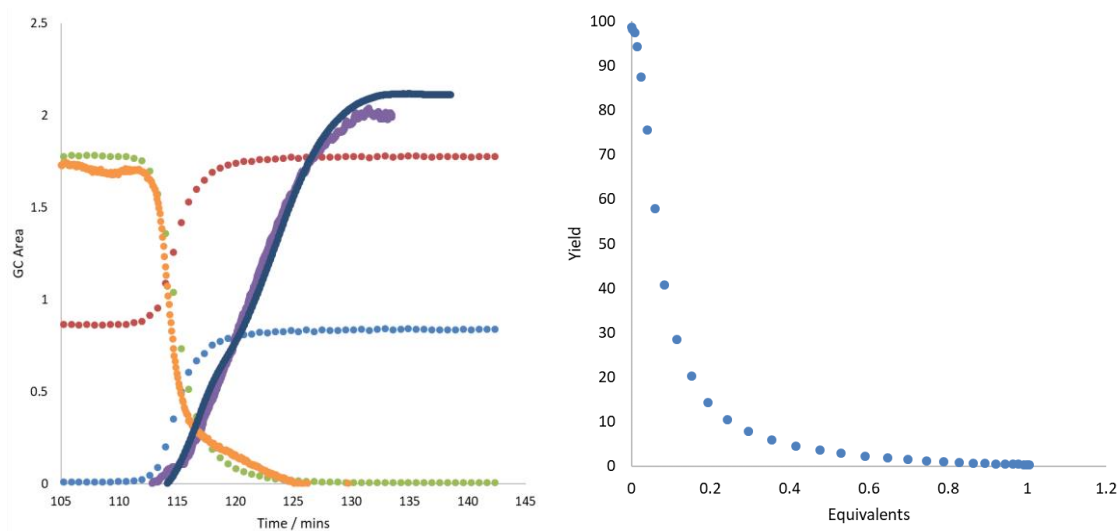


### 7.2.3.4.22 1-Octyne

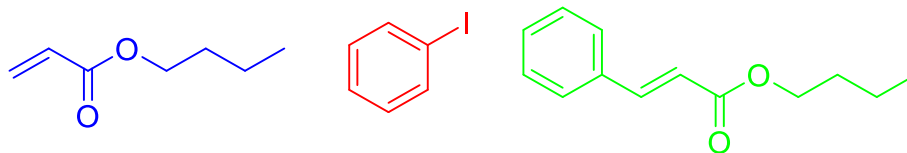
(0.551 g, 4.98 mmol) 1-Octyne was dissolved in 10 mL DMF and the same procedure as PPh<sub>3</sub> was followed.



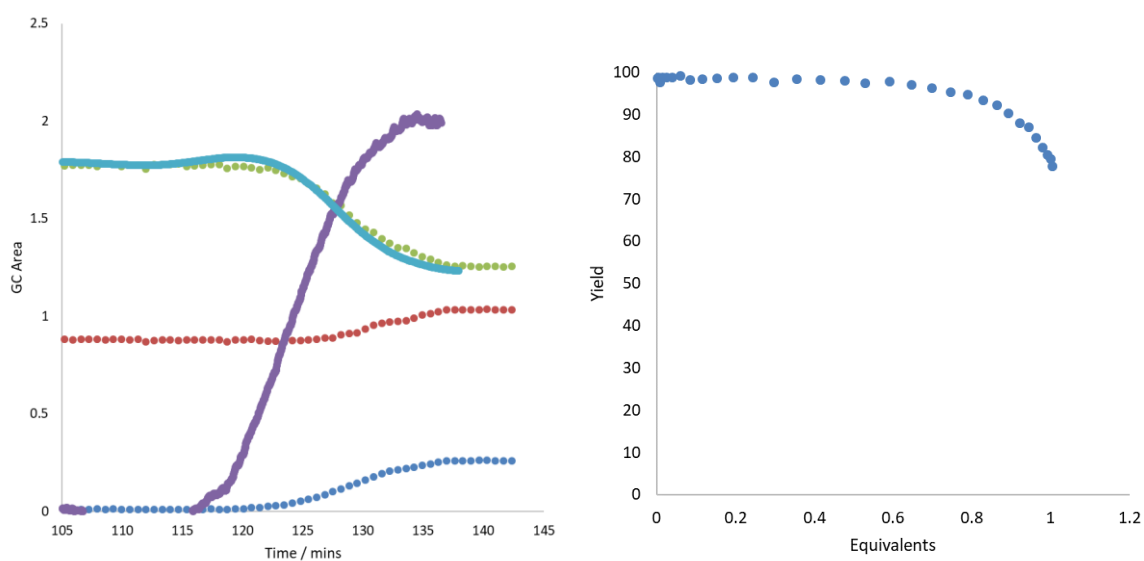
Dispersion profile

**7.2.3.4.23 1-Hexene**

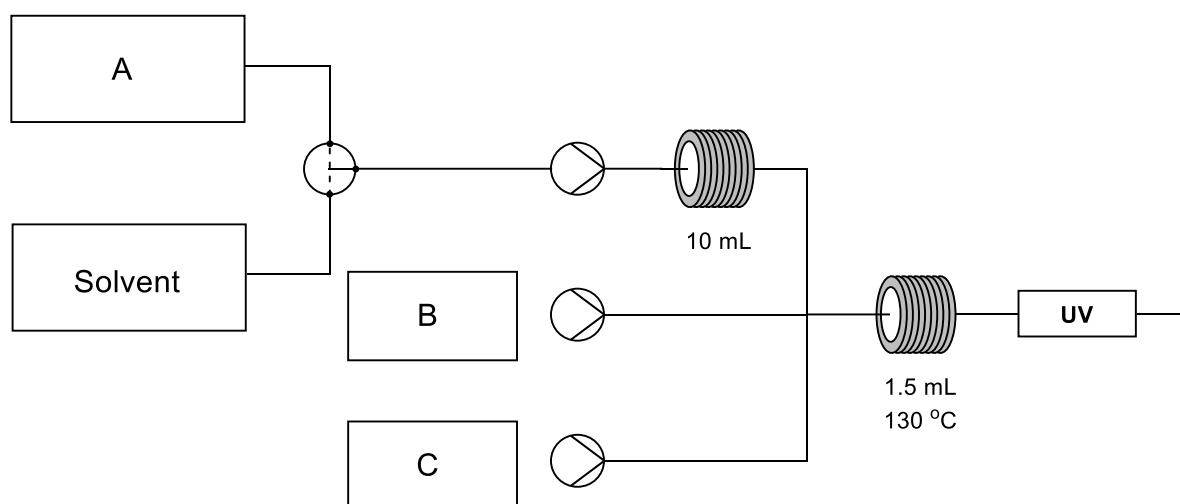
(0.421 g, 4.98 mmol) 1-Hexene was dissolved in 10 mL DMF and the same procedure as  $\text{PPh}_3$  was followed.



Dispersion profile



## 7.2.3.5 Sonogashira coupling: concentration gradient of ligands

7.2.3.5.1  $\text{PPh}_3$ 

In a rbf, (0.550 g, 2.10 mmol)  $\text{PPh}_3$  was dissolved in 15 mL DMF and attached to line A.

In a second rbf, 0.38 mL veratrole, (0.26 mL, 2.5 mmol) bromobenzene, (0.73 mL, 4.9 mmol) DBU, and (0.73 mL, 4.9 mmol) 1-octyne were added to 15 mL DMF and attached to line B.

0.055 g  $\text{Pd}(\text{OAc})_2$  was dissolved in 15 mL DMF. 0.75 mL of this solution was added to 14.25 mL DMF and this solution was attached to line C.

10 mL plugs were pumped from the solutions into the flow setup at 0.1 mL/min, giving a reaction time of 5 minutes. Lines B and C had a delay of 4.7 mL.

Reaction progress was monitored by offline GC *via* 0.2 mL samples taken at 105.3 mins experiment time, or *via* in-line UV monitoring with 1 sec delay between scans.

Data was interpreted as with Heck  $\text{Pd}(\text{OAc})_2$  gradient.

Representative GC spectra from reaction:



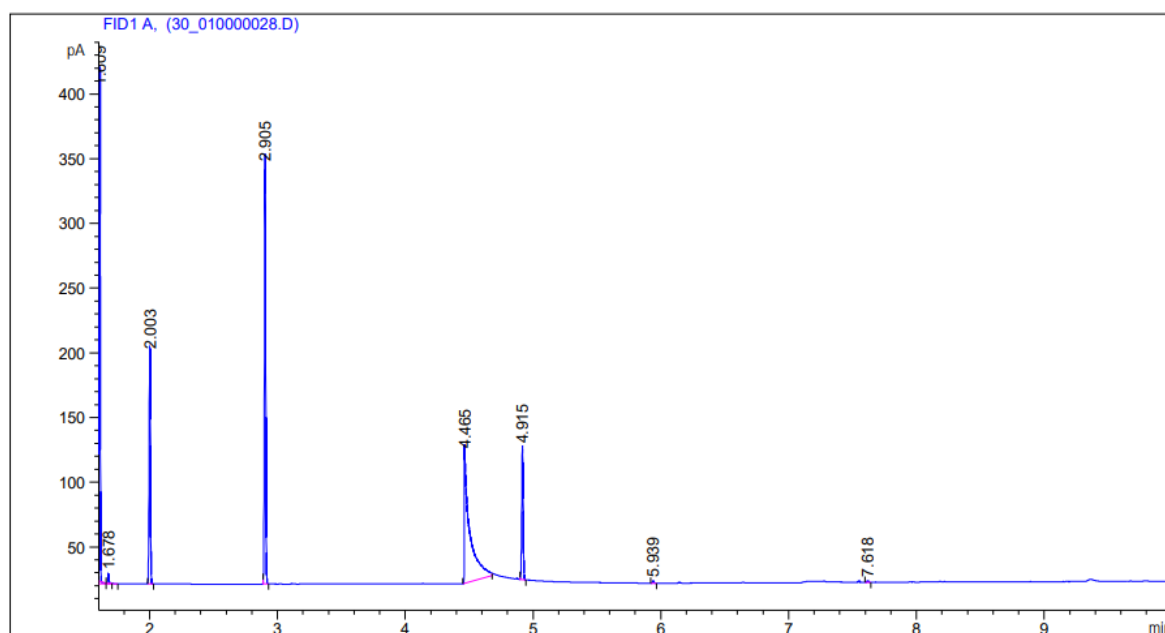
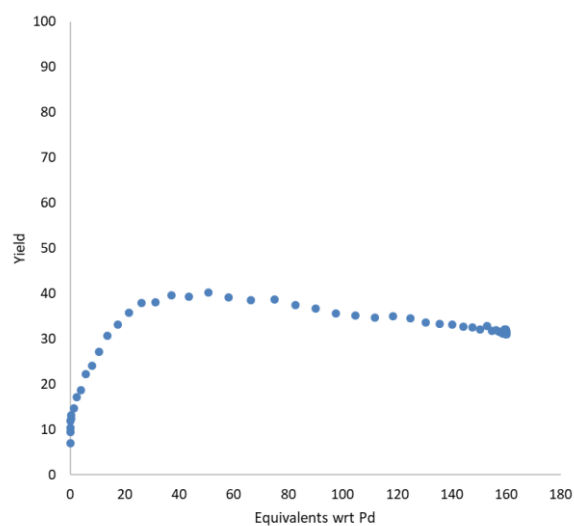
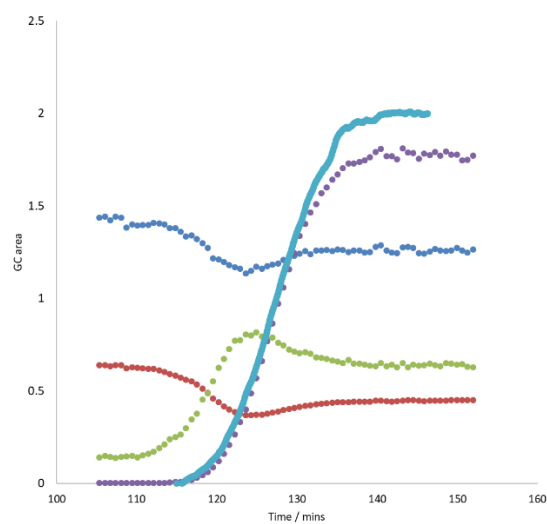
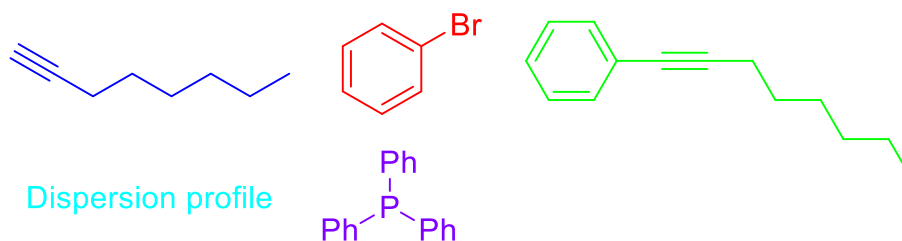
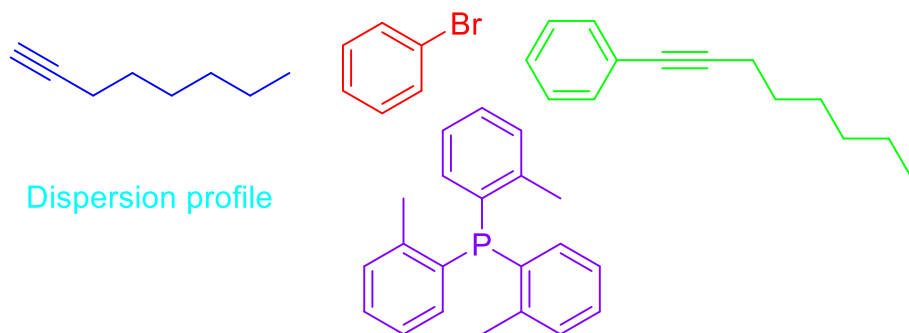


Figure 7.5: GC spectra from Sonogashira reaction. 1.609: 1-octyne. 2.003: Bromobenzene. 2.905: Veratrole. 4.915: Oct-1-yn-1-ylbenzene

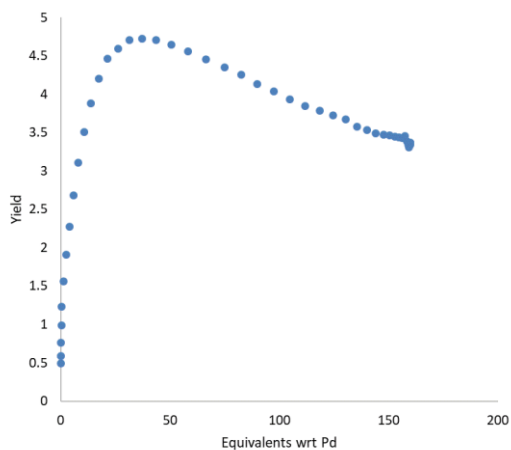
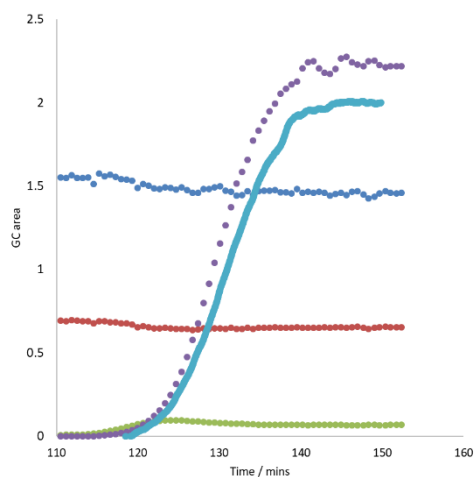


#### 7.2.3.5.2 Tri(o-tolyl)phosphine

(0.608 g, 2.00 mmol) Tri-(o-tolyl)phosphine was dissolved in 15 mL DMF and the same procedure as  $\text{PPh}_3$  was followed.

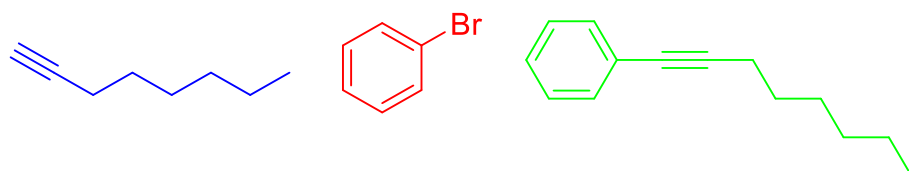


Dispersion profile

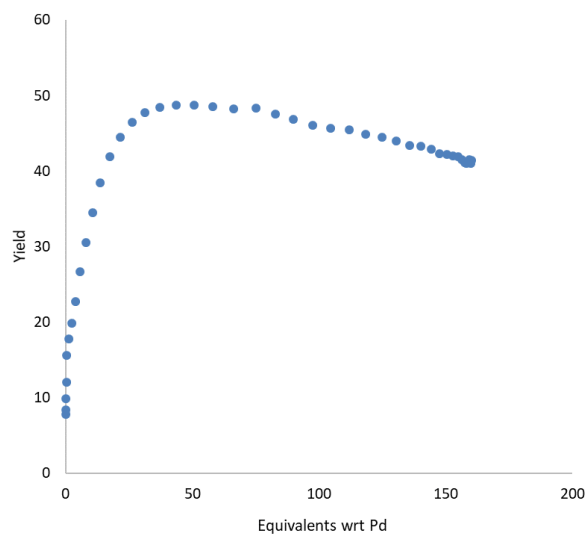
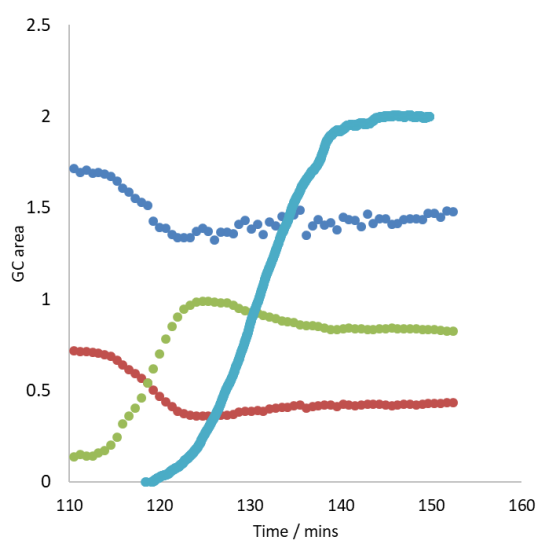


### 7.2.3.5.3 Tri(p-tolyl)phosphine

(0.609 g, 2.00 mmol) Tri-(p-tolyl)phosphine was dissolved in 15 mL DMF and the same procedure as  $\text{PPh}_3$  was followed.

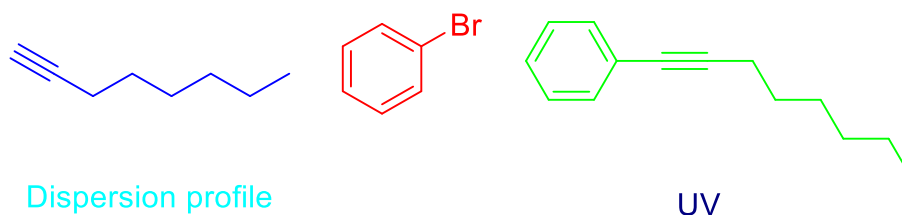


Dispersion profile



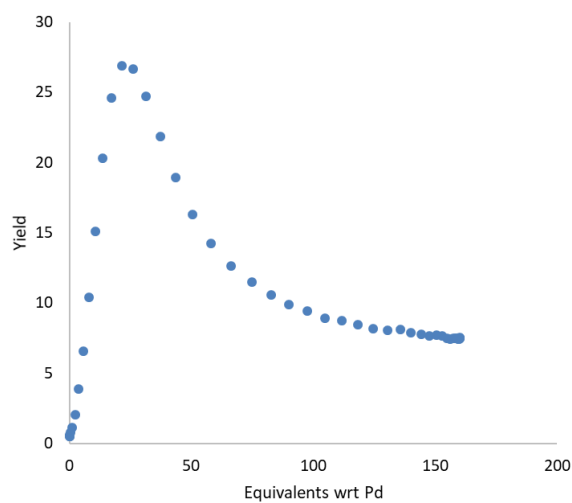
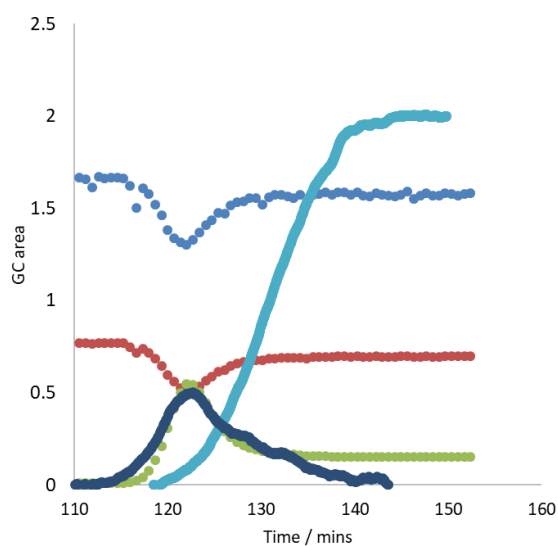
#### 7.2.3.5.4 Methyldiphenylphosphine

(0.37 mL, 2.0 mmol) Methyldiphenylphosphine was dissolved in 15 mL DMF and the same procedure as  $\text{PPh}_3$  was followed.



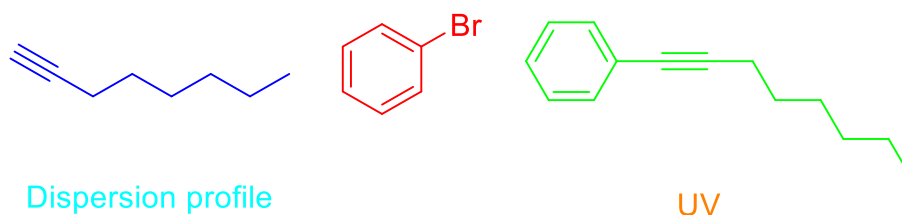
Dispersion profile

UV



#### 7.2.3.5.5 Ethyldiphenylphosphine

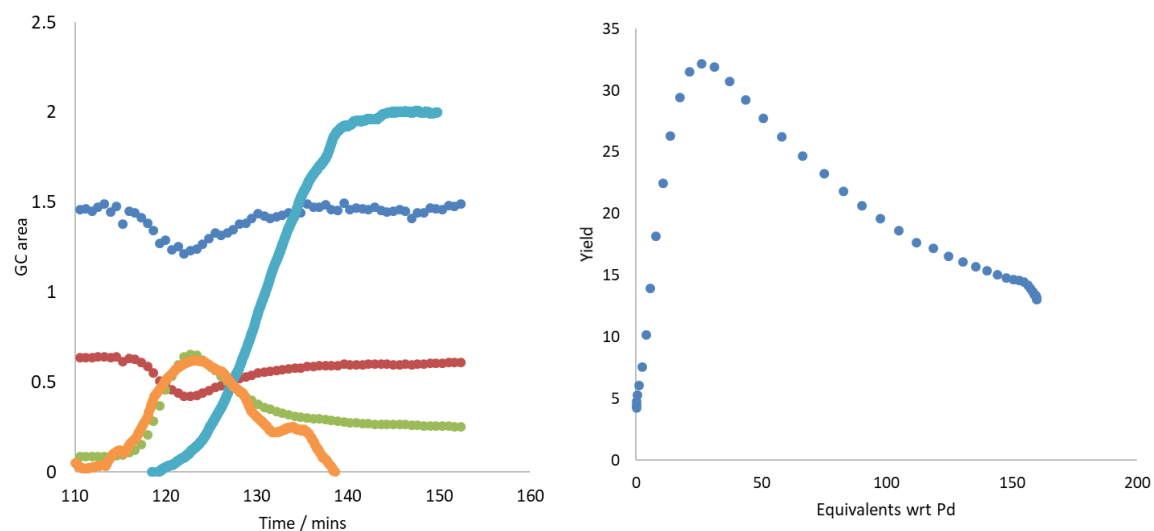
(0.41 mL, 2.0 mmol) Ethyldiphenylphosphine was dissolved in 15 mL DMF and the same procedure as  $\text{PPh}_3$  was followed.



Dispersion profile

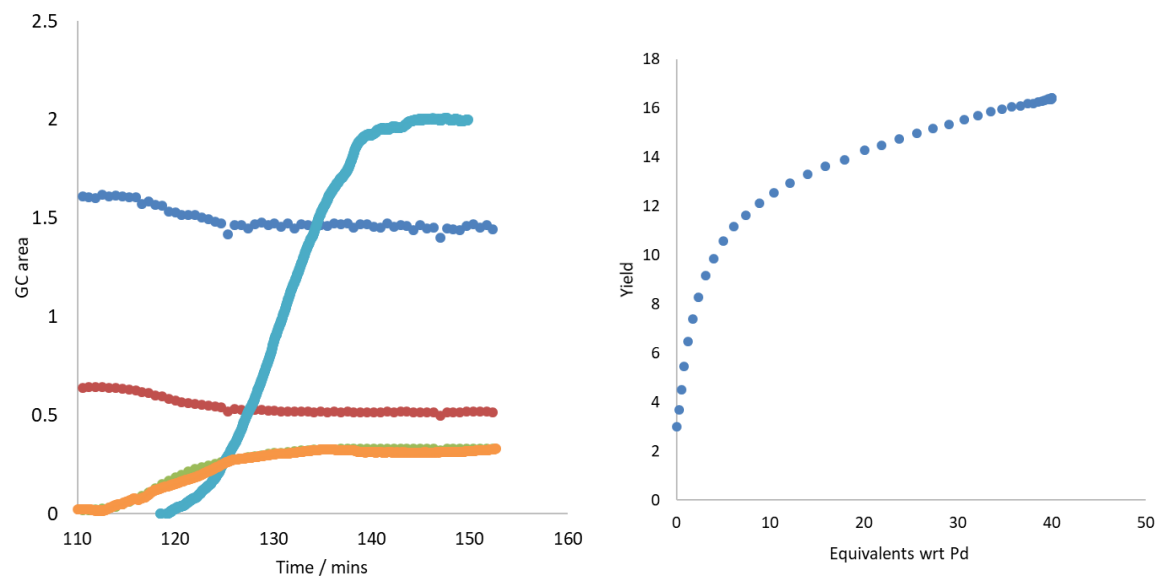
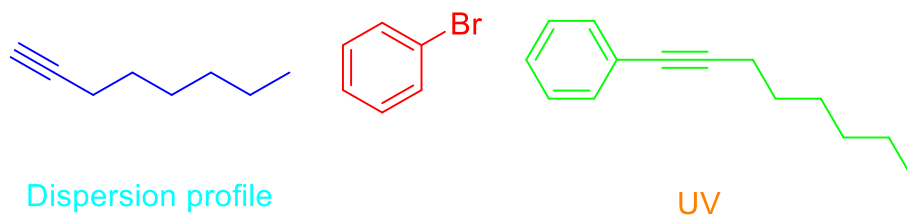
UV

## Chapter 7



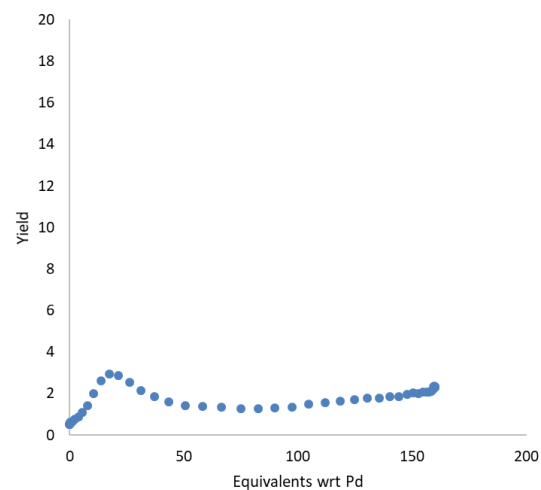
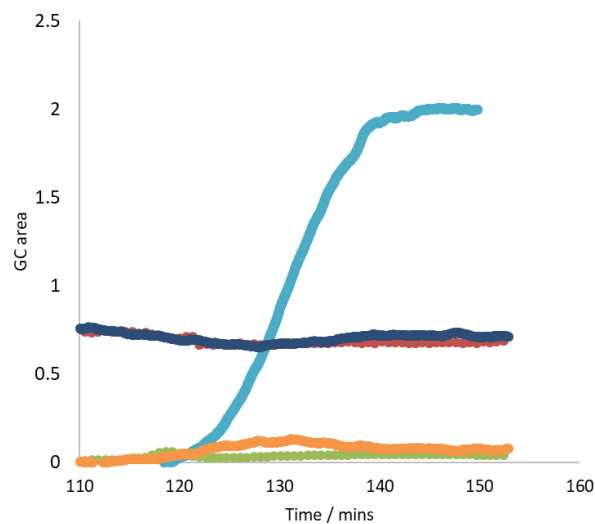
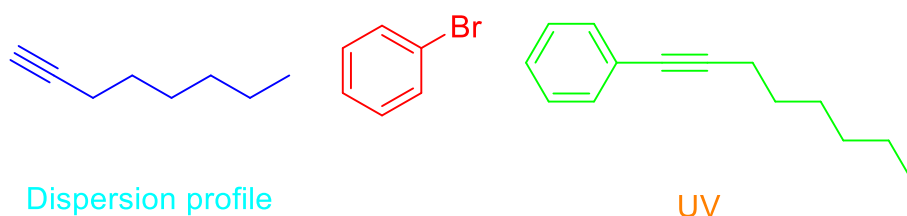
### 7.2.3.5.6 RuPhos

(0.236 g, 0.51 mmol) RuPhos was dissolved in 15 mL DMF and the same procedure as  $\text{PPh}_3$  was followed.



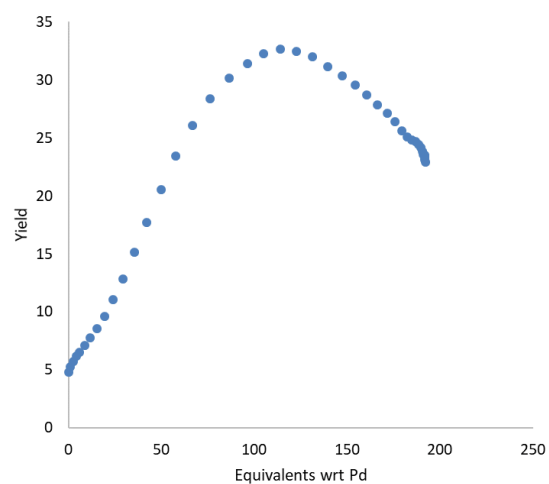
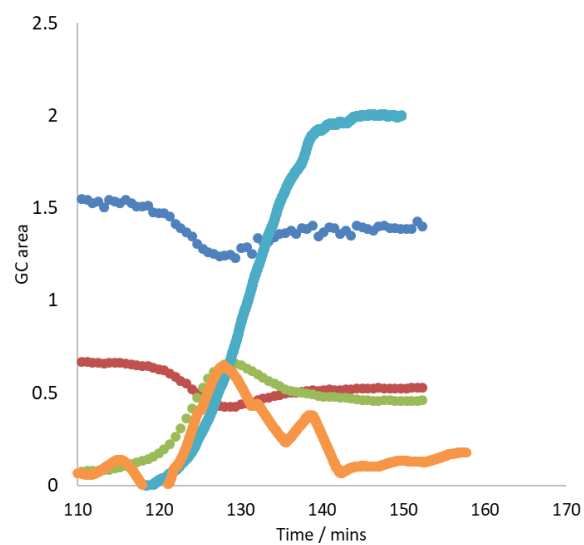
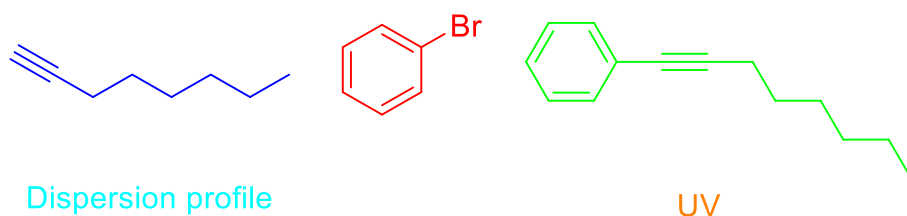
### 7.2.3.5.7 TTBP.HBF<sub>4</sub>

(0.580 g, 2.00 mmol) TTBP.HBF<sub>4</sub> was dissolved in 15 mL DMF and the same procedure as  $\text{PPh}_3$  was followed.



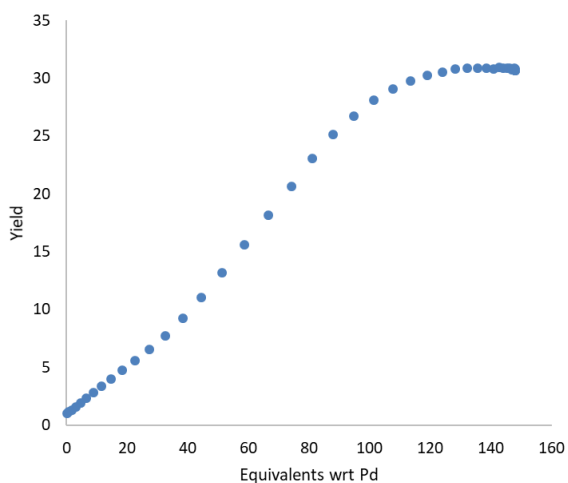
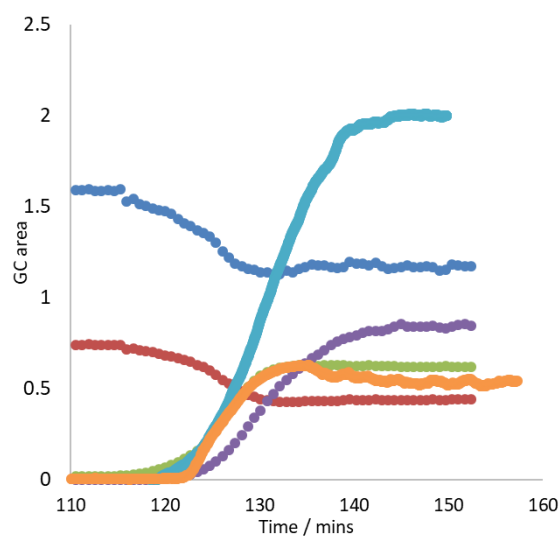
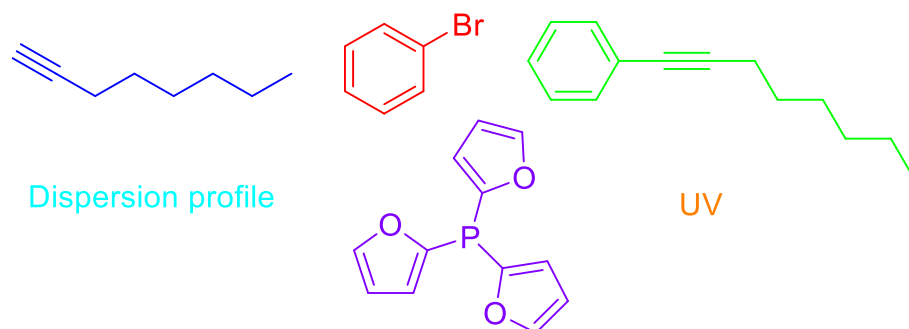
#### 7.2.3.5.8 Bis(2-furyl)phenylphosphine

(0.581 g, 2.40 mmol) Bis(2-furyl)phenylphosphine was dissolved in 15 mL DMF and the same procedure as  $\text{PPh}_3$  was followed.

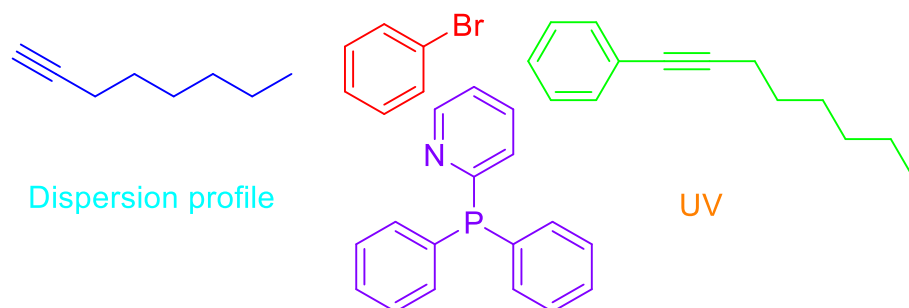


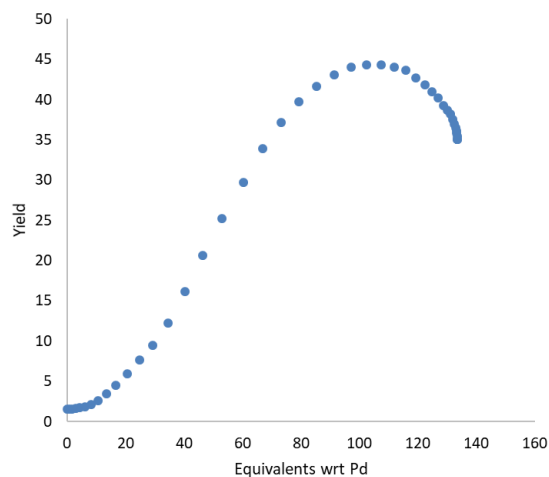
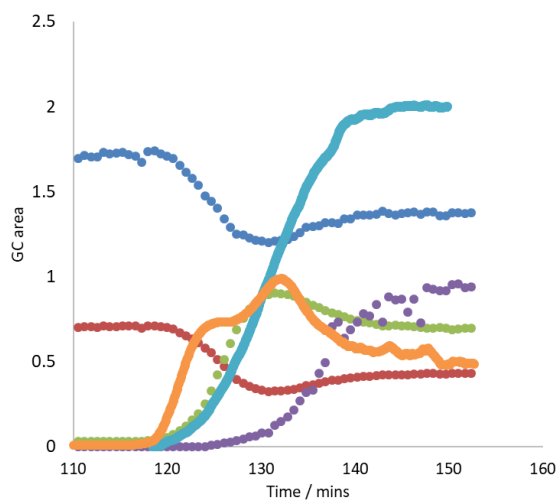
**7.2.3.5.9 Tri(2-furyl)phosphine**

(0.431 g, 1.86 mmol) Tri(2-furyl)phosphine was dissolved in 15 mL DMF and the same procedure as  $\text{PPh}_3$  was followed.

**7.2.3.5.10 Diphenyl-2-pyridyl phosphine**

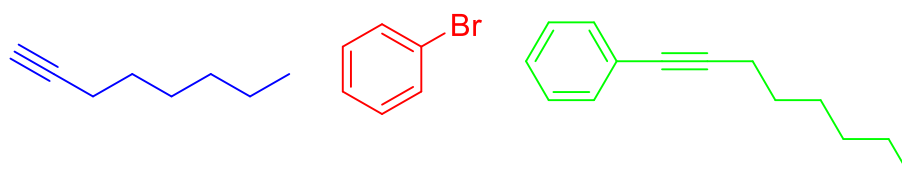
(0.439 g, 1.67 mmol) Diphenyl-2-pyridyl phosphine was dissolved in 15 mL DMF and the same procedure as  $\text{PPh}_3$  was followed.





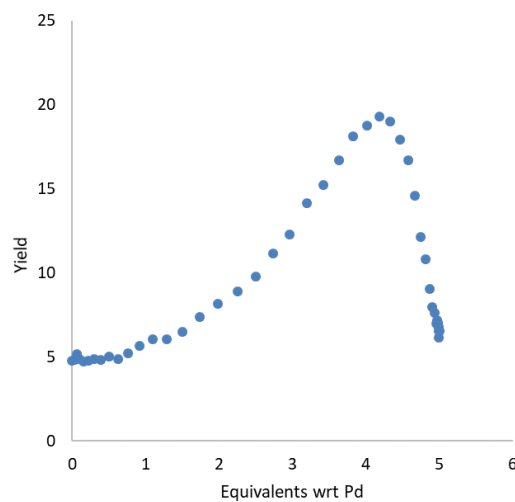
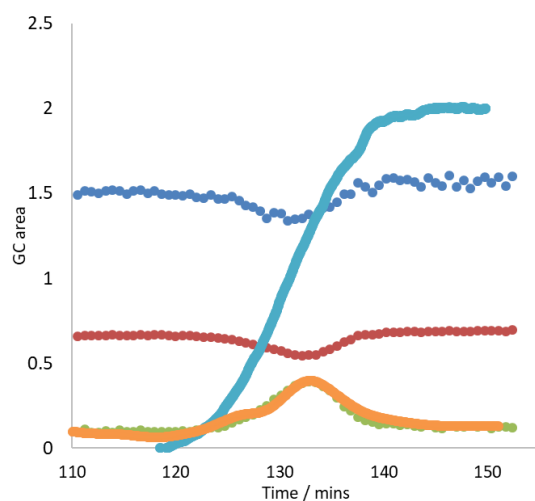
#### 7.2.3.5.11 DPPM

(0.024 g, 0.062 mmol) DPPM was dissolved in 15 mL DMF and the same procedure as  $\text{PPh}_3$  was followed.



Dispersion profile

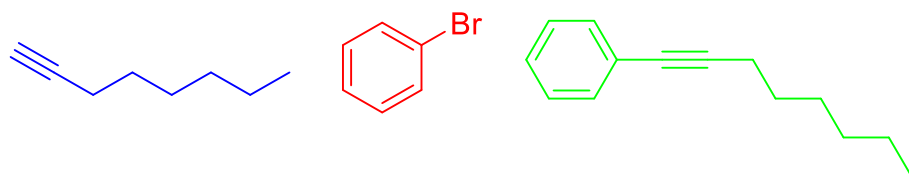
UV



#### 7.2.3.5.12 DPPE

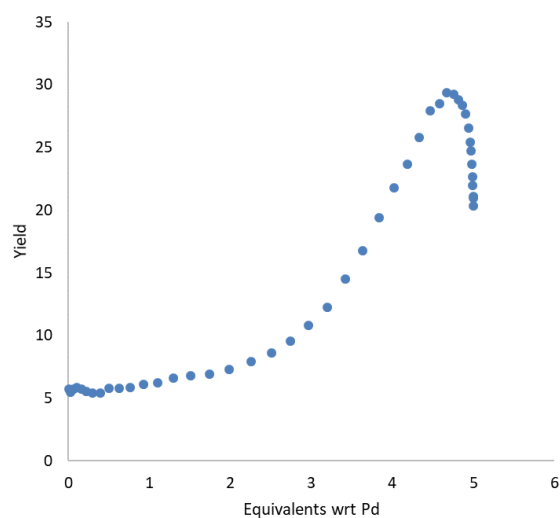
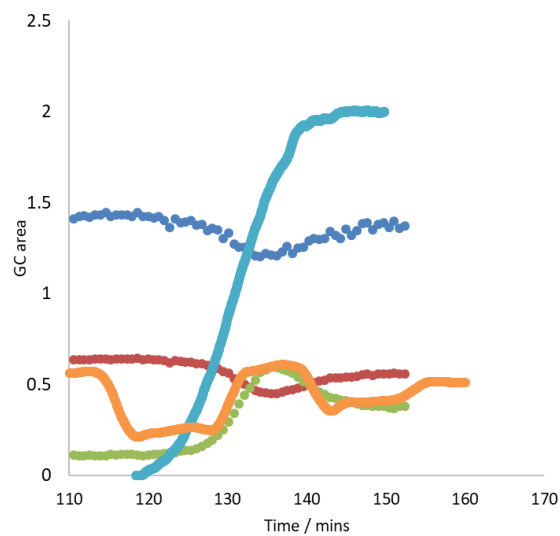
(0.025 g, 0.061 mmol) DPPE was dissolved in 15 mL DMF and the same procedure as  $\text{PPh}_3$  was followed.

## Chapter 7



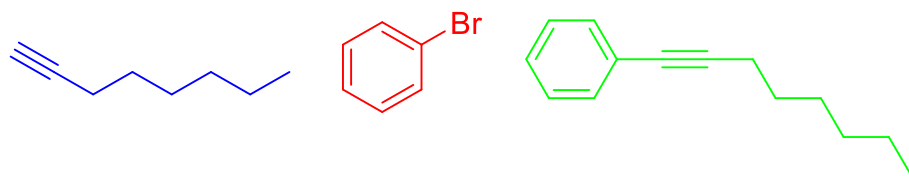
Dispersion profile

UV



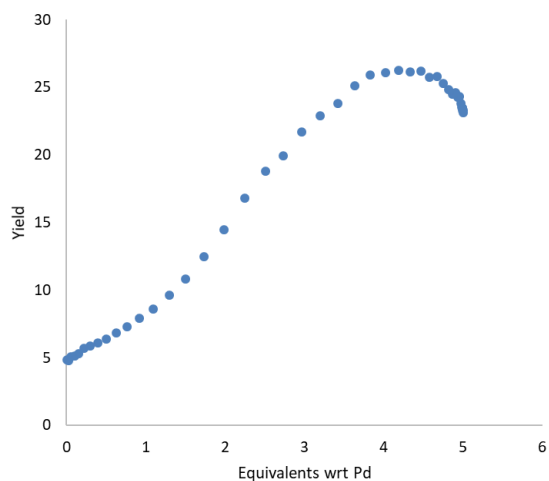
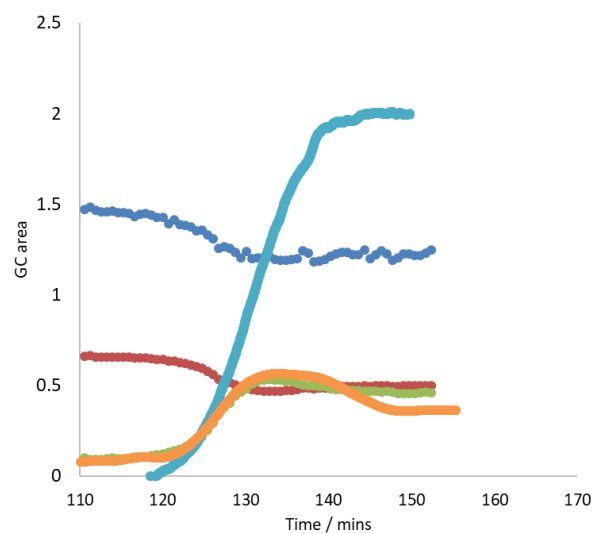
### 7.2.3.5.13 DPPP

(0.025 g, 0.061 mmol) DPPP was dissolved in 15 mL DMF and the same procedure as PPh<sub>3</sub> was followed.



Dispersion profile

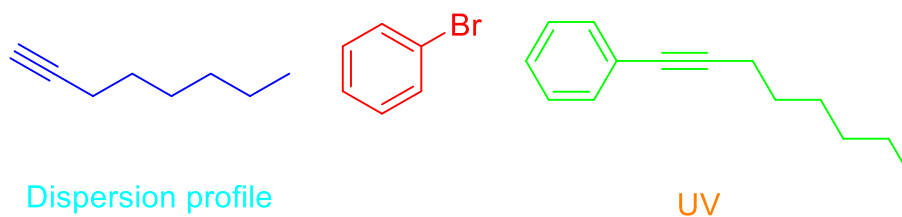
UV





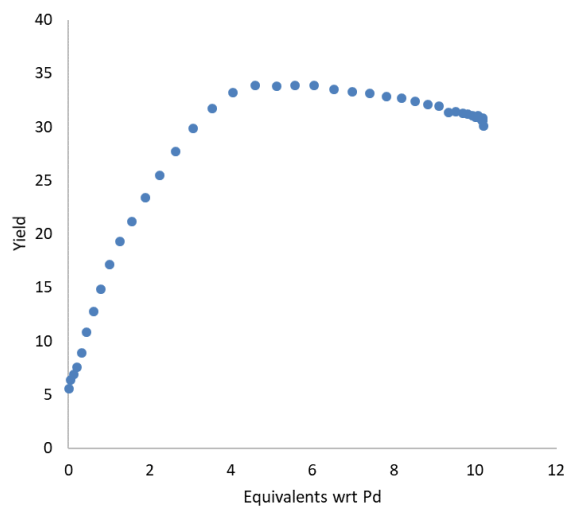
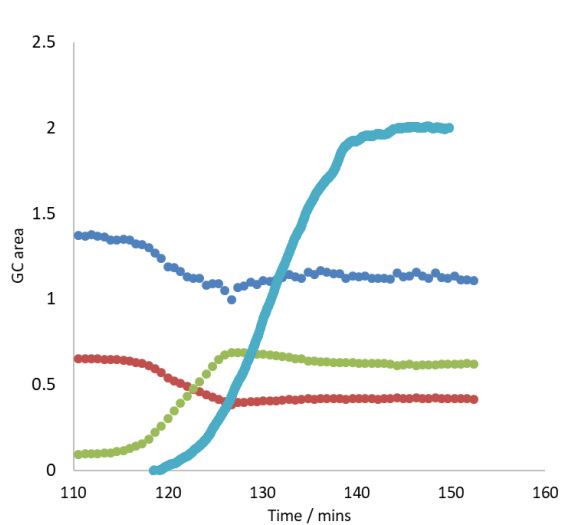
## 7.2.3.5.14 DPPB

(0.025 g, 0.127 mmol) DPPB was dissolved in 15 mL DMF and the same procedure as  $\text{PPh}_3$  was followed.



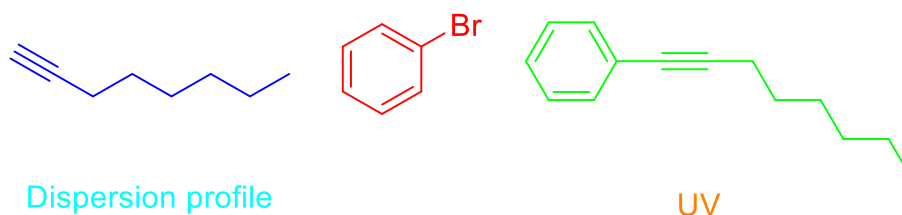
Dispersion profile

UV



## 7.2.3.5.15 XantPhos

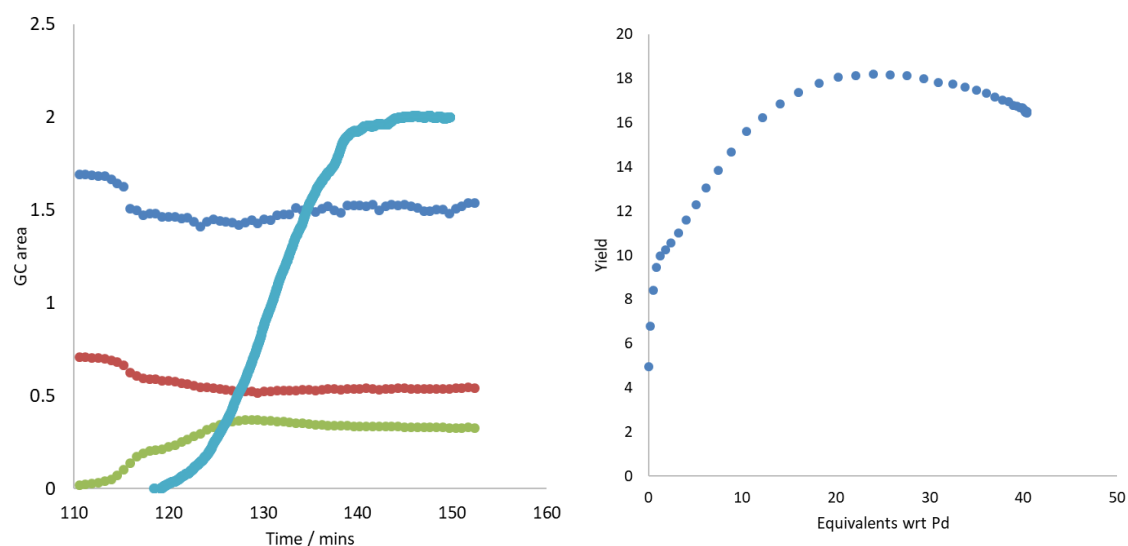
(0.293 g, 0.505 mmol) XantPhos was dissolved in 15 mL DMF and the same procedure as  $\text{PPh}_3$  was followed.



Dispersion profile

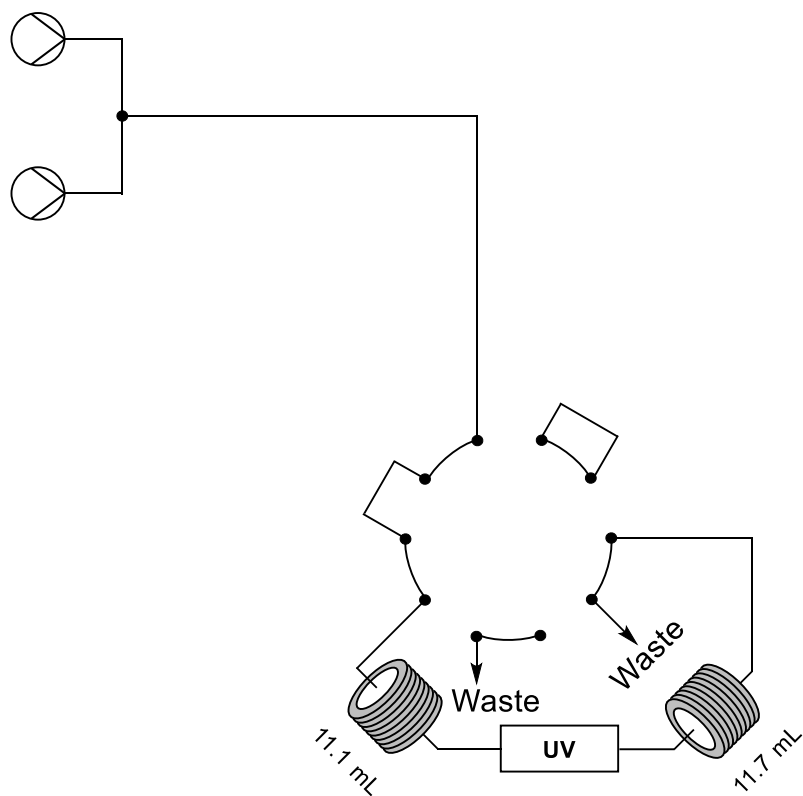
UV

## Chapter 7



### 7.2.4 C4: Multi-time point

#### 7.2.4.1 Reciprocating multi-time point method



(0.092 g, 0.652 mmol) 1-fluoro-4-nitrobenzene in 5 mL THF was attached to one line in the above flow diagram.

(0.459 g, 6.45 mmol) pyrrolidine in 5 mL THF was attached to the second line.

Reactors shown are glass bead filled reactors created from 1mm ID PFA tubing packed with 0.5 mm glass beds.

Reagents were pumped into the flow setup at 0.5 mL/min each with reaction progress monitored *via* in-line UV spectroscopy with spectra acquisition every second.

The valve switching was controlled using “Reciprocating multi-time point method” (Section 6.3.2.1) with options:

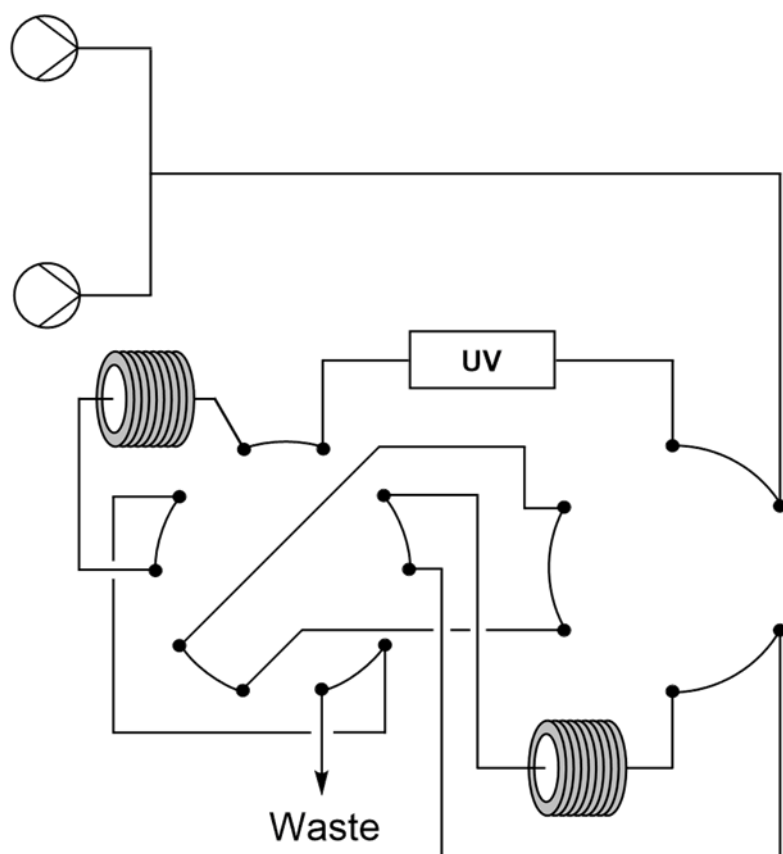
First wait: 734

Interval time: 330

Total time: 54000

The data analysis was performed by “Steady state, multi-time point” (Section 6.3.3.1) as described section 5.2.

The time between valve switching was determined by sending a UV active compound through the setup under the reaction conditions and monitoring when the plug passed through the in-line detector. The time was noted, and the valve manually switched to reverse the flow direction. This process was repeated until an average time for each interval could be calculated. The method was then repeated with automated control to obtain the complete dispersion profile for the desired reaction time.

**7.2.4.2 Non-reciprocating multi-time point method**

(0.093 g, 0.659 mmol) 1-fluoro-4-nitrobenzene in 5 mL THF was attached to one line in the above flow diagram.

(0.454 g, 6.38 mmol) pyrrolidine in 5 mL THF was attached to the second line.

Reactors shown are glass bead filled reactors created from 1mm ID PFA tubing packed with 0.5 mm glass beds, equalling 11.1 mL at the first position and 11.7 mL at the second.

Reagents were pumped into the flow setup at 1.0 mL/min each with reaction progress monitored *via* in-line UV spectroscopy with spectra acquisition every second.

The valve switching was controlled using “Non-reciprocating multi-time point method” (Section 6.3.2.2) with options:

First wait: 373

First interval: 353

Second interval: 374

Total time: 54000

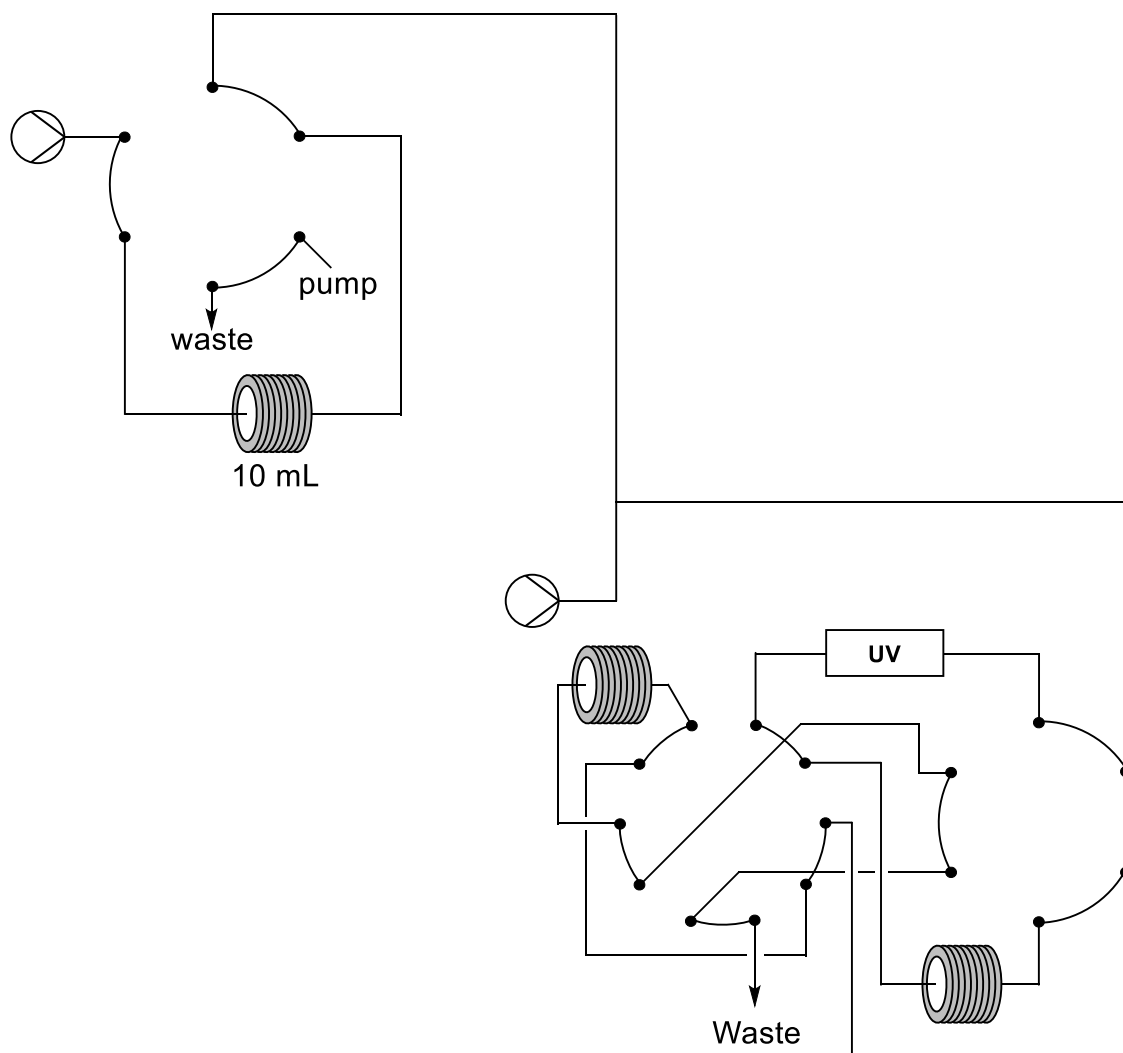
The raw data analysis was performed by “Steady state, multi-time point” (Section 6.3.3.1) which removed the non-steady state data utilising a dispersion profile previously performed on the system using the same conditions.

Experimental time was then converted into residence time for the steady states by equating each plug pass through to the first time it is detected minus the time taken to initially enter the multi-time point setup.

The resulting data was then graphed in Origin.

The time between valve switching was determined in the same method as 7.2.4.1.

#### 7.2.4.3 Concentration gradient multi-time point method



(0.184 g, 1.30 mmol) 1-fluoro-4-nitrobenzene in 10 mL THF was attached to the line directly connected to the mixing point.

(0.683 g, 9.60 mmol) pyrrolidine in 5 mL THF was attached to the second line.

## Chapter 7

Reactors shown are glass bead filled reactors created from 1mm ID PFA tubing packed with 0.5 mm glass beds, equalling 11.1 mL at the first position and 11.7 mL at the second.

Reagents were pumped into the flow setup at 1.0 mL/min each with reaction progress monitored *via* in-line UV spectroscopy with spectra acquisition every second.

The valve switching was controlled using “Concentration gradient non-reciprocating multi-time point method” (Section 6.3.2.3) with options:

First wait: 885

Gradient clip: 840

First interval: 350

Second interval: 370

Total: 54000

The raw data analysis was performed by “Gradient, multi-time point” (Section 6.3.3.2) which removed the data outside of the pass throughs by utilising a dispersion profile previously performed on the system using the same conditions as a template.

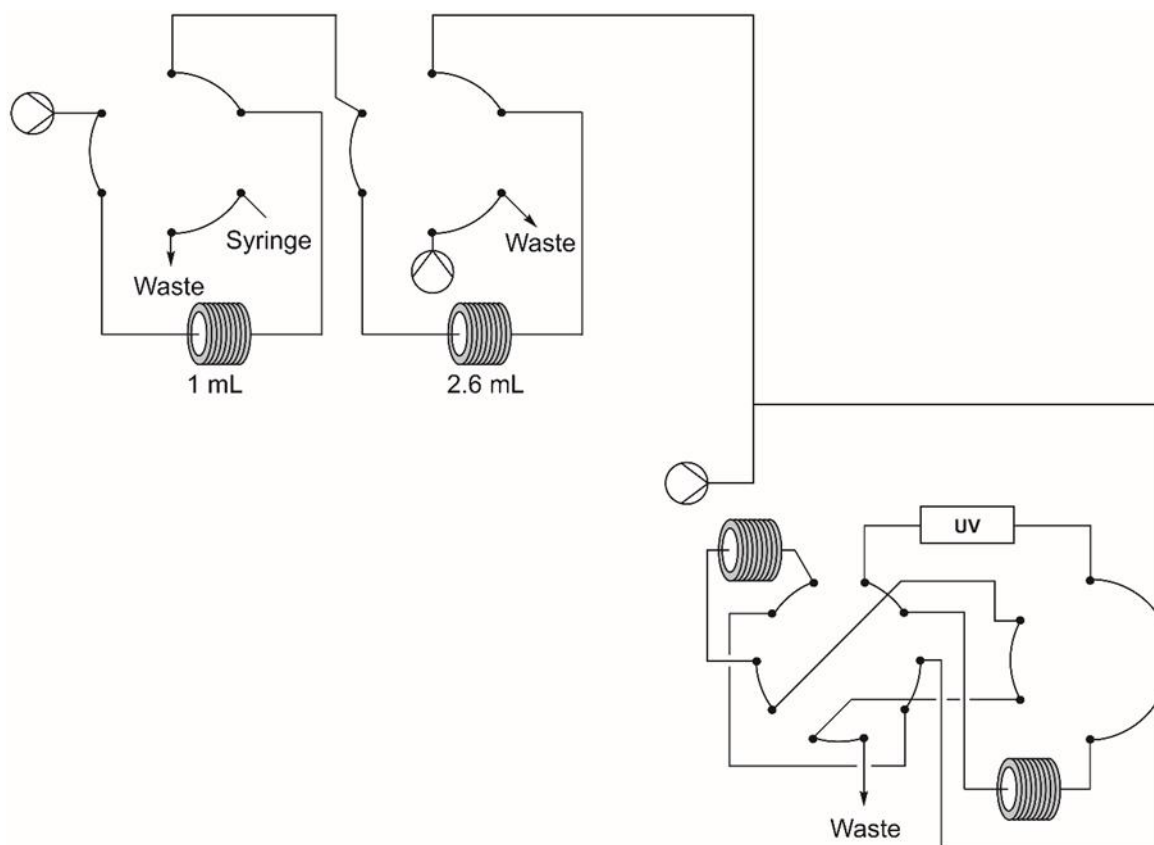
Experimental time was then converted into residence time for the gradients by equating each plug pass through to the first time it is detected minus the time taken to initially enter the multi-time point setup.

The resulting data was then graphed in Origin.

The time between switching was determined using the same method as 7.2.4.1.

The correct timing for the gradient clipping was determined by attaching the UV directly to the output of the clipping valve and pumping a UV active compound through the system using the reaction flow parameters. The resulting dispersion profile was used to calculate the clipping time.

#### 7.2.4.4 Multi-gradient, multi-time point method



(0.184 g, 1.30 mmol) 1-fluoro-4-nitrobenzene in 10 mL THF was attached to the line directly connected to the mixing point.

(0.27 mL, 3.3 mmol) pyrrolidine in 5 mL THF is syringed into the sample loop.

Reactors shown are glass bead filled reactors created from 1mm ID PFA tubing packed with 0.5 mm glass beds, equalling 11.1 mL at the first position and 11.7 mL at the second, reactors are heated to 75 °C.

Reagents were pumped into the flow setup at 1.0 mL/min each with reaction progress monitored *via* in-line UV spectroscopy with spectra acquisition every second. The gradient clipping pump was pumping solvent at 0.5 mL/min.

The valve switching was controlled manually:

0 s: Reaction start

45 s: Sample loop valve switched to A, sample loop filled with (0.32 mL, 3.3 mmol) piperidine in 5 mL THF.

1 min 15 s: Sample loop valve to B

## Chapter 7

2 min: Sample loop valve switched to A, sample loop filled with (0.37 mL, 3.3 mmol) azepane in 5 mL THF.

2 min 30 s: Sample loop valve to B

3 min 15 s: Sample loop valve to A

3 min 20 s: Gradient clip valve to A

4 min 20 s: Gradient clip valve to B

5 min 05 s: Gradient clip valve to A

6 min 10 s: Gradient clip valve to B

6 min 55 s: Gradient clip valve to A

7 min 20 s: Non-reciprocating valves to A

13 min 45 s: 10-port valve to B

20 min 02 s: 10-port valve to A

26 min 30 s: 10-port valve to B

32 min 55 s: 10-port valve to A

39 min 15 s: 10-port valve to B plugs flowed to waste.

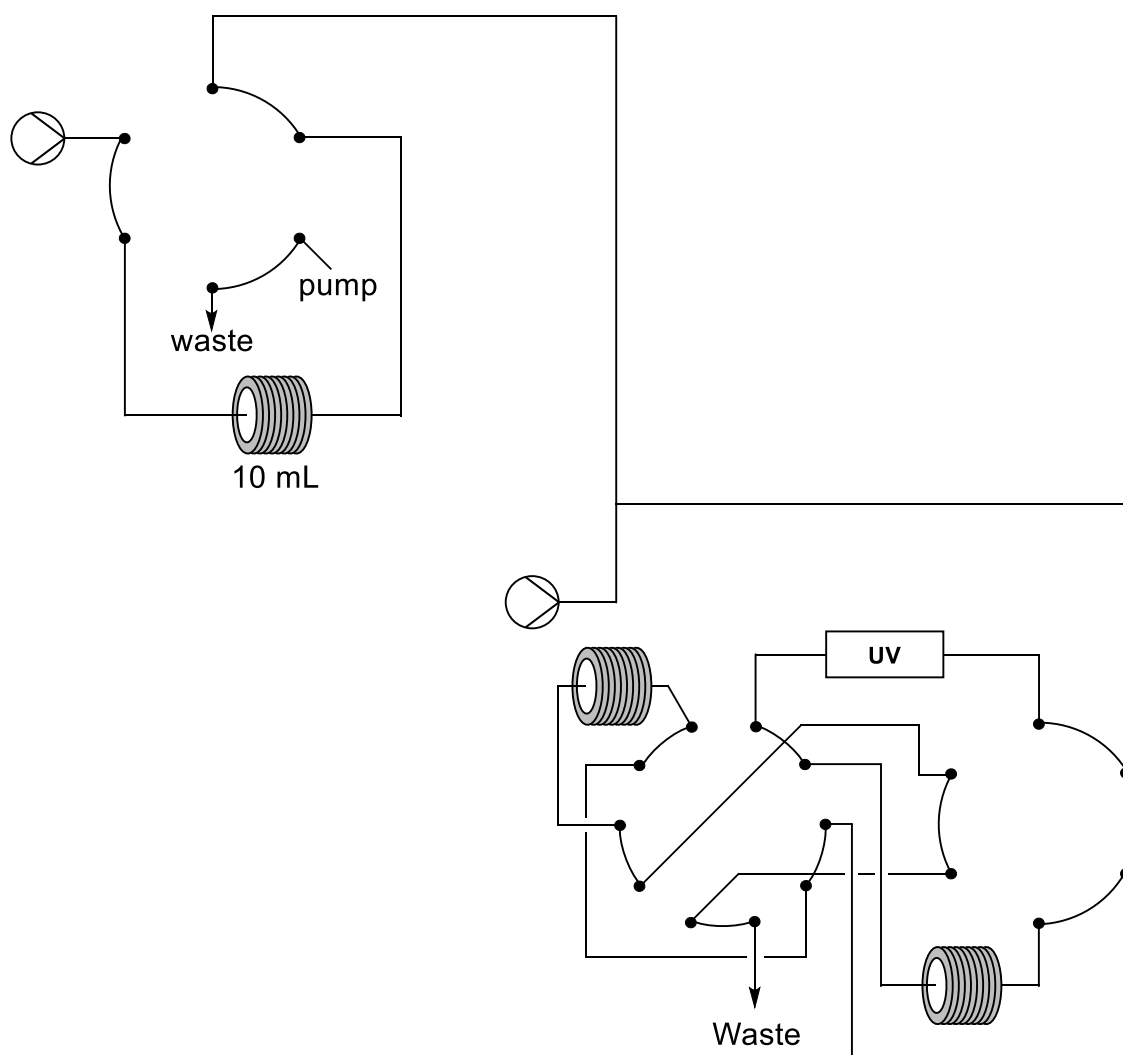
The data analysis was performed by “Gradient, multi-time point” (Section 6.3.3.2) in the same method to 6.2.4.3 except after data manipulation by the python script, the gradients corresponding to each reagent were separated into different sheets.

The time between valve switching was determined using the method described in 7.2.4.1.

The method for timing the gradient switching was the same as described in 7.2.4.3.



## 7.2.4.5 Optimisation of the formation of benzyl azide



(0.30 mL, 2.5 mmol) Benzyl chloride in 10 mL DMSO was attached to the line directly connected to the mixing point.

(0.324 g, 4.98 mmol)  $\text{NaN}_3$  in 11 mL DMSO was attached to the second line.

Reactors shown are glass bead filled reactors created from 1 mm ID PFA tubing packed with 0.5 mm glass beds, equalling 11.1 mL at the first position and 11.7 mL at the second.

Reagents were pumped into the flow setup at 0.4 mL/min each with reaction progress monitored *via* in-line UV spectroscopy with spectra acquisition every second. A 5 mL plug was used of the sodium azide solution and a 10 mL plug of the benzyl chloride solution.

The valve switching was controlled using “Concentration gradient non-reciprocating multi-time point method” (Section 6.3.2.3) with options:

First wait: 2218

## Chapter 7

Gradient clip: 2160

First interval: 914

Second interval: 935

Total: 54000

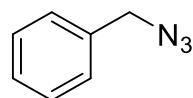
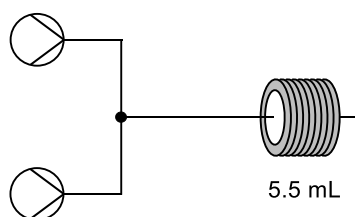
The data analysis was performed by “Gradient, multi-time point” (Section 6.3.3.2) as described in section 5.3.2.

The procedure was repeated at several temperatures.

The time between valve switching was determined using the method described in 7.2.4.1.

The method for timing the gradient switching was the same as described in 7.2.4.3.

### 7.2.4.6 Synthesis of benzyl azide



(0.718 g, 11.0 mmol) sodium azide in 40 mL DMSO was attached to one line of the above flow setup.

(1.19 mL, 10.0 mmol) benzyl chloride in 40 mL DMSO was attached to the second line

The reactor is heated at 75 °C.

39.5 mL plugs used, pumped at 0.183 mL/min each, collected 77.85 mL.

30 mL H<sub>2</sub>O was then added to the output and extracted with 6 x 30 mL Et<sub>2</sub>O.

The combined organic layer was then washed with 3 x 50 mL H<sub>2</sub>O and 80 mL brine before being concentrated giving a slight pale yellow liquid of benzyl azide (0.433 g 32.5% yield)

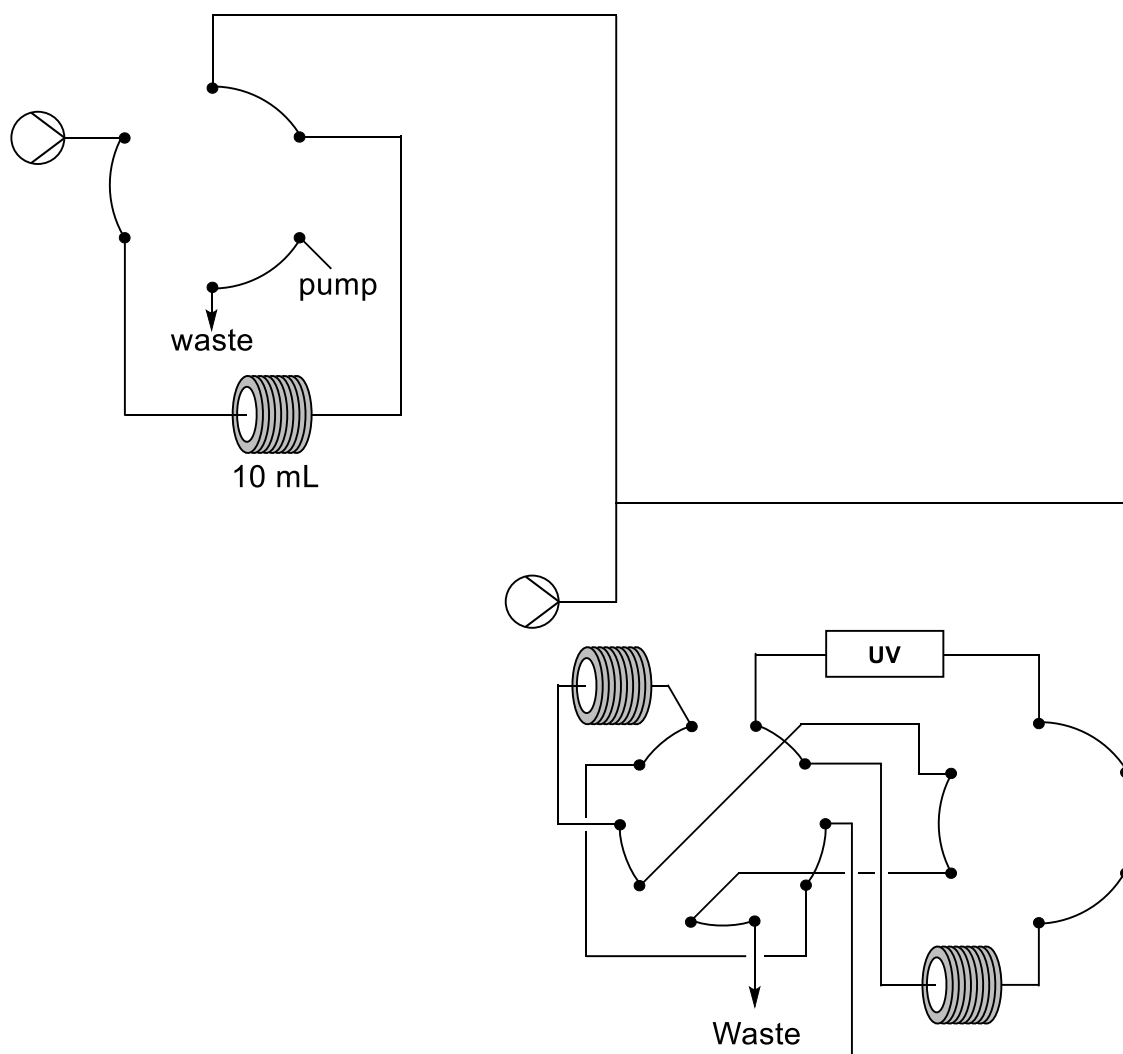
$^1\text{H}$  NMR (400 MHz,  $\text{CDCl}_3$ ):  $\delta$  7.42-7.26 (m, 5H), 4.35 (s, 2H) ppm

$^{13}\text{C}$  NMR (101 MHz,  $\text{CDCl}_3$ ):  $\delta$  135.41, 128.87, 128.34, 128.25, 54.83 ppm.

MS: LRMS (EI)  $m/z$  133.22  $[\text{M}]^+$

NMR consistent with literature values<sup>329</sup>

#### 7.2.4.7 Optimisation of the formation of 1-benzyl-4-phenyl-1H-1,2,3-triazole



(0.168 g, 1.26 mmol) Benzyl azide, (0.128 g, 1.25 mmol) phenylacetylene in 10 mL DMSO was attached to the line directly connected to the mixing point.

(0.082 g, 0.088 mmol)  $\text{CuBr}(\text{PPh}_3)_3$  in 5 mL DMSO was attached to the second line.

Reactors shown are glass bead filled reactors created from 1mm ID PFA tubing packed with 0.5 mm glass beds, equalling 11.1 mL at the first position and 11.7 mL at the second. Reactors are heated at 75 °C.

## Chapter 7

Reagents were pumped into the flow setup at 0.4 mL/min each with reaction progress monitored *via* in-line UV spectroscopy with spectra acquisition every second. A 5 mL plug was used of the Cu solution and a 10 mL plug of the benzyl azide solution.

The valve switching was controlled using “Concentration gradient non-reciprocating multi-time point method” (Section 6.3.2.3) with options:

First wait: 2218

Gradient clip: 2160

First interval: 914

Second interval: 935

Total: 54000

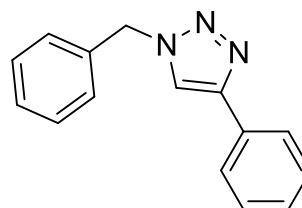
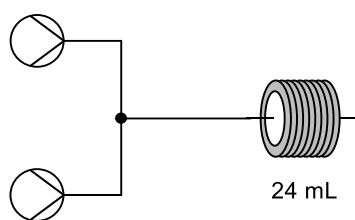
The data analysis was performed by “Gradient, multi-time point” (Section 6.3.3.2) as described in section 5.3.3.

The process was repeated at various temperatures and with varying Cu sources.

The time between valve switching was determined using the method described in 7.2.4.1.

The method for timing the gradient switching was the same as described in 7.2.4.3.

### 7.2.4.8 Synthesis of 1-benzyl-4-phenyl-1H-1,2,3-triazole



(0.355 g, 2.67 mmol) benzyl azide, (0.274 g, 2.67 mmol) in 21.35 mL DMSO was attached to one line of the above flow setup.

(0.354 g, 0.381 mmol)  $\text{CuBr}(\text{PPh}_3)_3$  in 21.35 mL DMSO was attached to the second line

The reactor is heated at 75 °C.

20 mL plugs used, pumped at 0.1 mL/min each, collected 35.79 mL at the output.

30 mL  $\text{H}_2\text{O}$  was then added to the output and extracted with 6 x 30 mL ethyl acetate.

The combined organic layer was then washed with 3 x 30 mL  $\text{H}_2\text{O}$  before being concentrated giving a yellow oil. Column chromatography (10% EtOAc in hexane) on crude material provided a white solid of title compound (0.339 g, 53.9% yield).

$^1\text{H}$  NMR (400 MHz,  $\text{CDCl}_3$ ):  $\delta$  7.81-7.79 (m, 2H), 7.66 (s, 1H), 7.42-7.29 (m, 8H), 5.58 (s, 2H) ppm

$^{13}\text{C}$  NMR (101 MHz,  $\text{CDCl}_3$ ):  $\delta$  148.25, 134.71, 130.56, 129.17, 128.81, 128.17, 128.07, 125.71, 119.48, 54.24 ppm.

MS: LRMS (ESI)  $m/z$  236.18  $[\text{M}+\text{H}]^+$

NMR consistent with literature values<sup>330,331</sup>

## 7.3 Python

Scripts were created using Python 3.0 using Notepad++ as the editor.

### 7.3.1 RS232 control commands

#### 7.3.1.1 Vapourtec

##### 6.3.1.1.1 RS232 Port settings

Baud: 19200

Bits: 8

Parity: None

Stop Bits: 1

Flow Control: None

##### 7.3.1.1.1 RS232 Serial commands

Set flow rate:

*FR pump rate*

*Pump = 0 to 3 where pump A = 0, pump B = 1 etc.*

*Rate = desired flow rate in  $\mu\text{L}/\text{min}$*

Power on:

*PN*

Power off:

*PF*

Set pressure:

*PL pres*

*pres = maximum wanted pressure in mbar*

Switch valves:

These commands are identical to the switches on the face of the Vapourtec.

*KP x*

*x = 0 Switch pump A to solvent*

*x = 1 Switch pump A to reagent*

*x = 2 Switch pump B to solvent*

*x = 3 Switch pump B to reagent*

*x = 4 Switch pump A sample loop to fill*

*x = 5 Switch pump A sample loop to release*

*x = 6 Switch pump B sample loop to fill*

*x = 7 Switch pump B sample loop to release*

*x = 8 Switch valve to waste*

*x = 9 Switch valve to collect*

Set temperature:

*ST reactor temp rate*

*reactor = 0 to 3 for desired reactor position*

*temp = Desired temperature*

*rate = Desired rate of temperature increase from 5 to 80*

Forward command:

If second set of pumps are present, commands must be prefaced with following to set pumps C and D.

*FW*

Reset history:

*HR*

Pressure history:

*HP*

Temperature history:

*HT*

Power history:

*HW*

Flow history:

*HF*

Valve history:

*HV*

#### **7.3.1.2 VICI valves**

For the following commands, prefacing the commands with a \* will apply the command to every attached valve. Prefacing the commands with a value will only apply the command to the valve with that device ID.

Firmware and product number:

*VR*

Set position:

*GO x*

*x = A or B for position A or B*

Set position A:

## Chapter 7

*CW*

Set position B:

*CC*

Change position:

*TO*

Change position, wait, change position:

*TT*

Set wait time:

*DT y*

*y = 0 to 65365 ms*

Display current position:

*CP*

Set device ID:

*ID z*

*z = 0 to 9*

Set baud rate:

*SB n*

*n = 2400 to 115220*

Display all commands:

*?*



## 7.3.2 Python control scripts

### 7.3.2.1 Reciprocating multi-time point method

```

import serial
import os
import time
from logo import *

def cls():
    os.system('cls' if os.name == 'nt' else 'clear')

cls()
RFM()
time.sleep(2)
while True:
    try:
        VICIport = int(input("Port number of VICI valve: "))
        if VICIport >= 0:
            cls()
            RFM()
            print("Port: COM" + str(VICIport))
            break
        else:
            cls()
            RFM()
            print("Port must be an integer")
            continue
    except ValueError:
        cls()
        RFM()
        print("Port must be an integer")
        continue

ser = serial.Serial(
    port = "COM" + str(VICIport),
    baudrate = 9600,
    parity = serial.PARITY_NONE,
    stopbits = serial.STOPBITS_ONE,
    bytesize = serial.EIGHTBITS,
)

SwitchB = [int(0x63)] + [int(0x63)] + [int(0x0D)]
SwitchA = [int(0x63)] + [int(0x77)] + [int(0x0D)]

while True:
    try:
        FirstWait = int(input("Time until first switch (seconds): "))
        if FirstWait >= 0:
            cls()
            RFM()
            print("Port: COM" + str(VICIport))
            print("Initial wait: " + str(FirstWait) + " seconds")
            break
        else:
            cls()
            RFM()
            print("Port: COM" + str(VICIport))
            print("Time must be a positive integer")
            continue
    except ValueError:
        cls()
        RFM()
        print("Port: COM" + str(VICIport))
        print("Time must be a positive integer")
        continue

while True:
    try:
        IntervalTime = int(input("Interval between valve switching (seconds): "))
        if IntervalTime >= 0:
            cls()
            RFM()
            print("Port: COM" + str(VICIport))
            print("Initial wait: " + str(FirstWait) + " seconds")
            print("Interval: " + str(IntervalTime) + " seconds")
            break
        else:
            cls()
            RFM()
            print("Port: COM" + str(VICIport))
            print("Initial wait: " + str(FirstWait) + " seconds")
            print("Time must be a positive integer")
            continue
    except ValueError:
        cls()
        RFM()
        print("Port: COM" + str(VICIport))
        print("Initial wait: " + str(FirstWait) + " seconds")
        print("Interval: " + str(IntervalTime) + " seconds")
        print("Time must be a positive integer")
        continue

ReactionTime = int(input("Total reaction time (seconds): "))
if FirstWait >= 0:
    cls()
    RFM()
    print("Port: COM" + str(VICIport))
    print("Initial wait: " + str(FirstWait) + " seconds")
    print("Interval: " + str(IntervalTime) + " seconds")
    print("Total reaction time: " + str(ReactionTime) + " seconds")
    break
else:
    cls()
    RFM()
    print("Port: COM" + str(VICIport))
    print("Initial wait: " + str(FirstWait) + " seconds")
    print("Interval: " + str(IntervalTime) + " seconds")
    print("Time must be a positive integer")
    continue
except ValueError:
    cls()
    RFM()
    print("Port: COM" + str(VICIport))
    print("Initial wait: " + str(FirstWait) + " seconds")
    print("Interval: " + str(IntervalTime) + " seconds")
    print("Time must be a positive integer")
    continue

MaxTime = (ReactionTime - FirstWait) / (2 * IntervalTime)
ser.isOpen()
time.sleep(FirstWait)
for x in range(0, int(round(MaxTime))):
    ser.write(SwitchA)
    time.sleep(IntervalTime)
    ser.write(SwitchB)
    time.sleep(IntervalTime)
ser.close()

```

## 7.3.2.2 Non-reciprocating multi-time point method

```

import serial
import os
import time
from logo import *

def cls():
    os.system('cls' if os.name == 'nt' else 'clear')

cls()
RFM()
time.sleep(2)
while True:
    try:
        VICIport = int(input("Port number of VICI valve: "))
        if VICIport >= 0:
            cls()
            RFM()
            print("Port: COM" + str(VICIport))
            break
        else:
            cls()
            RFM()
            print("Port must be an integer")
            continue
    except ValueError:
        cls()
        RFM()
        print("Port must be an integer")
        continue

ser = serial.Serial(
    port = "COM" + str(VICIport),
    baudrate = 9600,
    parity = serial.PARITY_NONE,
    stopbits = serial.STOPBITS_ONE,
    bytesize = serial.EIGHTBITS,

)

SwitchBothA = [int(0x2A)] + [int(0x63)] + [int(0x77)] + [int(0x0D)]

SwitchB = [int(0x33)] + [int(0x63)] + [int(0x63)] + [int(0x0D)]

SwitchA = [int(0x33)] + [int(0x63)] + [int(0x77)] + [int(0x0D)]

while True:
    try:
        FirstWait = int(input("Time until first switch (seconds): "))
        if FirstWait >= 0:
            cls()
            RFM()
            print("Port: COM" + str(VICIport))
            print("Initial wait: " + str(FirstWait) + " seconds")
            break
        else:
            cls()
            RFM()
            print("Port: COM" + str(VICIport))
            print("Time must be a positive integer")
            continue
    except ValueError:
        cls()
        RFM()
        print("Port: COM" + str(VICIport))
        print("Time must be a positive integer")
        continue

```

```

while True:
    try:
        IntervalTime = int(input("Interval between valve switching (seconds): "))
        if IntervalTime >= 0:
            cls()
            RFM()
            print("Port: COM" + str(VICIport))
            print("Initial wait: " + str(FirstWait) + " seconds")
            print("Interval: " + str(IntervalTime) + " seconds")
            break
        else:
            cls()
            RFM()
            print("Port: COM" + str(VICIport))
            print("Initial wait: " + str(FirstWait) + " seconds")
            print("Time must be a positive integer")
            continue
    except ValueError:
        cls()
        RFM()
        print("Port: COM" + str(VICIport))
        print("Initial wait: " + str(FirstWait) + " seconds")
        print("Time must be a positive integer")
        continue

while True:
    try:
        SecondIntervalTime = int(input("Interval between second valve switch (seconds): "))
        if IntervalTime >= 0:
            cls()
            RFM()
            print("Port: COM" + str(VICIport))
            print("Initial wait: " + str(FirstWait) + " seconds")
            print("Interval: " + str(IntervalTime) + " seconds")
            print("Second interval: " + str(SecondIntervalTime) + " seconds")
            break
        else:
            cls()
            RFM()
            print("Port: COM" + str(VICIport))
            print("Initial wait: " + str(FirstWait) + " seconds")
            print("Time must be a positive integer")
            continue
    except ValueError:
        cls()
        RFM()
        print("Port: COM" + str(VICIport))
        print("Initial wait: " + str(FirstWait) + " seconds")
        print("Time must be a positive integer")
        continue

while True:
    try:
        ReactionTime = int(input("Total reaction time (seconds): "))
        if FirstWait >= 0:
            cls()
            RFM()
            print("Port: COM" + str(VICIport))
            print("Initial wait: " + str(FirstWait) + " seconds")
            print("Interval: " + str(IntervalTime) + " seconds")
            print("Second interval: " + str(SecondIntervalTime) + " seconds")
            print("Total reaction time: " + str(ReactionTime) + " seconds")
            break
        else:
            cls()
            RFM()
            print("Port: COM" + str(VICIport))
            print("Initial wait: " + str(FirstWait) + " seconds")
            print("Interval: " + str(IntervalTime) + " seconds")
            print("Second interval: " + str(SecondIntervalTime) + " seconds")
            print("Time must be a positive integer")
            continue
    except ValueError:
        cls()
        RFM()
        print("Port: COM" + str(VICIport))
        print("Initial wait: " + str(FirstWait) + " seconds")
        print("Interval: " + str(IntervalTime) + " seconds")
        print("Second interval: " + str(SecondIntervalTime) + " seconds")
        print("Time must be a positive integer")
        continue

MaxTime = (ReactionTime-FirstWait)/(IntervalTime+SecondIntervalTime)

ser.isOpen()

time.sleep(FirstWait)

ser.write(SwitchBothA)

for x in range(0,int(round(MaxTime))):

    time.sleep(IntervalTime)

    ser.write(SwitchB)

    time.sleep(SecondIntervalTime)

    ser.write(SwitchA)

ser.close()

```

### 7.3.2.3 Concentration gradient non-reciprocating multi-time point method

## Chapter 7

```
import serial
import os
import time
from logo import *

def cls():
    os.system('cls' if os.name == 'nt' else 'clear')

cls()
RFM()
time.sleep(2)
while True:
    try:
        VICIport = int(input("Port number of VICI valve: "))
        if VICIport >= 0:
            cls()
            RFM()
            print("Port: COM" + str(VICIport))
            break
        else:
            cls()
            RFM()
            print("Port must be an integer")
            continue
    except ValueError:
        cls()
        RFM()
        print("Port must be an integer")
        continue

ser = serial.Serial(
    port = "COM" + str(VICIport),
    baudrate = 9600,
    parity = serial.PARITY_NONE,
    stopbits = serial.STOPBITS_ONE,
    bytesize = serial.EIGHTBITS,
)

SwitchBothA = [int(0x2A)] + [int(0x63)] + [int(0x77)] + [int(0x0D)]
SwitchB = [int(0x33)] + [int(0x63)] + [int(0x63)] + [int(0x0D)]
SwitchA = [int(0x33)] + [int(0x63)] + [int(0x77)] + [int(0x0D)]
GradientClip = [int(0x32)] + [int(0x63)] + [int(0x77)] + [int(0x0D)]

while True:
    try:
        FirstWait = int(input("Time until first switch (seconds): "))
        if FirstWait >= 0:
            cls()
            RFM()
            print("Port: COM" + str(VICIport))
            print("Initial wait: " + str(FirstWait) + " seconds")
            break
        else:
            cls()
            RFM()
            print("Port: COM" + str(VICIport))
            print("Time must be a positive integer")
            continue
    except ValueError:
        cls()
        RFM()
        print("Port: COM" + str(VICIport))
        print("Time must be a positive integer")
        continue
```

```

while True:
    try:
        GradClipWait = int(input("Time until gradient clip (seconds): "))
        if GradClipWait >= 0:
            cls()
            RFM()
            print("Port: COM" + str(VICIport))
            print("Initial wait: " + str(FirstWait) + " seconds")
            print("Gradient Clip wait: " + str(GradClipWait) + " seconds")
            break
        else:
            cls()
            RFM()
            print("Port: COM" + str(VICIport))
            print("Initial wait: " + str(FirstWait) + " seconds")
            print("Time must be a positive integer")
            continue
    except ValueError:
        cls()
        RFM()
        print("Port: COM" + str(VICIport))
        print("Initial wait: " + str(FirstWait) + " seconds")
        print("Time must be a positive integer")
        continue

while True:
    try:
        IntervalTime = int(input("Interval between valve switching (seconds): "))
        if IntervalTime >= 0:
            cls()
            RFM()
            print("Port: COM" + str(VICIport))
            print("Initial wait: " + str(FirstWait) + " seconds")
            print("Gradient Clip wait: " + str(GradClipWait) + " seconds")
            print("Interval: " + str(IntervalTime) + " seconds")
            break
        else:
            cls()
            RFM()
            print("Port: COM" + str(VICIport))
            print("Initial wait: " + str(FirstWait) + " seconds")
            print("Gradient Clip wait: " + str(GradClipWait) + " seconds")
            print("Time must be a positive integer")
            continue
    except ValueError:
        cls()
        RFM()
        print("Port: COM" + str(VICIport))
        print("Initial wait: " + str(FirstWait) + " seconds")
        print("Gradient Clip wait: " + str(GradClipWait) + " seconds")
        print("Time must be a positive integer")
        continue

while True:
    try:
        SecondIntervalTime = int(input("Interval between second valve switch (seconds): "))
        if SecondIntervalTime >= 0:
            cls()
            RFM()
            print("Port: COM" + str(VICIport))
            print("Initial wait: " + str(FirstWait) + " seconds")
            print("Gradient Clip wait: " + str(GradClipWait) + " seconds")
            print("Interval: " + str(IntervalTime) + " seconds")
            print("Second interval: " + str(SecondIntervalTime) + " seconds")
            break
        else:
            cls()
            RFM()
            print("Port: COM" + str(VICIport))
            print("Initial wait: " + str(FirstWait) + " seconds")
            print("Gradient Clip wait: " + str(GradClipWait) + " seconds")
            print("Interval: " + str(IntervalTime) + " seconds")
            print("Time must be a positive integer")
            continue
    except ValueError:
        cls()
        RFM()
        print("Port: COM" + str(VICIport))
        print("Initial wait: " + str(FirstWait) + " seconds")
        print("Gradient Clip wait: " + str(GradClipWait) + " seconds")
        print("Interval: " + str(IntervalTime) + " seconds")
        print("Time must be a positive integer")
        continue

while True:
    try:
        ReactionTime = int(input("Total reaction time (seconds): "))
        if FirstWait >= 0:
            cls()
            RFM()
            print("Port: COM" + str(VICIport))
            print("Initial wait: " + str(FirstWait) + " seconds")
            print("Gradient Clip wait: " + str(GradClipWait) + " seconds")
            print("Interval: " + str(IntervalTime) + " seconds")
            print("Second interval: " + str(SecondIntervalTime) + " seconds")
            print("Total reaction time: " + str(ReactionTime) + " seconds")
            break
        else:
            cls()
            RFM()
            print("Port: COM" + str(VICIport))
            print("Initial wait: " + str(FirstWait) + " seconds")
            print("Gradient Clip wait: " + str(GradClipWait) + " seconds")
            print("Interval: " + str(IntervalTime) + " seconds")
            print("Second interval: " + str(SecondIntervalTime) + " seconds")
            print("Time must be a positive integer")
            continue
    except ValueError:
        cls()
        RFM()
        print("Port: COM" + str(VICIport))
        print("Initial wait: " + str(FirstWait) + " seconds")
        print("Gradient Clip wait: " + str(GradClipWait) + " seconds")
        print("Interval: " + str(IntervalTime) + " seconds")
        print("Second interval: " + str(SecondIntervalTime) + " seconds")
        print("Time must be a positive integer")
        continue

MaxTime = (ReactionTime - (FirstWait) / (IntervalTime + SecondIntervalTime))
TimeGap = (FirstWait - GradClipWait)

ser.isOpen()
time.sleep(GradClipWait)
ser.write(GradientClip)
time.sleep(TimeGap)
ser.write(SwitchBothA)

for x in range(0, int(round(MaxTime))):
    time.sleep(IntervalTime)
    ser.write(SwitchB)
    time.sleep(SecondIntervalTime)
    ser.write(SwitchA)

ser.close()

```

### 7.3.3 Python data manipulation

#### 7.3.3.1 Steady state, multi-time point

```
import openpyxl

wb = openpyxl.load_workbook('test.xlsx')
sheet = wb.active

for rowNum in range(3, sheet.max_row):
    YieldDiff = abs(sheet.cell(row = rowNum, column = 12).value)
    if YieldDiff > 0.004:
        sheet['K'+ str(rowNum)] = 0
        sheet['A'+ str(rowNum)] = ''

#0.01, 0.003, 0.004#
for rowNum in range(3, sheet.max_row):
    Yield = abs(sheet.cell(row = rowNum, column = 11).value)
    if Yield < 15.3 :
        sheet['K' + str(rowNum)] = ''
        sheet['A'+ str(rowNum)] = ''

wb.save('test2.xlsx')
```

## 7.3.3.2 Gradient, multi-time point

```

import openpyxl

wb = openpyxl.load_workbook('test.xlsx')
#test.xlsx in Users folder. Can be changed by altering the path in python
sheet = wb.active

rowNum3 = 3
#Row number currently worked on after deletion
x = 3
#Row number if none deleted

while rowNum3 < sheet.max_row:

    YieldDiff = sheet.cell(row = rowNum3, column = 26).value
    #Z column on excel sheet, difference between neighbouring cells
    Absorbance = sheet.cell(row = rowNum3, column = 25).value
    #Y column on excel sheet, spectrometer reading
    if YieldDiff < 0.001 and Absorbance < 3:
        print(rowNum3, x)
        sheet.delete_rows(rowNum3, 1)
        rowNum3 = rowNum3-1
        x = x+1
    else:
        rowNum3 = rowNum3+1
        x = x+1
#Goes through every cell in Z and Y column and deletes the row if parameter not met.

wb.save('test2.xlsx')

```

## Chapter 8      References

1. M. B. Plutschack, B. Pieber, K. Gilmore and P. H. Seeberger, *Chem. Rev.*, 2017, **117**, 11796–11893.
2. T. Schwalbe, V. Autze, M. Hohmann and W. Stirner, *Org. Process Res. Dev.*, 2004, **8**, 440–454.
3. A. A. Kulkarni, V. S. Kalyani, R. A. Joshi and R. R. Joshi, *Org. Process Res. Dev.*, 2009, **13**, 999–1002.
4. H. Lehmann, *Green Chem.*, 2017, **19**, 1449–1453.
5. M. Movsisyan, E. I. P. Delbeke, J. K. E. T. Berton, C. Battilocchio, S. V. Ley and C. V. Stevens, *Chem. Soc. Rev.*, 2016, **45**, 4892–4928.
6. J. Yoshida, A. Nagaki and T. Yamada, *Chem.: Eur. J.*, 2008, **14**, 7450–7459.
7. J. Pelleter and F. Renaud, *Org. Process Res. Dev.*, 2009, **13**, 698–705.
8. K. P. Cole, J. M. Groh, M. D. Johnson, C. L. Burcham, B. M. Campbell, W. D. Diserod, M. R. Heller, J. R. Howell, N. J. Kallman, T. M. Koenig, S. A. May, R. D. Miller, D. Mitchell, D. P. Myers, S. S. Myers, J. L. Phillips, C. S. Polster, T. D. White, J. Cashman, D. Hurley, R. Moylan, P. Sheehan, R. D. Spencer, K. Desmond, P. Desmond and O. Gowran, *Science*, 2017, **356**, 1144–1150.
9. M. Balti, M. L. Efrat and N. E. Leadbeater, *Tetrahedron Lett.*, 2016, **57**, 1804–1806.
10. B. Gutmann and C. O. Kappe, *J. Flow. Chem.*, 2017, **7**, 65–71.
11. Forbidden Chemistries – The Kappe Laboratory, <http://goflow.at/research/forbidden-chemistries/>, (accessed 3 April 2019).
12. H. Herwig, in *Micro Process Engineering*, John Wiley & Sons, Ltd, 2008, pp. 47–70.
13. C. Jiménez-González, P. Poehlauer, Q. B. Broxterman, B.-S. Yang, D. am Ende, J. Baird, C. Bertsch, R. E. Hannah, P. Dell’Orco, H. Noorman, S. Yee, R. Reintjens, A. Wells, V. Massonneau and J. Manley, *Org. Process Res. Dev.*, 2011, **15**, 900–911.
14. B. P. Mason, K. E. Price, J. L. Steinbacher, A. R. Bogdan and D. T. McQuade, *Chem. Rev.*, 2007, **107**, 2300–2318.
15. S. G. Newman and K. F. Jensen, *Green Chem.*, 2013, **15**, 1456–1472.
16. J. Wegner, S. Ceylan and A. Kirschning, *Adv. Synth. Catal.*, 2012, **354**, 17–57.
17. P. L. Heider, S. C. Born, S. Basak, B. Benyahia, R. Lakerveld, H. Zhang, R. Hogan, L. Buchbinder, A. Wolfe, S. Mascia, J. M. B. Evans, T. F. Jamison and K. F. Jensen, *Org. Process Res. Dev.*, 2014, **18**, 402–409.
18. J. Britton and C. L. Raston, *Chem. Soc. Rev.*, 2017, **46**, 1250–1271.
19. A. Adamo, R. L. Beingessner, M. Behnam, J. Chen, T. F. Jamison, K. F. Jensen, J.-C. M. Monbaliu, A. S. Myerson, E. M. Revalor, D. R. Snead, T. Stelzer, N. Weeranoppanant, S. Y. Wong and P. Zhang, *Science*, 2016, **352**, 61–67.
20. Flow Chemistry Products | Chemtrix BV, <https://www.chemtrix.com/products>, (accessed 1 April 2019).



21. Advanced-Flow™ Reactors (AFR) | Continuous Lab Flow and Industrial Reactor Technology | Corning, <https://www.corning.com/emea/en/innovation/corning-emerging-innovations/advanced-flow-reactors.html>, (accessed 1 April 2019).
22. Products, <https://www.nitechsolutions.co.uk/products/>, (accessed 1 April 2019).
23. P. Poechlauer, J. Manley, R. Broxterman, B. Gregertsen and M. Ridemark, *Org. Process Res. Dev.*, 2012, **16**, 1586–1590.
24. J. I. Grayson, *Org. Process Res. Dev.*, 1997, **1**, 240–246.
25. S. G. Koenig and H. F. Sneddon, *Green Chem.*, 2017, **19**, 1418–1419.
26. M. Baumann and I. R. Baxendale, *Beilstein J. Org. Chem.*, 2015, **11**, 1194–1219.
27. M. Baumann, I. R. Baxendale and S. V. Ley, *Mol Divers*, 2011, **15**, 613–630.
28. A. I. Stankiewicz and J. A. Moulijn, *Chem. Eng. Prog.*, **96**, 22–34.
29. N. G. Anderson, *Org. Process Res. Dev.*, 2001, **5**, 613–621.
30. T. Laird, *Org. Process Res. Dev.*, 2001, **5**, 612–612.
31. V. Hessel, *Chem. Eng. Technol.*, 2009, **32**, 1655–1681.
32. F. E. Valera, M. Quaranta, A. Moran, J. Blacker, A. Armstrong, J. T. Cabral and D. G. Blackmond, *Angew. Chem. Int. Ed.*, 2010, **49**, 2478–2485.
33. R. L. Hartman, J. P. McMullen and K. F. Jensen, *Angew. Chem. Int. Ed.*, 2011, **50**, 7502–7519.
34. F. M. Akwi and P. Watts, *Chem. Commun.*, 2018, **54**, 13894–13928.
35. J. M. Neumaier, A. Madani, T. Klein and T. Ziegler, *Beilstein J. Org. Chem.*, 2019, **15**, 558–566.
36. B. Gutmann, M. Köckinger, G. Glotz, T. Ciaglia, E. Slama, M. Zdravec, S. Pfanner, M. C. Maier, H. Gruber-Wölfler and C. O. Kappe, *React. Chem. Eng.*, 2017, **2**, 919–927.
37. O. Okafor, A. Weilhard, J. A. Fernandes, E. Karjalainen, R. Goodridge and V. Sans, *React. Chem. Eng.*, 2017, **2**, 129–136.
38. R. L. Hartman, J. R. Naber, N. Zaborenko, S. L. Buchwald and K. F. Jensen, *Org. Process Res. Dev.*, 2010, **14**, 1347–1357.
39. R. L. Hartman, *Org. Process Res. Dev.*, 2012, **16**, 870–887.
40. T. Noël, J. R. Naber, R. L. Hartman, J. P. McMullen, K. F. Jensen and S. L. Buchwald, *Chem. Sci.*, 2011, **2**, 287–290.
41. V-3 Pump features, <https://www.vapourtec.com/products/e-series-reagent-pumping/the-v3-pump-features/>, (accessed 10 December 2018).
42. M. R. Chapman, M. H. T. Kwan, G. King, K. E. Jolley, M. Hussain, S. Hussain, I. E. Salama, C. González Niño, L. A. Thompson, M. E. Bayana, A. D. Clayton, B. N. Nguyen, N. J. Turner, N. Kapur and A. J. Blacker, *Org. Process Res. Dev.*, 2017, **21**, 1294–1301.
43. Y. Mo and K. F. Jensen, *React. Chem. Eng.*, 2016, **1**, 501–507.
44. R. J. Berger, F. Kapteijn, J. A. Moulijn, G. B. Marin, J. De Wilde, M. Olea, D. Chen, A. Holmen, L. Lietti, E. Tronconi and Y. Schuurman, *Appl. Catal., A*, 2008, **342**, 3–28.

45. Flow Commander software, <https://www.vapourtec.com/products/r-series-control/flow-commander-software-overview/>, (accessed 2 October 2018).
46. Asia Manager PC Software for Syrris Asia flow chemistry systems, <https://syrris.com/modules/asia-manager-pc-software/>, (accessed 2 October 2018).
47. Fusion 4000 | Multi-Channel Syringe Pump, <https://www.chemyx.com/syringe-pumps/fusion-4000/>, (accessed 2 October 2018).
48. K. Poschary, D. C. Fabry, S. Heddrich, E. Sugiono, M. A. Liauw and M. Rueping, *Tetrahedron*, 2018, **74**, 3171–3175.
49. C. Houben and A. A. Lapkin, *Curr Opin Chem Eng*, 2015, **9**, 1–7.
50. F. Venturoni, N. Nikbin, S. V. Ley and I. R. Baxendale, *Org. Biomol. Chem.*, 2010, **8**, 1798–1806.
51. S. A. Weissman and N. G. Anderson, *Org. Process Res. Dev.*, 2015, **19**, 1605–1633.
52. A. Palmieri, S. V. Ley, K. Hammond, A. Polyzos and I. R. Baxendale, *Tetrahedron Lett.*, 2009, **50**, 3287–3289.
53. A. Sugimoto, T. Fukuyama, Md. T. Rahman and I. Ryu, *Tetrahedron Lett.*, 2009, **50**, 6364–6367.
54. C. Wille, H.-P. Gabski, T. Haller, H. Kim, L. Unverdorben and R. Winter, *Chem. Eng. J.*, 2004, **101**, 179–185.
55. J. Wegner, S. Ceylan and A. Kirschning, *Chem. Commun.*, 2011, **47**, 4583–4592.
56. B. Walsh, J. R. Hyde, P. Licence and M. Poliakoff, *Green Chem.*, 2005, **7**, 456–463.
57. R. J. Ingham, C. Battilocchio, J. M. Hawkins and S. V. Ley, *Beilstein J. Org. Chem.*, 2014, **10**, 641–652.
58. R. P. Foundation, Raspberry Pi — Teach, Learn, and Make with Raspberry Pi, <https://www.raspberrypi.org>, (accessed 21 September 2018).
59. Welcome to Python.org, <https://www.python.org/>, (accessed 21 September 2018).
60. J. A. Nelder and R. Mead, *Comput J*, 1965, **7**, 308–313.
61. M. W. Routh, P. A. Swartz and M. B. Denton, *Anal. Chem.*, 1977, **49**, 1422–1428.
62. J. A. Snyman and D. N. Wilke, *Practical Mathematical Optimization: Basic Optimization Theory and Gradient-Based Algorithms*, Springer International Publishing, 2nd edn., 2018.
63. W. Huyer and A. Neumaier, *ACM Trans. Math. Softw.*, 2008, **35**, 9:1–9:25.
64. E. W. Kirchhoff, D. R. Anderson, S. Zhang, C. S. Cassidy and M. T. Flavin, *Org. Process Res. Dev.*, 2001, **5**, 50–53.
65. J. Zhang, E. W. Kirchhoff, D. E. Zembower, N. Jimenez, P. Sen, Z.-Q. Xu and M. T. Flavin, *Org. Process Res. Dev.*, 2000, **4**, 577–580.
66. A. J. Parrott, R. A. Bourne, G. R. Akien, D. J. Irvine and M. Poliakoff, *Angew. Chem. Int. Ed.*, 2011, **50**, 3788–3792.
67. P. N. Gooden, R. A. Bourne, A. J. Parrott, H. S. Bevinakatti, D. J. Irvine and M. Poliakoff, *Org. Process Res. Dev.*, 2010, **14**, 411–416.

68. R. A. Bourne, R. A. Skilton, A. J. Parrott, D. J. Irvine and M. Poliakoff, *Org. Process Res. Dev.*, 2011, **15**, 932–938.
69. C. F. Carter, H. Lange, S. V. Ley, I. R. Baxendale, B. Wittkamp, J. G. Goode and N. L. Gaunt, *Org. Process Res. Dev.*, 2010, **14**, 393–404.
70. M.-T. I. I. all rights reserved, ReactIR For Continuous Flow Chemistry, [https://www.mt.com/gb/en/home/products/L1\\_AutochemProducts/ReactIR/flow-ir-chemis.html](https://www.mt.com/gb/en/home/products/L1_AutochemProducts/ReactIR/flow-ir-chemis.html), (accessed 25 September 2018).
71. R. A. Skilton, A. J. Parrott, M. W. George, M. Poliakoff and R. A. Bourne, *Appl Spectrosc*, 2013, **67**, 1127–1131.
72. E. Morgan, K. W. Burton and G. Nickless, *Chemom. Intell. Lab. Syst.*, 1990, **7**, 209–222.
73. D. C. Fabry, E. Sugiono and M. Rueping, *Isr. J. Chem.*, 2014, **54**, 341–350.
74. ThalesNano Nanotechnology Inc - H-Cube Series, <http://thalesnano.com/h-cube-series>, (accessed 19 October 2018).
75. V. Sans, L. Porwol, V. Dragone and L. Cronin, *Chem. Sci.*, 2015, **6**, 1258–1264.
76. Spinsolve Benchtop NMR | Magritek, <http://www.magritek.com/products/spinsolve/>, (accessed 24 October 2018).
77. D. Cortés-Borda, E. Wimmer, B. Gouilleux, E. Barré, N. Oger, L. Goulamaly, L. Peault, B. Charrier, C. Truchet, P. Giraudeau, M. Rodriguez-Zubiri, E. Le Grogneec and F.-X. Felpin, *J. Org. Chem.*, 2018, **83**, 14286–14299.
78. J. Kiefer, *Proc. Amer. Math. Soc.*, 1953, **4**, 502–506.
79. B. Gouilleux, B. Charrier, S. Akoka and P. Giraudeau, *Magn. Reson. Chem.*, 2017, **55**, 91–98.
80. J. P. McMullen, M. T. Stone, S. L. Buchwald and K. F. Jensen, *Angew. Chem. Int. Ed.*, 2010, **49**, 7076–7080.
81. J. P. McMullen and K. F. Jensen, *Org. Process Res. Dev.*, 2010, **14**, 1169–1176.
82. T. A. Nijhuis, J. Chen, S. M. A. Kriescher and J. C. Schouten, *Ind. Eng. Chem. Res.*, 2010, **49**, 10479–10485.
83. T. Salmi, J. Hernández Carucci, M. Roche, K. Eränen, J. Wärnå and D. Murzin, *Chem. Eng. Sci.*, 2013, **87**, 306–314.
84. A. Echtermeyer, Y. Amar, J. Zakrzewski and A. Lapkin, *Beilstein J. Org. Chem.*, 2017, **13**, 150–163.
85. G. Franceschini and S. Macchietto, *Chem. Eng. Sci.*, 2008, **63**, 4846–4872.
86. J. Zakrzewski, A. P. Smalley, M. A. Kabeshov, M. J. Gaunt and A. A. Lapkin, *Angew. Chem. Int. Ed.*, 2016, **55**, 8878–8883.
87. A. P. Smalley and M. J. Gaunt, *J. Am. Chem. Soc.*, 2015, **137**, 10632–10641.
88. J. P. McMullen and K. F. Jensen, *Org. Process Res. Dev.*, 2011, **15**, 398–407.
89. B. J. Reizman and K. F. Jensen, *Org. Process Res. Dev.*, 2012, **16**, 1770–1782.
90. S. Mozharov, A. Nordon, J. M. Girkin and D. Littlejohn, *Lab Chip*, 2010, **10**, 2101–2107.

91. B. D. A. Hook, W. Dohle, P. R. Hirst, M. Pickworth, M. B. Berry and K. I. Booker-Milburn, *J. Org. Chem.*, 2005, **70**, 7558–7564.
92. L. D. Elliott, M. Berry, B. Harji, D. Klauber, J. Leonard and K. I. Booker-Milburn, *Org. Process Res. Dev.*, 2016, **20**, 1806–1811.
93. T. Aillet, K. Loubière, O. Dechy-Cabaret and L. Prat, *Chem. Eng. Technol.*, 2016, **39**, 115–122.
94. S. Mozharov, A. Nordon, D. Littlejohn, C. Wiles, P. Watts, P. Dallin and J. M. Girkin, *J. Am. Chem. Soc.*, 2011, **133**, 3601–3608.
95. T. Durand, C. Henry, D. Bolien, D. C. Harrowven, S. Bloodworth, X. Franck and R. J. Whitby, *React. Chem. Eng.*, 2016, **1**, 82–89.
96. R. J. Clemens and J. S. Witzeman, *J. Am. Chem. Soc.*, 1989, **111**, 2186–2193.
97. J. S. Moore and K. F. Jensen, *Angew. Chem. Int. Ed.*, 2014, **53**, 470–473.
98. C. A. Hone, N. Holmes, G. R. Akien, R. A. Bourne and F. L. Muller, *React. Chem. Eng.*, 2017, **2**, 103–108.
99. K. C. Aroh and K. F. Jensen, *React. Chem. Eng.*, 2018, **3**, 94–101.
100. M. V. Gomez, A. M. Rodriguez, A. de la Hoz, F. Jimenez-Marquez, R. M. Fratila, P. A. Barneveld and A. H. Velders, *Anal. Chem.*, 2015, **87**, 10547–10555.
101. B. Ahmed-Omer, J. C. Brandt and T. Wirth, *Org. Biomol. Chem.*, 2007, **5**, 733–740.
102. S. V. Ley, *Chem. Rec.*, 2012, **12**, 378–390.
103. G. K. Batchelor, *An Introduction to Fluid Dynamics*, Cambridge University Press, 2000.
104. H. Tennekes, *A first course in turbulence*, Cambridge, Mass. : MIT Press, [1972], 1972.
105. S. B. Pope, *Turbulent Flows*, Cambridge University Press, Cambridge, 2000.
106. G. Taylor, *Proc. Royal Soc. A*, 1953, **219**, 186–203.
107. O. Levenspiel, *Chemical Reaction Engineering*, Wiley and Sons, 1972, vol. 2nd ed.
108. K. D. Nagy, B. Shen, T. F. Jamison and K. F. Jensen, *Org. Process Res. Dev.*, 2012, **16**, 976–981.
109. W. R. Dean, *Philos. Mag.*, 1927, **4**, 208–223.
110. W. R. D. M.A, *Philos. Mag.*, 1928, **5**, 673–695.
111. P. M. Ligrani, *A study of Dean vortex development and structure in a curved rectangular channel with aspect ratio of 40 at Dean numbers up to 430 [microform]* / Philip M. Ligrani, National Aeronautics and Space Administration, Office of Management, Scientific and Technical Information Program ; National Technical Information Service, distributor, [Washington, D.C.] : [Cleveland, Ohio] ; U.S. Army Research Laboratory ; [Springfield, Va, 1994.
112. M. Johnson and R. Kamm, *J. Fluid Mech.*, 1986, **172**, 329–345.
113. C. Henry, *PhD Thesis, Southampton University*, 2014.
114. M. S. R. Abbott, A. P. Harvey, G. V. Perez and M. K. Theodorou, *Interface Focus*, 2013, **3**, 20120036.

115. N. Reis, A. P. Harvey, M. R. Mackley, A. A. Vicente and J. A. Teixeira, *Chem. Eng. Res. Des.*, 2005, **83**, 357–371.
116. C. R. Brunold, J. C. B. Hunns, M. R. Mackley and J. W. Thompson, *Chem. Eng. Sci.*, 1989, **44**, 1227–1244.
117. A. W. Dickens, M. R. Mackley and H. R. Williams, *Chem. Eng. Sci.*, 1989, **44**, 1471–1479.
118. J. R. McDonough, A. N. Phan and A. P. Harvey, *Chem. Eng. J.*, 2015, **265**, 110–121.
119. J. R. McDonough, A. N. Phan, D. A. Reay and A. P. Harvey, *Chem. Eng. Process.*, 2016, **110**, 201–213.
120. A. N. Phan and A. P. Harvey, *Chem. Eng. J.*, 2012, **180**, 229–236.
121. S. Klutz, S. K. Kurt, M. Lobedann and N. Kockmann, *Chem. Eng. Res. Des.*, 2015, **95**, 22–33.
122. W. Luyben, in *Chemical Reactor Design and Control*, John Wiley & Sons, Ltd, 2006, pp. i–xvi.
123. Knitted reactor coil 57405, <https://www.sigmaaldrich.com/catalog/product/supelco/57405>, (accessed 12 November 2018).
124. HiChrom LC Consumables and Accessories Knitted Open Tubulat (KOT) Reactor, [http://www.hichrom.com/assets/HichromCat9-pdfs/CONSUMABLES\\_and\\_ACCESSORIES-Knitted\\_Open\\_Tubular\\_Reactor\\_p354.pdf](http://www.hichrom.com/assets/HichromCat9-pdfs/CONSUMABLES_and_ACCESSORIES-Knitted_Open_Tubular_Reactor_p354.pdf), (accessed 11 December 2018).
125. S. Afandizadeh and E. A. Foumeny, *Appl. Therm. Eng.*, 2001, **21**, 669–682.
126. G. Eigenberger and W. Ruppel, in *Ullmann's Encyclopedia of Industrial Chemistry*, American Cancer Society, 2012.
127. A. Bogdan and D. T. McQuade, *Beilstein J. Org. Chem.*, 2009, **5**, 17.
128. J. R. Naber and S. L. Buchwald, *Angew. Chem. Int. Ed.*, 2010, **49**, 9469–9474.
129. Glass beads Z250465, <https://www.sigmaaldrich.com/catalog/product/aldrich/z250465>, (accessed 13 November 2018).
130. M. Rhodes, in *Introduction to Particle Technology*, John Wiley & Sons, Ltd, 2008, pp. 153–168.
131. P. N. Dwivedi and S. N. Upadhyay, *Ind. Eng. Chem. Proc. Des. Dev.*, 1977, **16**, 157–165.
132. L. R. Snyder and H. J. Adler, *Anal. Chem.*, 1976, **48**, 1017–1022.
133. L. R. Snyder and H. J. Adler, *Anal. Chem.*, 1976, **48**, 1022–1027.
134. N. Hawbaker, E. Wittgrove, B. Christensen, N. Sach and D. G. Blackmond, *Org. Process Res. Dev.*, 2016, **20**, 465–473.
135. V. Hessel, H. Löwe and F. Schönfeld, *Chem. Eng. Sci.*, 2005, **60**, 2479–2501.
136. Large diameter tubular reactor for rapid mixing, <https://www.vapourtec.com/products/flow-reactors/large-diameter-tubular-reactor-for-rapid-mixing-features/>, (accessed 12 November 2018).
137. Multiport Connectors - Connectors for Fluidic Applications | IDEX Health & Science, <https://www.idex-hs.com/store/fluidics/fluidic-connections/connectors.html>, (accessed 19 November 2018).

138. D. Bothe, C. Stemich and H.-J. Warnecke, *Chem. Eng. Sci.*, 2006, **61**, 2950–2958.
139. D. Bolien, *PhD Thesis, Southampton University*, 2014.
140. P. Koos, D. L. Browne and S. V. Ley, *Green Process. Synth.*, 2012, **1**, 11–18.
141. K. Wang, H. Zhang, Y. Shen, A. Adamo and K. F. Jensen, *React. Chem. Eng.*, 2018, **3**, 707–713.
142. M. S. Williams, K. J. Longmuir and P. Yager, *Lab Chip*, 2008, **8**, 1121–1129.
143. A. D. Stroock, S. K. W. Dertinger, A. Ajdari, I. Mezić, H. A. Stone and G. M. Whitesides, *Science*, 2002, **295**, 647–651.
144. J. Peter B. Howell, D. R. Mott, J. P. Golden and F. S. Ligler, *Lab Chip*, 2004, **4**, 663–669.
145. R. A. Angnes, Z. Li, C. R. D. Correia and G. B. Hammond, *Org. Biomol. Chem.*, 2015, **13**, 9152–9167.
146. S. Poplata, A. Tröster, Y.-Q. Zou and T. Bach, *Chem. Rev.*, , DOI:10.1021/acs.chemrev.5b00723.
147. T. Bach and J. P. Hehn, *Angew. Chem. Int. Ed.*, 2011, **50**, 1000–1045.
148. N. Hoffmann, *Chem. Rev.*, 2008, **108**, 1052–1103.
149. A. A. Ghogare and A. Greer, *Chem. Rev.*, 2016, **116**, 9994–10034.
150. D. Cambié, C. Bottecchia, N. J. W. Straathof, V. Hessel and T. Noël, *Chem. Rev.*, 2016, **116**, 10276–10341.
151. M. D. Kärkäs, J. A. Porco and C. R. J. Stephenson, *Chem. Rev.*, 2016, **116**, 9683–9747.
152. F. Politano and G. Oksdath-Mansilla, *Org. Process Res. Dev.*, 2018, **22**, 1045–1062.
153. K. H. Pfoertner, *J. Photochem. Photobiol. A*, 1990, **51**, 81–86.
154. H. Metzger, D. Fries, U. Heuschkel, K. Witte, E. Waidelich and G. Schmid, *Angew. Chem.*, 1959, **71**, 229–236.
155. M. Fischer, *Angew. Chem. Int. Ed.*, 1978, **17**, 16–26.
156. K. N. Loponov, J. Lopes, M. Barlog, E. V. Astrova, A. V. Malkov and A. A. Lapkin, *Org. Process Res. Dev.*, 2014, **18**, 1443–1454.
157. N. Emmanuel, C. Mendoza, M. Winter, C. R. Horn, A. Vizza, L. Dreesen, B. Heinrichs and J.-C. M. Monbaliu, *Org. Process Res. Dev.*, 2017, **21**, 1435–1438.
158. K. C. Harper, E. G. Moschetta, S. V. Bordawekar and S. J. Wittenberger, *ACS Cent. Sci.*, 2019, **5**, 109–115.
159. T.-L. Ho and Z. U. Din, *Synth. Commun.*, 1982, **12**, 1099–1102.
160. R. B. Woodward and R. Hoffmann, *Angew. Chem. Int. Ed. Engl.*, 1969, **8**, 781–853.
161. J. Zhao, W. Wu, J. Sun and S. Guo, *Chem. Soc. Rev.*, 2013, **42**, 5323–5351.
162. Rayonet - Reactors, <https://rayonet.org/reactors.php>, (accessed 21 November 2018).

163. J. P. Knowles, L. D. Elliott and K. I. Booker-Milburn, *Beilstein J. Org. Chem.*, 2012, **8**, 2025–2052.
164. B. D. A. Hook, W. Dohle, P. R. Hirst, M. Pickworth, M. B. Berry and K. I. Booker-Milburn, *J. Org. Chem.*, 2005, **70**, 7558–7564.
165. D. C. Harrowven, M. Mohamed, T. P. Gonçalves, R. J. Whitby, D. Bolien and H. F. Sneddon, *Angew. Chem. Int. Ed.*, 2012, **51**, 4405–4408.
166. O. Shvydkiv, A. Yavorsky, S. B. Tan, K. Nolan, N. Hoffmann, A. Youssef and M. Oelgemöller, *Photochem. Photobiol. Sci.*, 2011, **10**, 1399–1404.
167. C. A. Clark, D. S. Lee, S. J. Pickering, M. Poliakoff and M. W. George, *Org. Process Res. Dev.*, 2016, **20**, 1792–1798.
168. UV-150 Photochemical Reactor | Vapourtec Ltd,  
<https://www.vapourtec.com/products/flow-reactors/photochemistry-uv-150-photochemical-reactor-features/>, (accessed 21 November 2018).
169. Y. Chen, D. C. Blakemore, P. Pasau and S. V. Ley, *Org. Lett.*, 2018, **20**, 6569–6572.
170. A. M. S. Galante, O. L. Galante and L. L. Campos, *Nucl. Instrum. Methods Phys. Res. a*, 2010, **619**, 177–180.
171. E. E. Coyle and M. Oelgemöller, *Photochem. Photobiol. Sci.*, 2008, **7**, 1313–1322.
172. 4058075001060 | LEDVANCE LED Floodlight, 1 LED, 20 W, IP65 230 V | RS Components,  
<https://uk.rs-online.com/web/p/led-floodlights/1223587/>, (accessed 22 November 2018).
173. D. Belluš and B. Ernst, *Angew. Chem. Int. Ed. Engl.*, 1988, **27**, 797–827.
174. E. Lee-Ruff and G. Mladenova, *Chem. Rev.*, 2003, **103**, 1449–1484.
175. T. Bach, *Synthesis*, 1998, **1998**, 683–703.
176. Y.-Y. Fan, X.-H. Gao and J.-M. Yue, *Sci. China Chem.*, 2016, **59**, 1126–1141.
177. A. Sergeiko, Poroikov, V. V, Hanuš, L. O, Dembitsky and V. M, *Open Med Chem J*, 2008, **2**, 26–37.
178. A. Figueras, R. Miralles-Llumà, R. Flores, A. Rustullet, F. Busqué, M. Figueredo, J. Font, R. Alibés and J.-D. Maréchal, *ChemMedChem*, 2012, **7**, 1044–1056.
179. R. Miralles-Llumà, A. Figueras, F. Busqué, A. Alvarez-Larena, J. Balzarini, M. Figueredo, J. Font, R. Alibés and J.-D. Maréchal, *Eur. J. Org. Chem.*, 2013, **2013**, 7761–7775.
180. K. G. Maskill, J. P. Knowles, L. D. Elliott, R. W. Alder and K. I. Booker-Milburn, *Angew. Chem. Int. Ed.*, 2013, **52**, 1499–1502.
181. M. Ralph, S. Ng and K. I. Booker-Milburn, *Org. Lett.*, 2016, **18**, 968–971.
182. C. Battilocchio, G. Iannucci, S. Wang, E. Godineau, A. Kolleth, A. D. Mesmaeker and S. V. Ley, *React. Chem. Eng.*, 2017, **2**, 295–298.
183. T. Fukuyama, Y. Hino, N. Kamata and I. Ryu, *Chem. Lett.*, 2004, **33**, 1430–1431.
184. S. Bachollet, K. Terao, S. Aida, Y. Nishiyama, K. Kakiuchi and M. Oelgemöller, *Beilstein J. Org. Chem.*, 2013, **9**, 2015–2021.

185. T. Mizoroki, K. Mori and A. Ozaki, *BCSJ*, 1971, **44**, 581–581.
186. K. Mori, T. Mizoroki and A. Ozaki, *BCSJ*, 1973, **46**, 1505–1508.
187. R. F. Heck and J. P. Nolley, *J. Org. Chem.*, 1972, **37**, 2320–2322.
188. H. A. Dieck and R. F. Heck, *J. Am. Chem. Soc.*, 1974, **96**, 1133–1136.
189. H. A. Dieck and R. F. Heck, *J. Org. Chem.*, 1975, **40**, 1083–1090.
190. I. P. Beletskaya and A. V. Cheprakov, *Chem. Rev.*, 2000, **100**, 3009–3066.
191. J. Le Bras and J. Muzart, *Chem. Rev.*, 2011, **111**, 1170–1214.
192. A. de Meijere and F. E. Meyer, *Angew. Chem. Int. Ed. Engl.*, 1995, **33**, 2379–2411.
193. G. T. Crisp, *Chem. Soc. Rev.*, 1998, **27**, 427–436.
194. G. D. Daves and A. Hallberg, *Chem. Rev.*, 1989, **89**, 1433–1445.
195. P. Devendar, R.-Y. Qu, W.-M. Kang, B. He and G.-F. Yang, *J. Agric. Food Chem.*, 2018, **66**, 8914–8934.
196. C. Torborg and M. Beller, *Adv. Synth. Catal.*, 2009, **351**, 3027–3043.
197. A. L. Casado and P. Espinet, *Organometallics*, 1998, **17**, 954–959.
198. C. G. Frost and L. Mutton, *Green Chem.*, 2010, **12**, 1687–1703.
199. T. Ichikawa, M. Mizuno, S. Ueda, N. Ohneda, H. Odajima, Y. Sawama, Y. Monguchi and H. Sajiki, *Tetrahedron*, 2018, **74**, 1810–1816.
200. D. A. Snyder, C. Noti, P. H. Seeberger, F. Schael, T. Bieber, G. Rimmel and W. Ehrfeld, *Helv. Chim. Acta*, 2005, **88**, 1–9.
201. B. Urbán, D. Srankó, G. Sáfrán, L. Üрге, F. Darvas, J. Bakos and R. Skoda-Földes, *J. Mol. Catal. A. Chem.*, 2014, **395**, 364–372.
202. P. L. Lau, R. W. K. Allen and P. Styring, *Beilstein J. Org. Chem.*, 2013, **9**, 2886–2897.
203. R. Narayanan and M. A. El-Sayed, *J. Am. Chem. Soc.*, 2003, **125**, 8340–8347.
204. R. Narayanan and M. A. El-Sayed, *J. Phys. Chem. B*, 2003, **107**, 12416–12424.
205. A. H. M. de Vries, J. M. C. A. Mulders, J. H. M. Mommers, H. J. W. Henderickx and J. G. de Vries, *Org. Lett.*, 2003, **5**, 3285–3288.
206. J. G. de Vries, *Dalton Trans.*, 2006, **0**, 421–429.
207. F. Zhao, B. M. Bhanage, M. Shirai and M. Arai, *Chem. Eur. J.*, 2000, **6**, 843–848.
208. B. M. Bhanage, M. Shirai and M. Arai, *J. Mol. Catal. A. Chem.*, 1999, **145**, 69–74.
209. M. T. Reetz and E. Westermann, *Angew. Chem. Int. Ed.*, 2000, **39**, 165–168.
210. M. T. Reetz, W. Helbig, S. A. Quaiser, U. Stimming, N. Breuer and R. Vogel, *Science*, 1995, **267**, 367–369.
211. M. B. Thathagar, J. E. ten Elshof and G. Rothenberg, *Angew. Chem. Int. Ed.*, 2006, **45**, 2886–2890.



212. V. P. Ananikov and I. P. Beletskaya, *Organometallics*, 2012, **31**, 1595–1604.
213. A. S. Kashin and V. P. Ananikov, *J. Org. Chem.*, 2013, **78**, 11117–11125.
214. M. Pagliaro, V. Pandarus, R. Ciriminna, F. Béland and P. Demma Carà, *ChemCatChem*, 2012, **4**, 432–445.
215. A. V. Gaikwad, A. Holuigue, M. B. Thathagar, J. E. ten Elshof and G. Rothenberg, *Chem.: Eur. J.*, 2007, **13**, 6908–6913.
216. T. N. Glasnov, S. Findenig and C. O. Kappe, *Chem. Eur. J.*, 2009, **15**, 1001–1010.
217. E. R. Strieter, D. G. Blackmond and S. L. Buchwald, *J. Am. Chem. Soc.*, 2003, **125**, 13978–13980.
218. A. F. Littke and G. C. Fu, *J. Org. Chem.*, 1999, **64**, 10–11.
219. A. F. Littke and G. C. Fu, *J. Am. Chem. Soc.*, 2001, **123**, 6989–7000.
220. K. H. Shaughnessy, P. Kim and J. F. Hartwig, *J. Am. Chem. Soc.*, 1999, **121**, 2123–2132.
221. G. C. Fu, *Acc. Chem. Res.*, 2008, **41**, 1555–1564.
222. W. A. Herrmann, C. Brossmer, K. Öfele, C.-P. Reisinger, T. Priermeier, M. Beller and H. Fischer, *Angew. Chem. Int. Ed. Engl.*, 1995, **34**, 1844–1848.
223. M. Ohff, A. Ohff, M. E. van der Boom and D. Milstein, *J. Am. Chem. Soc.*, 1997, **119**, 11687–11688.
224. C. Rocaboy and J. A. Gladysz, *Org. Lett.*, 2002, **4**, 1993–1996.
225. M. Ohff, A. Ohff and D. Milstein, *Chem. Commun.*, 1999, **0**, 357–358.
226. I. P. Beletskaya, A. N. Kashin, N. B. Karlstedt, A. V. Mitin, A. V. Cheprakov and G. M. Kazankov, *J. Organomet. Chem.*, 2001, **622**, 89–96.
227. D. E. Bergbreiter, P. L. Osburn, A. Wilson and E. M. Sink, *J. Am. Chem. Soc.*, 2000, **122**, 9058–9064.
228. A. S. Gruber, D. Zim, G. Ebeling, A. L. Monteiro and J. Dupont, *Org. Lett.*, 2000, **2**, 1287–1290.
229. J.-Y. Lee, P.-Y. Cheng, Y.-H. Tsai, G.-R. Lin, S.-P. Liu, M.-H. Sie and H. M. Lee, *Organometallics*, 2010, **29**, 3901–3911.
230. K. Selvakumar, A. Zapf and M. Beller, *Org. Lett.*, 2002, **4**, 3031–3033.
231. N. Marion and S. P. Nolan, *Acc. Chem. Res.*, 2008, **41**, 1440–1449.
232. S. L. Bourne, M. O'Brien, S. Kasinathan, P. Koos, P. Tolstoy, D. X. Hu, R. W. Bates, B. Martin, B. Schenkel and S. V. Ley, *ChemCatChem*, 2013, **5**, 159–172.
233. P. Koos, U. Gross, A. Polyzos, M. O'Brien, I. Baxendale and S. V. Ley, *Org. Biomol. Chem.*, 2011, **9**, 6903–6908.
234. I. D. Hills and G. C. Fu, *J. Am. Chem. Soc.*, 2004, **126**, 13178–13179.
235. B. Ahmed-Omer, D. A. Barrow and T. Wirth, *Tetrahedron Lett.*, 2009, **50**, 3352–3355.
236. S. Sharma, K. C. Basavaraju, A. K. Singh and D.-P. Kim, *Org. Lett.*, 2014, **16**, 3974–3977.

237. P. Li, J. S. Moore and K. F. Jensen, *ChemCatChem*, 2013, **5**, 1729–1733.
238. S. Liu, T. Fukuyama, M. Sato and I. Ryu, *Org. Process Res. Dev.*, 2004, **8**, 477–481.
239. M. T. Reetz and J. G. de Vries, *Chem. Commun.*, 2004, **0**, 1559–1563.
240. T. Jeffery, *Tetrahedron*, 1996, **52**, 10113–10130.
241. P. Cyr, S. T. Deng, J. M. Hawkins and K. E. Price, *Org. Lett.*, 2013, **15**, 4342–4345.
242. B. Movassagh, S. Yasham and M. Navidi, *Synlett*, 2013, **24**, 2671–2674.
243. K. Königsberger, G.-P. Chen, R. R. Wu, M. J. Girgis, K. Prasad, O. Repič and T. J. Blacklock, *Org. Process Res. Dev.*, 2003, **7**, 733–742.
244. D. H. B. Ripin, D. E. Bourassa, T. Brandt, M. J. Castaldi, H. N. Frost, J. Hawkins, P. J. Johnson, S. S. Massett, K. Neumann, J. Phillips, J. W. Raggon, P. R. Rose, J. L. Rutherford, B. Sitter, A. M. Stewart, M. G. Vetelino and L. Wei, *Org. Process Res. Dev.*, 2005, **9**, 440–450.
245. X. Jiang, G. T. Lee, K. Prasad and O. Repič, *Org. Process Res. Dev.*, 2008, **12**, 1137–1141.
246. B. P. Chekal, S. M. Guinness, B. M. Lillie, R. W. McLaughlin, C. W. Palmer, R. J. Post, J. E. Sieser, R. A. Singer, G. W. Sluggett, R. Vaidyanathan and G. J. Withbroe, *Org. Process Res. Dev.*, 2014, **18**, 266–274.
247. J. Magano and J. R. Dunetz, *Chem. Rev.*, 2011, **111**, 2177–2250.
248. C. Amatore, E. Carre, A. Jutand, M. A. M'Barki and G. Meyer, *Organometallics*, 1995, **14**, 5605–5614.
249. J.-F. Fauvarque, F. Pflüger and M. Troupel, *J. Organomet. Chem.*, 1981, **208**, 419–427.
250. B. P. Carrow and John. F. Hartwig, *J. Am. Chem. Soc.*, 2010, **132**, 79–81.
251. F. d'Orlyé and A. Jutand, *Tetrahedron*, 2005, **61**, 9670–9678.
252. C. Amatore, E. Carre, A. Jutand and M. A. M'Barki, *Organometallics*, 1995, **14**, 1818–1826.
253. M. Qadir, T. Möchel and K. K. (Mimi) Hii, *Tetrahedron*, 2000, **56**, 7975–7979.
254. S. Iyer, G. M. Kulkarni and C. Ramesh, *Tetrahedron*, 2004, **60**, 2163–2172.
255. E. H. Rahim, F. S. Kamounah, J. Frederiksen and J. B. Christensen, *Nano Lett.*, 2001, **1**, 499–501.
256. T. Iwasawa, M. Tokunaga, Y. Obora and Y. Tsuji, *J. Am. Chem. Soc.*, 2004, **126**, 6554–6555.
257. K. D. Collins and F. Glorius, *Nat Chem*, 2013, **5**, 597–601.
258. R. Kecili, D. Nivhede, J. Billing, M. Leeman, B. Sellergren and E. Yilmaz, *Org. Process Res. Dev.*, 2012, **16**, 1225–1229.
259. D. B. and S. Gorog, Recent Advances in the Impurity Profiling of Drugs, <http://www.eurekaselect.com/67935/article>, (accessed 19 July 2019).
260. N. S. Nasri, J. M. Jones, V. A. Dupont and A. Williams, *Energy Fuels*, 1998, **12**, 1130–1134.
261. A. Kolpin, G. Jones, S. Jones, W. Zheng, J. Cookson, A. P. E. York, P. J. Collier and S. C. E. Tsang, *ACS Catal.*, 2017, **7**, 592–605.

262. C. E. Garrett and K. Prasad, *Adv. Synth. Catal.*, 2004, **346**, 889–900.
- 263 B. P. S. Chauhan, J. S. Rathore and T. Bando, *J. Am. Chem. Soc.*, 2004, **126**, 8493–8500.
264. A. S. Hoffman, *Macromolecular Symposia*, 1996, **101**, 443–454.
265. C. A. Lipinski, F. Lombardo, B. W. Dominy and P. J. Feeney, *Adv. Drug Deliv. Rev.*, 2001, **46**, 3–26.
266. C. A. Lipinski, *Drug Discov. Today Technol.*, 2004, **1**, 337–341.
267. M. W. Harrold and R. M. Zavod, *Basic Concepts in Medicinal Chemistry*, American Society of Health-System Pharmacists, 2013.
268. A. Gomtsyan, *Chem Heterocycl Comp*, 2012, **48**, 7–10.
269. Top Pharmaceuticals Poster | Njarðarson, <https://njarðarson.lab.arizona.edu/content/top-pharmaceuticals-poster>, (accessed 2 December 2018).
270. M. K. M. Young and T. J. Gries, *J. Chem. Educ.*, 2015, **92**, 2173–2175.
271. R. Chinchilla and C. Nájera, *Chem. Soc. Rev.*, 2011, **40**, 5084–5121.
272. R. Chinchilla and C. Nájera, *Chem. Rev.*, 2007, **107**, 874–922.
273. M. Schilz and H. Plenio, *J. Org. Chem.*, 2012, **77**, 2798–2807.
274. M. Bakherad, *Appl. Organomet. Chem.*, 2013, **27**, 125–140.
275. K. Sonogashira, Y. Tohda and N. Hagihara, *Tetrahedron Lett.*, 1975, **16**, 4467–4470.
276. M. W. Miller and C. R. Johnson, *J. Org. Chem.*, 1997, **62**, 1582–1583.
277. K. C. Nicolaou, T. Ladduwahetty, I. M. Taffer and R. E. Zipkin, *Synthesis*, 1986, **1986**, 344–347.
278. T. Sakamoto, F. Shiga, A. Yasuhara, D. Uchiyama, Y. Kondo and H. Yamanaka, *Synthesis*, 1992, **1992**, 746–748.
279. A. S. Hay, *J. Org. Chem.*, 1962, **27**, 3320–3321.
280. C. Glaser, *Ber. Dtsch. Chem. Ges.*, 1869, **2**, 422–424.
281. M. Bakherad, A. Keivanloo, B. Bahramian and S. Mihanparast, *Tetrahedron Lett.*, 2009, **50**, 6418–6420.
282. T. Suzuka, Y. Okada, K. Ooshiro and Y. Uozumi, *Tetrahedron*, 2010, **66**, 1064–1069.
283. M. Gredičak and I. Jerić, *Synlett*, 2009, **2009**, 1063–1066.
284. C. Sotiriou-Leventis, X. Wang, S. Mulik, A. Thangavel and N. Leventis, *Synth. Commun.*, 2008, **38**, 2285–2298.
285. E. Tyrrell, L. Whiteman and N. Williams, *Synthesis*, 2009, **2009**, 829–835.
286. S. S. Palimkar, V. S. More, P. H. Kumar and K. V. Srinivasan, *Tetrahedron*, 2007, **63**, 12786–12790.
287. S. S. Palimkar, P. Harish Kumar, R. J. Lahoti and K. V. Srinivasan, *Tetrahedron*, 2006, **62**, 5109–5115.

288. B. Liang, M. Dai, J. Chen and Z. Yang, *J. Org. Chem.*, 2005, **70**, 391–393.
289. A. Soheili, J. Albaneze-Walker, J. A. Murry, P. G. Dormer and D. L. Hughes, *Org. Lett.*, 2003, **5**, 4191–4194.
290. Z. Gu, Z. Li, Z. Liu, Y. Wang, C. Liu and J. Xiang, *Catal. Commun.*, 2008, **9**, 2154–2157.
291. F. N. Ngassa, E. A. Lindsey and B. E. Haines, *Tetrahedron*, 2009, **65**, 4085–4091.
292. H. Huang, H. Liu, H. Jiang and K. Chen, *J. Org. Chem.*, 2008, **73**, 6037–6040.
293. D. Gelman and S. L. Buchwald, *Angew. Chem. Int. Ed.*, 2003, **42**, 5993–5996.
294. K. Prabakaran, F. Nawaz Khan and J. S. Jin, *Tetrahedron Lett.*, 2011, **52**, 2566–2570.
295. T. Fukuyama, M. Shinmen, S. Nishitani, M. Sato and I. Ryu, *Org. Lett.*, 2002, **4**, 1691–1694.
296. W. Shu and S. L. Buchwald, *Chem. Sci.*, 2011, **2**, 2321–2325.
297. H. Kawanami, K. Matsushima, M. Sato and Y. Ikushima, *Angew. Chem.*, 2007, **119**, 5221–5224.
298. M. Matiur. Rahman, H. Ye. Liu, Klaas. Eriks, Alfred. Prock and W. P. Giering, *Organometallics*, 1989, **8**, 1–7.
299. M. Iizuka and Y. Kondo, *Chem. Commun.*, 2006, **0**, 1739–1741.
300. N. G. Andersen and B. A. Keay, *Chem. Rev.*, 2001, **101**, 997–1030.
301. V. Farina and B. Krishnan, *J. Am. Chem. Soc.*, 1991, **113**, 9585–9595.
302. E. Drent, P. Arnoldy and P. H. M. Budzelaar, *J. Organomet. Chem.*, 1994, **475**, 57–63.
303. P. Dierkes and P. W. N. M. van Leeuwen, *J. Chem. Soc., Dalton Trans.*, 1999, **0**, 1519–1530.
304. P. C. J. Kamer, P. W. N. M. van Leeuwen and J. N. H. Reek, *Acc. Chem. Res.*, 2001, **34**, 895–904.
305. T. Hayashi, M. Konishi, Y. Kobori, M. Kumada, T. Higuchi and K. Hirotsu, *J. Am. Chem. Soc.*, 1984, **106**, 158–163.
306. P. W. N. M. van Leeuwen, P. C. J. Kamer, J. N. H. Reek and P. Dierkes, *Chem. Rev.*, 2000, **100**, 2741–2770.
307. M. Kranenburg, P. C. J. Kamer and P. W. N. M. van Leeuwen, *Eur. J. Inorg. Chem.*, 1998, **1998**, 155–157.
308. C. A. Tolman, *Chem. Rev.*, 1977, **77**, 313–348.
309. J. A. Bilbrey, A. H. Kazez, J. Locklin and W. D. Allen, *J. Comput. Chem.*, 2013, **34**, 1189–1197.
310. H. Mayr and M. Patz, *Angew. Chem. Int. Ed. Engl.*, 1994, **33**, 938–957.
311. T. Kanzian, T. A. Nigst, A. Maier, S. Pichl and H. Mayr, *Eur. J. Org. Chem.*, 2009, **2009**, 6379–6385.
312. S. Lal and S. Díez-González, *J. Org. Chem.*, 2011, **76**, 2367–2373.
313. R. D. Padmaja, D. R. Meena, B. Maiti and K. Chanda, *Res Chem Intermed*, 2017, **43**, 7365–7374.

314. V. O. Rodionov, V. V. Fokin and M. G. Finn, *Angew. Chem. Int. Ed.*, **44**, 2210–2215.
315. CuI | Sigma-Aldrich,  
<https://www.sigmaaldrich.com/catalog/search?term=CuI&interface=All&N=0&mode=match%20partialmax&lang=en&region=GB&focus=product>, (accessed 17 December 2018).
316. (1,10-<WBR>Phenanthroline)<WBR>bis(triphenylphosphine)<WBR>copper(I) nitrate dichloromethane adduct 707007,  
<https://www.sigmaaldrich.com/catalog/product/aldrich/707007>, (accessed 17 December 2018).
317. J. E. Hein and V. V. Fokin, *Chem. Soc. Rev.*, 2010, **39**, 1302–1315.
318. R. M. Moorman, M. B. Collier, B. H. Frohock, M. D. Womble and J. M. Chalker, *Org. Biomol. Chem.*, 2015, **13**, 1974–1978.
319. J. Ichikawa, *Org. Synth.*, 2011, **88**, 238.
320. M. Stefaniak, M. Jasiński and J. Romański, *Synthesis*, 2013, **45**, 2245–2250.
321. C. W. Tornøe, C. Christensen and M. Meldal, *J. Org. Chem.*, 2002, **67**, 3057–3064.
322. Z.-Y. Yan, Y.-B. Zhao, M.-J. Fan, W.-M. Liu and Y.-M. Liang, *Tetrahedron*, 2005, **61**, 9331–9337.
323. V. O. Rodionov, S. I. Presolski, S. Gardinier, Y.-H. Lim and M. G. Finn, *J. Am. Chem. Soc.*, 2007, **129**, 12696–12704.
324. B. R. Buckley, S. E. Dann and H. Heaney, *Chem. Eur. J.*, 2010, **16**, 6278–6284.
325. A. Martell, in *Ascorbic Acid: Chemistry, Metabolism, and Uses*, AMERICAN CHEMICAL SOCIETY, 1982, vol. 200, pp. 153–178.
326. M. Carmona, A. Lech, A. de Lucas, A. Pérez and J. F. Rodriguez, *J. Chem. Technol. Biotechnol.*, 2009, **84**, 1130–1135.
327. S. Alston and R. J. Whitby, DOI: 10.5258/SOTON/D1066, 2021.
328. H. M. Rosenberg and M. P. Serve, *J. Org. Chem.*, 1968, **33**, 1653–1654.
329. S. G. Alvarez and M. T. Alvarez, *Synthesis*, 1997, **1997**, 413–414.
330. D. Wang, N. Li, M. Zhao, W. Shi, C. Ma and B. Chen, *Green Chem.*, 2010, **12**, 2120–2123.
331. K. Kamata, Y. Nakagawa, K. Yamaguchi and N. Mizuno, *J. Am. Chem. Soc.*, 2008, **130**, 15304–15310.